MONASH University

Stability and Heat Transfer Characteristics of Hydrodynamic Channel Flows and Quasi-two-dimensional Magnetohydrodynamic Duct Flows with Repeated Wedge-shaped Protrusions

by

Sneha Murali

A thesis submitted for the degree of

Doctor of Philosophy

at

Monash University

March 2022

Department of Mechanical and Aerospace Engineering

To Amma & Appa.

Copyright Notice

"*If nature were not beautiful, it would not be worth studying it. And life would not be worth living*".

– Henry Poincaré

Abstract

This thesis reports on a numerical study of hydrodynamic channel flows and quasi-two-dimensional magnetohydrodynamic duct flows with repeated flow-facing wedge protrusions and the heat transfer enhancement achieved in these flows. The study is motivated by an interest in inciting instabilities and mixing for heat transfer enhancement in cooling blanket modules in nuclear fusion reactors. Previous research in the hydrodynamic cases has focused only on the high Reynolds number regimes to study the heat transfer behaviour. For the quasi-two-dimensional MHD cases, previous research explored either using passive and active bluff bodies in the flow, using variable wall conductivity and using electrically generated vortices for vortex generation. The current study reports on the stability characteristics and the route to turbulence in both hydrodynamic channel flows and quasi-two-dimensional magnetohydrodynamic duct flows using a modification on the duct walls. The heat transfer enhancement with the use of surface modification, which has not received much attention in MHD flows is also reported in this thesis.

Flow in a channel with repeated wedge-shaped surface protrusions is considered for various blockage ratios (wedge height to duct height), pitch (distance between wedges) and wedge angles. Different flow regimes based on the flow structure are identified and the temperature field associated with the steady and unsteady regimes is presented. Global linear stability analysis is performed to characterise the stability of the two-dimensional base flow, and its dependence on various geometric parameters of the wedge is elucidated. A two-dimensional mode through which the onset of unsteadiness occurs was found, differing from similar confined flow setups.

The primary instability, however, is found to occur through a three-dimensional mode which manifests as counter-rotating streamwise vortices over the wedge tip. The physical mechanism driving the instability was studied by analysing the perturbation velocity contribution and kinetic energy budget. A lift-up mechanism was found responsible for flow instability with the dominant energy

gain of the global 3D mode due to shear in the base flow.

Analysis of the sensitivity of the instability to momentum forcing or base flow modifications is used to identify the core of the instability and locations in the flow which are important from a flow control perspective. An endogeneity approach shows that the component arising from the local perturbation pressure gradient term can have a dominant influence on the growth rate of the linear global eigenmode in most cases considered, which was not identified from the presented exogeneous appoaches. Through the transient growth studies, low algebraic energy gain by convective instabilities was found in the linearly stable regimes of the flow, being orders of magnitude lower than in other channel flow setups reported in the literature.

Non-linear simulations were conducted to verify and validate the findings from the linear analysis. The linear global modes are found to compare well with the flow structures from the non-linear simulations in the linear and weakly non-linear stages. The effect of non-linearity is elucidated through flow visualisations highlighting how these structures could be favourable to enhance heat transfer rate. Weakly non-linear Stuart–Landau analysis shows that the primary bifurcation is supercritical for the flow at selected geometric parameter combinations.

The flow regimes for a quasi-two-dimensional magnetodydrodynamic flow in a duct with repeated wedge-shaped protrusions are identified for different blockage ratios considering a range of Hartmann friction parameters. The quasi-two-dimensional mode through which instability manifests and the critical Reynolds number are also elucidated in the same parameter range. Large transient amplification of quasi-two-dimensional perturbations are found at higher Hartmann friction parameters, differing from what was observed for the hydrodynamic cases. Non-linear effects are found to increase the time for energy dissipation of the quasi-two-dimensional disturbance, though sub-critical transitions were not observed.

The influence of wedge protrusions on the duct walls on the heat transfer efficiency as well as its overall effectiveness taking into account the pressure losses are explored for a range of Hartmann friction parameters. The effect of blockage ratio, pitch and wedge angle on heat transfer ratio as well as efficiency are considered. A monotonic increase in the heat transfer ratio with increasing blockage ratio is observed in the range of parameters investigated. It is possible to further improve the heat transfer rate by changing the geometric parameter to an optimal pitch and optimal wedge angle. Corresponding to each Hartmann friction parameter there exists an optimal geometric parameter condition where maximum heat transfer efficiency could be achieved. In contrast to the optimal blockage ratio

which showed a monotonic increase with increasing Hartmann friction parameter, the optimal pitch and wedge angle showed a reversal in the trend after a critical value. Effectiveness of surface modification on the heated wall is also established through a net power analysis. A comparison of the technique of surface modification used in the present study with other vortex generation techniques showed the range of the operating parameters, where the current vortex generation method could be most effective for obtaining maximum heat transfer efficiency.

The current study contributes to the understanding of the flow dynamics in hydrodynamic channel flows and quasi-2D magnetohydrodynamic duct flows with repeated wedges, as well as in studying the effectiveness of the surface modification technique as a means to promote heat transfer efficiency in quasi-2D MHD duct flows. These understanding are beneficial for effective design and control of duct flows.

Declaration

This thesis is an original work of my research and contains no material which has been accepted for the award of any other degree or diploma at any university or equivalent institution and that, to the best of my knowledge and belief, this thesis contains no material previously published or written by another person, except where due reference is made in the text of the thesis.

Sneha Murali

March 2022

Publications from this project

Journal articles

Murali, S., Hussam, W. K. & Sheard, G. J. 2021 Heat transfer enhancement in quasi-two-dimensional magnetohydrodynamic duct flows using repeated flow-facing wedge-shaped protrusions. *Int. J. Heat Mass Trans.* **171**, 121066.

Murali, S, Ng, Z. Y. & Sheard, G. J. 2022 Stability of flow in a channel with repeated flow-facing wedge-shaped protrusions. *Journal of Fluid Mechanics.* **941**, A59.

Conference papers

Murali, S. & Sheard, G. J. 2020 Wedge shaped protrusions in duct flows for heat transfer enhancement. *In Proceedings of the 22nd Australasian Fluid Mechanics Conference: AFMC 2020*, Editors H. Chanson and R. Brown, Queensland University of Technology, Brisbane, Australia.

Acknowledgements

I am extremely grateful to my supervisor Professor Gregory J. Sheard for his assistance and guidance throughout the completion of this project. I have always been inspired by his passion towards research. I am thankful to my co-supervisors, Dr. Zhi Yuen Ng for his support and for the many useful discussions I have had with him, and Dr. Wissam K. Hussam for his help in one of the manuscripts.

This research was supported by the Australian Government Research Training Program (RTP) Scholarship and the Monash international tuition fee scholarship. Their financial support is highly appreciated. I am also grateful for the financial support from graduate research completion award (GRCA) and the Faculty of Engineering during the last phase of the thesis which was a relief during the difficult times of the pandemic. I am thankful for the computational time which was provided by the high-performance compute facilities of the National Computational Infrastructure (NCI), the Pawsey Supercomputing Centre, and the Monash MonARCH machine. I would like to thank the department of Mechanical and Aerospace Engineering, Monash University for providing a good working environment and all the resources required for the completion of this work. Thank you to Jacelyn Tan for her help in the GRCA application, and Lilian Khaw for suggesting structural improvements in parts of the thesis in the final stages of its preparation.

I appreciate the support from our research group members, Chris, Sajjad, Peyman, Tze Khi, Jamie, Oliver and Tony. I thank the teaching coordinators and the team for the teaching units I have been associated with - MEC3451, MAE2404 and MAE3456, for the demonstration opportunity which has helped me learn and further develop my interpersonal skills. I am thankful for the evening (or whichever time) coffee, the 'non-PhD talk' time, the endless fooseball matches, and all the trips with my friends, Gargi, Somnath, Shibani, Joe and Stella. I extend my love to my buddies for life, Ambuj, Koshy and Bhuvana who have been continents apart, but still been there for me through my best and worst times. I am grateful to my parents for their unconditional love, understanding

and support.

Last, but never the least, thank you ‘Australia’ for the beautiful experiences I have had here during my PhD journey and all the lessons I have learnt, which I will carry with me for a lifetime.

Nomenclature

A list of nomenclature contained in the thesis is covered here. All symbols used are presented first which is followed by greek alphabets, english alphabets, abbreviations and non-dimensional numbers.

Symbol	**Description**
§	Thesis section
$\int$	Integration
$\boldsymbol{\nabla}$	Gradient operator
∇^2	Divergence of the gradient operator (Laplace operator)
$\boldsymbol{\nabla}_\perp$	Gradient operator for quasi-two-dimensional cases
$\nabla^2_\perp$	Divergence of the quasi-two-dimensional gradient operator
$\hat{(\,)}$	Eigenvector field
$(\,)'$	Perturbation field
$(\,)_\perp$	Quasi-two-dimensional field
$\overline{(\,)}$	Spanwise averaged value
$\langle\,\rangle$	Domain averaged value
$\overline{\overline{(\,)}}$	Time averaged value
$(\,)^*$	Adjoint field
$(\,)^T$	Transpose
$(\,)_{opt}$	Optimal value
$\tilde{(\,)}$	Non-dimensional form of a flow field

Continued on the next page

Continued from the previous page

Symbol	Description
α	Thermal diffusivity of the fluid
α_q	Weighing coefficients for discretisation
β	Blockage ratio
β_q	Weighing coefficients for discretisation
χ	Local to global coordinate mapping
δ_h	Viscous boundary layer thickness
δ_t	Thermal boundary layer thickness
ε_{2D}	Ratio of Reynolds number to the critical Reynolds number for 2D instability
ε_{3D}	Ratio of Reynolds number to the critical Reynolds number for 3D instability
ε_{Q2D}	Ratio of Reynolds number to the critical Reynolds number for quasi-2D instability
ϕ	Wedge angle
ϕ_p	One-dimensional local expansion function of poynomial order n_p
ϕ_{pq}	Two-dimensional local expansion function
ϕ_e	Electric potential field
γ	Pitch
γ_q	Weighing coefficients for discretisation
η	Heat transfer efficiency
λ	Wavelength of the eigenmode
λ_{cr}	Wavelength of the destabilising global eigenmode
μ_d	Dynamic viscosity of the fluid
μ_i	Complex eigenvalues of the linear operator $\mathscr{A}$
μ	Eigenvalue of the dominant eigenmode of $\mathscr{A}$
μ_{hi}	Complex eigenvalues of the Hessenberg matrix H_m
μ_m	Magnetic permeability of the fluid
ν	Kinematic viscosity of the fluid
ρ	Density of the fluid

Continued on the next page

Continued from the previous page

Symbol	Description
σ	Growth rate of the eigenmode
σ_c	Electrical conductivity of the fluid
$\boldsymbol{\sigma}_f$	Shear stress tensor
τ	Time horizon for transient growth
τ_w	Wall shear stress
$\boldsymbol{\omega}$	Vorticity vector
ω_{zx}	Spanwise vorticity at each streamwise location x
ω_{zxp}	Vortex intensity at each streamwise location x
ω_p	Maximum vortex intensity in the flow domain
ω_f	Angular frequency of the global mode
ξ^e	Local coordinate system within an element
ξ_p	Nodal points corresponding to roots of Gauss–Legendre–Lobatto polynomial
ψ_i	Eigenvectors of the Hessenberg matrix H_m
Δ	Change in any quantity
Φ	Global trial function or expansion function
Φ_v	Viscous heating term in the energy equation
Φ_j	Joule heating term in the energy equation
Φ_b	Buoyancy effect term in the energy equation
$\sum$	Sum of all spanwise integral terms contributing to the growth rate of the global mode
$\sum_{i=a}^{b}$	Sum of arguments with i starting from a to b
Ω	Flow domain
a	Spanwise duct width
$\boldsymbol{f}$	Momentum forcing vector
$\boldsymbol{f}_b$	Body forces in the momentum equation
f	Friction factor
f_0	Friction factor for a plane duct without wedge protrusions
f_l	Lorentz force
h	Heat transfer coefficient

Continued on the next page

Continued from the previous page

Symbol	Description
h_w	Height of the wedge
$\boldsymbol{j}$	Current density
k	Spanwise wavenumber
k'	Kinetic energy of the perturbation per unit mass
k_f	Thermal conductivity of the fluid
l_p	Length between two subsequent wedges
l_w	Streamwise length of the inclined surface
l_d	Total streamwise length of the channel/duct
m	Fourier mode number
n	Number of Hartmann walls
$\boldsymbol{n}$	Wall normal vector
n_p	Element polynomial order for base flow
p	Non-dimensional pressure field
$p_\perp$	Quasi two-dimensional non-dimensional pressure field
r	Duct aspect ratio
$\boldsymbol{s}'$	Strain rate tensor of the perturbation field
t	Time
$\boldsymbol{u}$	Velocity vector
$\boldsymbol{u}_\perp$	Quasi-two-dimensional velocity vector
u	Streamwise component of velocity vector
u^δ	Approximate solution of a linear operation $\mathcal{L}$
v	Transverse component of velocity vector
w	Spanwise component of velocity vector
w_t	Weighing function or test function
x	Streamwise direction
x_{s1}	x-coordinate of separation point of recirculation region-1
x_{s2}	x-coordinate of separation point of recirculation region-2
x_{s3}	x-coordinate of separation point of recirculation region-3
x_{r2}	x-coordinate of reattachment point of recirculation region-2

Continued on the next page

Continued from the previous page

Symbol	Description
x_{r3}	x-coordinate of reattachment point of recirculation region-3
y	Transverse direction
y_{r2}	y-coordinate of reattachment point of recirculation region-2
z	Spanwise direction
A	Complex amplitude of a perturbation field
A_k	Amplitude of a global eigenmode with spanwise wavenumber k
$\mathscr{A}$	Linear evolution operator
$\mathscr{A}^*$	Linear adjoint operator
$\boldsymbol{B}$	Magnetic field vector
B_0	Applied magnetic field strength in the spanwise direction
C_p	Specific heat capacity of the fluid
$\mathscr{D}$	Dissipation term in energetics analysis
$\boldsymbol{E}$	Electric field
E_k	Kinetic energy of the 3D flow
E_{kt}	Total perturbation kinetic energy in the flow domain
$E_{k,0}$	Kinetic energy of the fundamental Fourier mode
$E_{k,1}$	Kinetic energy of the dominant Fourier mode
E	Endogeneity
E_{conv}	Contribution from convection term in momentum equation to endogeneity
E_{prod}	Contribution from production term in momentum equation to endogeneity
E_{pres}	Contribution from pressure term in momentum equation to endogeneity
E_{diss}	Contribution from dissipation term in momentum equation to endogeneity
E_σ	Local endogeneity contribution to the growth rate of the global destabilising mode
E_ω	Local endogeneity contribution to the frequency of the global destabilising mode

Continued on the next page

Continued from the previous page

Symbol	Description
F_Q	Electrostatic force experiences by charge Q
$\mathcal{F}$	Fourier transformation operator
G	Optimal energy growth
H	Hartmann friction parameter
H_m	Hessenberg matrix
I_i	Transverse integrals of the magnitude of perturbation velocity components at different streamwise locations
I_{total}	Transverse integrals of the magnitude of total perturbation velocity at different streamwise locations
J	Order of the integration scheme
K	Transient energy growth of the perturbation
K_e	Length of the eigenvector space
$\boldsymbol{K}$	Velocity gradient tensor
$\boldsymbol{K}_S$	Strain-rate tensor (symmetric part of $\boldsymbol{K}$)
$\boldsymbol{K}_A$	Vorticity tensor (anti-symmetric part of $\boldsymbol{K}$)
L	Half-duct height
L_p	Legendre polynomial
$\mathscr{L}^2$	2-norm of velocity field
L_{char}	Characteristic length scale
M	Number of Fourier modes
M1	Two-dimensional real mode
M2	Destabilising two-dimensional complex mode
M3	Sub-dominant two-dimensional complex mode
N	Interaction parameter or Stuart number
$\boldsymbol{N}'$	Linearised advection operator
$\boldsymbol{N}^*$	Linearised advection operator of adjoint equations
$\mathscr{P}$	Production term in energetics analysis
P	Base flow pressure field
P_{heat}	Non-dimensional power gain as heat
P_{flow}	Non-dimensional power loss as pressure drop

Continued on the next page

Continued from the previous page

Symbol	Description
$P_{0,heat}$	Non-dimensional power gain as heat for a duct without wedge protrusions
$P_{0,flow}$	Non-dimensional power loss as pressure drop for a duct without wedge protrusions
ΔP_{net}	Net power gain or loss by the system
Q	Electric charge
QM1	Quasi-two-dimensional real mode
QM2	Destabilising quasi-two-dimensional complex mode
QM3	Sub-dominant quasi-two-dimensional complex mode
R	Residual from approximate solution
S	Sensitivity
S_h	Volumetric and radiative heating term in the energy equation
$\mathscr{T}$	Transport term in energetics analysis
T	Non-dimensional temperature field
$T_{f,x}$	Local bulk fluid temperature
T_f	Domain averaged bulk fluid temperature
T_h	Non-dimensional hot wall temperature
T_c	Non-dimensional cold wall temperature
$T_\perp$	Non-dimensional quasi-two-dimensional temperature field
$\boldsymbol{U}$	Base flow velocity vector
U_0	Horizontal mean velocity
V	Characteristic velocity
DNS	Direct numerical simulation
HR	Heat transfer ratio
MHD	Magnetohydrodynamic
PR	Pressure ratio
Q2D	Quasi-two-dimensional

Continued on the next page

Continued from the previous page

Symbol	**Description**
Ec	Eckert number
Ha	Hartmann number
Pr	Prandtl number
Nu	Nusselt number (domain and time averaged)
Nu_x	Local Nusselt number
Nu_0	Nusselt number for a plane duct without wedge protrusions
Pe	Peclet number
Re	Reynolds number
$Re_{cr,\mathrm{2D}}$	Critical Reynolds number for the onset of two-dimensional instability / unsteadiness
$Re_{cr,\mathrm{3D}}$	Critical Reynolds number for the onset of three-dimensional instability
Re_{Ri}	Reynolds number for the onset of regime-i
$Re_{cr,\beta}$	Rescaled Reynolds number based on constriction gap $(2L - h_w)$
$Re_{cr,\gamma}$	Rescaled Reynolds numbner based on wedge gap length lp
$Re_{cr,\mathrm{Q2D}}$	Critical Reynolds number for the onset of quasi-two-dimensional instability / unsteadiness
R_m	Magnetic Reynolds number

Contents

Introduction

A numerical study of hydrodynamic flow in a channel and magnetohydrodynamic flow in a duct with repeated flow-facing wedge-shaped protrusions and the heat transfer enhancement achieved using these surface geometries is presented in this thesis. The motivation of the current study and the gaps in the literature to be addressed in this thesis are presented first, giving a broad overview of the problem. Thereafter, the main aims of the study are discussed along with description of the setup under consideration. Some of the fundamental concepts in hydrodynamic and magnetodynamic flows underpinning the works of this thesis are explained in the following sections. Finally, the assumptions made and the structure of the thesis is provided.

Broad overview and motivations

Confined flows in channels and ducts with and without the presence of a magnetic field have been subjects of numerous investigations over the years given their many engineering and industrial applications (Larson, 1959; Chilcott, 1967; Alam *et al.*, 2014) and for the understanding of several fundamental mechanisms in fluid dynamics (Carlson *et al.*, 1982; Reddy & Henningson, 1993; Trefethen *et al.*, 1993; Henderson & Barkley, 1996; Schmid & Henningson, 2001; Drazin & Reid, 2004). Hydrodynamic flows over forward-facing step, FFS (Stüer *et al.*, 1999; Wilhelm *et al.*, 2003; Lanzerstorfer & Kuhlmann, 2012*b*) and backward facing step, BFS (Armaly *et al.*, 1983; Kaiktsis *et al.*, 1996; Erturk, 2008; Barkley *et al.*, 2002; Blackburn *et al.*, 2008*a*) have also been studied extensively as these simple geometries served as benchmarks for myriad problems associated with changing duct geometry.

Similarly, magnetohydrodynamic (MHD) duct flows have been an ongoing subject of investigation over years due to their relevance in engineering applications such as electromagnetic casting, leviating, pumping and stirring liquid metals, vaccum-arc remelting of titanium and nickel-based alloys, electromag-

netic removal of non-metallic inclusions from melts and electromagentic launchers, electrolysis process particularly to reduce aluminium oxide to aluminium, in generators and the cooling blankets of magnetic confinement nuclear fusion reactors, etc. (Barleon *et al.*, 1991; Davidson, 1997; Müller & Bühler, 2013). Cooling blanket modules surround the reactor chamber of magnetic confinement fusion reactors with the side wall or the first wall of the modules exposed to the reactor chamber. In the cooling blankets, electrically conducting fluids flow under the presence of a strong magnetic field which is used to confine plasma in the reactor chamber (figure 1). Electrically conducting fluids flowing under the presence of a magnetic field are subjected to a Lorentz force, produced due to the interaction of the induced current with the magnetic field. This force has a damping effect on the turbulent fluctuations, thereby laminarising the flow and diminishing convective heat transfer in such ducts (Malang *et al.*, 1991; Kirillov *et al.*, 1995; Smolentsev *et al.*, 2010*a*). This can cause a high temperature to develop on the walls and result in structural damage of the cooling module (Abdou *et al.*, 2015).

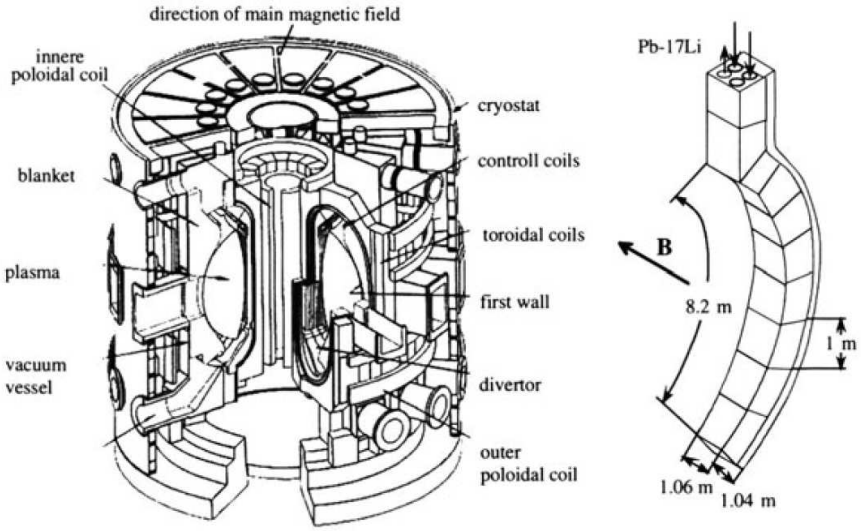

Figure 1: Structure of a nuclear fusion reactor and a blanket module surrounding the central reactor chamber. The figure has been reproduced from Müller & Bühler (2013) with permission of the publisher.

The problem primarily motivating the present study is the detrimental impact that strong magnetic fields have on the heat transfer efficiency of the cooling blankets fluids surrounding the reactor chamber (Barleon *et al.*, 1991; Smolentsev *et al.*, 2008, 2010*a*, 2013). The lower heat transfer efficiency has a direct effect on the power generation efficiency of these reactors (Sukoriansky *et al.*, 1989; Smolentsev *et al.*, 2010*a*).

A number of studies have been carried out to enhance the convective heat

transfer from the heated wall to the conducting fluid flowing through a duct. The presence of a strong magnetic field results in the suppression of isotropic turbulence by Joule dissipation (Hossain, 1992). However anisotropic turbulent structures are promoted by stretching of the vortical structures in the direction of the magnetic field as they are least impacted by Joule dissipation (Sommeria & Moreau, 1982; Davidson, 1997). Most studies make use of this effect to promote or generate vortices aligned with the magnetic field to produce flow disturbances, which interact with the thermal boundary layer, sweeping hot fluid from the near-wall region into the flow, in turn increasing the Nusselt number. Different vortex generation and promotion techniques have been investigated, such as the use of walls of varying electrical conductivity (Huang & Li, 2011), generating electrically generated vortices using point electrodes (Hamid *et al.*, 2016*b*,*a*) and the use of obstacles in the flow such as a bluff body (Hussam & Sheard, 2013; Chatterjee & Gupta, 2015; Cassells *et al.*, 2016), and grids (Branover *et al.*, 1995; Kolesnikov & Tsinober, 1972).

The enhancement obtained in heat transfer by the use of various techniques are different and sensitive to the technique being used. None of the studies in the literature have explored the use of surface modification of the sidewall for heat transfer enhancement in MHD flows. Additionally, previous studies in MHD duct flows have mostly concentrated on a single vortex generator in the flow and its influence on the heat transfer behaviour. Subsequent positioning of the vortex promoters are significant, as the vortices generated are dissipated when convecting downstream in the flow and the rate of dissipation increases drastically with stronger magnetic fields (Hamid *et al.*, 2015).

Separately, the literature contains many investigations into the use of surface modifications in hydrodynamic flow through ducts (Karwa (2003); Bhagoria *et al.* (2002); Alam *et al.* (2014) and references therein), but most have focused on the heat transfer characteristics of high Reynolds number (Re) turbulent flows. In the cooling blankets of fusion reactors, the bulk flows are generally in a steady or transitional state (Smolentsev *et al.*, 2013), as shown in the operating regime for different types of cooling blanket modules in figure 2, and hydrodynamic flow characterisation in these regimes using surface geometries has received limited attention in the litererature. Therefore, interest lies in the mechanisms promoting the destabilisation of steady, laminar flows. Additionally, from a fundamental perspective, understanding the onset of transition in non-parallel flows is an ongoing area of interest. Thus, the present study adds to the existing understanding in this aspect as well on separating and reattaching confined flows.

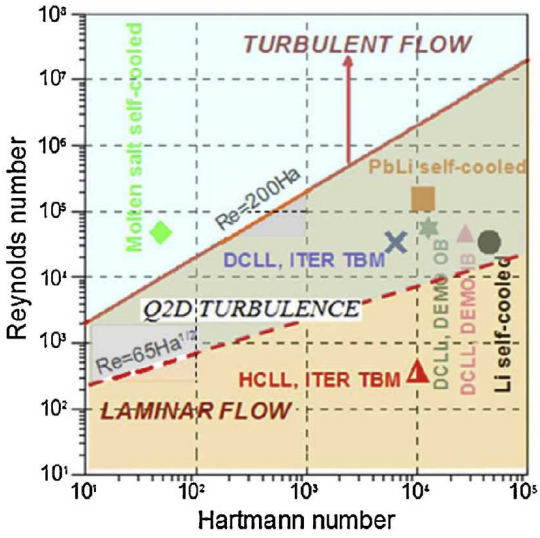

Figure 2: Flow regimes in different types of cooling blanket designs for magnetic confinement fusion reactors shown in the $Re-Ha$ parameter space. The figure has been reproduced from Smolentsev *et al.* (2015) with permission of the publisher.

Aims of the study and problem setup

Considering the various studies in the literature and the gap in existing knowledge as discussed in the previous section, the hydrodynamic flow in a channel and magnetohydrodynamic flow in a duct with repeated flow-facing wedge-shaped-wall protrusion are considered in this thesis, as this geometry showed a better heat transfer perfomance in hydrodynamic flow experiments (Bhagoria *et al.*, 2002). This section firstly presents the aims of this study and thereafter presents the problem setup considered in the thesis.

The main aims of the work presented in this thesis can be broadly divided into three parts:

1. To investigate the stability and dynamics of hydrodynamic channel flow with repeated flow-facing wedge-shaped protrusions by

   (a) identifying and classifying the different flow regimes associated with the 2D flow,

   (b) characterising the long-time dynamics of the flow and its dependence on the geometry of the protrusion and flow conditions by quantifying the eigenmodes causing breakdown of the two-dimensional flow using a global linear stability analysis,

   (c) understanding the mechanisms causing the onset of primary instability via analysis of the energetics of the perturbation and endogeneity

analysis,

(d) characterising the short-time dynamics of the flow via a transient growth analysis,

(e) analysing the sensitivity of the flow to structural modifications and elucidate regions in the flow that are important from a flow control perspective, and

(f) understanding the effects of non-linear interactions in the flow.

2. To investigate the stability and dynamics of a quasi-2D magnetohydrodynamic (MHD) flow in a duct with repeated flow-facing wedge-shaped protrusions by

   (a) identifying and classifying the different flow regimes associated with the quasi-2D MHD flow with varying Hartmann friction parameters,

   (b) characterising the global linear stability of the quasi-2D MHD flow to quasi-2D perturbations and its dependence on the geometry of the protrusion and flow conditions, and compare it with the corresponding hydrodynamic cases,

   (c) characterising the short-time dynamics of the flow via a transient growth analysis and determining how the optimal growth changes with change in Hartmann friction parameter, along with comparisons with the non-MHD cases, and

   (d) understanding the effects of non-linear interactions in the flow.

3. To characterise the heat transfer enhancement achieved using wedge-shaped protrusions in quasi-2D MHD duct flows by

   (a) understanding how the onset of instability using wedges influences the local and global heat transfer behaviour,

   (b) quantifying the improvement in the heat transfer rate over a range of geometric parameters and Hartmann friction parameters,

   (c) quantifying the heat transfer efficiency that could be achieved using wedges and determining the optimal geometric parameter setting at different Hartmann friction parameter values, and

   (d) comparing the heat transfer efficiency achieved using repeated surface protrusions with other vortex generation techniques used for heat transfer enhancement.

The problem setup for the hydrodynamic cases is shown in figure 3. It consists of a streamwise (x) periodic channel of height $2L$ with flow-facing wedge-shaped protrusions of height h_w and angle of inclination ϕ, with a distance of l_p between the wedges on the bottom wall and a streamwise wedge length of l_w. The fluid is considered to be Newtonian and incompressible with kinematic viscosity ν and constant density ρ. The bottom wall (side wall or first wall) is maintained at constant wall temperature T_h whereas the top wall is maintained at constant wall temperature T_c. No-slip boundary conditions are applied on the bottom and top walls.

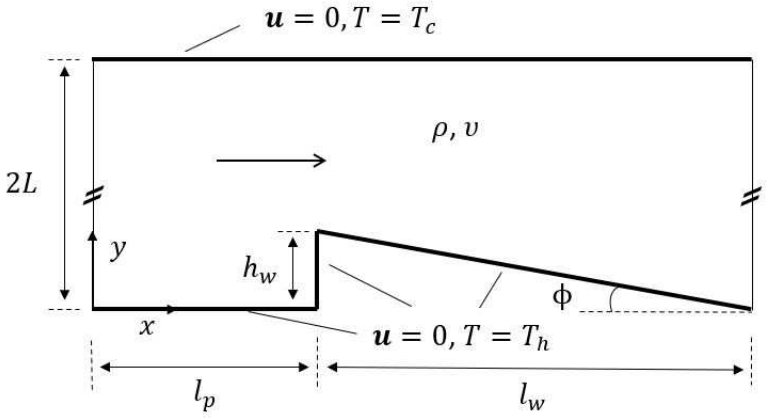

Figure 3: Flow geometry for the hydrodynamic cases with periodic condition enforced at the vertical boundaries $x = 0$ and $x = l_p + l_w$. Flow is left to right.

For the MHD cases considered in the study, the problem setup is shown in figure 4. It consists of a streamwise periodic duct with flow-facing wedges on the bottom wall with the aforementioned dimensions, and velocity and temperature boundary conditions as for the hydrodynamic cases. Additionally, the duct has a spanwise (z) width of a, with a uniform magnetic field of strength B applied in the z-direction. The duct walls are electrically non-conducting. The fluid is electrically conducting with electrical conductivity σ_c.

Dimensionless geometric parameters identified for the setup are:

1. blockage ratio
$$\beta = \frac{h_w}{2L}, \tag{1}$$

2. pitch
$$\gamma = \frac{l_p}{L}, \tag{2}$$

3. wedge angle
$$\phi = \tan^{-1}\left(\frac{h_w}{l_w}\right), \tag{3}$$

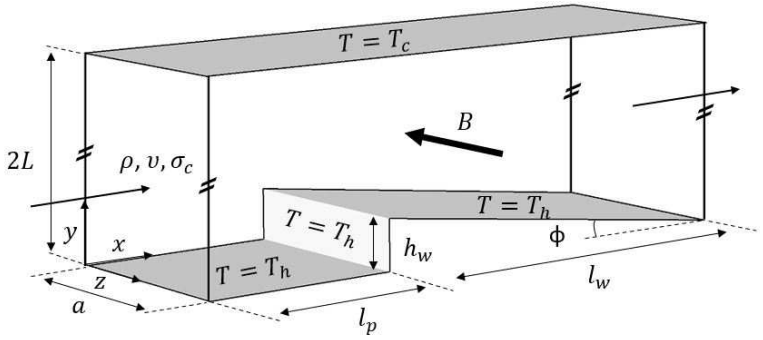

Figure 4: Flow geometry for the MHD cases with periodic condition enforced at the vertical boundaries $x = 0$ and $x = l_p + l_w$. Flow is left to right.

4. Aspect ratio of the duct cross-section

$$r = \frac{2L}{a}. \tag{4}$$

Some fundamental concepts

Some of the fundamental concepts that are relevant for understanding the work presented in this thesis are briefly discussed in this section. More details on these topics and concepts can be found in any of the standard textbooks on fluid dynamics (Kundu & Cohen, 2002; White, 2006; Munson *et al.*, 2009), heat transfer (Bergman *et al.*, 2007; Holman, 2010) and magnetohydrodynamic flows in ducts and channels (Müller & Bühler, 2013).

Fluids are ubiquitous to human life and in nature in numerous forms, scales and conditions. Fluids are defined as any substance that deforms continuously under the action of shear stress of any magnitude. Properties such as density (ρ), and dynamic viscocity (μ_d) respectively characterise the 'heaviness' and 'fluidity' of the fluid, and its flow must obey the laws of conservation of mass, momentum and energy. The equations governing fluid motion are derived using these basic laws.

Most of the information about the flow required to characterise and understand the flow features can be obtained from the velocity gradient tensor ($\boldsymbol{K}$) of the flow. The shearing contribution to the flow is measured by the symmetric ($\boldsymbol{K}_S$) part of the velocity gradient tensor whereas the rotational contribution comes from the anti-symmetric part ($\boldsymbol{K}_A$). For a Newtonian fluid, the shear stress tensor ($\boldsymbol{\sigma}_f$) is linearly proportional to the shear strain rate, and according

to Newton's law of viscocity is given by

$$\boldsymbol{\sigma}_f = 2\mu_d \boldsymbol{K}_S, \tag{5}$$

where $\boldsymbol{K}_S = \boldsymbol{\nabla u} + (\boldsymbol{\nabla u})^T$, and $\boldsymbol{u}$ is the velocity vector field. Wall shear stress can in turn be obtained from

$$\boldsymbol{\tau}_w = \boldsymbol{\sigma}_f \cdot \hat{\boldsymbol{n}}, \tag{6}$$

where $\hat{\boldsymbol{n}}$ is the unit wall normal vector. Vorticity ($\boldsymbol{\omega}$) characterises local rotation in a flow, and is obtained from the components of the rotational tensor $\boldsymbol{K}_A$. It is succinctly expressed as

$$\boldsymbol{\omega} = \boldsymbol{\nabla} \times \boldsymbol{u}. \tag{7}$$

Flow between parallel plates

Flow between two parallel plates driven by a pressure gradient is called a plane Poiseuille flow. The flow presents in multiple states: an orderly and smooth (laminar) state, a disordered and fluctuating (turbulent) state or in the intermediate regime between these two states (transitional state). Though the state of the flow may be dependent on multiple parameters, a key non-dimensional parameter used to identify the state of the flow is the Reynolds number (Re) which could be defined as the ratio of the inertial to the viscous forces and is given by

$$Re = \frac{\rho V L_{\text{char}}}{\mu_d}, \tag{8}$$

where V and L_{char} are respectively the characteristic velocity and length scales associated with the problem under consideration. The non-dimensional parameter associated with the pressure drop resulting due to the wall shear stresses is the friction factor (f) given by

$$f = \frac{\Delta p}{\rho V^2}. \tag{9}$$

Flow in a duct under the presence of a uniform magnetic field

Magnetohydrodynamics (MHD) deals with the flow of an electrically conducting fluid in the presence of a magnetic field. A fully developed flow driven by a pressure gradient in an electrically insulated duct with a unidirectional velocity $\boldsymbol{v} = ue_x$ and exposed to a uniform magnetic field $\boldsymbol{B}$ is shown in figure 5(a). The

walls perpendicular and parallel to the field direction are the Hartmann walls and side walls, respectively. An electric field ($\boldsymbol{v} \times \boldsymbol{B}$) is induced when the electrically conducting fluid flows under the influence of the magnetic field, producing current density vector field $\boldsymbol{j}$ which forms a closed loop running through the core and the Hartmann layers since the walls are insulated. The induced current in the presence of the applied magnetic field results in a force called the Lorentz force $\boldsymbol{f}_L = \boldsymbol{j} \times \boldsymbol{B}$. In the core, the Lorentz force acts opposite to the flow direction balancing the driving pressure gradient, whereas in the thin Hartmann layers formed on the Hartmann walls, Lorentz force drives the flow against viscous shear as the current direction (and hence the Lorentz force) is opposite to that in the core in these layers. This results in a steeper velocity gradient and flattening of the core velocity profile with increasing magnetic field strength for these cases (figure 5b). At the side walls where layers known as Shercliff layers develop, the current direction is approximately coincident with the magnetic field, therefore Lorentz forces in these layers are negligible. This is reflected in the velocity profile along these layers, which almost matches the cases with no magnetic field applied (figure 5c).

Thus, for flow under the influence of magnetic field, an extra dissipation mechanism other than the viscous dissipation exists due to the induced electric current. This is called the Joule effect characterised by a magnetic diffusivity of $1/\mu_m\sigma_c$, where μ_m is the magnetic permeability and σ_c is the electrical conductivity of the fluid. Some of the significant non-dimensional parameters associated with MHD flows are introduced here. The magnetic Reynolds number ($R_m = \sigma_c\mu_m L_{char}V$) is the ratio between time scale for Joule effect and that for eddy turnover. In the laboratory scale $R_m \ll 1$ for liquid metals, hence the induced magnetic field is much weaker than the applied magnetic field and its effect can be neglected. The ratio of the electromagnetic and viscous forces is given by the Hartmann number

$$Ha = L_{char}B_0\sqrt{\frac{\sigma_c}{\rho\nu}}, \tag{10}$$

where $\nu = \mu_d/\rho$ is the kinematic viscocity of the fluid and B_0 is the applied magnetic field strength. The ratio of electromagnetic and inertial forces leads to the interaction parameter, otherwise known as Stuart number,

$$N = \frac{\sigma_c L_{char} B_0^2}{\rho V}, \tag{11}$$

The interaction parameter, Reynolds number and Hartmann number are inter-

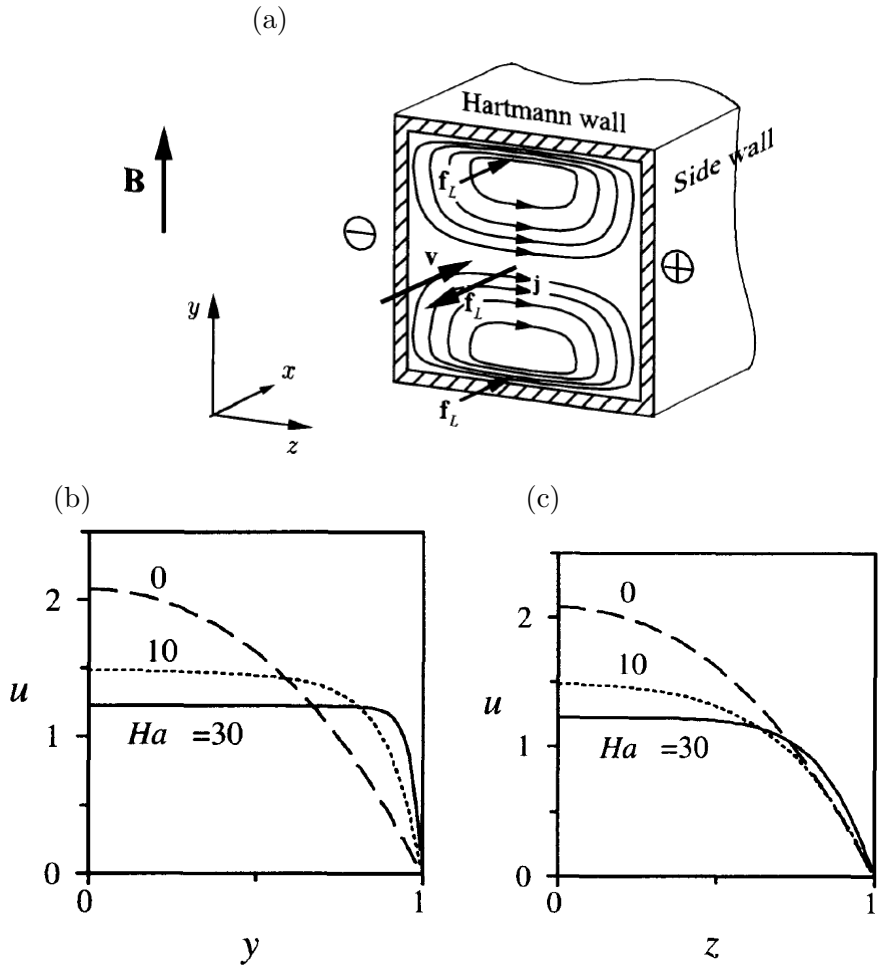

Figure 5: (a) Sketch showing typical MHD duct flow with induced current and Lorentz force, and the corresponding velocity profile for different Ha near the (b) Hartmann wall and (c) side wall. The figure has been reproduced from Müller & Bühler (2013) with permission of the publisher.

related via $N = Ha/Re$.

Convective heat transfer

Convective heat transfer is the transfer of heat from a bounding surface to the fluid due to the motion of fluid over the surface on which either a constant heat flux or constant temperature boundary condition is imposed. It depends on the different fluid properties in addition to its density and viscocity such as thermal conductivity k_f, specific heat capacity C_p and heat transfer coefficient h which again depends on the surface geometry and flow conditions. Similar to the viscous boundary layer, a thermal boundary layer develops on the surface on which temperature boundary condition is imposed. The Prandlt number Pr gives the

relative importance of the momentum and thermal diffusivity (α) and is given by

$$Pr = \frac{\nu}{\alpha}. \tag{12}$$

It could hence be related to the thickness of the viscous and thermal boundary layer and is approximately related as

$$Pr^n = \frac{\delta_h}{\delta_t}. \tag{13}$$

where n takes positive values typically about 0.33. So for fluids with $Pr \ll 1$ which is the case of the liquid metals in cooling blanket modules, the thermal boundary thickness exceeds the velocity boundary layer thickness, and the heat transfer from the surface is highly diffusive. Another important non-dimensional parameter which characterises the relative importance of convective and the conductive heat transfer is the Nusselt number

$$Nu = \frac{hL_{char}}{k_f}, \tag{14}$$

where h is the convective heat transfer coefficient and k_f is the thermal conductivity of the fluid. The Nusselt number typically exhibits a dependence on control parameters such as Pr and Re.

Assumptions made for the work

The various assumptions made to carry out the work in this thesis are summarised in this section. The fluid is considered to be Newtonian and incompressible, with all fluid properties assumed to be constant. The viscous and Joule heating terms in the energy equation are neglected since the order of magnitude of these terms are much lower that the thermal diffusion term. Justification of this for applications relevant to this project can be found in Hussam *et al.* (2018). For the heat transfer analysis, the flow is considered under a forced convection condition and the effects of buoyancy has been neglected according to findings from Burr *et al.* (1999), where they found the effect of natural convection to be suppressed for flow between a hot and cold horizontal plate arrangement under a strong magnetic field. Similar studies such as Barleon *et al.* (2000); Morley *et al.* (2000) also support these findings and have neglected the effects of natural convection in their investigations.

Structure of the thesis

An introduction to some fundamental concepts underpinning the works in the thesis was provided here. The main content of the thesis consists of the literature review in chapter-1. The governing equations, numerical methods, and grid resolution and validation studies are described in chapter-2. The results are divided into 4 chapters. Chapters-3 and 4 focus on the hydrodynamic channel flow with wedge-protrusions, its stability characteristics and non-linear interactions in the flow. Chapter-5 discusses the stability characteristics of quasi-2D MHD duct flows, through linear stability and transient growth studies. In chapter-6, the heat transfer enhancement using wedge protrusions in quasi-2D MHD duct flows are discussed. Conclusions and directions for future work are provided in chapter-7.

Chapter 1

Literature Review

This chapter presents a review of the literature underpinning this project and is divided into three main sections based on the three broad objectives as outlined in the introduction. The flow setup investigated in the current study draws features from similar confined flow setups such as the forward and the backward-facing steps. Therefore previous studies conducted on flow over forward- and backward-facing setups are presented first, highlighting the flow features, stability and transition behaviour in such flows along with various other studies available in the literature on similar confined geometries. Second, a review of the literature available in magnetohydrodynamic (MHD) channel and duct flows are presented. The instabilities and transition in the Hartmann layers and the Shercliff layers are discussed, followed by a discussion of instabilities, optimal growth and transitions in MHD duct flows, and finally studies conducted on the formation of anisotropic turbulent structures and their evolution are discussed. The last section of this chapter focuses on the heat transfer studies in hydrodynamic channel/duct flows using differently shaped surface protrusions. Thereafter, various techniques used for quasi-2D turbulence generation in MHD duct flows for heat transfer improvement are presented.

1.1 Hydrodynamic flows in confined flow setups

In this section, the main flow features associated with the laminar hydrodynamic flow in various confined flow setups are presented. Furthermore, a detailed review of the findings from numerous investigations conducted to understand the onset of instabilities in these flows are also provided. The focus is on the key findings associated with primary instability in these types of flows, which answers the question regarding the first step on the route to turbulence in these laminar

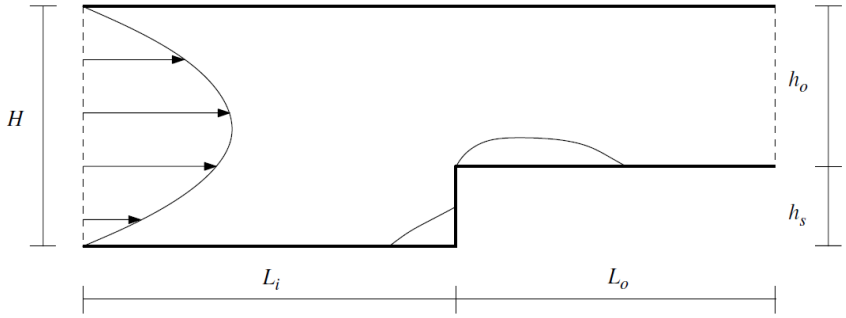

Figure 1.1: Flow geometry and the recirculation regions formed in flow over a forward-facing step in a channel. Flow is left to right. Reproduced from Lanzerstorfer & Kuhlmann (2012*b*) with permission of the publisher.

flows, how and through what mechanism the laminar state bifurcates to another state, and its associated critical flow parameters. Different numerical studies using linear stability theory and DNS are included along with observations that have been made in experiments. First, the two most studied of these types of flows which share common features with the present flow setup, the forward and the backward-facing step setups, are discussed. This is followed by a brief review of studies conducted in other related confined flow setups.

1.1.1 Laminar flow over forward-facing step (FFS) and onset of instability

A laminar flow over a forward-facing step (FFS) is characterised by the formation of a recirculation region in front of the step at low values of Reynolds number which grows in size with increase in Re. The Reynolds number for the FFS case is based on the mean velocity of the inlet flow and the height of the inlet channel as the velocity and length scaling, respectively. With further increase in Re, another recirculation region appears immediately after the step corner at $Re \approx 180$ and grows in size before becoming the dominant recirculation zone in the flow (Mei & Plotkin, 1986; Dennis & Smith, 1980). A sketch of a forward-facing step geometry and the two recirculation regions is shown in figure 1.1.

Experimental investigations report the primary recirculation region to be of open type, having a three-dimensional nature, rather than closed type, thereby resulting in fluid entrainment and its subsequent release from this region. This is observed as streaks immediately after the step (Chiba *et al.*, 1995; Pollard *et al.*, 1996). Hydrogen bubble visualisation experiments (Stüer *et al.*, 1999) demonstrated that the primary instability of the laminar flow over a FFS occurs

due to the breakdown of the primary recirculation region formed in front of the step, resulting in the formation of streaks immediately after the step. The spacing between streaks was observed to decrease with increasing Re. The experimental observation made using hydrogen-bubble visualisations in Stüer *et al.* (1999) is shown in figure 1.2.

Further investigations on the linear stability of the laminar flow was carried out to understand the cause of the instability in these flows (Wilhelm *et al.*, 2003). For the single Reynolds number of $Re = 330$ considered in their study, they did not identify an absolute instability of the flow to three-dimensional perturbations. However, their DNS conducted at the same Reynolds number suggested that the onset of instability in the flow over a FFS was a sensitive reaction of the flow to incoming perturbations and was localised in the step region. The resulting flow features matched well with the streaks observed in the experiments with gap between streaks being approximately about three times the step height.

The previous study by Wilhelm *et al.* (2003) focused only on a single Reynolds number, making it difficult for a confident conclusion about the flow instability. Later, Marino & Luchini (2009) used an adjoint analysis to study the sensitivity of the flow to external disturbances as well as to localised structural disturbances considering two different constriction ratios, Γ (ratio of step to channel height). Their investigation not only supported the previous findings of Wilhelm *et al.* (2003) but also verified the power of the adjoint method more generally. The technique had previously been applied to cylinder wakes in Giannetti & Luchini (2007). Marino & Luchini (2009) further extended the analysis to different Re and observed a shift in the structural sensitivity region from ahead to aft of the step on approach to the critical Re, thereby indicating the role played by the dominant recirculation zone on the origin of the instability. This could not be observed in the study of Wilhelm *et al.* (2003) since only a single Re was considered.

For $\Gamma = 0.25$, the critical Reynolds number for the onset of instability was observed to be approximately $Re \approx 4800$ in the experiments of Stüer *et al.* (1999), $Re \approx 1320$ in the study Wilhelm *et al.* (2003) and $Re \approx 3440$ in Marino & Luchini (2009). This spread of critical Reynolds number estimates and theories on the onset of instabilities motivated a further detailed study conducted by Lanzerstorfer & Kuhlmann (2012*b*), where they performed a global linear stability of flow over a FFS covering a range of constriction ratios ($0.23 \leq \Gamma \leq 0.965$) and an energetics analysis to understand the underlying mechanism leading to the instability. They found the destabilising global mode to be stationary and localised near the secondary recirculation region formed immediately after the

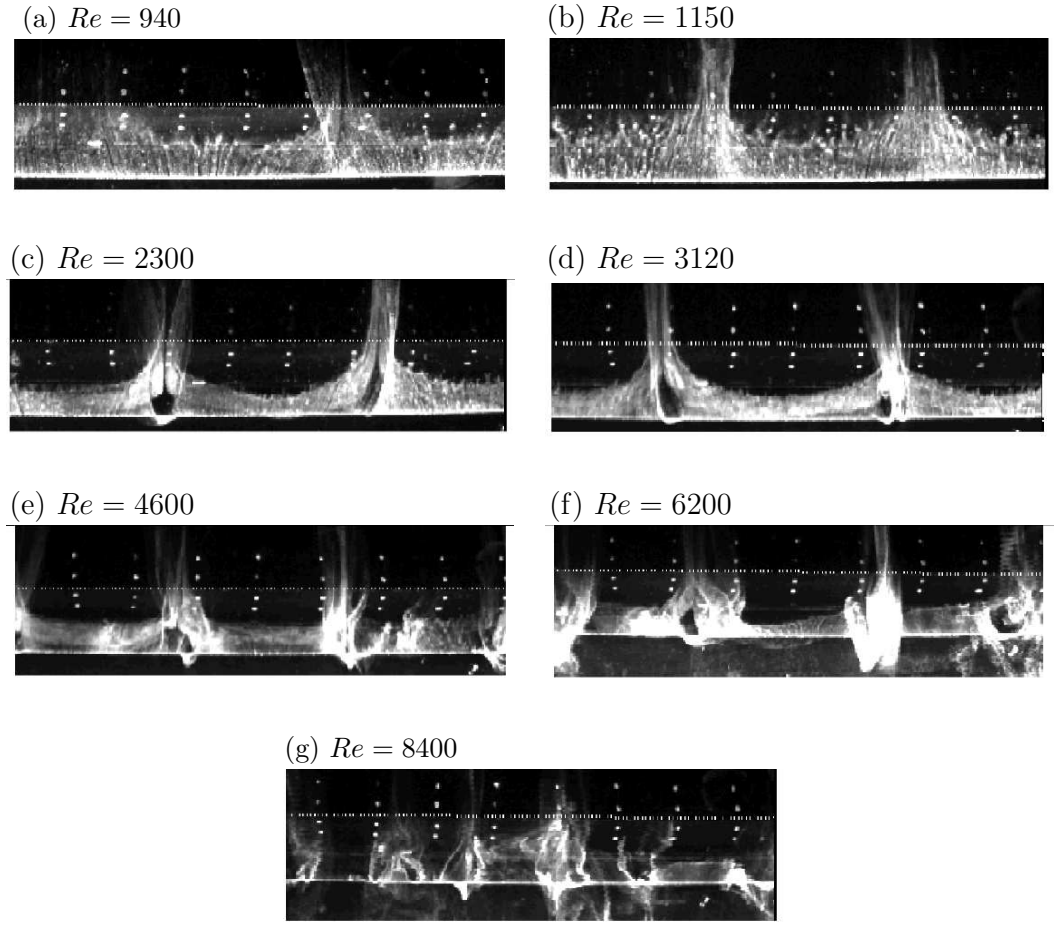

Figure 1.2: Hydrogen bubble visualisation of streamwise streak formation at different Reynolds number showing the middle 160 mm of the channel. Flow is from bottom to top. The dotted line indicates the location of the edge of the step. The figure has been reproduced from Stüer *et al.* (1999) with permission of the publisher.

step for all Γ values investigated and the critical Re for $\Gamma = 0.25$ to be $Re \approx 5888$. The modes appeared as alternating rolls of streamwise velocity in the secondary recirculation region after the step as shown in figure 1.3. The difference in the critical value from Marino & Luchini (2009) is attributed to an insufficient inflow and outflow length and grid resolution in their study, whereas from Stüer *et al.* (1999) to the side wall-effects in the experiments. By analysing the energy budget between the base flow and the perturbations, the study by Lanzerstorfer & Kuhlmann (2012*b*) concluded that a combination of lift-up mechanism and deceleration of the flow caused the instability which was observed as steady streaks with wavelength scaling about three times the step height agreeing well with earlier investigations. Further, for a constriction ratio of 0.25, they show the flow to be highly receptive to incoming perturbations or initial conditions in the region

ahead of the step, matching the results obtained from previous studies (Marino & Luchini, 2009), and the secondary recirculation region to be most sensitive with regard to any localised structural perturbations.

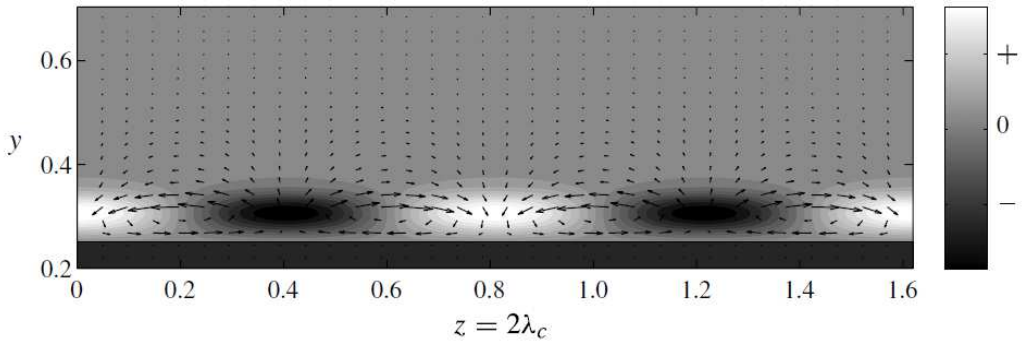

Figure 1.3: Streamwise velocity of the global mode destabilising the 2D laminar base flow over a forward-facing step with expansion ratio 0.25. Reproduced from Lanzerstorfer & Kuhlmann (2012*b*) with permission of the publisher.

1.1.2 Flow over backward-facing step (BFS)

Laminar flow over a backward-facing step and the onset of instability and transition in these flows have been widely studied. A confined flow over a BFS at a low Re features a recirculation region immediately downstream of the step. An additional secondary recirculation region also forms on the top wall with an increase in Re due to the development of an adverse pressure gradient immediately after the step (Armaly *et al.*, 1983; Kaiktsis *et al.*, 1996; Ghia *et al.*, 1989; Erturk, 2008), as shown in figure 1.4.

Early experimental studies (Armaly *et al.*, 1983) of air flow over a BFS having an expansion ratio (height of the outlet channel to the inlet channel) of 2 have covered the laminar, transitional and turbulent flow states over a range of Reynolds numbers $70 < Re < 8000$. The flow transition from the laminar state was observed at $Re \approx 1200$. Their experiments revealed three-dimensionality near the step for $Re \gtrsim 400$, with the appearance of the secondary recirculation region on the top wall, also being supported by a numerical analysis in the same study.

At a similar Re, Ghia *et al.* (1989) observed the formation of counter-rotating streamwise vortices with the onset of instability, which they suggested to be Taylor–Göertler vortices manifesting due to the streamline curvature of the bulk flow, owing to the formation of the primary recirculation region after the step and the secondary recirculation region on the top wall.

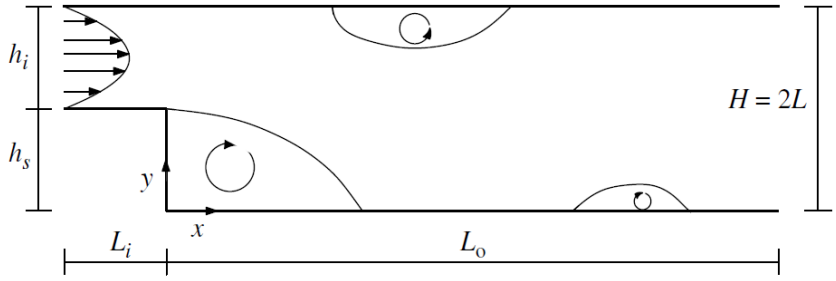

Figure 1.4: Flow geometry and the recirculation regions formed in flow over a backward-facing step in a channel. Flow is left to right. Reproduced from Lanzerstorfer & Kuhlmann (2012*a*) with permission of the publisher.

Three-dimensional simulations in Williams & Baker (1997) also supported the previous flow features, though through a particle tracking analysis they concluded that three-dimensionality observed in the flow is due to the interaction of the side wall jets with the bulk flow and unlike the previous studies, they postulated that the three-dimensional effects develop gradually from Re as low as 100.

At a similar expansion ratio, the flow was found to remain steady until $Re = 800$ in a later study (Gresho *et al.*, 1993), whereas the stability analysis by Kaiktsis *et al.* (1996) found the flow to remain steady up to $Re = 2500$. The study illustrated that the flow was convectively unstable for $Re \geq 700$, which they attributed to the onset of unsteadiness in the flow in the presence of noise. Propagation of 3D vortical structures having zig-zag structures was also reported in the three-dimensional simulations conducted by Yanase *et al.* (2001) by using different inflow perturbations over $525 \leq Re \leq 700$.

Linear stability of the local 2D velocity profiles at various location downstream of the step at a high Reynolds number of $Re = 3700$ predicted an absolutely unstable region in the middle of the primary recirculation region (Wee *et al.*, 2004) which was argued to be responsible for the onset of self-sustained 2D oscillations. The centre of the recirculation zone after the step was also shown to be the region of maximum backflow. This study was completely based on 2D analysis, thereby precluding any 3D mechanisms which were found in earlier studies.

There existed a lot of disparities on the critical Re predicted for the onset of instability, about the type and origin of the primary instability in these types of flow, and the Re up to which the flow remains steady.

In order to characterise the breakdown of the 2D flow solution and study the global modes responsible for the onset of transition, Barkley *et al.* (2002) conducted a global linear stability analysis considering a setup with expansion ratio similar to that in Armaly *et al.* (1983). Their investigation showed that the

onset of three-dimensionality occured through a stationary mode concentrated in the recirculation region behind the step at a critical Reynolds number of $Re = 748$. The global eigenmode appeared as flat rolls within the recirculation region as shown in figure 1.5. Unlike the previous findings in the literature, they show a centrifugal instability mechanism of the recirculation bubble to be responsible for the instability. They found the flow to be stable to 2D perturbations over the range of Re that they investigated (up to $Re = 1500$).

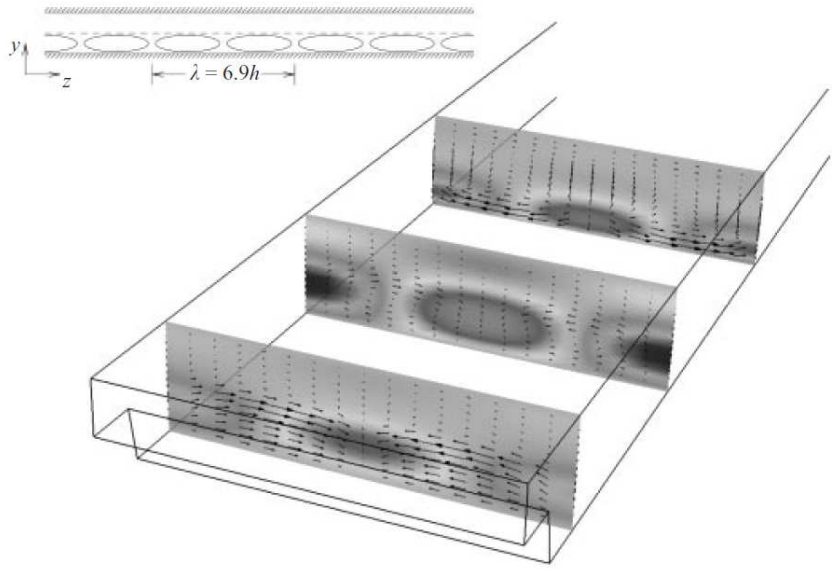

Figure 1.5: Three-dimensional critical eigenmode in the recirculation region behind a backward-facing step at $Re = 750$, expansion ratio = 0.9. Shown are the streamwise velocity contours overlaid with the transverse and spanwise velocity vectors at three cross-sectional planes behind the step. Flow is into the plane. Reproduced from (Barkley *et al.*, 2002) with permission of the publisher.

In the linearly stable regimes predicted by Barkley *et al.* (2002), a large transient growth behaviour due to a local convective instability was reported in Blackburn *et al.* (2008*a*). Reynolds numbers up to $Re = 500$ were considered, and the predicted maximum amplification in energy was $\mathcal{O}(10^4)$. The optimal modes were strained slanted structures concentrated near the step which evolved into rollers as they advected further downstream of the step. The maximum amplification occured when the structures completely passed over the two-recirculation regions. They found the three-dimensional optimal energy growth to be slightly higher than the corresponding two-dimensional optimal growth. Morover, on perturbing the inflow in the non-linear simulations with white noise, they observed narrowband random velocity perturbations in the channel downstream of the step matching the location of maximum transient growth. The effect of weak

non-linearity was stabilising in these flows.

To understand the physical mechanism driving the instability, Lanzerstorfer & Kuhlmann (2012*a*) used an energy-transfer analysis, covering a range of expansion ratios (0.25 to 0.975). Although the primary instability in these flows were three-dimensional, the instability mechansim driving the instability was found to vary with decrease in the expansion ratio (Γ). For large expansion ratios a centrifugal instability mechanism was found responsible for destabilising the base flow. A switch in the instability mechanism to an elliptical type instability was found in the moderate range of Γ up to $\Gamma \approx 0.8$, followed by a change from oscillatory to a stationary mode. On further lowering Γ, the primary recirculation region was strained and extended downstream further than in the higher cases. In those cases, a combination of flow decelaration and lift-up effect was found to be the governing mechanism of instability, contradicting the centrifugal instability mechanism in Barkley *et al.* (2002).

1.1.3 Other confined flow setups

Studies conducted on confined setups other than the conventional forward or backward-facing step, such as flow over a rounded backward-facing step (Marquet *et al.*, 2008), stenosis flows (Griffith *et al.*, 2008; Blackburn *et al.*, 2008*b*) and flow in a 180^o bend (Sapardi *et al.*, 2017) have also found the primary bifurcation to be of three-dimensional nature. Another feature of these flows is the large transient amplification associated with convective instabilities in the linearly stable region in these flows, raising a question as to the possible route to transition in a realistic flow.

Both the global linear stability and transient growth of flow in a curved channel consisting of a rounded BFS was studied in Marquet *et al.* (2008). The distinguishing feature of this flow to that of a BFS flow was the absence of the secondary recirculation region on the top wall. The global destabilising modes were very similar to that for a BFS (Barkley *et al.*, 2002) and flow over a bump (Gallaire *et al.*, 2007). Through an investigation of the short term dynamics of the flow, they found the optimal modes to be concentrated before the separation point of the recirculation bubble upstream of the channel, manifesting as elongated wave packets. The main energy gain of these modes was through an Orr type mechanism and an inflectional mechanism while passing over the recirculation zone. For a subcritical Reynolds number of $Re = 772$, the study conducted by Marquet *et al.* (2008) found a maximum two-dimensional amplification of $\sim \mathcal{O}(10^2)$. A comparison of the strength of both the long-time (or resonator) dynamics and

the short-time (or amplifier dynamics) was made considering a super-critical Re to get a realistic picture of which might be the dominant dynamics at play in a practical experimental setup. They find that for $Re = 1500$, optimal disturbances could be amplified to a magnitude of $\sim \mathcal{O}(10^5)$ in a short time period ($T = 14$), whereas the global three-dimensional mode would take an approximate time of $T = 510$ to achieve the same growth. Hence, they suggest that the possibility of the short time dynamics to dominate in a real scenario where external disturbances could feed energy to the optimal modes and be amplified. These questions could be answered with more clarity and confidence by studying the non-linear dynamics in these flows and investigations of how external disturbances feed the optimal and the global modes.

For the same curved BFS step case, direct and adjoint mode computations were carried out in a later study (Marquet *et al.*, 2009) with two broad aims. Firstly, to show the lift-up and convective non-normalities in these flows by studying the spatial location and the dominant velocity component of both the direct and adjoint modes (Marquet *et al.*, 2009) and, secondly from a flow control perspective near the critical Re. The region near the separation point of the recirculation region was where the spatial location of both the adjoint mode velocity and pressure were maximum. Hence, these locations were the most receptive to initial perturbations and local forcing, which in a physical sense could be critical from an active control framework for the placement of an actuator. The sensitive location found as the overlap region of the direct and adjoint modes was within the recirculation region, and was where placement of a passive control mechanism would be most effective. The corresponding regions are shown in figure 1.6.

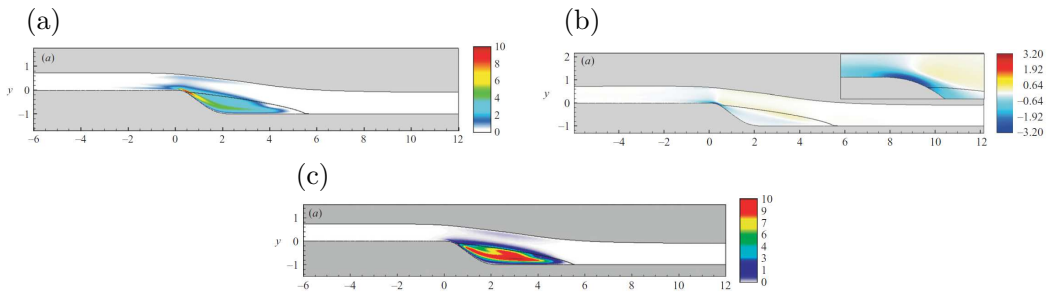

Figure 1.6: Spatial contours of (a) velocity and (b) pressure field of the adjoint mode, and (c) sensitivity field for flow in a curved channel with a rounded backward-facing step at a supercritical Reynolds number of $Re = 800$. Reproduced from Marquet *et al.* (2009) with permission of the publisher.

Another similar confined flow geometry is the axisymmetric stenosis flow which features the formation of two recircualtion regions immediately after the

blockage region in the flow. These are also associated with a primary three-dimensional bifurcation occuring at a critical Reynolds number of $Re = 770$. However, experiments carried out in this setup by Griffith *et al.* (2008) shows an onset of instability at a much lower Re associated with the instability of the shear layer which develops after the blockage in the flow, with the instability modes found from the linear stability analysis not being observed in the experiments, as shown in figure 1.7(a). Therefore, a convective type instability is associated with the onset of transition in these flows. Numerical and experimental analysis of the effect of forcing was also studied in their study, at a Re lower than the limit for the convective instability to understand the shear layer behaviour better. These showed the maximum response when the forcing frequency was lower than the one measured from the unsteady flow, which is explained as the non-linear interaction between the turbulent flow downstream with the unstable shear layers upstream.

Transient growth analysis carried out in Blackburn *et al.* (2008*b*) support the previous study (Griffith *et al.*, 2008) by showing an energy amplification of the optimal modes as high as $\mathcal{O}(10^8)$ at $Re = 700$. The optimal modes had energy highly concentrated near the separation point of the shear layer which grew in energy when convecting downstream along the shear layer in a very short time period. The disturbance wave packets are observed to be lying along the shear layers (figure 1.7b) matching well with the experimental observation in Griffith *et al.* (2008).

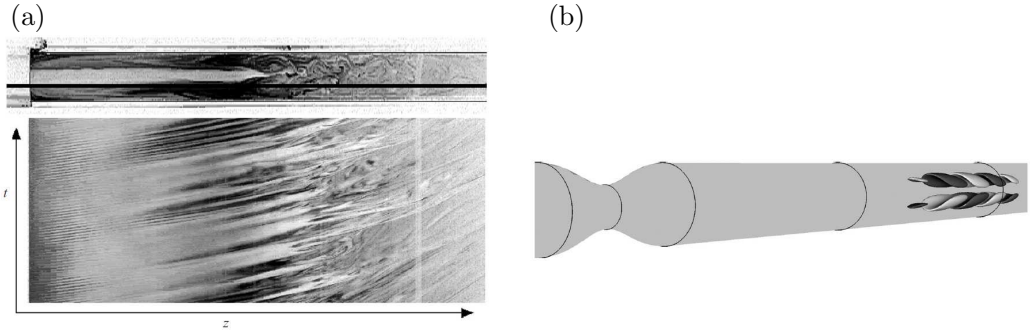

Figure 1.7: (a) Instantaneous snapshot of an unsteady flow in a stenosis and the spatio-temporal diagram constructed from the line shown in black at the bottom for $Re = 194$. Reproduced from Griffith *et al.* (2008) with permission of the publisher. (b) Iso-contours of the axial velocity of the optimal disturbance at maximum amplification at a downstream location along the shear layer for $Re = 400$. Reproduced from Blackburn *et al.* (2008*b*) with permission of the publisher.

1.2 Magnetohydrodynamic (MHD) flows in confined flow setups

The onset of instability and the route to transition in various confined flow setups for the hydrodynamic cases were discussed in the previous section. In this section, the focus is shifted to duct flows in the presence of a uniform magnetic field. As discussed in the introduction, for flow in a duct under the presence of uniform magnetic field, two boundary layers develop on the walls parallel and perpendicular to the direction of the magnetic field, namely the Hartmann and the Shercliff boundary layers. In the initial part of this section, various studies which have investigated the stability and transition character, the associated global modes, and the optimal growth focusing on the Hartmann layers in channel flows are discussed. This is followed by studies which focus on the stability characteristics of Shercliff layers in a channel flow with a spanwise magnetic field as well in ducts flows. Various investigations which have added to the understanding of formation of quasi-2D structures under the influence of high magnetic field strength, their stability and evolution are presented to complete this section.

1.2.1 Instability and transition in Hartmann layers

Hartmann channel flow

Some of the earlier studies focused on understanding the stability and transitional characteristics of the Hartmann layer. The critical Reynolds number based on Hartmann layer thickness ($R_c = Re/Ha$) was found to be approximately 50 000 for the instability of Hartmann layers in a pressure driven flow under a transverse magnetic field (Lock, 1955). A similar critical value was found for plane Couette and plane Poiseuille flows with transverse magnetic field in theoretical studies by Takashima (1996, 1998). This was approximately two orders of magnitude higher than what was observed in experimental studies (Hartmann & Lazarus, 1937) where transition was found to occur at $R_c \approx 250$.

To understand the discrepency between numerical analysis and experiments, the stability of an isolated Hartmann layer was investigated by Lingwood & Alboussiere (1999). Their study predicted a critical Reynolds number for instability from linear stability analysis to be $R_c \approx 48\,250$ which was close to what was observed for Poiseuille and Couette flows under a transverse magnetic field (Lock, 1955; Takashima, 1996, 1998). They also found an approximately three orders of magnitude difference between the R_c and the lower bound Reynolds number for

perturbations to experience energy growth, Re_E, found from energetic stability analysis. They suggested that the transition may be governed by the stability of the Hartmann layer to finite amplitude perturbations supporting the previous hypothesis by Lock (1955).

Further support came from the study conducted by Gerard-Varet (2002) in which the significance of non-linear effects on the growth of small amplitude perturbations were found through a rigorous expansion of the velocity field in terms of powers of the initial energy. They highlighted the differences in the linear and non-linear evolution of perturbation energy even at low Reynolds numbers and initial perturbation energy, further supporting the possibility of a bypass transition. In such a case, the flow bypasses the route to transition predicted by the linear stability analysis. This happens due to the interaction between the non-orthogonal eigenmodes, which can produce brief periods of large amplification of kinetic energy of linearised perturbations, even when the flow is asymptotically stable (Reddy & Henningson, 1993; Trefethen *et al.*, 1993; Henningson & Reddy, 1994).

Previous experiments had based their results by considering only the scenario of relaminarisation of the flow starting from a turbulent state. Therefore, Moresco & Alboussiére (2004), in their experiment considering both transition to turbulence from a laminar state as well as the relaminarisation of the flow starting from turbulent state to check for any behaviour not captured through earlier analyses. However, they observed no hysteresis behaviour and obtained a critical Reynolds number of $R_c = 380$ for the onset of instability in Hartmann layers, again differing substantially from predictions made from linear stability theory.

Transient growth was hence considered to be the possible route through which transition in the Hartmann layer started. To understand the nonmodal dynamics, the optimal mode shapes, optimal magnetic field and scalings of the different components of the optimal disturbance, numerical simulations were carried out in Airiau & Castets (2004) for Hartmann numbers up to $Ha = 20$. The transient growth analysis conducted in their study for a plane Poiseuille flow under the influence of a magnetic field showed that the optimal modes appeared as streamwise rolls which developed into streamwise streaks with the streamwise velocity component becoming dominant at the optimal time.

Further confirmation and support came from the study of Krasnov *et al.* (2004), who conducted DNS at lower Ha and Re. They postulated a two-step process of transition where streamwise invariant 2D optimal modes undergo transient growth and thereafter break down into streaks due to introduction of ran-

dom noise in the modulated flow, holding similarity to the non-magnetic case. Their prediction of the critical Reynolds number R_c was found to be between 350 and 400, matching quite well with the experimental prediction by Moresco & Alboussiére (2004).

1.2.2 Instability and transition in Shercliff layers

Channel flows with spanwise magnetic field

The studies on the instability of the Hartmann layers considered only the presence of the Hartmann walls, disregarding any influence of the side walls (walls parallel to the magnetic field direction) on which the Shercliff layers form. The understanding of the transition in MHD duct flows would only be complete with the knowledge of instabilities arising in these boundary layers. Optimal growth and transition to turbulence in a channel flow in the presence of a spanwise magnetic field was studied in Krasnov *et al.* (2008) covering Hartmann numbers in the low, intermediate and high-Ha range ($5 < Ha < 100$) at two sub-critical Reynolds numbers ($Re = 3000, 5000$). An increase in the magnetic field strength was found to strongly suppress the maximum amplification of the optimal mode following a power law behaviour ($\sim Ha^{-2}$). The structure of the optimal mode was also observed to change from a streamwise mode to an oblique mode, and to a spanwise dominant mode with increasing Ha. A different scenario of transition to turbulence was also explored in their study by non-linear evolution of the three-different optimal modes found from the linear analysis and their modulation. The streamwise optimal modes at low Ha showed a similar transitional behaviour as a purely hydrodynamic channel flow case characterised by the formation of streamwise streaks and their breakdown with the addition of 3D noise at optimal energy levels through lift-up and Orr mechanisms. The oblique disturbances at moderate-Ha if introduced as symmetric modes could trigger transition without any noise addition by serving as a secondary perturbation to each other. In the high-Ha range (≈ 100), only the spanwise modes (Tollmien–Schlichting waves) experienced transient growth and any addition of 3D noise could not trigger a transition as they were dissipated strongly by Joule dissipation.

MHD duct flows

Previous numerical studies on the stability of Hartmann and Shercliff layers have excluded the existence of the other wall. For a more realistic understanding of transitions, studies started to focus on properly enclosed duct flows. Linear

stability analysis and transient growth of quasi-2D perturbations in an MHD duct flow using the SM82 quasi-2D model, (Sommeria & Moreau, 1982) was investigated in Pothérat (2007) for a range of Hartmann friction parameters $0 \leq H \leq 1000$, where H accounts for both the Hartmann number and the aspect ratio of the duct cross-section. The critical modes found from linear stability studies were quasi-2D Tollmien–Shlichting (TS) waves concentrated in the Shercliff layers with a critical Reynolds number (based on Shercliff layer thickness) for transition $Re_s = Re/H^{1/2} = 48\,350$. The lower stability limit found from energy stability studies was $Re_E/H^{1/2} = 65.33$. A large transient growth of quasi-2D perturbation was observed between these two limits and hence they hypothesised that the Shercliff layers were more likely to become unstable due to the significant transient growth of quasi-2D perturbations. Another key point they raised is that the Shercliff layers become unstable long before the instability of the Hartmann layer since the critical Reynolds number for the Shercliff layer instability is lower than that for the Hartmann layers in a duct with a similar configuration (Moresco & Alboussiére, 2004). Computational studies in a toroidal duct with square cross section under the influence of an axial magnetic field have also demonstrated that instabilities arise in the side layers much before the instability threshold for the Hartmann layers (Zhao & Zikanov, 2012).

The investigation of Pothérat (2007) explored the 2D dynamics of Shercliff layer instability as they considered a quasi-2D model in which the Hartmann layer is assumed to be stable and its effect is modelled in the governing momentum equation as a linear friction acting on the quasi-2D core of the duct flow. To understand the 3D dynamics in an MHD duct flow, Krasnov *et al.* (2010) conducted a detailed study on the optimal growth in these flows covering a wide range of duct aspect ratios (r) ranging from $1/9 \leq r \leq 3$ for $0 \leq Ha \leq 50$ at a single Reynolds number $Re = 5000$. The duct configuration and the base flow profile for a low r case ($r < 1$), a square duct case ($r = 1$) and a higher r case ($r > 1$) considered in their study are reproduced in figure 1.8. Their investigation revealed a strong suppression of purely streamwise perturbations with increasing magnetic field strength and the localised spatial location of the optimal modes in the Shercliff layers for all the cases. Just as in the channel flow case with a spanwise magnetic field (Krasnov *et al.*, 2008), increasing Ha results in a dominance of a non-zero streamwise wavenumber optimal mode. The optimal perturbations were overlapping structures inhomogeneous in the streamwise direction (x) and concentrated in the Shercliff layers gaining energy predominantly though lift-up mechanism. For the low r cases, a reduction in r was found to cause an increase

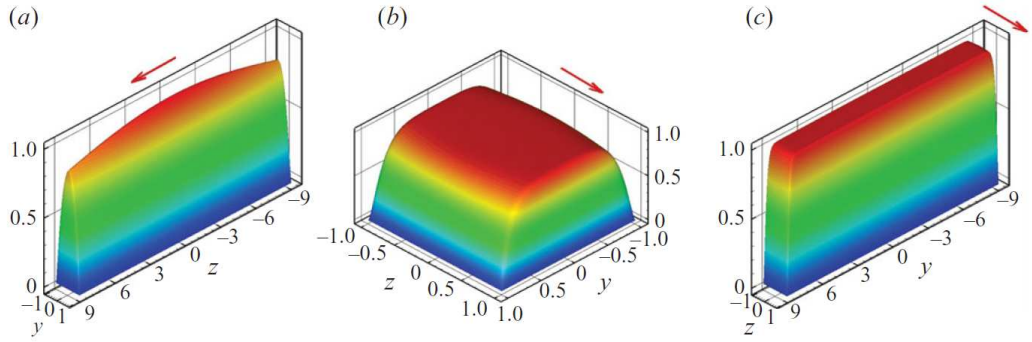

Figure 1.8: Base flow profile of flow in an MHD duct with aspect ratio (a) $r = 1/9$, (b) $r = 1$ and (c) $r = 9$ at $Ha = 50$, $Re = 5000$. The applied magnetic field direction is represented by the red arrow. Reproduced from Krasnov *et al.* (2010) with permission of the publisher.

in the maximum energy amplification of the optimal mode and a reduction in the optimal wavenumber, and approached the channel flow results in the limit of $r \to 0$. The optimal wavenumber was almost invariant with change in r for the high-r cases considered as the velocity profile had negligible changes in the Shercliff layer. Convergence to a Hartmann channel case was not observed as $r \to \infty$.

The question then arises as to the existence of a purely quasi-2D transient growth at higher Hartmann numbers, and how accurately the quasi-2D model SM82 can capture the dynamics relative to the corresponding three-dimensional case in MHD duct flows. A recent study (Cassells *et al.*, 2019) sought to answer these questions. They considered a range of Hartmann numbers $0 \leq Ha \leq 800$ extending beyond the range considered in Krasnov *et al.* (2010) at $Re = 2000$ and $Re = 10\,000$. In this range of Ha, they found three broad regimes based on the optimal growth rate (G_{max}) scaling. In the lower magnetic field range $Ha \leq 1$, G_{max} remains almost independent of Ha, scaling as $\sim Re^2$. An approximate power law scaling of $G_{max} \sim Ha^{-1.5}$ was found in the moderate magnetic field range $10 \leq Ha \leq 50$. The transition to the higher magnetic field range was at a critical Reynolds number (based on the Hartmann layer thickness), $R_H = Re/Ha \approx 33.3$ where G_{max} was found to hold a scaling of $Ha^{-0.44\pm0.07}$ matching closely with that found from quasi-2D models. The three-dimensional optimal modes in the low and intermediate range of Ha, concentrated in the Shercliff layers is found to elongate and match the length scale of the duct in the magnetic field direction in the higher Ha regime (reproduced in figure 1.9). Another key aspect investigated in this study is the validity of the SM82 model. It is shown that not only is the SM82 model accurate with respect to capturing the amplification and scalings,

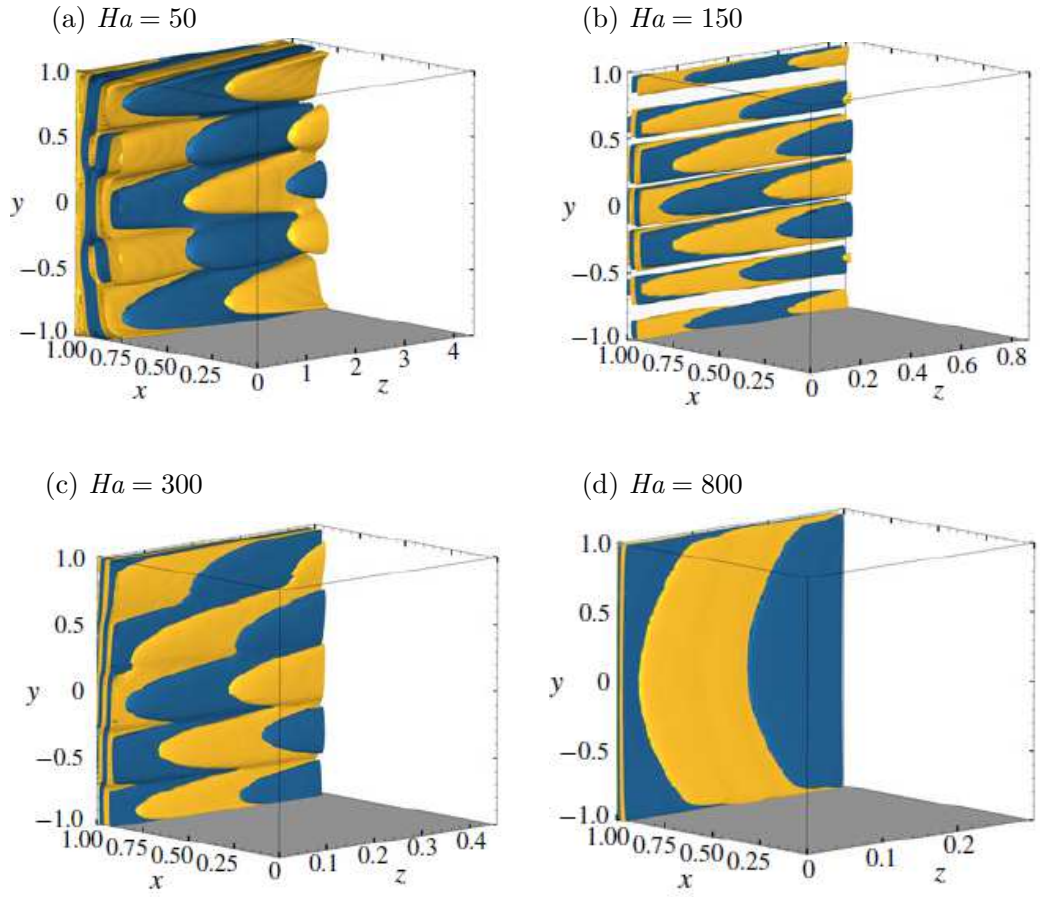

Figure 1.9: Positive and negative iso-contours of the vertical component of vorticity ω_y of the optimal mode corresponding to the maximum optimal energy growth in MHD duct flows at different Hartmann numbers. Magnetic field is in the vertical (y) direction and flow is from left to right. Only one side wall is shown for clarity. Reproduced from Cassells *et al.* (2019) with permission of the publisher.

the mean topology of the optimal mode is also approximately captured, except for the inherently three-dimensional barelling effect observed (Pothérat, 2012) at the ends of the Hartmann wall in the three-dimensional case. This is visualised in figure 1.10 which is more pronounced in lower interaction parameter values.

1.2.3 Quasi-2D turbulence generation in MHD duct flows

The onset of instabilities and the modes through which transition from a laminar state occurs in MHD duct flows were discussed in the previous sub-sections. Under the influence of increasing Hartmann number, strong laminarisation and dominance of quasi-2D structures oriented along the direction magnetic field were found. Under high magnetic field strengths prevelant in nuclear fusion blanket

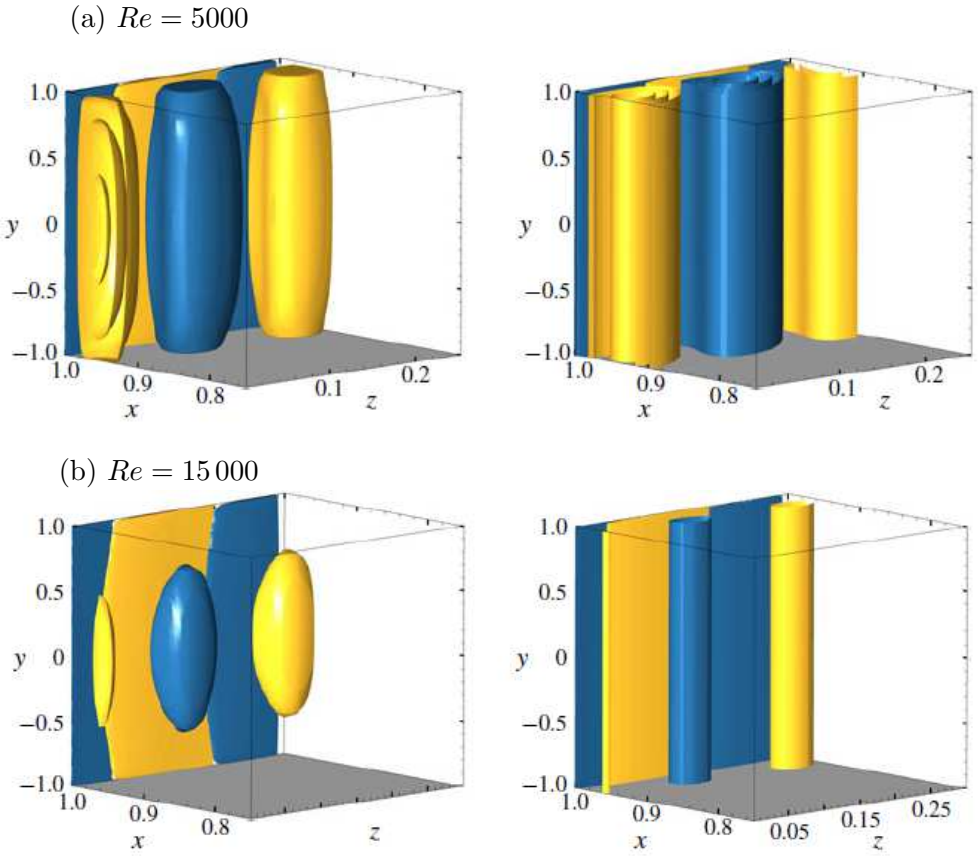

Figure 1.10: Comparison of the optimal mode from the 3D analysis (left column) to the corresponding quasi-2D optimal modes at $Ha = 800$. Shown are the positive and negative iso-contours of the vertical component of vorticity ω_y of the optimal mode. Magnetic field is in the vertical (y) direction and flow is from left to right. Only one side wall is shown for clarity. Reproduced from Cassells *et al.* (2019) with permission of the publisher.

modules which is one of the key motivators of the present work, these quasi-2D structures needs to be exploited and be well understood for heat transfer enhancement. In this section, turbulence generated using generators in MHD duct flows at low magnetic Reynolds number R_m under the influence of a uniform magnetic field is discussed. The main focus will be on the formation of anisotropic turbulence, its evolution and the key features of the quasi-2D structures in MHD ducts.

Earlier experimental investigations have observed the formation of two-dimensional turbulent structures behind a grid (Kolesnikov & Tsinober, 1972). A turbulent flow contains eddies of different length scales. On plotting the kinetic energy spectrum, the cascade of energy from the energy containing eddies to the dissipation range can be obtained with the inertial subrange in between the two. In a three-dimensional turbulent flow, the flow typically has most of the

energy contained in the high frequency regime with the inertial sub-range obeying a scaling of -5/3. However, a -3 law is obeyed by a typical two-dimensional tubulent flow where most of the energy is contained by the large scale eddies and energy transfer to the high frequency small scale structures are absent. In a weak magnetic field, the turbulent structures had characteristics of three-dimensional turbulence which was evident from the -5/3 law followed by the energy spectrum, whereas under the presence of a strong magnetic field, the turbulent structures became two-dimensional, obeying a -3 law in the energy spectrum. This was further verified qualitatively in experiments by introducing impurities and studying their concentration distribution in the three-directions. Similar behaviour was also observed in other experimental studies (Alemany *et al.*, 1979).

Theoretical studies followed, trying to explain the formation of anisotropic structures which were observed in previous experiments. The decay of turbulence under the influence of a strong magnetic field ($N \gg 1$) was analysed in Moffatt (1967). They found a decay in the turbulent kinetic energy (K) with time following a power law behaviour $K(t) \sim t^{-1/2}$ in the domian where anisotropy was dominant. The formation of two-dimensional turbulence was explained as the channeling of kinetic energy into the component parallel to the magnetic field direction.

The condition of formation of quasi-two-dimensional turbulent structures, its corresponding length and velocity scalings and the effect of Hartmann walls were theoretically found in the subsequent study (Sommeria & Moreau, 1982) in the assymptotic range of high magnetic field strength. The following conditions were to be satisfied for quasi-two-dimensional structures to exist in an MHD duct flow:

$$\begin{aligned} Re \gg 1,\ R_m \ll 1 \\ N \gg 1,\ Ha \gg 1 \end{aligned} \tag{1.1}$$

It is shown that, if the conditions in equation (1.1) are satisfied, then velocity gradients and the velocity component in the direction of the applied magnetic field become negligible compared to the components in the other directions, revealing that the eddies become elongated in the magnetic field direction. A comparison of the evolution of an eddy in a non-MHD and an MHD case is shown in figure 1.11. This process explains the inverse energy cascade in two-dimensional turbulence as the eddies align with the field, facilitating their coalescence into larger eddies, unlike the energy cascade to smaller scales in the absence of magnetic field. The effect of the Hartmann layers is to create a braking effect since the current passing through the layer is closed in the bulk, which ultimately acts as an additional

friction term in the equation governing the fluid momentum.

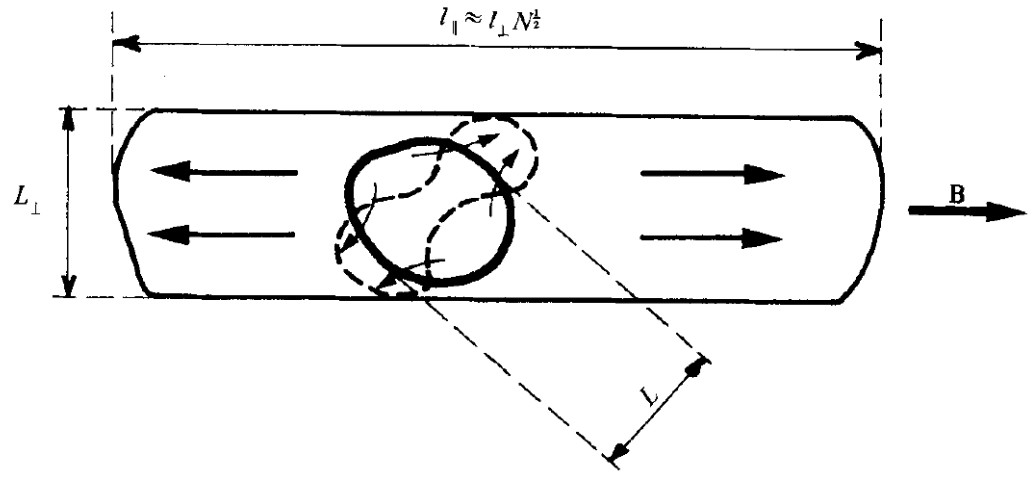

Figure 1.11: Sketch showing the evolution of an eddy of initial size L without and with the presence of magnetic field of strength B in a turnover time of the eddy. The final form of the eddy in the presence of the magnetic field is shown with solid lines whereas the non-magnetic case is shown with dashed lines. Reproduced from Sommeria & Moreau (1982) with permission of the publisher.

Unlike Sommeria & Moreau (1982) in which the elongation of the vortices in the magnetic field direction was explained as a diffusion phenomenon, Davidson (1997) explains this elongation as the need to conserve angular momentum in the direction of magnetic field with the continuous decrease in the kinetic energy of the turbulent structures.

Two-dimensional turbulence formation in shallow containers and inverse energy cascades were demonstarted in earlier experiments of Sommeria (1986). Much later, Klein & Pothérat (2010) performed experiments in a cubic container subjected to a uniform magnetic field covering a range of Hartmann numbers in the low and high range. They studied the flow structures by comparing the flow pattern on the top and bottom wall of the container and found both strong and weak three-dimensionality to persist in the lower Hartmann number range. However at the high Hartmann number, where the time for Lorentz force to diffuse in the magnetic field direction is much less than the turn-over time of the eddies, they demonstrated the existence of both steady and unsteady quasi-2D structures.

Direct numerical simulation of the evolution of MHD turbulence in a 3D cubic box with periodic boundary conditions was studied in Zikanov & Thess (1998). In the low interaction parameter range, three-dimensioanl MHD turbulence, which was statistically similar to ordinary turbulence was observed. In the moderate

range of N, an intermix of periods of existence of quasi-2D dynamics, and turbulent bursts of the quasi-2D structure leading to complete three-dimensional dynamics to dominate, was observed due to comparable strength of both Joule dissipation and non-linear energy transfer. However, in the high range of N, two-dimensional dynamics was the only dominant feature. This supported the previous DNS of Schumann (1976) which also found transition from the three-dimensional turbulent state to quasi-two-dimensionality.

Three-dimensional simulations of MHD flow in rectangular ducts with a square cylinder as an obstacle (Mück *et al.*, 2000) clearly captured the transition to quasi-two-dimensionality with increasing Hartmann number and interaction parameter. This was found to occur somewhere between $0.2 \leq N \lesssim 1$, as depicted in figure 1.12(a-c). The secondary instability of the Kármán vortex streets which occurs in hydrodynamic flows is strongly suppresed with the presence of a magnetic field resulting in prevalence of only quasi-2D structures. The effect of Hartmann walls in damping the quasi-2D vortices through Hartmann braking were also demonstrated as the reduction in the diameter of the quasi-2D vortices with their evolution downstream, in the presence of magnetic field aligned along their axis. This is shown in figure 1.12(c-e). Another interesting and key observation was that the quasi-2D vortices adopted a cigar-shape with core diameter being greater than that near the Hartmann walls, with increasing N (figures 1.12d,e). This is attributed to the magnetic potential variation in the magnetic field direction due to inertial contribution. Experimental studies of cylinder wakes in the high Hartmann number and interaction parameter range (Frank *et al.*, 2001) have also demonstrated the Hartmann damping effect and a linear increase in the transitional Reynolds number with increasing Ha.

Further support to the quasi-2D vortices taking a cigar-shape came from the study of Pothérat (2012) in which they show the quasi-2D columnar structure in MHD ducts to exhibit a 'barrel' shape in the core. It was claimed that this effect would be important in the 2D to 3D transition regimes. The barrel effect was shown to be due to 2D vorticity that causes field-aligned current to pass across the boundary layer.

An investigation of 3D flow past cylinders in an MHD duct covering Hartmann numbers in the low, moderate and high range was conducted in Kanaris *et al.* (2013) and a comparison was made with the results from the corresponding quasi-2D flow simulations (Dousset & Pothérat, 2008). A counter-intuitive feature of decreasing stability with increasing Ha was observed by Kanaris *et al.* (2013) study in the low-Ha range, which they argued was due to the flattening of the

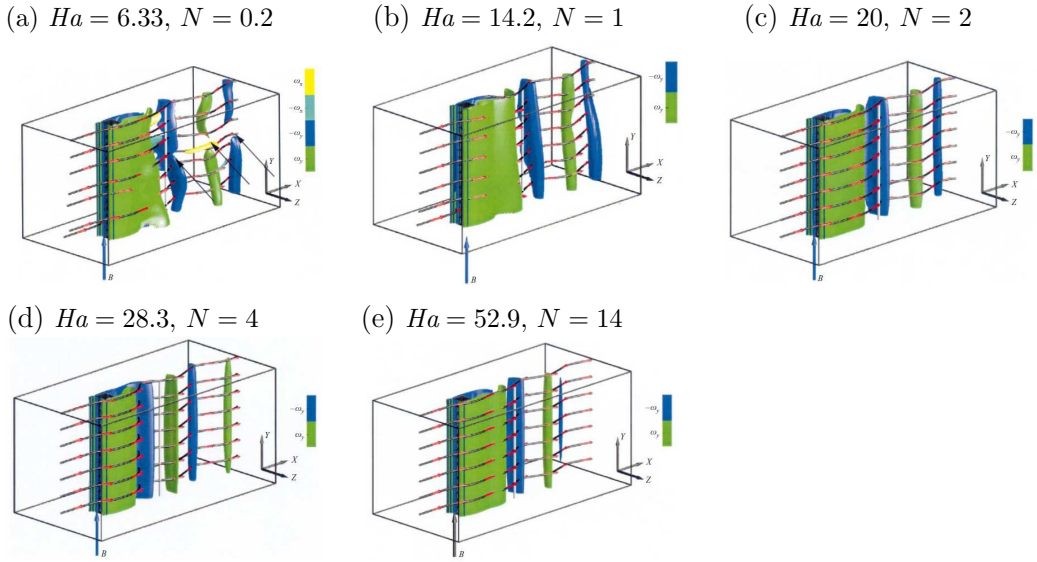

Figure 1.12: (a-c) Formation of quasi-2D vortices with increasing Hartmann number (Ha) and interaction parameter (N), (c-e) Hartmann damping of the quasi-2D vortices and (d,e) formation of cigar shaped structures with increasing N. Reproduced from Mück *et al.* (2000) with permission of the publisher. Flow is left to right in each frame and the cylinder and magnetic field are both vertical. Shown are the iso-surfaces of transverse vorticity field.

velocity profile with increasing Ha. The velocity profile flattening had a similar effect as changing the blockage ratio of the flow or having a moving wall causing a deceleration of the flow near the vicinity of the cylinder and thereby destabilising the flow. However, in the high-Ha range a linear increase in the critical Reynolds number with Ha was found, closely matching results from corresponding quasi-2D simulations (Dousset & Pothérat, 2008). Although the quasi-2D model fails to capture the three-dimensionality of global characteristics such as the lift and pressure coefficients in the spanwise direction due to varying Lorentz force distribution, the spanwise averaged values of these quantities were in good agreement with the values predicted from the quasi-2D models. The inertial effects leading to strong three-dimensionality and formation of small scale turbulent structures near the cylinder especially in the moderate range of Ha are also not captured in the quasi-2D models.

An analytical model for the decay of a quasi-2D MHD vortex generated using a cylindrical obstacle as vortex promoter in an MHD duct was developed in Hamid *et al.* (2015) taking into account the effect of blockage ratio, magnetic field strength and Reynolds number. A spatially evolving quasi-2D vortex is subjected to both viscous and Hartmann frictional effects both acting to lower the strength of the vortex quantified using peak vorticity (ξ_p). Viscocity was the

major contributor to the vortex decay in the near wake region, while further away from the vortex generator, Hartmann friction was the significant contributor to the vortex decay. The model gave a reasonabily good prediction of the peak vorticity and the decay rate in the high interaction parameter range. This was validated by comparing the model predictions with the corresponding numerical simulation of quasi-2D vortices and the 3D simulations of Kanaris *et al.* (2013).

Later, in § 1.4 the effect of the quasi-2D vortices generated using various techniques in promoting the heat transfer rate, their influence on a passive temperature field and the overall heat transfer efficiency that could be achieved will be presented. First, though, § 1.3 will review the use of wall protrusions for non-MHD heat transfer enhancement.

1.3 Heat transfer enhancement in hydrodynamic channel flows or duct flows using surface protrusions

This section reviews studies on hydrodynamic channel or duct flows which use two-dimensional transverse surface protrusions of different shapes as a means to generate turbulence and enhance heat transfer. The configuration and conditions responsible for improvement in the local heat transfer rate and an overall improvement in heat transfer efficiency found from these studies are discussed.

Computational and experimental studies for Re in the range 3000-20 000 using two-dimensional rectangular ribbed protrusions have shown a maximum local heat transfer coefficient value to be at the location of flow reattachment and where turbulent intensity was maximum (Chaube *et al.*, 2006). Various other geometrical shapes of the protrusion were also explored in this study; however, a proper validation with experimental studies was provided only for the rectangular-shaped geometry. Although the heat transfer rate was higher using a chamfered rectangular protrusion due to the increased Strouhal number of vortex shedding, the rectangular-shaped geometry was found to have the best performance by giving a better enhancement ratio.

Chen *et al.* (2006) carried out 3D simulations of a laminar flow in a rectangular duct with inclined BFS. They studied the effect of inclination angle of the BFS on the heat transfer behaviour, and found the maximum Nusselt number to vary between approximately 2.04 to 2.39 in the range of inclination angles considered ($15^o \leq \alpha \leq 90^o$). A higher temperature region observed near the region of

maximum backflow in their study highlighted the negative effect that recirculation zones can have on the structural stability of the duct. The local Nusselt number was found to achieve a peak value at locations of maximum transverse-velocity.

A transverse wedge shaped geometry for heat transfer enhancement in duct flows was studied experimentally by Bhagoria *et al.* (2002), where the effect of the various geometrical parameters of the wedge protrusion on heat transfer efficiency were quantified for high Reynolds number flow of air in range $3000 \leq Re \leq 18\,000$. The existence of an optimal wedge spacing, height and wedge angle for maximum heat transfer enhancement was found in the turbulent regimes investigated. A sketch of the flow pattern (figure 1.13) for different pitch (distance between subsequent wedges) shows that for the same streamwise length of the channel, the number of reattachment points increases initially, followed by a decrease, which is the reason for the existence of an optimal pitch. Various other studies have also pointed out the importance of having multiple reattachment points as these were the locations where the local Nusselt number was found to be high (Edwards, 1961; Emerson, 1966). A more streamlined shape of the protrusion was found to be a better option compared to a square shaped protrusion as these shapes could avoid the formation of hot spots of high-temperature which are found in the concave corner of square or rectangular ribs (Liou & Hwang, 1993).

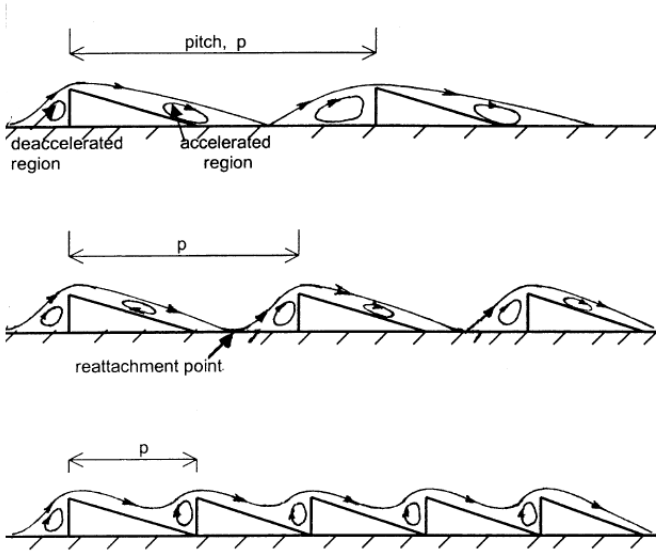

Figure 1.13: Sketch of the flow patterns observed by Bhagoria *et al.* (2002) for different inter-wedge spacing. Reproduced with permission of the publisher.

For a turbulent flow with $Re = 20\,000$, a comparison of the performance of four different transverse 2D protrusion shapes were made as shown in figure 1.14 (Kamali & Binesh, 2008). The significance of the shape of the geometry under

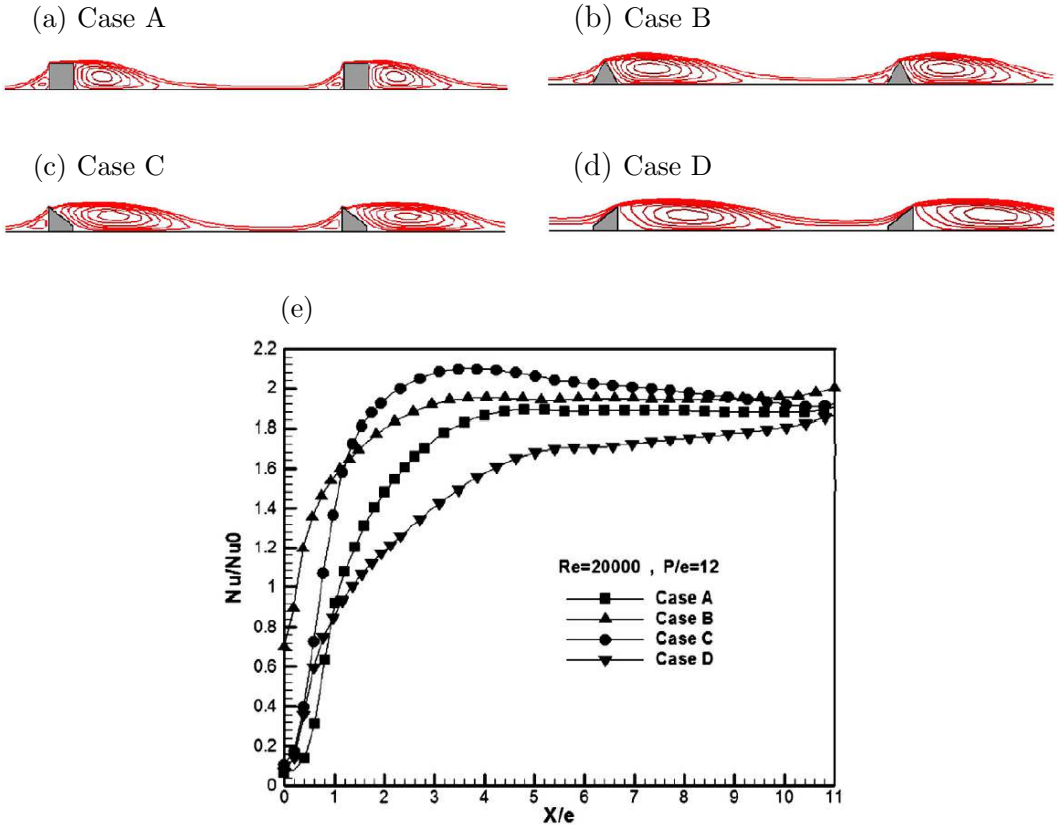

Figure 1.14: (a-d) Flow streamlines for flow over different shaped protrusions and (e) the corresponding local Nusselt number variation for $Re = 20\,000$. Reproduced from Kamali & Binesh (2008) with permission of the publisher.

consideration in influencing the local Nusselt number distribution and friction characteristics in the inter-rib region is demonstrated in this study. A trapezoidal rib configuration with decreasing height in the streamwise direction was found to be a better choice for enhancing the heat transfer efficiency, further supporting the better performance of the wedge shaped protrusion over a rectangular geometry.

For inlet Reynolds numbers in the range 20 000 to 160 000, different rib arrangements consisting of combinations of ribs of different heights placed at different gaps were studied, considering six distinct cases (Xie *et al.*, 2013). They showed how proper design and arrangement of downstream ribs in a channel could effect the flow structure and the heat transfer characteristics in channel flows and how these could facilitate passive flow control in these types of flows. The local Nusselt number contours for each of the six cases investigated along with the average heat transfer enhancement ratio and thermal efficiency achieved is shown in figure 1.15. Although the placement of closely spaced inter-rib half-ribs as in case B and C can be beneficial from the point of enhancing the overall heat transfer,

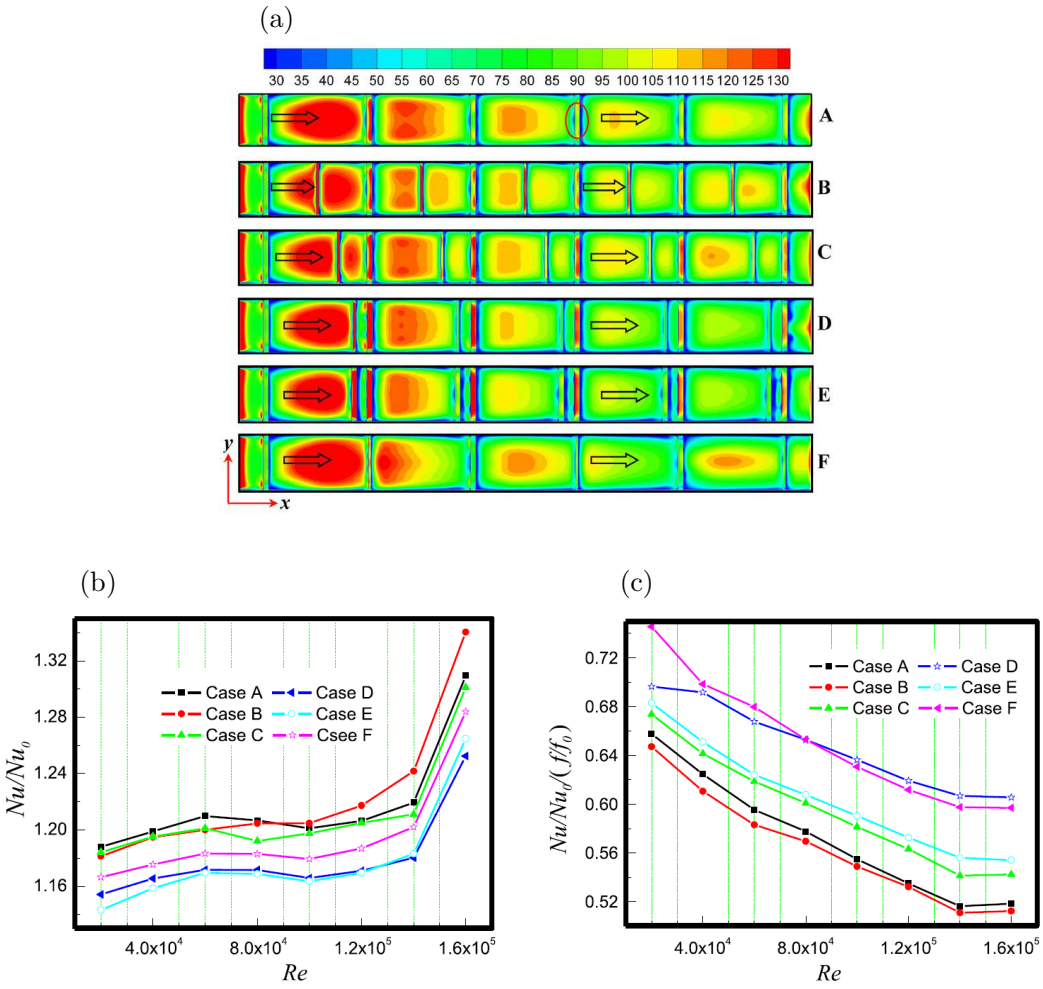

Figure 1.15: (a) Local inter-rib Nusselt number distribution for multiple rib-arrangement and the corresponding domain and time-averaged (b) enhancement ratio (Nu/Nu_0) and (c) overall heat transfer efficiency variation with Reynolds number. Reproduced from Xie *et al.* (2013) with permission of the publisher.

the associated pressure losses were high, driving the thermal efficiency to lower values. Case F without the inter-rib placement was found to have the highest efficiency. The placement of inter-rib half ribs had a significant contribution to the overall efficiency when placed at larger gaps as in case D.

In the turbulent regimes, numerous other surface protrusion shapes other than the two-dimensional transverse type have also been studied extensively, such as the arc shaped wires on the hot wall of a duct (Kumar & Saini, 2009), angled ribs to promote secondary motion in the spanwise direction (Han & Park, 1988) and staggered array of rectangular elements with varying streamwise and spanwise spacing (Garimella & Eibeck, 1990), among many alternatives. The experimental study by (Garimella & Eibeck, 1990), which used water flow in the Reynolds number range $150 - 5150$, showed that streamwise spacing has a more dominant

impact on the heat transfer rate than the spanwise spacing, as it leads to a better interaction between the cavity flow in between the surface protrusions and the main flow. Angled ribs were found to be slighly more beneficial for promoting heat transfer in a square duct than in a rectangular duct (Han & Park, 1988). Detailed reviews elaborating the effect of the shape and size of the protrusion, their placement and position are available in Alam *et al.* (2014) and Singh & Singh (2018), and the references provided therein.

It is also important to consider the Prandtl number (Pr) of the fluid flowing through the duct/channel. For a turbulent flow case, the design of the protrusion in a duct/channel for fluids with $Pr > 5$ would need more closely spaced elements which could disturb the thin boundary layer, whereas for flow of gases, design should focus on generating multiple reattachment points in the flow to promote mixing in the more diffusive boundary layer (Šlančiauskas, 2001).

Most of the studies for hydrodynamic flow through a duct/channel have largely considered a turbulent flow regime taking into account the application which motivated their work. The main aim of most of these studies has been purely on the flow features and the corresponding effect on the local Nusselt number and friction factor, and quantification of the heat transfer augmentation that could be achieved using these structures on the walls of the duct in the turbulent regimes. A better understanding of the flow dynamics in the laminar and transition regimes is important for the application motivating the present work, which are lacking in the literature. Hence, the present study explores the onset of instabilities and the route to turbulence in a laminar hydrodynamic channel flow with wedge-shaped protrusions. Besides contributing to the understanding of the flow dynamics, these would also be beneficial for effective design and control of the duct or channel flows using passive structures on the walls and augmenting the heat transfer efficiency in those regimes.

1.4 Heat transfer enhancement in quasi-2D MHD flows

Surface protrusions have been found to be an effective means to promote instabilites and heat transfer in hydrodynamic channel/duct flows. For the MHD flows, this method of vortex promotion is unexplored in the literature. However, various other vortex generation techniques as a means to promote heat transfer have been reported in the literature for the flow of a conducting fluid through an MHD duct. Most of the studies in the high Hartmann number range use the idea

of promoting quasi-2D vortical structures in the flow domain to promote heat transfer. These different techniques, the corresponding heat transfer characteristics and the enhancement achieved are presented in detail in this section.

1.4.1 Using inhomogeneous wall conductance

Inhomogeneous wall conductance was used for promoting mixing and enhancing the heat transfer rate in a numerical study of free surface MHD flows (Huang & Li, 2011). Conducting strips placed in the streamwise direction were used on the electrically insulating Hartmann walls. The setup used in this study is reproduced in figure 1.16.

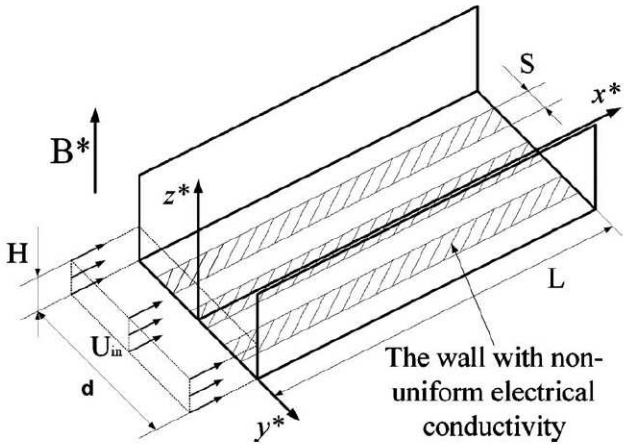

Figure 1.16: Use of conducting strips as means to promote heat transfer in free surface MHD flows. Reproduced from Huang & Li (2011) with permission of the publisher.

The inhomogeneity in wall conductance leads to a change in the electric current distribution near the wall, as current enters the wall at locations were the conducting strips are placed rather than passing through the viscous boundary layer as would be the case in a completely insulating channel wall (figure 1.17a). This leads to a change in the Lorentz force and velocity distribution, resulting in an increase in the turbulent fluctuations. This is also found to increase with increasing Hartmann number in the range considered in this study ($30 \leq Ha \leq 100$), thereby increasing the local Nusselt number in the interface between the conducting and non-conducting region and a drop in friction factor over the conducting strip as shown in figure 1.17(b). This study also explored the use of multiple conducting strips and found an optimal number between 3-5 to be most favouble to achieve a maximum efficiency of approximately 2 in the range of Ha they considered.

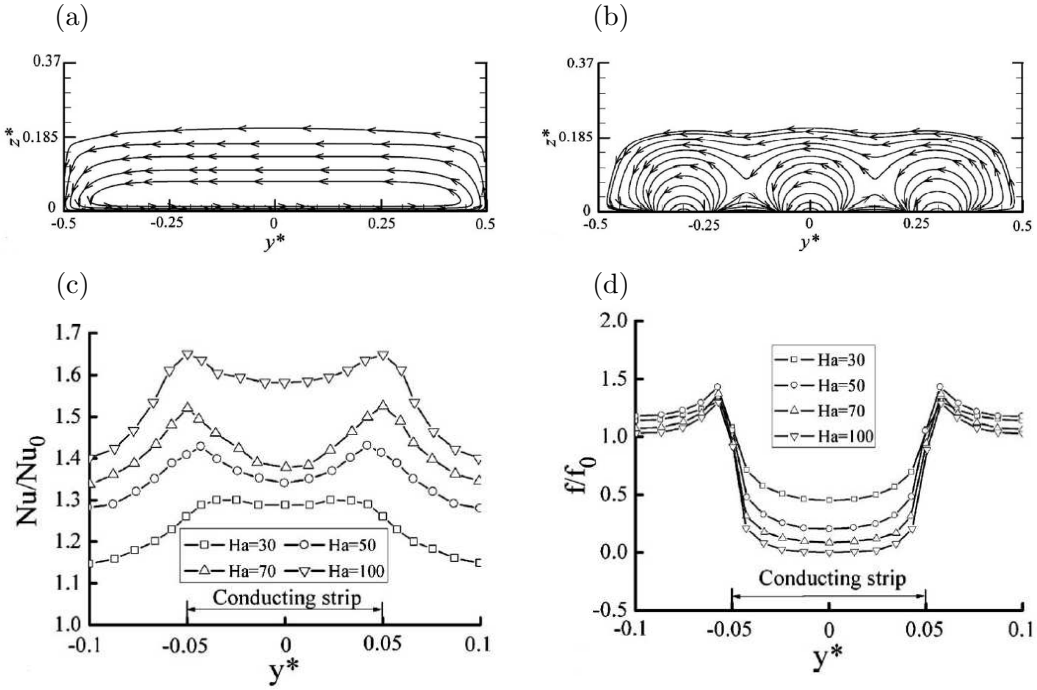

Figure 1.17: Comparison of electric current distribution for (a) an insulating channel wall with (b) a channel wall with non-uniform wall conductivity, and (c) the Nusselt number and (d) friction factor distribution over the channel wall with non-uniform wall conductivity as in (b). Reproduced from Huang & Li (2011) with permission of the publisher.

1.4.2 Using grids

Unlike the previous technique which considered heat transfer from the Hartmann wall, studies conducted using turbulent modifiers in the form of grids placed in the flow with orientation along, and perpendicular to, the magnetic field direction (Branover *et al.*, 1995) have looked at improving the heat transfer rate from the side walls which is more relevant for the application being considered in this thesis. These experiments have shown that the favourable orientation for turbulence intensity to be present away from the grid location is the one parallel to the magnetic field as shown in figure 1.18, as Joule dissipation leads to the attenuation of vortices normal to the field direction. Experiments conducted in an earlier study (Kolesnikov & Tsinober, 1972) have also found formation of two-dimensional turbulent structures behind grids oriented parallel to the field direction, in the case of a strong magnetic field strength. These conditions hence favour an increase in the local heat transfer rate from the wall to the fluid, which was evident from the higher Nusselt number value in the locations corresponding to higher turbulent intensity. Their comparison of the Nusselt number and its dependence on Ha/Re and grid orientation is reproduced in figure 1.19.

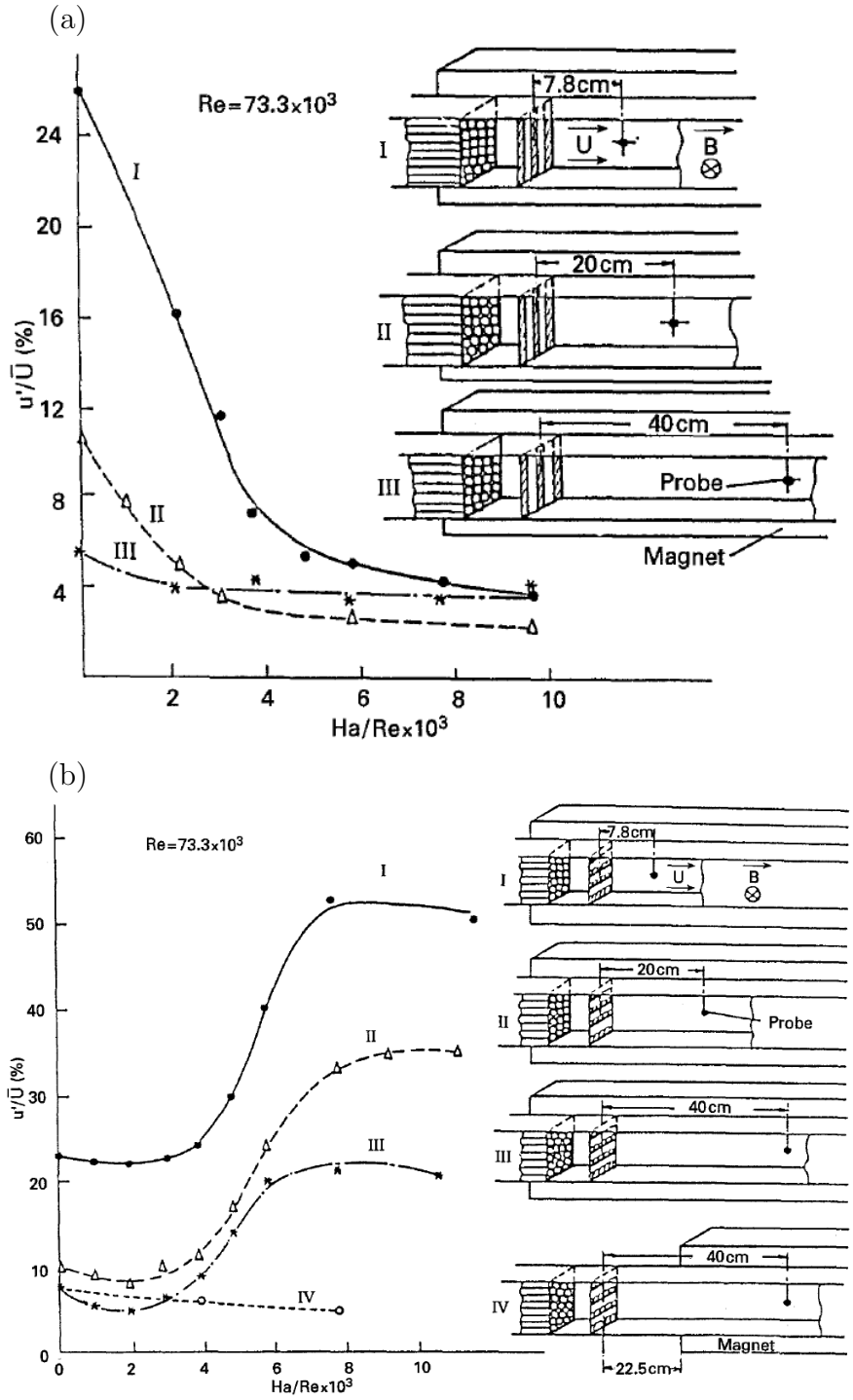

Figure 1.18: Turbulent intensity at different streamwise location downstream of grids placed in the flow with orientation (a) perpendicular and (b) parallel to the magnetic field direction. Reproduced from Branover *et al.* (1995) with permission of the publisher.

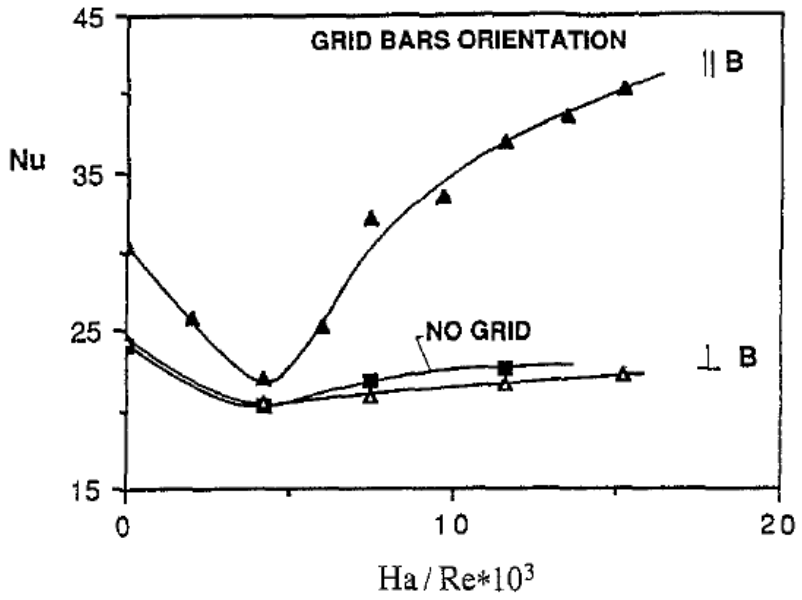

Figure 1.19: Nusselt number variation as a function of Ha/Re for grids oriented perpendicular and parallel to the magnetic field direction, and without the placement of grids. Reproduced from Branover *et al.* (1995) with permission of the publisher.

1.4.3 Using passive and active bluff bodies

Investigations focusing on quasi-two-dimensional turbulence generation using bluff bodies in a duct flow for heat transfer enhancement are discussed in this section. A cylindrical bluff body placed in the centre of a duct with axis oriented parallel to the magnetic field was considered in Hussam *et al.* (2011). The effect of Hartmann number ($0 \leq Ha \leq 1200$) and blockage ratio (ratio of cylinder diameter to the duct height) were explored. The critical Reynolds number for the onset of unsteadiness was found to increase with increasing Ha as transverse fluctuations are dampened due to increase in the field strength. An unsteady flow at a higher blockage ratio showed a superior heat transfer increase as the vortex shedding from the cylinder interacted with the thermal boundary layer on the side wall, entraining fluid from the boundary layer and inducing a higher heat transfer coefficient.

Another study (Hussam & Sheard, 2013), which could be considered an extension of the aforementioned work, explored the influence of the lateral positioning of a cylindrical bluff body in a duct flow on the associated heat transfer efficiency. The lateral position was quantified using a gap ratio which was the ratio of the cylinder distance from the side wall to its diameter (G/d). A sketch of the flow configuration and the associated geometric parameters are reproduced in figure

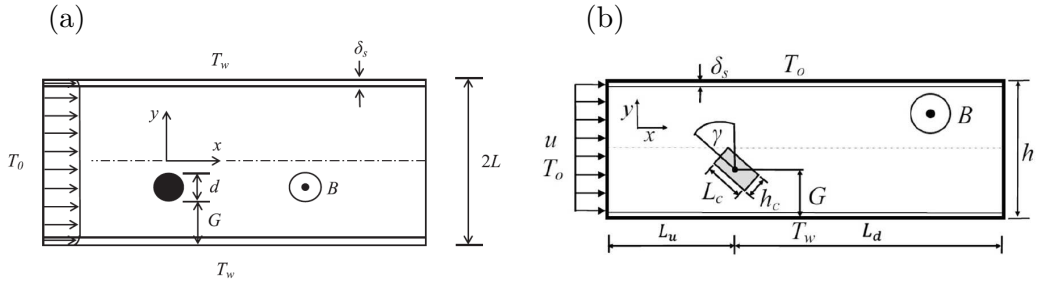

Figure 1.20: Schematic of the flow configuration and the associated geometric parameters for (a) cylindrical and (b) rectangular vortex promoter. The figures have been reproduced respectively from Hussam & Sheard (2013) and Cassells *et al.* (2016) with permission of the publishers.

1.20(a). With an initial decrease in the gap ratio, interaction of the vortex shedding from the cylinder with the side walls was improved, leading to thinning of the thermal boundary layers on the side walls and thereby an improvement in heat transfer rate. Further decreases in the gap ratio leads to suppression of vortex shedding, resulting in a lower heat transfer rate. Thus, for each blockage ratio, there existed an optimal gap ratio which gave a maximum heat transfer efficiency. The vorticity fields and the corresponding temperature fields with change in gap ratio for the two extreme values of blockage ratio considered in their investigation are reproduced here in figure 1.21.

The use of square cylinder in a square duct as a means to promote instabilities and heat transfer (Chatterjee & Gupta, 2015) were considered in a subsequent study. Using a quasi-2D model, they classified the various regimes and reported on the aerodynamic responses for flow past a square bluff body in a bounded flow. Even though the flow regimes were qualitatively similar to flow past a circular cylinder (Dousset & Pothérat, 2008), using a square cylinder was found to prepone the onset of instability due to the presence of sharp corners. The heat transfer improvement in each of the regimes was also studied and a comparison was made with the circular cylinder case and the corresponding non-MHD case. The circular cylinder was found to be a better option for enhancing heat transfer in a moderate range of magnetic field strength ($Ha = 500$) whereas enhancement was almost comparable for both the cases in the higher magnetic filed strength ($Ha = 1200$). Heat transfer was highest in the last regime where separation of the secondary counter-rotating vortices from the Shercliff walls accompanied the Kármán vortices shedding from the cylinder, and decreased with increasing Ha.

Cassells *et al.* (2016) used rectangular vortex promoter shapes in an MHD duct flow and studied the effect of varying the gap height and incidence angle of the

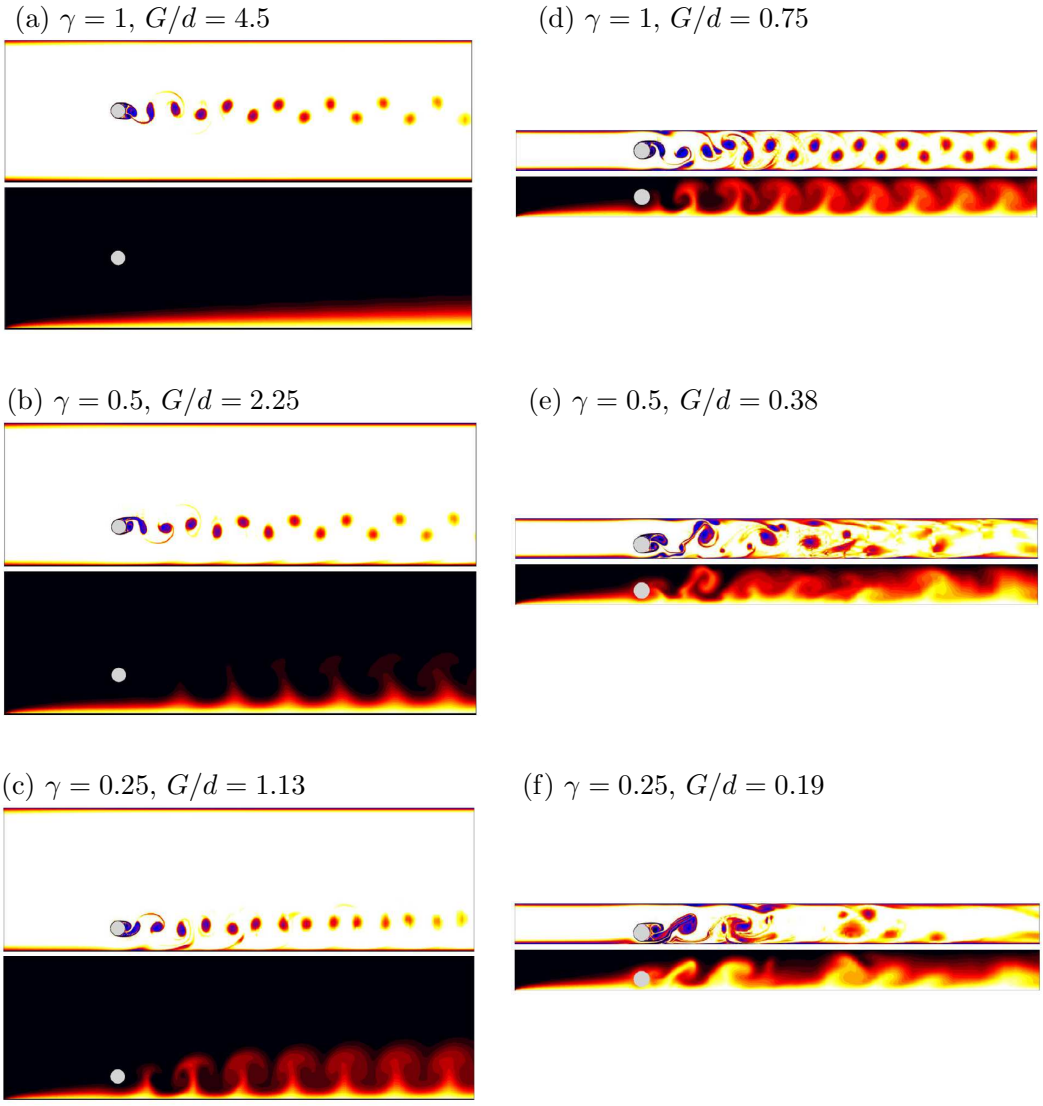

Figure 1.21: Contours of the logarithm of spanwise vorticity (upper) and temperature (lower) for $Ha = 100$, $Re = 2000$ for blockage ratio (a-c) $\beta = 0.1$ and (d-f) $\beta = 0.4$. Shown are the absolute value of vorticity with levels plotted over $-1 \leq \log|x| \leq -3$, with darker contours corresponding to regions of stronger vorticity, and the temperature field, with dark and light contours corresponding respectively to colder and hotter regions, plotted over $T_o \leq T \leq T_w$, where T_o and T_w are the cold and hot wall temperature, respectively. The figures have been reproduced from Hussam & Sheard (2013) with permission of the publisher.

bluff body on heat transfer efficiency. A sketch of the flow configuration used in their study is reproduced alongside the corresponding cylindrical bluff body case for comparison in figure 1.20(b). Even though changing the incidence angle for the cylinder placed in the duct centreline and at the optimal gap height could increase the heat transfer efficiency, an upright cylinder at an optimal gap height of 1.5 gave the maximum possible efficiency of $\eta = 1.6$. The size of the wake formed

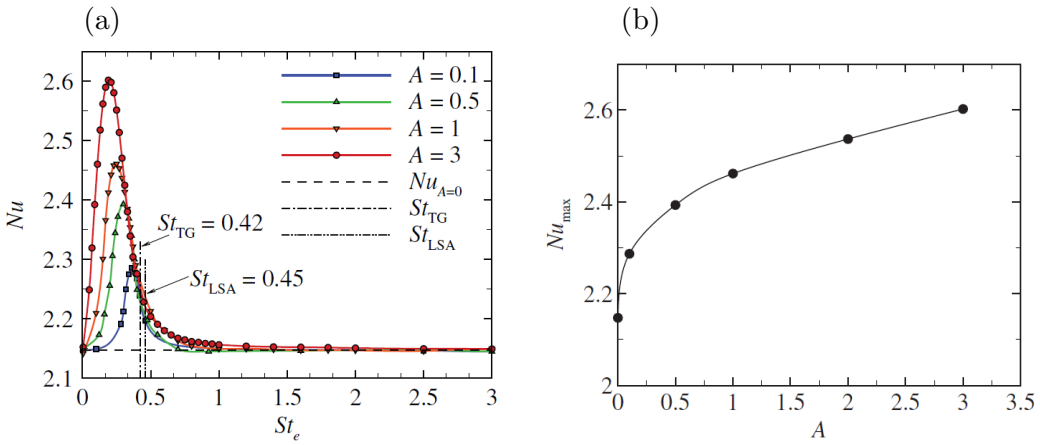

Figure 1.22: Plot showing (a) time-averaged Nusselt number plotted against cylinder oscillating frequency (St_e) at different oscillating amplitudes (A), St_{TG} and St_{LSA} are frequencies obtained from evolving the linearised optimal perturbation obtained from transient growth analysis and the leading mode from linear stability analysis, both for a fixed cylinder, and (b) peak time-averaged Nusselt number $Nu_{\max}$ against cylinder oscillating amplitude for $Re = 1075$ and Hartmann friction $Ha^* = 151.5$. The figures have been reproduced from Hussam *et al.* (2012*a*) with permission of the publisher.

behind the cylinder and its coherence and interaction with the thermal boundary layer largely influenced the heat transfer rate and the associated pressure losses in the flow. For selected cases, an exponential decrease in the heat transfer rate and an approximate linear pressure loss was found with increasing Ha in their study.

An active cylindrical bluff body (rotationally oscillating circular cylinder) was studied instead of a passive bluff body in an MHD duct in Hussam *et al.* (2012*a*). The oscillations were used as a way to encourage vortex shedding, as it was found that the optimal perturbations maximising kinetic energy growth of disturbances were found to be concentrated near cylinder (Hussam *et al.*, 2012*b*). An increased amplitude of oscillation was found favourable to increase the heat transfer rate from the hot side wall of the duct, and also widened the range of frequencies over which the Nusselt number was elevated. This was because the intensity of the generated vortices correlated with the oscillation amplitude. A shift to lower frequency was also observed with increasing angular velocity of oscillation. Figure 1.22(a) reproduces their plot, demonstrating the influence of increasing amplitude and oscillation frequency on the time-averaged Nusselt number. Even though heat transfer is found to increase monotonically with increasing amplitude, the study illustrates that there might exist a certain amplitude beyond which any increase could no longer be effective. This is clear from the peak time-averaged

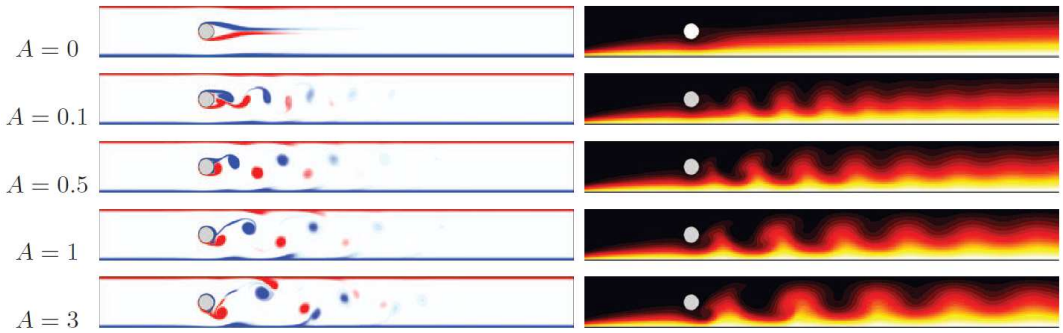

Figure 1.23: Plots showing contours of spanwise vorticity (left column) and the corresponding temperature field (right column) with increasing oscillating amplitude for $Re = 1075$ and Hartmann friction parameter $Ha^* = 151.5$. The figure has been reproduced from Hussam *et al.* (2012*a*) with permission of the publisher.

	$Ha = 320$		$Ha = 2400$	
Re	1000	2000	1000	2000
◯	46 %	52 %	-1.2 %	16%
□	78%	73%	10%	33%
△	62%	75%	16%	40%

Table 1.1: Comparison of the overall heat transfer increment with different vortex promoter shapes in an MHD duct with blockage ratio = 0.25. Data reproduced from Hussam *et al.* (2018).

Nusselt number plot (figure 1.22b) where a strong gradient in $Nu_{\max}$ is found in the lower amplitude range, whereas the benefits of increasing amplitude lowers in the higher range of oscillating amplitudes. The spanwise vorticity contours and the corresponding temperature plots shown in figure 1.23 demonstrate the benefit gained through the torsionally oscillating cylinder, where vortex shedding is promoted in an otherwise steady state flow ($A = 0$), where the temperature field can be seen to be diffusion dominated.

A comparative study of triangular, square and circular cylindrical vortex promoter shapes demonstrated that a higher heat transfer increment was achievable using a triangular-shaped bluff body, especially at higher magnetic field strengths. This was attributed to a stronger wake-boundary layer interaction that persisted downstream further than in the other cases. The heat transfer increment achieved using different vortex promoter shapes are compared in table 1.1 for two different Reynolds and Hartmann numbers.

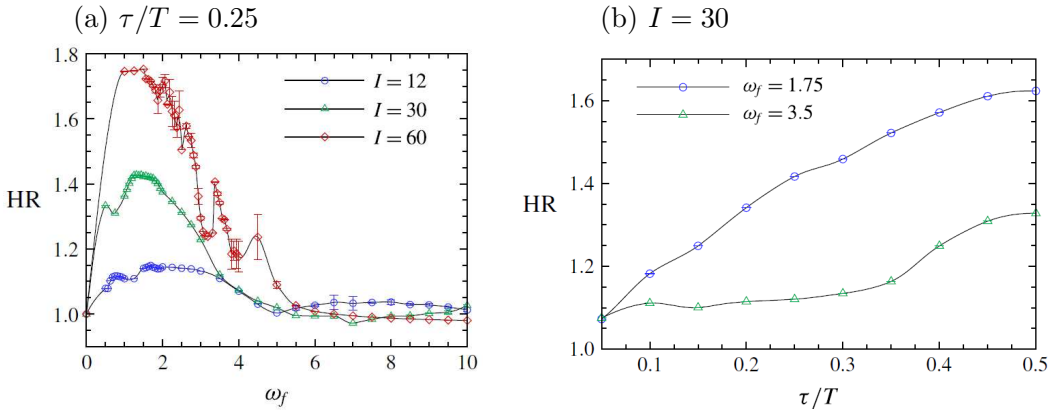

Figure 1.24: Plot showing the variation of heat transfer enhancement ratio (HR) as a function of (a) forcing frequency ω_f and non-dimensional current amplitudes I, and (b) current injection pulse width τ/T and ω_f for flow in an MHD duct with cylinderical bluff body and an electrode placed near the cylinder for $H = 500$ and gap ratio $G/d = 2$. Reproduced from Hamid *et al.* (2016*a*) with permission of the publisher.

1.4.4 Using point electrodes

Another technique used to promote heat transfer in quasi-2D MHD duct flows was using electrically driven vortices generated by point electrodes. A rotational force is produced around the electrode due to the Lorentz force as current travels radially from the electrode embedded in the Hartmann layer, thereby generating quasi-2D vortices with axis aligned along the magnetic field direction (Sommeria, 1988; Baker *et al.*, 2015).

These electrically driven vortices were used with the motive of intensifying the vortices formed behind a cylindrical bluff body in Hamid *et al.* (2016*a*). The role that current intensity, forcing frequency, pulse width of current injection and electrode position play in modifying the vortex street formed behind a cylinder and how these could influence the heat transfer dynamics were investigated in detail in this study. Almost a monotonic increase in heat transfer enhancement was found with increasing current injection amplitude, though it showed a non-monotonic trend with forcing frequency (figure 1.24a) which was attributed to the competing effect of vortex size and the number of vortices shed. The vortex street behind the cylinder and the corresponding temperature field at different forcing frequencies is shown in figure 1.25, demonstrating this competing effect.

The complex interaction between the cylinder wake vortices with varying current injection amplitude at different gap ratios was also considered. A lower range of current amplitude was favourable when the cylinder was placed closer to the wall, and vice-versa. Increasing the current injection pulse width always had a

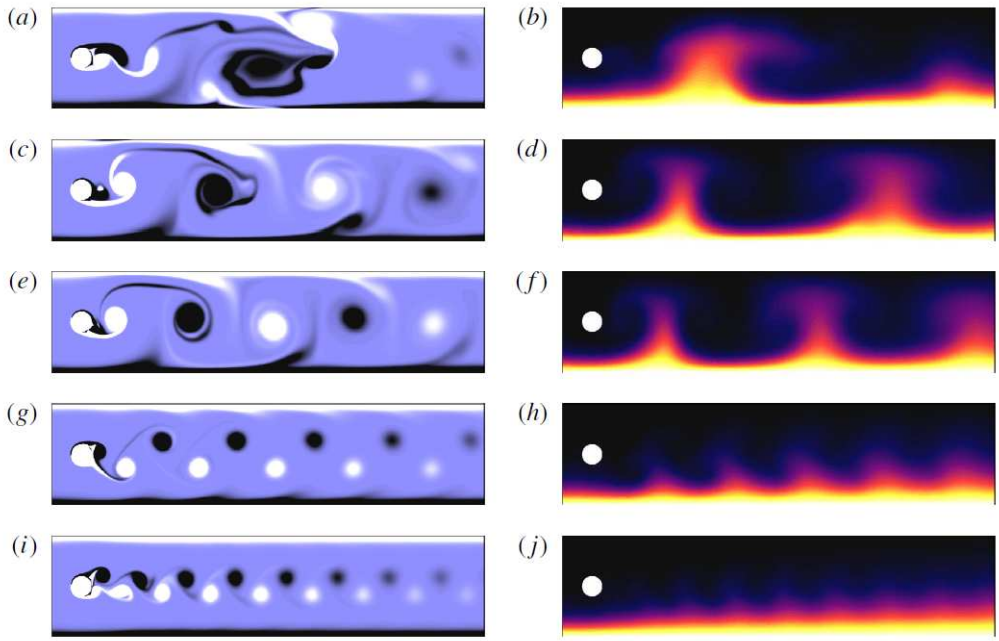

Figure 1.25: Contours of vorticity (left column) and corresponding temperature field for $I = 30$, $H = 500$ and (a,b) $\omega_f = 0.5$, (c,d) $\omega_f = 1.5$, (e,f) $\omega_f = 2$, (g,h) $\omega_f = 4$ and (i,j) $\omega_f = 6$, showing the competing effect of vortex size and number of vortices on the temperature field. Reproduced from Hamid *et al.* (2016*a*) with permission of the publisher.

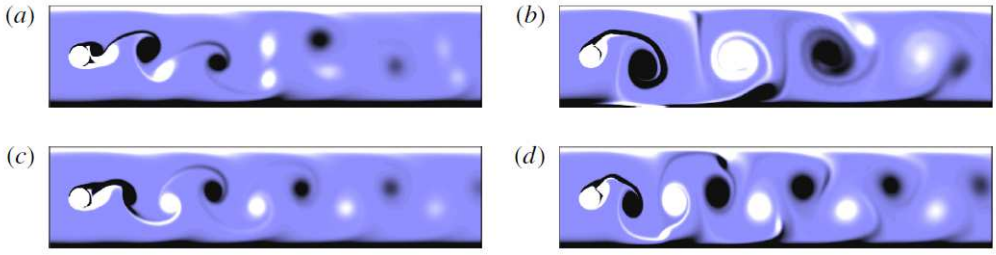

Figure 1.26: Contours of vorticity (left column) and corresponding temperature field for $I = 30$, $H = 500$ and (a,b) $\omega_f = 1.75$ and (c,d) $\omega_f = 3.5$ and (a,c) $\tau/T = 0.05$ and (b,d) $\tau/T = 0.5$ showing the widening of the vortex street with increasing pulse width of current injection τ/T. Reproduced from Hamid *et al.* (2016*a*) with permission of the publisher. Flow is left to right.

positive effect on heat transfer enhancement irrespective of the the forcing frequency (figure 1.24b) as they helped increase the vortex size (figure 1.26) and enhanced the wake-boundary layer interaction. A non-monotonic trend in heat transfer enhancement ratio with Hartmann friction parameter was also shown in this study. The use of electrodes for vortex generation was also shown to have significantly lower effect on the pressure drop compared to solid obstacles, thereby increasing the overall efficiency.

Following this, Hamid *et al.* (2016*b*) studied how electrically generated vortices alone perform, without the presence of the bluff body, by varying the current amplitudes, frequency and the pulse width. The results were compared with those from the earlier study which also contained the physical cylinder (Hamid *et al.*, 2016*a*). The presence of the cylinder helped produce wider vortices and was more beneficial in the shorter current pulse cases due to stronger wake and boundary layer interactions. However, for long current pulse duration, the presence of a cylinder in addition to the electrically driven vortices are detrimental to heat transfer as the interaction between the two vortices reduces the vortex intensity. At low forcing frequencies the coherence of the vortices was lost, resulting in a lower heat transfer enhancement, whereas at high forcing frequencies the vortices were lined up along the duct axis reducing the interaction with the boundary layer, thereby lowering the heat transfer enhancement. The investigation of Reynolds number and Hartmann number dependence showed that the presence of a cylinder along with electrodes were more useful in the lower Hartmann damping and higher inertia regimes, whereas solely electrodes were more beneficial in the higher Hartmann number cases. An optimal gap for electrode placement in the duct was also found in this study.

Chapter summary

This chapter has presented a review of the literature of hydrodynamic flows in confined setups in the initial part, from which the setup used in the present study draws its features. The perpendicular front face of the wedge-shaped protrusions under investigation in this study presents a sudden partial obstruction similar to the well-known forward-facing step (FFS) geometry (Stüer *et al.*, 1999; Wilhelm *et al.*, 2003; Lanzerstorfer & Kuhlmann, 2012*b*), while the inclined rear surface may invoke recirculating flows similar to backward facing step (BFS) flows (Armaly *et al.*, 1983; Ghia *et al.*, 1989; Kaiktsis *et al.*, 1996; Barkley *et al.*, 2002; Blackburn *et al.*, 2008*a*). However, one key differentiating feature of the present work is the streamwise-periodic repetition of the geometric feature. Flow past BFS and FFS has been found to be extremely sensitive to incoming flow conditions (Gartling, 1990; Marino & Luchini, 2009; Lanzerstorfer & Kuhlmann, 2012*b*; Barkley *et al.*, 2002), making a direct comparison with these geometries difficult. Following this, studies on the onset of instabilities in MHD duct flows were presented. Under the influence of a magnetic field, 3D turbulence was found to be strongly damped due to Joule dissipation, and in the high magnetic field strength

regime, quasi-2D turbulence was prevelant in the duct.

Heat transfer enhancement studies using various vortex generator techniques for promoting quasi-2D turbulence have been elucidated, showing the effectiveness of quasi-2D turbulence in achieving a higher heat transfer efficiency. Nevertheless, none of the studies have explored the use of surface modifications for vortex generation in MHD duct flows. However, numerous hydrodynamic cases utilising this technique in the literature were found to be effective to enhance heat transfer efficiency. Most of these studies had a focus only in the turbulent flow regimes considering high Reynolds numbers. Past studies investigating hydrodynamic flow past two-dimensional surface-mounted obstacles at low Re include Tropea & Gackstatter (1985) and Carvalho *et al.* (1987) who focused only on the two-dimensional flow conditions. Those studies found that at low blockage ratios, the reattachment length for the low Re cases compared well with high Re results. The effective design and control of flow in cooling blanket ducts of magnetic confinement fusion reactors requires a thorough understanding of the flow dynamics focused on the steady and transitional regimes which are not coverered much in the literature, hence contributing to this understanding is a primary motivation of the present work .

From the literature review, it is found that a better understanding of the flow over repeated modified walls in confined channels and ducts in the low Reynolds number range is required. Furthermore, attention has not been paid in the literature to utilising a surface modification method as a means to enhance heat transfer in MHD flows. This study sought to contribute to this aspect by characterising the flow dynamics, studying the onset of instabilites and the first step towards the route to turbulence in both hydrodynamic channel flows and MHD duct flows with repeated wedge protrusions. The effectiveness of using repeated wedge-shaped protrusions on the duct walls for enhancing heat transfer in MHD flows are also explored in this thesis.

In the next chapter, the equations governing these flows and the numerical methodology and techniques used to understand the flow dynamics and heat transfer effectiveness are discussed.

Chapter 2

Methodology

This chapter describes the methods employed in this study. The equations governing the flow evolution for both the hydrodynamic and magnetohydrodynamic cases are introduced, as are techniques used for characterising the dynamics of the flow including global linear stability analysis, perturbations kinetic energy analysis, receptivity and sensitivity analyses, endogeneity and linear transient growth analysis. The Stuart–Landau model used for studying the weakly non-linear effects and the nature of bifurcation are discussed thereafter. The parameters for quantifying the heat transfer rate and efficiency are also presented. This is followed by a description of the numerical techniques used to solve the governing equations. Grid resolution tests and validation studies conducted for the base flow simulations and the various techniques culminates this chapter.

2.1 Governing equations

In this section, the equations governing the hydrodynamic flow in a channel and the MHD flow in a duct are presented first, followed by elaboration of a quasi-2D model adopted for the MHD cases. Thereafter, different techniques used to understand the dynamics of these flows with respect to their routes to turbulence, the modes through which instability manifests, and the underlying mechanism contributing to their growth are presented.

2.1.1 Hydrodynamic and MHD flow equations

Navier–Stokes and energy equations

Throughout the thesis, the fluid is considered to be Newtonian and incompressible, with all fluid properties assumed to be a constant. Under these assumptions,

the dimensional form of the continuity, momentum and energy equations are given by,

$$\tilde{\boldsymbol{\nabla}} \cdot \tilde{\boldsymbol{u}} = 0, \tag{2.1}$$

$$\frac{\partial \tilde{\boldsymbol{u}}}{\partial \tilde{t}} + (\tilde{\boldsymbol{u}} \cdot \tilde{\boldsymbol{\nabla}})\tilde{\boldsymbol{u}} = -\frac{1}{\rho}\tilde{\boldsymbol{\nabla}}\tilde{p} + \frac{\mu_d}{\rho}\tilde{\nabla}^2\tilde{\boldsymbol{u}} + \boldsymbol{f_b}, \tag{2.2}$$

$$\frac{\partial \tilde{T}}{\partial \tilde{t}} + (\tilde{\boldsymbol{u}} \cdot \tilde{\boldsymbol{\nabla}})\tilde{T} = \frac{k_f}{\rho C_p}\tilde{\nabla}^2\tilde{T} + \Phi_v + \Phi_j + \Phi_b + S_h, \tag{2.3}$$

where $\tilde{\boldsymbol{u}}$, $\tilde{p}$ and $\tilde{T}$ are the dimensional velocity, pressure and temperature fields, respectively, and C_p is the specific heat capacity of the fluid. The term $\boldsymbol{f_b}$ accounts for the body forces (gravity, centrifugal, Coriolis or electromagnetic forces) acting on the fluid, whereas Φ_v, Φ_j and Φ_b are the viscous, Joule heating and the bouyancy effect on the temperature field, respectively, and S_h accounts for any volumetric and radiative heating. For the hydrodynamic cases, the body forces are neglected in the momentum equation. Volumetric, radiative heating and buoyancy effects are not considered in the study. From an order of magnitude analysis, the effect of viscous and Joule heating was found to be negligible relative to the thermal diffusion, hence these terms are not considered in the energy equation. The following scaling is used to non-dimensionalise equations (2.1 - 2.3),

$$\begin{gathered} \tilde{\boldsymbol{u}} = U_0\boldsymbol{u}, \quad \tilde{p} = p\rho U_0^2, \quad \tilde{T} = T(T_h - T_c) + T_c, \\ \tilde{\nabla} = \frac{\nabla}{L}, \qquad \tilde{t} = \frac{L}{U_0}t, \end{gathered} \tag{2.4}$$

where U_0 is the horizontal mean velocity through the channel used to maintain a constant flow rate and $\tilde{()}$ denotes the dimensional form of the variable.

Considering the aforementioned assumptions and scalings, the dimensionless form of the continuity, momentum and energy equations for the hydrodynamic channel flow case are given by,

$$\boldsymbol{\nabla} \cdot \boldsymbol{u} = 0, \tag{2.5}$$

$$\frac{\partial \boldsymbol{u}}{\partial t} + (\boldsymbol{u} \cdot \boldsymbol{\nabla})\boldsymbol{u} = -\boldsymbol{\nabla}p + \frac{1}{Re}\nabla^2\boldsymbol{u}, \tag{2.6}$$

$$\frac{\partial T}{\partial t} + (\boldsymbol{u} \cdot \boldsymbol{\nabla})T = \frac{1}{Pe}\nabla^2 T, \tag{2.7}$$

where $\boldsymbol{u}$, p and T are the non-dimensional velocity, pressure and temperature fields, respectively. The flow parameters are the Reynolds number $Re = \rho L U_0/\mu_d$, Prandtl number $Pr = \mu_d C_p/k_f$ and the Peclet number $Pe = RePr$.

Quasi-static MHD equations

The dimensional form of the continuity and energy equation for the MHD flow is the same as for the hydrodynamic cases (2.1) and (2.3) respectively. However, the MHD momentum equation includes the electromagnetic forces in the body force term. An inductionless approximation is used under which the magnetic Reynolds number $R_m \ll 1$, which is typical in laboratory scales (Müller & Bühler, 2013; Davidson, 2002). This approximation makes the induced magnetic field strength negligible compared to the applied uniform and time invariant magnetic field strength. Hence, the dimensional form of the momentum equation for the MHD flow cases is given by

$$\frac{\partial \tilde{\boldsymbol{u}}}{\partial \tilde{t}} + (\tilde{\boldsymbol{u}} \cdot \tilde{\boldsymbol{\nabla}})\tilde{\boldsymbol{u}} = -\frac{1}{\rho}\tilde{\boldsymbol{\nabla}}\tilde{p} + \frac{\mu_d}{\rho}\tilde{\nabla}^2\tilde{\boldsymbol{u}} + \frac{1}{\rho}(\tilde{\boldsymbol{j}} \times \tilde{\boldsymbol{B}}), \tag{2.8}$$

where the last term on the R.H.S accounts for the Lorentz force induced by the electrically conducting fluid flowing in the presence of magnetic field. The action of Coulomb forces (electrostatic force between electric charges) is negligible compared to the Lorentz forces. The current density $\tilde{\boldsymbol{j}}$ is given by Ohm's law as

$$\tilde{\boldsymbol{j}} = \sigma_c(\tilde{\boldsymbol{E}} + \tilde{\boldsymbol{u}} \times \tilde{\boldsymbol{B}}), \tag{2.9}$$

where $\tilde{\boldsymbol{E}}$ is the electric field. The electrostatic force experienced by a charge Q is related to the electric field $\tilde{\boldsymbol{E}}$ as $\tilde{\boldsymbol{F}_Q} = Q\tilde{\boldsymbol{E}}$. Electric field can be shown to be irrotational (i.e. $\tilde{\nabla} \times \tilde{\boldsymbol{E}} = 0$) using the Stoke's integral relation, since the work done by force $\tilde{\boldsymbol{F}_Q}$ to move a charge Q along a closed path C in space is zero,

$$\frac{1}{Q}\int_C \tilde{\boldsymbol{F}_Q} \cdot \hat{\boldsymbol{n}}_t \, \mathrm{d}c = \int_C \tilde{\boldsymbol{E}} \cdot \hat{\boldsymbol{n}}_t \, \mathrm{d}c = \int_{A_c} (\tilde{\boldsymbol{\nabla}} \times \tilde{\boldsymbol{E}}) \cdot \hat{\boldsymbol{n}}_n \, \mathrm{d}A_c = 0. \tag{2.10}$$

Here, $\hat{\boldsymbol{n}}_t$ and $\hat{\boldsymbol{n}}_n$ are the unit vectors tangential to the closed path C and normal to surface area A_c bounded by C, respectively. The electric field being irrotational can be expressed as a gradient of an electric potential $\tilde{\phi}_e$. Therefore the current density in equation (2.9) can be written as,

$$\tilde{\boldsymbol{j}} = \sigma_c(\tilde{\boldsymbol{\nabla}}\tilde{\phi}_e + \tilde{\boldsymbol{u}} \times \tilde{\boldsymbol{B}}). \tag{2.11}$$

Since velocities for the application being considered are smaller than the speed of light, and considering a slowly varying electromagnetic process, the displacement currents can be neglected. Under these assumptions, the relation between current

density and the magnetic field is given by Ampere's law, according to which,

$$\int_C \tilde{\boldsymbol{B}} \cdot \hat{\boldsymbol{n}}_t \, \mathrm{d}c = \int_{A_c} \tilde{\boldsymbol{j}} \cdot \hat{\boldsymbol{n}}_n \, \mathrm{d}A_c. \tag{2.12}$$

Using Stoke's integral formula, it can be written as,

$$\tilde{\boldsymbol{\nabla}} \times \tilde{\boldsymbol{B}} = \tilde{\boldsymbol{j}}. \tag{2.13}$$

Taking the divergence of equation (2.13) gives

$$\tilde{\boldsymbol{\nabla}} \cdot \tilde{\boldsymbol{j}} = 0. \tag{2.14}$$

Using the scaling as in equation (2.4) together with

$$\tilde{\boldsymbol{B}} = \boldsymbol{B} B_0, \quad \tilde{\phi_e} = \phi_e L U_0 B_0, \tag{2.15}$$

the dimensionless equations governing the MHD flow are obtained, where B_0 is the applied magnetic field strength in the spanwise direction. The set of quasi-static MHD equations in the non-dimensional form are given by,

$$\boldsymbol{\nabla} \cdot \boldsymbol{u} = 0, \tag{2.16}$$

$$\frac{\partial \boldsymbol{u}}{\partial t} + (\boldsymbol{u} \cdot \boldsymbol{\nabla})\boldsymbol{u} = -\boldsymbol{\nabla} p + \frac{1}{Re}\nabla^2 \boldsymbol{u} + \left(\frac{r}{2}\right)^2 \frac{Ha^2}{Re}[(\boldsymbol{\nabla}\phi_e + \boldsymbol{u} \times \boldsymbol{B}) \times \boldsymbol{B}], \tag{2.17}$$

$$\frac{\partial T}{\partial t} + (\boldsymbol{u} \cdot \boldsymbol{\nabla})T = \frac{1}{Pe}\nabla^2 T, \tag{2.18}$$

$$\boldsymbol{\nabla} \cdot \boldsymbol{j} = 0, \tag{2.19}$$

where $r = 2L/a$ is the aspect ratio of the duct cross-section, $Ha = aB_0\sqrt{\sigma_c/\mu_d}$ is the Hartmann number, and

$$\nabla^2 \phi_e = \boldsymbol{\nabla} \cdot (\boldsymbol{u} \times \boldsymbol{B}). \tag{2.20}$$

Quasi-two-dimensional MHD equations

A quasi-2D model described in Sommeria & Moreau (1982), hereafter referred to as SM82 model can be used to describe the MHD flow under conditions of strong magnetic field strength, when

$$Ha \gg 1, \quad N \gg 1, \tag{2.21}$$

where $N = Ha^2/Re$ is the Stuart number or interaction parameter. Under equations (2.21), the velocity variations in the bulk are negligible, with strong gradients concentrated only in the thin Hartmann layers on the duct walls perpendicular to the magnetic field direction. Isotropic turbulence is dissipated strongly by Joule dissipation and the most energy-containing eddies are stretched in the magnetic field direction, hence

$$\begin{aligned} \frac{\partial}{\partial z} \ll \frac{\partial}{\partial x}, \frac{\partial}{\partial y}, \\ v_z \ll v_x, v_y. \end{aligned} \tag{2.22}$$

The dimensionless form of the SM82 model is given by,

$$\boldsymbol{\nabla}_\perp \cdot \boldsymbol{u}_\perp = 0, \tag{2.23}$$

$$\frac{\partial \boldsymbol{u}_\perp}{\partial t} + (\boldsymbol{u}_\perp \cdot \boldsymbol{\nabla}_\perp)\boldsymbol{u}_\perp = -\boldsymbol{\nabla}_\perp p_\perp + \frac{1}{Re}\nabla^2 \boldsymbol{u}_\perp - \frac{H}{Re}\boldsymbol{u}_\perp, \tag{2.24}$$

$$\frac{\partial T_\perp}{\partial t} + (\boldsymbol{u}_\perp \cdot \boldsymbol{\nabla}_\perp)T_\perp = \frac{1}{Pe}\nabla_\perp^2 T_\perp, \tag{2.25}$$

where $\boldsymbol{u}_\perp$, $p_\perp$ and $T_\perp$ are the quasi-2D velocity, pressure and temperature fields, respectively. The term $H = n(r/2)^2 Ha$ is the Hartmann friction parameter which takes into account both the Hartmann number and the aspect ratio of the duct cross-section, and is the sole parameter characterising the MHD effects in these solutions, where n is the number of Hartmann walls, which for the present study is 2. The quasi-2D equations are obtained by averaging the corresponding quasi-static equations in the magnetic field direction (Sommeria & Moreau, 1982; Pothérat *et al.*, 2000). SM82 model resembles the two-dimensional hydrodynamic equations except for the additional linear friction term in the momentum equation which captures the influence of the Hartmann layers formed on the walls perpendicular to the applied magnetic field direction on the core flow.

2.2 Linear stability analysis

Linear stability analysis (LSA) is used to study the stability of some base flow state to infinitesimally small perturbations to that base state. The infinitesimality renders the equations governing the perturbations linear. In this thesis, the linear stability of time steady two-dimensional base flows to unsteady three-dimensional perturbations is considered. The linearised equation for this analysis is obtained by decomposing the flow variables into a steady base state and a disturbance

field. The disturbance field is then decomposed into Fourier modes of distinct wavenumbers in a homogeneous flow direction, say for example

$$f(x,y) = \int_{-\infty}^{\infty} f(x) e^{ky} \, \mathrm{d}k, \tag{2.26}$$

where y is the homogenous direction. Using the Fourier decomposition, the linearised equation obtained for the perturbation is framed as an eigenvalue problem, with the eigenvalue magnitude used to evaluate the growth rate of the eigenmodes. The eigenvector with the largest growth rate, called the dominant mode describes the underlying eigenmode causing the instability of the flow. The linearised equations governing the perturbation evolution, framing of the eigenvalue problem and obtaining the growth rate of the dominant mode are discussed in this section.

Linearised perturbation equation for hydrodynamic base flow

For the hydrodynamic cases, the 2D flow variables $\{\boldsymbol{u}, p\}$ are decomposed into a 2D component $\{\boldsymbol{U}, P\}$ and a small 3D disturbance, $\{\boldsymbol{u}', p'\}$, i.e.

$$[\boldsymbol{u}, p] = [\boldsymbol{U}, P] + \epsilon[\boldsymbol{u}', p'], \tag{2.27}$$

where constant $|\epsilon| \ll 1$. The linearised Navier–Stokes equations (LNSE) are obtained from (2.5, 2.6) and (2.27), and retaining terms of order $O(\epsilon)$ yields

$$\boldsymbol{\nabla} \cdot \boldsymbol{u}' = 0, \tag{2.28}$$

$$\frac{\partial \boldsymbol{u}'}{\partial t} = -\mathbf{N}'(\boldsymbol{u}') - \boldsymbol{\nabla} p' + \frac{1}{Re} \nabla^2 \boldsymbol{u}', \tag{2.29}$$

where $\mathbf{N}'$ is the linearised advection operator, convective form of which is $\mathbf{N}'(\boldsymbol{u}') = (\boldsymbol{U} \cdot \boldsymbol{\nabla})\boldsymbol{u}' + (\boldsymbol{u}' \cdot \boldsymbol{\nabla})\boldsymbol{U}$.

Linearised quasi-2D perturbation equation for quasi-2D MHD base flow

The linearised equations governing the evolution of quasi-2D perturbations $\{\boldsymbol{u}'_\perp, p_\perp\}$, are obtained from equations (2.23) and (2.24) along with the decomposition

$$[\boldsymbol{u}_\perp, p_\perp] = [\boldsymbol{U}_\perp, P_\perp] + \epsilon[\boldsymbol{u}'_\perp, p'_\perp], \tag{2.30}$$

and are given by

$$\boldsymbol{\nabla}_\perp \cdot \boldsymbol{u}'_\perp = 0, \tag{2.31}$$

$$\frac{\partial \boldsymbol{u}'_\perp}{\partial t} = -\mathbf{N}'(\boldsymbol{u}'_\perp) - \boldsymbol{\nabla}_\perp p'_\perp + \frac{1}{Re} \nabla^2_\perp \boldsymbol{u}'_\perp - \frac{H}{Re} \boldsymbol{u}'_\perp, \tag{2.32}$$

where $\mathbf{N}'(\boldsymbol{u}'_\perp) = (\boldsymbol{U}_\perp \cdot \boldsymbol{\nabla}_\perp)\boldsymbol{u}'_\perp + (\boldsymbol{u}'_\perp \cdot \boldsymbol{\nabla}_\perp)\boldsymbol{U}_\perp$.

Considering the homogeneity of the flow domain in the spanwise direction, the perturbations are further decomposed into Fourier modes having spanwise wavenumbers k as

$$(\boldsymbol{u}', p') = \int_{-\infty}^{\infty} (\hat{\boldsymbol{u}}, \hat{p})(x, y, t) e^{ikz} \mathrm{d}k. \tag{2.33}$$

Linearisation decouples each Fourier mode, reducing the stability analysis from a 3D problem in one or more of the parameters in Re, H, r to a set of 2D problems whose parameters are augmented by wavenumber k. Introducing a linear evolution operator $\mathscr{A}(\tau)$ representing time integration of a linearised perturbation field over time interval τ, and assuming exponential growth over long times, linear stability is dictated by the eigenvalue problem

$$\mathscr{A}(\tau)\hat{\boldsymbol{u}}_i = \mu_i \hat{\boldsymbol{u}}_i, \tag{2.34}$$

where μ_i are the (complex) eigenvalues and $\hat{\boldsymbol{u}}_i$ the corresponding eigenvectors of $\mathscr{A}$. The leading eigenvalue satisfying $\max|\mu_i|$ determines the instability growth rate σ and phase speed ω_f through

$$\mu = e^{(\sigma + i\omega_f)\tau}, \tag{2.35}$$

where τ can be chosen arbitary for a steady base flow. In a flow where perturbations of any wavenumber may evolve, a stable flow is one having $|\mu| < 1$ for *all* k, while an unstable flow is one where $|\mu| > 1$ at *any* k. The numerical implementation of this technique is covered later, in § 2.9.3.

2.3 Energetics analysis: spanwise-averaged perturbation kinetic energy evolution

In this section, energetics analysis is presented, which is used to understand the energy transfer from the base flow to the eigenmodes by evaluating contributions to the span-averaged kinetic energy evolution of the eigenmodes (Sheard *et al.*, 2016; Lanzerstorfer & Kuhlmann, 2012*b*,*a*). This helps gain insight about the instability mechanisms causing the base flow to become unstable. The perturbation kinetic energy equation is obtained by taking the dot product of $\boldsymbol{u}'$ with the

linearised momentum equation (2.29),

$$\boldsymbol{u'} \cdot \frac{\partial \boldsymbol{u'}}{\partial t} = \frac{\partial}{\partial t}\left(\frac{\boldsymbol{u'} \cdot \boldsymbol{u'}}{2}\right) = \frac{\partial}{\partial t}\left(\frac{1}{2}|\boldsymbol{u'}|^2\right) = \frac{\partial k'}{\partial t}, \tag{2.36}$$

where k' is the kinetic energy of the perturbation per unit mass. Equation (2.36) can be further simplified by averaging in the spanwise direction owing to the spanwise periodicity of the perturbations. The resulting equation (in tensor notation with the summation convention used for brevity) reads as

$$\frac{\partial \overline{k'}}{\partial t} = -U_j \frac{\partial \overline{k'}}{\partial x_j} - \overline{u_i' u_j'} \frac{\partial U_i}{\partial x_j} - \frac{2}{Re} \overline{s_{ij}' s_{ij}'}, \tag{2.37}$$

which in the Cartesian form can be expanded as

$$\begin{aligned} \frac{\partial \overline{k'}}{\partial t} = &-\left[U \frac{\partial \overline{k'}}{\partial x} + V \frac{\partial \overline{k'}}{\partial y}\right] \\ &- \left[\overline{u'^2} \frac{\partial U}{\partial x} + \overline{u'v'} \frac{\partial U}{\partial y} \right. \\ &\left. + \overline{u'v'} \frac{\partial V}{\partial x} + \overline{v'^2} \frac{\partial V}{\partial y}\right] \\ &- \frac{2}{Re} \overline{s_{ij}' s_{ij}'}. \end{aligned} \tag{2.38}$$

Here $\overline{s_{ij}' s_{ij}'}$ is the spanwise averaged double dot product of the strain-rate tensor s_{ij}' which in Cartesian coordinates is given by

$$\boldsymbol{s'} = \frac{1}{2} \begin{bmatrix} 2\frac{\partial u'}{\partial x} & \frac{\partial u'}{\partial y} + \frac{\partial v'}{\partial y} & \frac{\partial u'}{\partial z} + \frac{\partial w'}{\partial x} \\ \frac{\partial v'}{\partial x} + \frac{\partial u'}{\partial y} & 2\frac{\partial v'}{\partial y} & \frac{\partial v'}{\partial z} + \frac{\partial w'}{\partial y} \\ \frac{\partial w'}{\partial x} + \frac{\partial u'}{\partial z} & \frac{\partial w'}{\partial y} + \frac{\partial v'}{\partial z} & 2\frac{\partial w'}{\partial z} \end{bmatrix}. \tag{2.39}$$

Note that in equations (2.37) and (2.38), divergence terms including the pressure term have been omitted as they identically provide a zero contribution to the overall perturbation kinetic energy evolution. It is possible to relate the growth rate of the eigenmode to perturbation kinetic energy (PKE) evolution through

$$\begin{aligned} \sigma &= \frac{1}{2E_{kt}} \int_\Omega \frac{\partial \overline{k'}}{\partial t} \, \mathrm{d}\Omega \\ &= -\frac{1}{2E_{kt}} \int_\Omega \left[U_j \frac{\partial \overline{k'}}{\partial x_j} + \overline{u_i' u_j'} \frac{\partial U_i}{\partial x_j} + \frac{2}{Re} \overline{s_{ij}' s_{ij}'}\right] \mathrm{d}\Omega, \end{aligned} \tag{2.40}$$

where $E_{kt} = \int_\Omega \overline{k'}\ \mathrm{d}\Omega$ is the total perturbation kinetic energy in the domain Ω (Sheard *et al.*, 2016). Each term on the right hand side of equation (2.40) contributes to the instability growth rate and for convenience in this thesis will be separated as

$$\sigma = \langle \mathscr{T} \rangle + \langle \mathscr{P} \rangle + \langle \mathscr{D} \rangle, \tag{2.41}$$

where $\langle \mathscr{T} \rangle$ comprise the transport terms, $\langle \mathscr{P} \rangle$ the production terms and $\langle \mathscr{D} \rangle$ the dissipation term, each of which are given by

$$\begin{aligned} \langle \mathscr{T} \rangle &= \langle \mathscr{T}_1 \rangle + \langle \mathscr{T}_2 \rangle \\ &= -\frac{1}{2E_{kt}} \int_\Omega \left[U \frac{\partial \overline{k'}}{\partial x} + V \frac{\partial \overline{k'}}{\partial y} \right] \mathrm{d}\Omega, \end{aligned} \tag{2.42}$$

$$\begin{aligned} \langle \mathscr{P} \rangle &= \langle \mathscr{P}_1 \rangle + \langle \mathscr{P}_2 \rangle + \langle \mathscr{P}_3 \rangle + \langle \mathscr{P}_4 \rangle \\ &= -\frac{1}{2E_{kt}} \int_\Omega \left[\overline{u'^2} \frac{\partial U}{\partial x} + \overline{u'v'} \frac{\partial U}{\partial y} \right. \\ &\quad \left. + \overline{u'v'} \frac{\partial V}{\partial x} + \overline{v'^2} \frac{\partial V}{\partial y} \right] \mathrm{d}\Omega, \end{aligned} \tag{2.43}$$

$$\langle \mathscr{D} \rangle = -\frac{1}{E_{kt}} \int_\Omega \frac{1}{Re} \overline{s'_{ij} s'_{ij}}\ \mathrm{d}\Omega. \tag{2.44}$$

The transport terms $\langle \mathscr{T}_1 \rangle$ and $\langle \mathscr{T}_2 \rangle$ describe the transport of perturbation kinetic energy by the base flow within the domain. Owing to the streamwise periodicity of the flow domain considered, their sum is zero (any deviation from which is attributable to numerical error), thus having no contribution to the growth rate of the eigenmode.

2.4 Receptivity and structural sensitivity analyses

This section discusses the method used to study the receptivity of the global mode to initial conditions and momentum forcing, and its structural sensitivity to base flow modifications. The receptivity is studied by obtaining adjoint modes corresponding to the adjoint to the linearised Navier–Stokes equations. The adjoint equations for both the hydrodynamic and MHD cases are obtained following the method described in Barkley *et al.* (2008). For the hydrodynamic cases the adjoint equations are given by

$$\boldsymbol{\nabla} \cdot \boldsymbol{u}^* = 0, \tag{2.45}$$

$$-\frac{\partial \boldsymbol{u}^*}{\partial t} = -\mathbf{N}^*(\boldsymbol{u}^*) - \boldsymbol{\nabla} p^* + \frac{1}{Re}\nabla^2 \boldsymbol{u}^*, \tag{2.46}$$

where $\mathbf{N}^*$ is the linearised advection operator of the adjoint equations, $\mathbf{N}^*(\boldsymbol{u}^*) = (\boldsymbol{\nabla U})^T \cdot \boldsymbol{u}^* - (\boldsymbol{U} \cdot \boldsymbol{\nabla})\boldsymbol{u}^*$, and $\boldsymbol{u}^*$ and p^* are the respective adjoint velocity and pressure fields. Notice that the adjoint to the advection operator takes a different form to its counterpart in equation (2.29), and the time derivative is negative. The adjoint to the linearised quasi-2D MHD momentum equation is given by

$$-\frac{\partial \boldsymbol{u}^*_\perp}{\partial t} = -\mathbf{N}^*(\boldsymbol{u}^*_\perp) - \boldsymbol{\nabla}_\perp p^*_\perp + \frac{1}{Re}\nabla^2_\perp \boldsymbol{u}^*_\perp - \frac{H}{Re}\boldsymbol{u}^*_\perp, \tag{2.47}$$

where $\mathbf{N}^*(\boldsymbol{u}^*_\perp) = (\boldsymbol{\nabla}_\perp \boldsymbol{U})^T \cdot \boldsymbol{u}^*_\perp - (\boldsymbol{U}_\perp \cdot \boldsymbol{\nabla}_\perp)\boldsymbol{u}^*_\perp$.

The adjoint eigenvectors ($\hat{\boldsymbol{u}}^*_i$) of the linear adjoint operator $\mathscr{A}^*$ are obtained from an eigenvalue decomposition as discussed in §2.2 (equation 2.34). The velocity field of an initial perturbation can be expressed using the eigenvector basis as

$$\hat{\boldsymbol{u}}_0 = \sum_i A_i \hat{\boldsymbol{u}}_i. \tag{2.48}$$

The adjoint eigenmode $\hat{\boldsymbol{u}}^*_k$ is orthogonal to all except the corresponding direct eigenmode $\hat{\boldsymbol{u}}_k$ for a linearised perturbation field with spanwise wavenumber k corresponding to a growth rate σ. Hence, the coefficient A_k of $\hat{\boldsymbol{u}}_k$, which corresponds to the amplitude of the eigenmode can be expressed as

$$A_k = \frac{\int \hat{\boldsymbol{u}}^*_k \cdot \hat{\boldsymbol{u}}_0 \, \mathrm{d}\Omega}{\int \hat{\boldsymbol{u}}^*_k \cdot \hat{\boldsymbol{u}}_k \, \mathrm{d}\Omega}. \tag{2.49}$$

A similar method can also be used to describe the global mode amplitude in terms of mometum forcing $\hat{\boldsymbol{f}}$. Therefore, in general the global mode amplitude in terms of $\hat{\boldsymbol{u}}_0$ and $\hat{\boldsymbol{f}}$ can be expressed as

$$A_k = \frac{\int \hat{\boldsymbol{u}}^*_k \cdot [\hat{\boldsymbol{u}}_0 + \hat{\boldsymbol{f}}] \, \mathrm{d}\Omega}{\int \hat{\boldsymbol{u}}^*_k \cdot \hat{\boldsymbol{u}}_k \, \mathrm{d}\Omega}. \tag{2.50}$$

The location of the adjoint mode ($\hat{\boldsymbol{u}}^*_k$) in the flow domain corresponds to the most receptive regions in the flow, where localised initial condition ($\hat{\boldsymbol{u}}_0$) or momentum forcing ($\hat{\boldsymbol{f}}$) can amplify the global mode amplitude (Giannetti & Luchini, 2007). Physically, the location of the adjoint modes corresponds to regions in the flow most effective for the placement of an active flow control mechanism.

Structural sensitivity analysis is used to study how the eigenvalue spectrum changes with the perturbation of the linear operator. The perturbation of the linear operator from a physical perspective may be thought of as a modification in the base flow or the presence of a passive structure in the flow. The eigenvalue problem can be written as

$$(\mathscr{A} - \mu_i \mathrm{B}) \cdot \hat{\boldsymbol{u}}_i = 0. \tag{2.51}$$

With a small amplitude perturbation of the linear operator, equation (2.51) can be written as

$$(\mathscr{A} + \epsilon\delta\mathscr{A}) \cdot (\hat{\boldsymbol{u}}_i + \epsilon\delta\hat{\boldsymbol{u}}_i) = (\mu_i + \epsilon\delta\mu_i)\mathrm{B} \cdot (\hat{\boldsymbol{u}}_i + \epsilon\delta\hat{\boldsymbol{u}}_i), \tag{2.52}$$

where $|\epsilon| \ll 1$. Retaining the terms of order $\mathcal{O}(\epsilon)$ yields

$$(\mathscr{A} - \mu_i \mathrm{B}) \cdot \delta\hat{\boldsymbol{u}}_i + \delta\mathscr{A} \cdot \hat{\boldsymbol{u}}_i = \delta\mu_i \mathrm{B} \cdot \hat{\boldsymbol{u}}_i. \tag{2.53}$$

Taking the dot product of $\hat{\boldsymbol{u}}_i^*$ with equation (2.53) gives

$$\hat{\boldsymbol{u}}_i^* \cdot (\mathscr{A} - \mu_i \mathrm{B}) \cdot \delta\hat{\boldsymbol{u}}_i + \hat{\boldsymbol{u}}_i^* \cdot \delta\mathscr{A} \cdot \hat{\boldsymbol{u}}_i = \hat{\boldsymbol{u}}_i^* \cdot \delta\mu_i \mathrm{B} \cdot \hat{\boldsymbol{u}}_i. \tag{2.54}$$

From the adjoint eigenvalue problem formulation,

$$\hat{\boldsymbol{u}}_i^* \cdot (\mathscr{A} - \mu_i \mathrm{B}) = 0. \tag{2.55}$$

Therefore, from equations (2.54) and (2.55), the change in eigenvalue due to perturbations in the linear operator can be found to be

$$\delta\mu_i = \frac{\hat{\boldsymbol{u}}_i^* \cdot \delta\mathscr{A} \cdot \hat{\boldsymbol{u}}_i}{\hat{\boldsymbol{u}}_i^* \cdot \mathrm{B} \cdot \hat{\boldsymbol{u}}_i}. \tag{2.56}$$

A localised structural perturbation $\delta\mathscr{A}$, at say (x_0,y_0), can be written as

$$\delta\mathscr{A}(x, y) = \delta(x - x_0, y - y_0)\ \delta\mathscr{A}_0, \tag{2.57}$$

where $\delta(x - x_0, y - y_0)$ is the Kronecker delta function and $\delta\mathscr{A}_0$ is a constant coefficient matrix. Then, the bound of the eigenvalue drift is limited by

$$|\delta\mu_i| \leq ||\delta\mathscr{A}_0|| \frac{|\hat{\boldsymbol{u}}_i||\hat{\boldsymbol{u}}_i^*|}{\int \hat{\boldsymbol{u}}_i^* \cdot \hat{\boldsymbol{u}}_i \ \mathrm{d}\Omega}, \tag{2.58}$$

from which the *structural sensitivity* of the eigenvalues to any localised perturbations in the absence of any mass and momentum forcing,

$$S_i(x,y) = \frac{|\hat{\boldsymbol{u}}_i||\hat{\boldsymbol{u}}_i^*|}{\int \hat{\boldsymbol{u}}_i^* \cdot \hat{\boldsymbol{u}}_i \, \mathrm{d}\Omega}. \tag{2.59}$$

Thus, for a dominant eigenmode with a spanwise wavenumber of k corresponding to growth rate σ,

$$S_k(x,y) = \frac{|\hat{\boldsymbol{u}}_k||\hat{\boldsymbol{u}}_k^*|}{\int \hat{\boldsymbol{u}}_k^* \cdot \hat{\boldsymbol{u}}_k \, \mathrm{d}\Omega}. \tag{2.60}$$

Any passive control mechanism will be most effective when placed in regions corresponding to large values of S_k as these locations have the largest impact on the growth rate of the global modes. Further details can be found in Giannetti & Luchini (2007).

2.5 Endogeneity

The previous approach discussed in § 2.4 is used to obtain the wavemaker region in the flow, which corresponds to local region in the flow where any external forcing leads to maximum change in the linearised operator's eigenvalue and hence could be where a flow control mechanism would be most effective leading to the largest growth of the global eigenmode. However, it uses an exogeneous approach in which the internal eigendynamics is not considered. The endogeneous approach (Marquet & Lesshafft, 2015) uses a slightly different concept, in which the direct contribution of localized regions in the flow to the global eigendynamics can be obtained.

Unlike the sensitivity analysis in which a localised perturbation in the linearised operator is considered proportional to an arbitary constant coefficient as in equation (2.57), in the endogeneity approach sensitivity to localised changes to the operator is confined to changes that preserve the local structure of the operator, leading to

$$\delta\mathscr{A}(x,y) = \delta(x - x_0, y - y_0)\ \mathscr{A}(x,y). \tag{2.61}$$

The endogeneity of the eigenmode (μ_i,$\hat{\boldsymbol{u}}_i$) is then given by

$$E(x,y) = \hat{\boldsymbol{u}}_i^*(x,y) \cdot (\mathscr{A}\hat{\boldsymbol{u}}_i)(x,y), \tag{2.62}$$

the integral of which in the domain is equal to the complex growth rate. The

endogeneity is defined such that $E(x,y) = E_\sigma(x,y) - iE_\omega(x,y)$, hence this approach can also be useful as it separates the growth rate (from $E_\sigma(x,y)$) from the frequency contribution (from $E_\omega(x,y)$). Equation (2.62) can thus be expanded to find the individual contributions of each term of the momentum equation to $E(x,y)$ as

$$E(x,y) = -\underbrace{\boldsymbol{u}^* \cdot [(\boldsymbol{U}\cdot\nabla)\boldsymbol{u}']}_{E_{\text{conv}}} - \underbrace{\boldsymbol{u}^* \cdot [(\boldsymbol{u}'\cdot\nabla)\boldsymbol{U}]}_{E_{\text{prod}}} - \underbrace{\boldsymbol{u}^* \cdot \nabla p}_{E_{\text{pres}}} + \underbrace{\frac{1}{Re}\boldsymbol{u}^* \cdot \nabla^2 \boldsymbol{u}'}_{E_{\text{diss}}}. \quad (2.63)$$

Here, E_{conv}, E_{prod}, E_{pres} and E_{diss} respectively aggregate contributions arising from the convection of the eigenmode via the base flow, the production of perturbation energy via base flow shear, pressure and viscous dissipation. This equation bears similarity to equation (2.40) from the perturbation kinetic energy analysis, except that here the adjoint mode is invoked; similarities and differences between these methods will be explored later in this thesis.

2.6 Linear transient growth analysis

Linear transient growth analysis to study the short time dynamics of the flow is discussed in this section. The interaction between the non-orthogonal eigenmodes of $\mathscr{A}$ can produce brief periods of large amplification of kinetic energy of linearised perturbations even when the flow is asymptotically stable (Reddy & Henningson, 1993; Trefethen *et al.*, 1993; Henningson & Reddy, 1994). In some cases, this large amplification can result in a subcritical transition (bypass transition) of the flow at Reynolds number below the critical Reynolds number predicted by the LSA. The mechanism responsible for such a transition is the excursion to the perturbation amplitudes so large that its dynamics become nonlinear; thus bypassing the linear predictions.

The maximum growth in kinetic energy of the perturbation achievable over a finite time τ is determined using the eigenvalue method described in Barkley *et al.* (2008). The kinetic energy of the perturbation relates to the L^2 inner product (the 1/2 is omitted for simplicity)

$$K = (\boldsymbol{u}', \boldsymbol{u}') \equiv \int \boldsymbol{u}' \cdot \boldsymbol{u}' \, \mathrm{d}\Omega. \quad (2.64)$$

Transient growth of an initial disturbance $\boldsymbol{u}'(0)$ over an interval of time, can thus

be written as

$$\frac{K(\tau)}{K(0)} = \frac{(\boldsymbol{u}'(\tau), \boldsymbol{u}'(\tau))}{(\boldsymbol{u}'(0), \boldsymbol{u}'(0))} = \frac{(\mathscr{A}(\tau)\boldsymbol{u}'(0), \mathscr{A}(\tau)\boldsymbol{u}'(0))}{(\boldsymbol{u}'(0), \boldsymbol{u}'(0))} = \frac{(\boldsymbol{u}'(0), \mathscr{A}^*(\tau)\mathscr{A}(\tau)\boldsymbol{u}'(0))}{(\boldsymbol{u}'(0), \boldsymbol{u}'(0))}. \tag{2.65}$$

The maximum possible amplification of energy at time τ over all possible initial conditions $\boldsymbol{u'}(0)$ is called the optimal energy growth $G(\tau)$ expressed as

$$G(\tau) = \max_{\boldsymbol{u'}(0)} \frac{K(\tau)}{K(0)} = \max_{\boldsymbol{u'}(0)} \frac{(\boldsymbol{u}'(0), \mathscr{A}^*(\tau)\mathscr{A}(\tau)\boldsymbol{u}'(0))}{(\boldsymbol{u}'(0), \boldsymbol{u}'(0))}, \tag{2.66}$$

which is given by the largest eigenvalue of the operator $\mathscr{A}^*(\tau)\mathscr{A}(\tau)$ (equivalent to the largest singular value of the operator $\mathscr{A}$). For a given Re and k, the optimal mode is the eigenvector corresponding to maximum optimal energy growth, G_{max} at time $\tau = \tau_{opt}$ (Barkley *et al.*, 2008).

2.7 Weakly non-linear Stuart–Landau analysis

This section presents the Stuart–Landau equation which is used to study the weakly non-linear effects and to understand the nature of bifurcations of the flow arising from linear instability mode growth. This model has been widely used to classify weakly non-linear features of bifurcations in various flows such as the Hopf bifurcation leading to 2D vortex shedding in flows past cylindrical (Provansal *et al.*, 1987; Dušek *et al.*, 1994) and spherical (Thompson *et al.*, 2001) bluff bodies, regular and Hopf bifucations in triangular (Ng *et al.*, 2018) and toroidal bluff bodies (Sheard *et al.*, 2004*b*,*a*) and Pitchfork bifurcations for confined flows such as a 180-degree bend (Sapardi *et al.*, 2017). In this model (Landau & Lifshitz, 1976), the evolution of the complex amplitude (A) of perturbations is modelled as

$$\frac{\mathrm{d}A}{\mathrm{d}t} = (\sigma + i\omega)A - l(1 + ic)|A|^2 A + \cdots, \tag{2.67}$$

where the complex amplitude $A = |A|e^{i\phi t}$. Substituting this in equation (2.67) and ignoring higher order terms, it is possible to decompose the evolution equation into real and complex parts

$$\frac{\mathrm{d}|A|}{\mathrm{d}t} = \sigma|A| - l|A|^3, \tag{2.68}$$

$$\frac{\mathrm{d}\phi}{\mathrm{d}t} = \omega|A| - lc|A|^3. \tag{2.69}$$

The real part in equation (2.68) is sufficient to describe the transition for regular (non-oscillatory) transitions in which the growth rate only has a real component. Equation (2.68) can further be simplified as

$$\frac{\mathrm{d}\log|A|}{\mathrm{d}t} = \sigma - l|A|^2, \tag{2.70}$$

which expresses a linear relation between $\mathrm{d}(\log|A|)/\mathrm{d}t$ and $|A|^2$. The sign of l is an indicator of the type of bifurcation of the flow. For cases with $l > 0$ (i.e. a negative slope as $|A| \to 0$), the bifurcation is supercritical with the non-linear term resulting in the saturation of the perturbation amplitude, whereas when $l < 0$ (i.e. a positive slope as $|A| \to 0$), the bifurcation is subcritical and a hysteretic behaviour is observed near the critical Reynolds number for the transition. Due to the global nature of the linear instability modes, any measure that captures the time history of a growing mode may be used as is convenient. In this work, the kinetic energy of the leading 3D Fourier mode is used as a measure of perturbation amplitude for growth of 3D instabilities.

2.8 Quantifying the effectiveness of the wedges for heat transfer enhancement

This section presents the parameters used for quantifying the effectiveness of heat transfer achieved by the use of repeated wedge-shaped protrusions on one of the walls of a channel and a duct for the hydrodynamic and MHD cases respectively. Two quantitative measures are considered, which are

1. heat transfer efficiency η, and
2. net power ΔP_{net}.

These are elucidated in the subsections to follow.

2.8.1 Heat transfer efficiency η

Heat transfer efficiency η is a measure of the improvement in heat transfer achieved at the expense of pressure drop penalties in the flow, each relative to a plane channel or duct without the wedges, and is defined as

$$\eta = \frac{HR}{PR}, \tag{2.71}$$

where HR is the heat transfer ratio and PR is the pressure ratio. These are respectively given by

$$HR = \frac{Nu}{Nu_0}, \tag{2.72}$$

and

$$PR = \frac{f}{f_0}. \tag{2.73}$$

Nu and f are the domain and time averaged Nusselt number and friction factor, respectively. Subscript 0 is used to denote the plane channel or duct flow cases without the wedges present.

Nusselt number is defined as the ratio of the convective to the conductive heat transfer and expressed as

$$Nu = h(L_{char})/k_f, \tag{2.74}$$

where h is the convective heat transfer coefficient, k_f is the thermal conductivity of the fluid, and L_{char} is the characteristic length scale (Bergman *et al.*, 2007) which for the current setup is $2L$.

For the current setup, the local Nusselt number along the constant temperature bottom wall, obtained as a ratio of the wall normal convective to the conductive heat transfer, is calculated as

$$Nu_x(x,t) = \frac{2L}{(T_{f,x} - T_h)} \frac{\mathrm{d}T}{\mathrm{d}n}\Big|_{y_{b,x}}, \tag{2.75}$$

where $T_{f,x}$ is the local bulk fluid temperature given by

$$T_{f,x}(x,t) = \frac{\int_{y_{b,x}}^{2L} uT \ \mathrm{d}y}{\int_{y_{b,x}}^{2L} u \ \mathrm{d}y}, \tag{2.76}$$

where $y_{b,x}$ is the y coordinate of the bottom wall at any streamwise position x and $\mathrm{d}T/\mathrm{d}n|_{y_{b,x}}$ is the wall normal temperature gradient at $y_{b,x}$. It should be noted that Nu_x does not take into account the influence of the vertical front wall of length l_w (figure 3, 4) to the overall heat transfer, hence to calculate the domain average Nusselt number $\langle Nu \rangle$ in the present study, the following method is adopted:

$$\langle Nu(t) \rangle = \frac{2L}{(T_f - T_h)} \frac{\mathrm{d}T}{\mathrm{d}n}\Big|_{y_b}, \tag{2.77}$$

where $T_f = \langle T_{f,x} \rangle$ is the domain averaged bulk fluid temperature calculated as

$$T_f(t) = \frac{\iint_\Omega uT \ \mathrm{d}\Omega}{\iint_\Omega u \ \mathrm{d}\Omega}, \tag{2.78}$$

and $\mathrm{d}T/\mathrm{d}n|_{y_b}$ is the average wall normal temperature gradient from the bottom wall comprising the horizontal, vertical and the tapered surface's contributions. The domain and time averaged Nusselt number Nu is obtained by taking the time average of $\langle Nu(t) \rangle$.

The friction factor accounts for the pressure loss in the flow from inlet to outlet due to friction and is given by

$$f = \frac{\Delta \tilde{p}/l_d}{\rho U_0^2/2} L, \tag{2.79}$$

where $l_d = l_p + l_w$ is the total length of the channel/duct.

2.8.2 Net power ΔP_{net}

Another parameter used to quantify the effectiveness of the wedge is the net power, which has been found to be an effective quantitative measure in other studies which used various other vortex generation techniques to enhance heat transfer to the fluid (Cassells *et al.*, 2016; Hamid *et al.*, 2016*b*). The net power to the system is calculated as

$$\Delta P_{net} = \Delta P_{heat} - \Delta P_{flow}, \tag{2.80}$$

where $\Delta P_{heat} = P_{heat} - P_{0,heat}$ and $\Delta P_{flow} = P_{flow} - P_{0,flow}$ are respective increments in heat power and pumping power achieved by the presence of the wedge. P_{heat} is the non-dimensional power gained as heat from the constant temperature bottom wall with the use of the wedge, whereas P_{flow} is the non-dimensional power spent on pumping the fluid through the flow domain comprising the wedges. Subscript 0 is used to denote the corresponding powers for a plane duct without wedges.
P_{heat} is expressed as:

$$P_{heat} = \frac{a\alpha C_p}{L^2 U_0^3} \int_0^{l_d} \frac{\mathrm{d}T}{\mathrm{d}n} \, \mathrm{d}x, \tag{2.81}$$

where C_p is the specific heat capacity and α is the thermal diffusivity of the fluid. Equation (2.81) can be re-written in terms of Nu as

$$P_{heat} = \frac{a\alpha C_p l_d \delta T}{L^3 U_0^3} Nu, \tag{2.82}$$

where $\delta T = T_h - T_f$.
P_{flow} is expressed as

$$P_{flow} = \frac{2a}{L}\Delta p, \tag{2.83}$$

where Δp is the non-dimensional pressure drop in the duct. Equation (2.83) can be re-written in terms of f as

$$P_{flow} = \frac{al_d}{L^2}f. \tag{2.84}$$

From equations (2.80), (2.82) and (2.84), ΔP_{net} is given by

$$\Delta P_{net} = \frac{a\alpha C_p l_d \delta T}{L^3 U_0^3}(Nu - Nu_0) - \frac{al_d}{L^2}(f - f_0). \tag{2.85}$$

Multiplying by L^2/al_d, ΔP_{net} can be simplified as

$$\Delta P_{net} = \frac{1}{PeEc}(Nu - Nu_0) - (f - f_0), \tag{2.86}$$

where Ec is the the Eckert number, defined as $U_0^2/C_p\delta T$, which is a measure of the kinetic energy at the wall to the specific enthalpy difference between the hot wall and the fluid. A typical value of Ec in the cooling blanket modules of magnetic confinement nuclear fusion reactors is approximately 10^{-9}, based on the velocity and temperature difference in these applications (Smolentsev *et al.*, 2010*b*) and the properties of Pb-Li alloys (Schulz, 1991; de les Valls *et al.*, 2008). For a heated rotating cylinder in crossflow the value of Ec could range from 0 to 1 in experiments (Gschwendtner, 2004).

2.9 Numerical method

An in-house solver implementing a nodal spectral-element method for spatial discretisation in the $x-y$ plane (Karniadakis & Sherwin, 2013) and a third-order operator splitting scheme based on backward differentiation for time integration (Karniadakis *et al.*, 1991) is used to numerically solve the governing equations and to obtain the base flow solutions. The spectral element method is described in detail in Karniadakis & Sherwin (2013). In this section, a brief description of the key points of the numerical method is provided. The method employs high order polynomial functions within each element unlike the finite element method which typically employs low order interpolating polynomials within each element. Therefore, a two-way refinement in terms of the number of elements

within a computational domain (h-refinement) and an increase in the order of the interpolating polynomial employed within an element (p-refinement) is possible in Spectral methods.

2.9.1 Spatial discretisation

Spectral element methods are typically constructed using one of the two approaches (i) pseuo-spectral or collocation methods or (ii) the Galerkin method. The present code employs the Galerkin method, which will be briefly presented here. In general, both these categories fall under the method of weighted residuals in which a linear differential equation subjected to proper initial and boundary conditions in a domain Ω is denoted by

$$\mathcal{L}(u) = 0. \tag{2.87}$$

The solution of equation (2.87) $u(\boldsymbol{x}, t)$, which is assumed to take the form

$$u^{\delta}(\boldsymbol{x}, t) = u_0(\boldsymbol{x}, t) + \sum_{i=1}^{N} \hat{u}_i(t)\Phi_i(\boldsymbol{x}), \tag{2.88}$$

where $u_0(\boldsymbol{x}, t)$ satisfies the initial and boundary conditions, $\hat{u}_i(t)$ are the N unknown coefficients and $\Phi_i(\boldsymbol{x})$ are analytical functions called trial or expansion functions. Substitituting the approximate solution in equation (2.88) into equation (2.87) gives the residual R, and

$$\mathcal{L}(u^{\delta}) = R(u^{\delta}). \tag{2.89}$$

The constraint placed on R to determine the unknown coefficients is that the Legendre inner product of R with respect to a weighing or test function $w_{tj}(\boldsymbol{x})$ is equated to zero, i.e.

$$(w_{tj}(\boldsymbol{x}), R) = 0, \quad j = 1, 2, ...N, \tag{2.90}$$

where the Legendre inner product of any two functions, say f and g, is defined as

$$(f, g) = \int_{\Omega} f(\boldsymbol{x})g(\boldsymbol{x})\ \mathrm{d}\boldsymbol{x}. \tag{2.91}$$

The type of scheme is determined by the trial function $\Phi_i(\boldsymbol{x})$ and the test function $w_{tj}(\boldsymbol{x})$ used. The present code uses a Galerkin method in which the trial function and the test function are chosen as the same, i.e. $w_{tj}(\boldsymbol{x}) = \Phi_i(\boldsymbol{x})$. In the Galerkin

formulation, the differential equation is initially converted from its strong form by setting the residual $R = 0$ and integrating to obtain the weak form of the equation. The solution domain is sub-divided into non-overlapping regions or elements and a polynomial expansion function is used within each element. For a 2D domain, the present code uses quadrilateral elements with angles between adjacent edges being less than 180^o. This constraint arises from parametric mapping between physical space and the bi-unit square on which integration is performed. The expansion functions or the trial functions are built and defined within a standard element region and then assembled from the local definitions to the global bases.

The expansion functions for one-dimensional system are discussed first followed by an introduction of the expansion bases for multi-dimensional solution domains. The solution domain Ω is the assembly of multiple elements denoted as Ω_e. Expressing the global coordinate in terms of the local expansion function is known as parametric mapping and is achieved by mapping the standard element Ω_{st} to each element domain Ω_e. For a one-dimensional system, the global coordinates x can be expressed in terms of the local coordinates ξ and the corresponding transformation or mapping can be written as

$$x = \chi^e(\xi), \tag{2.92}$$

where $x \,\epsilon\, \Omega_e$ and $\xi \,\epsilon\, \Omega_{st}$. Using this transformation the global expansion functions $\Phi_i(x)$ can be expressed in terms of the local expansion functions $\phi_p(\xi)$, and the approximate solution u^δ in terms of the local expansion bases can be written as

$$u^\delta(x) = \sum_{i=1}^{N-1} \hat{u}_i \Phi_i(x) = \sum_{e=1}^{N_e} \sum_{p=0}^{n_p} \hat{u}_p^e \phi_p^e(\xi), \tag{2.93}$$

where n_p is the order of the polynomial of the expansion function.

The present code employs polynomial nodal expansions which are based on Lagrange polynomials. These polynomials are associated with a set of nodes which includes the ends of the domain in the boundary elements. The interior nodes are located at the zeros of Gauss-Legendre-Lobatto polynomials as these are found to exhibit lesser oscillations compared to equispaced nodal points and are more accurate for numerical integration. The expansion bases having a polynomial order n_p within a standard element Ω_{st} are

$$\phi_p(\xi) = \begin{cases} 1, & \xi = \xi_p \\ \frac{(\xi^2-1)L_p'(\xi)}{n_p(n_p+1)L_p(\xi_p)(\xi_p-\xi)}, & \text{otherwise,} \quad \text{where} \quad 0 \leq p \leq n_p. \end{cases} \tag{2.94}$$

Here ξ_p are the nodal points which corresponds to the roots of the polynomial

$$g(\xi) = (1-\xi^2)L'_p(\xi), \quad \text{where} \quad -1 \leq \xi \leq 1, \tag{2.95}$$

and $L'_p(\xi)$ is the derivative of the Legendre polynomial $L_p(\xi)$. These polynomials are a special form of Jacobi polynomials which using the Rodriguez formula can be written as

$$L_p(\xi) = \frac{(-1)^1}{2^n n!}\frac{\mathrm{d}^n}{\mathrm{d}x^n}(1-\xi^2)^n, \quad \text{where} \quad n = 0, 1, 2.... \tag{2.96}$$

The Legendre polynomials can also be generated from the recursive relationship

$$L_p(\xi) = \begin{cases} 1, \quad \text{for} \quad p = 0, \\ \xi \quad \text{for} \quad p = 1, \\ \frac{1}{p}[(2p-1)\xi L_{p-1} - (p-1)L_{p-2}] \quad \text{for} \quad p = 2, 3, ... \end{cases} \tag{2.97}$$

The nodal expansion basis functions for $n_p = 6$ are shown in figure 2.1 as an example. To obtain the solution within each element, the Galerkin formulation requires evaluation of integrals to place the constaint on the residuals (equation 2.90) and conversion to the weak form. The integrals are approximated as

$$\int_{-1}^{1} u(\xi)\mathrm{d}\xi = \sum_{i=0}^{n_p-1} w_{ti}u(\xi_i) + R(u). \tag{2.98}$$

Gauss-Lobatto-Legendre quadrature rule is used for numerical integration in which the integrands are obtained at the zeros of the Legendre polynomial and the end points of the interval (i.e. $\xi = \pm 1$). The weighing function for evaluating equation (2.98) is given by

$$w_{ti} = \frac{2}{n_p(n_p-1)[L_P - 1(\xi_i)]^2}, \quad i = 0, 1, 2, ...n_p - 1. \tag{2.99}$$

The quadrilateral non-overlapping elements (Ω_e) in the present code for the 2D solution domain are first mapped to a standard bi-unit square region (Ω_{st}) as shown in figure 2.2. The expansion function used within this standard region for a two-dimensional solution domain is obtained by a simple product of the one-dimensional expansion functions (equation 2.94) in each coordinate direction considered, i.e.

$$\phi_{pq}(\xi_1, \xi_2) = \phi_p(\xi_1)\phi_q(\xi_2), \quad 0 \leq p, q, \quad p \leq n_{p1}, \quad q \leq n_{p2}. \tag{2.100}$$

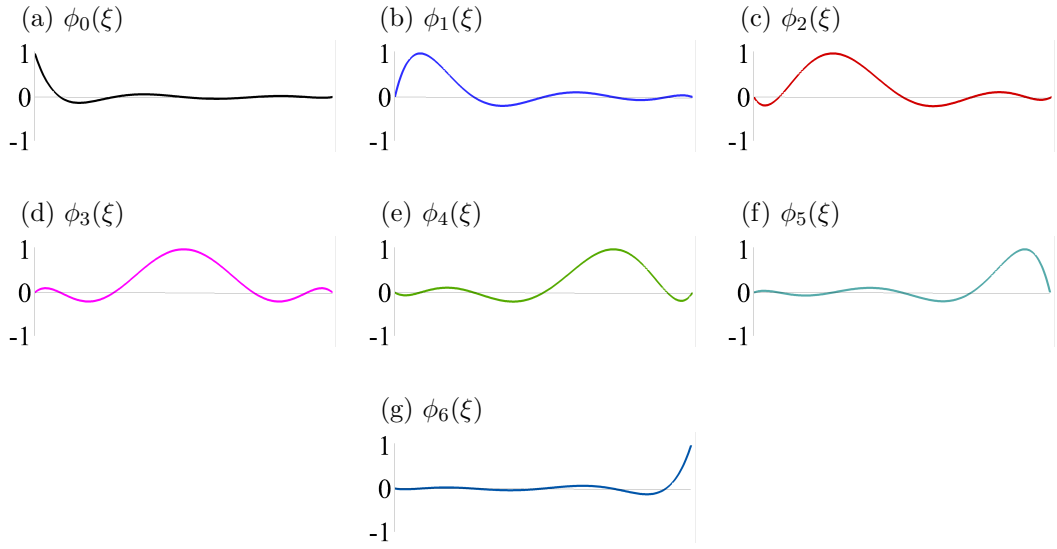

Figure 2.1: One-dimensional nodal expansion function for polynomial order $n_p = 6$.

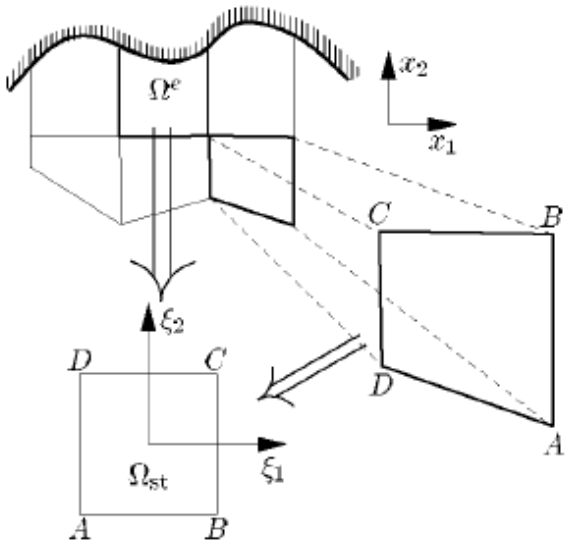

Figure 2.2: Mapping a 2D element from an element region Ω_e to a standard region Ω_{st}, where x_i corresponds to the global coordinate system and ξ_i to the local coordinate system. The figure has been reproduced from Karniadakis & Sherwin (2013) with permission of the publisher.

The order of the polynomial n_{p1} and n_{p2} in each coordinate direction ξ_1 and ξ_2 can in general be different, though they are constrained to be equal in the present code, i.e. $n_{p1} = n_{p2}$. The tensor product expansion in a standard quadrilateral solution domain using the tensor product of 1D Lagrange polynomial expansion function as in equation (2.94) is shown in figure 2.3 for polynomial order $n_p = 3$ and $n_p = 6$.

(a) $n_p = 3$

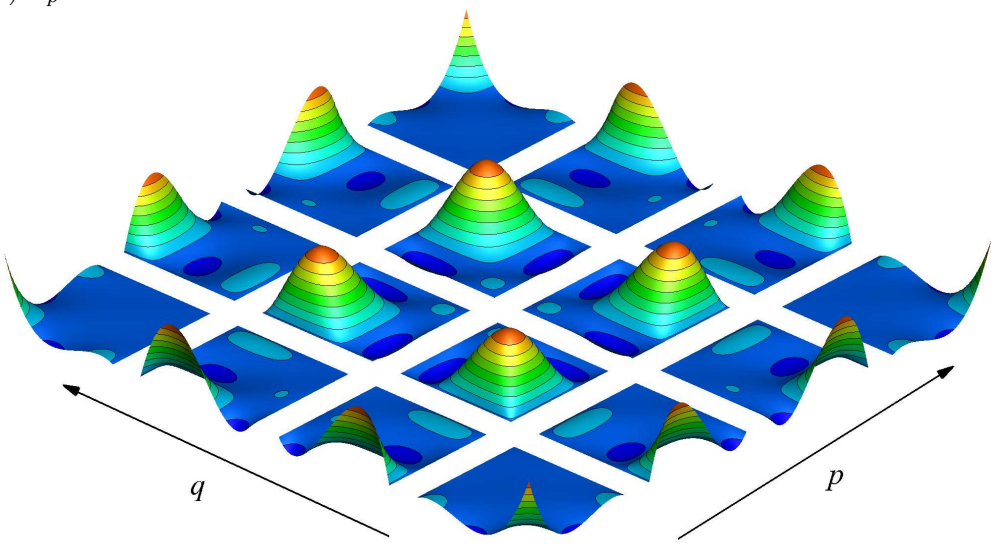

(b) $n_p = 6$

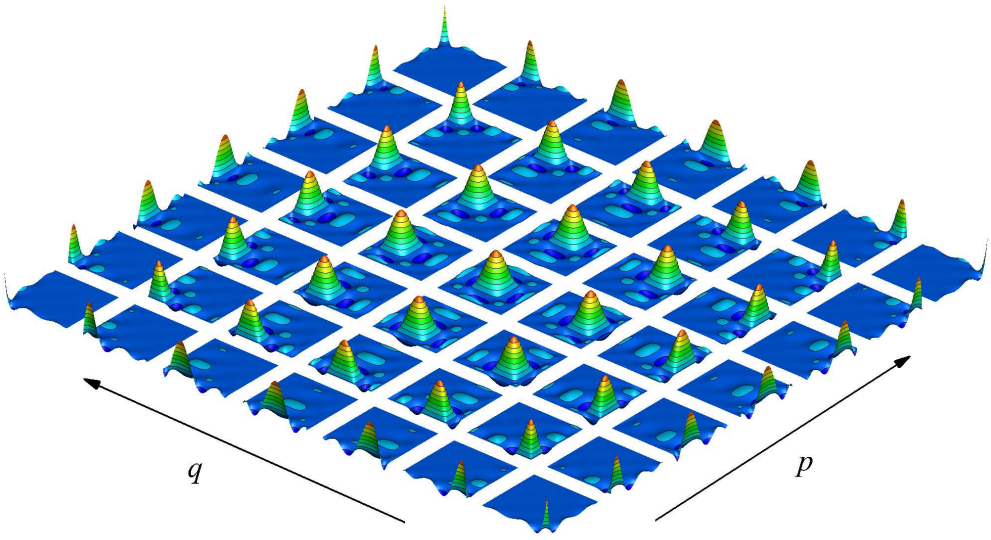

Figure 2.3: Two-dimensional nodal expansion function constructed from one-dimensional Lagrange expansion function for polynomial order (a) $n_p = 3$ and (b) $n_p = 6$.

At the interface between adjacent elements, each node on one element edge shares a single global node with its counterpart on the edge of the adjacent element. This preserves (C_0) continuity of velocity and pressure values across element interfaces in the global solution. Element edge nodes along the left periodic boundary are connected to the edge nodes along the right periodic boundary in the same fashion. The periodic boundary is therefore numerically indistinguishable from any other element interface within the flow domain.

2.9.2 Temporal discretisation

The temporal discretisation scheme implemented in the present solver is briefly explained in this section. In the present study, the pressure field in equation (2.6) and (2.24) is decomposed into a streamwise-periodic fluctuating part and a background horizontal linear pressure gradient, i.e. $p = \tilde{\tilde{p}} - F(t)x$. Thus the momentum equation (2.6) becomes

$$\frac{\partial \boldsymbol{u}}{\partial t} + (\boldsymbol{u} \cdot \boldsymbol{\nabla})\boldsymbol{u} = F(t)\boldsymbol{e}_x - \boldsymbol{\nabla}\tilde{\tilde{p}} + \frac{1}{Re}\boldsymbol{\nabla}^2\boldsymbol{u}, \tag{2.101}$$

and the quasi-2D momentum equation (2.24) becomes

$$\frac{\partial \boldsymbol{u}_\perp}{\partial t} + (\boldsymbol{u}_\perp \cdot \boldsymbol{\nabla}_\perp)\boldsymbol{u}_\perp = F(t)\boldsymbol{e}_x - \boldsymbol{\nabla}_\perp\tilde{\tilde{p}}_\perp + \frac{1}{Re}\nabla^2\boldsymbol{u}_\perp - \frac{H}{Re}\boldsymbol{u}_\perp, \tag{2.102}$$

where $F(t)$ is a time-varying horizontal forcing function and its value is determined within each time integration step to maintain the desired flow rate. The solver employs a third order backward multi-step method for time integration of the Navier–Stokes equations (2.5-2.7) and the quasi-2D MHD equations (2.23-2.25). The convection (material derivative) form of the non-linear advection term is used for the discretisation (Zang, 1991; Blackburn & Sherwin, 2004). Following a similar approach to that described in Karniadakis *et al.* (1991), to integrate from time n to time $n+1$, the equations are cast at the future time, the time derivative term is approximated using backwards differencing, and an appropriate-order extrapolation of the non-linear term to the future time is used. The non-MHD and quasi-2D momentum equations then becomes

$$\begin{aligned}
\frac{\gamma_0\boldsymbol{u}^{n+1} - \sum_{q=0}^{J_i-1}\alpha_q\boldsymbol{u}^{n-q}}{\Delta t} &= \sum_{q=0}^{J_e-1}\beta_q\boldsymbol{N}(\boldsymbol{u}^{n-q}) + F^{n+1}\boldsymbol{e}_x - \boldsymbol{\nabla}\tilde{\tilde{p}}^{n+1} \\
&\quad + \frac{1}{Re}\nabla^2\boldsymbol{u}^{n+1}, \\
\frac{\gamma_0\boldsymbol{u}_\perp^{n+1} - \sum_{q=0}^{J-1}\alpha_q\boldsymbol{u}_\perp^{n-q}}{\Delta t} &= \sum_{q=0}^{J_e-1}\beta_q\boldsymbol{N}_\perp(\boldsymbol{u}_\perp^{n-q}) + F^{n+1}\boldsymbol{e}_x - \boldsymbol{\nabla}\tilde{\tilde{p}}_\perp^{n+1} \\
&\quad + \frac{1}{Re}\nabla^2\boldsymbol{u}_\perp^{n+1} + \beta_q\frac{H}{Re}\boldsymbol{u}_\perp^{n-q}.
\end{aligned} \tag{2.103}$$

The solution of the momentum equation is split into four sub-steps, which are identical to the standard scheme described in Karniadakis *et al.* (1991), except for the addition of a second sub-step. Initially, the velocity field is extrapolated to time $n+1$, to evaluate the advection operator. The first sub-step considers only

the advection term and the additional friction term in the case of the quasi-2D equation, and is used to evaluate the intermediate velocity field $\boldsymbol{u}^{\dagger}$ and $\boldsymbol{u}_{\perp}^{\dagger}$, for each of the case respectively. The corresponding equation from which these are obtained is respectively written as

$$\begin{aligned}
\frac{\boldsymbol{u}^{\dagger} - \sum_{q=0}^{J-1} \alpha_q \boldsymbol{u}^{n-q}}{\Delta t} &= -\sum_{q=0}^{J-1} \beta_q [(\boldsymbol{u} \cdot \nabla)\boldsymbol{u}]^{n-q}, \\
\frac{\boldsymbol{u}_{\perp}^{\dagger} - \sum_{q=0}^{J-1} \alpha_q \boldsymbol{u}_{\perp}^{n-q}}{\Delta t} &= -\sum_{q=0}^{J-1} \beta_q \{[(\boldsymbol{u}_{\perp} \cdot \nabla_{\perp})\boldsymbol{u}_{\perp}]^{n-q} + \frac{H}{Re}\boldsymbol{u}_{\perp}^{n-q}\},
\end{aligned} \tag{2.104}$$

where J is the order of the integration scheme. The second sub-step determines the forcing by prescribing the target velocity u_{target} (desired mean horizontal velocity) on $\boldsymbol{u}^{\ddagger}$ via

$$\frac{\boldsymbol{u}^{\ddagger} - \boldsymbol{u}^{\dagger}}{\Delta t} = F^{n+1} e_x, \tag{2.105}$$

to obtain

$$F^{n+1} = (\gamma_0 u_{target} - u^{\dagger})/\Delta t. \tag{2.106}$$

The third sub-step treats the pressure gradient term and introduces a second intermediate velocity field $\boldsymbol{u}^{\ddagger\dagger}$, as

$$\frac{\boldsymbol{u}^{\ddagger\dagger} - \boldsymbol{u}^{\ddagger}}{\Delta t} = -\nabla \tilde{\tilde{p}}^{n+1}. \tag{2.107}$$

The pressure $\tilde{\tilde{p}}^{n+1}$ is obtained from a Poisson equation constructed by taking the divergence of equation (2.107) and imposing the divergence free constraint on $\boldsymbol{u}^{\ddagger\dagger}$. i.e.

$$\nabla^2 \tilde{\tilde{p}}^{n+1} = \nabla \cdot \left(\frac{\boldsymbol{u}^{\ddagger}}{\Delta t} \right). \tag{2.108}$$

After obtaining the intermediate velocity $\boldsymbol{u}^{\ddagger\dagger}$, the last sub-step involves the diffusion term which is recast into a Helmholtz equation. The unknown velocity at time $n+1$ is solved by applying appropriate velocity boundary conditions. This last sub-step is written as

$$\left(\nabla^2 - \frac{\gamma_0}{Re\Delta t} \right) \boldsymbol{u}^{n+1} = -\left(\frac{\boldsymbol{u}^{\ddagger\dagger}}{Re\Delta t} \right). \tag{2.109}$$

The energy equation in (2.7) and (2.25) is solved in a similar manner using a two-step scheme, with the first step advancing based on the advection term and

Weighing coefficient	$q=0$	$q=1$	$q=2$
α_q	3	-3/2	1/3
β_q	3	-3	1
γ_q	11/6		

Table 2.1: Weighing factors for integration of advection and diffusion equations using a third-order mixed explicit-implicit integration scheme.

the second using the diffusion term. These sub-steps are respectively written

$$\begin{aligned} \frac{T^{\dagger} - \sum_{q=0}^{J-1} \alpha_q T^{n-q}}{\Delta t} &= -\sum_{q=0}^{J-1} \beta_q (\boldsymbol{u}^{n-q} \cdot \nabla) T^{n-q}, \\ \frac{\gamma_0 T^{n+1} - T^{\dagger}}{\Delta t} &= \frac{1}{Pe} \nabla^2 T^{n+1}. \end{aligned} \tag{2.110}$$

The weighing factors used in these schemes are given in table 2.1.

2.9.3 Linear stability analysis - numerical implementation

A BiGlobal stability analysis is implemented in the present code in which a steady or time-periodic base flow that has spatial dependence in two directions is considered with three-dimensional disturbances in the third homogeneous spatial direction. The spatial discretisation of the linear equation governing the evolution of the small amplitude perturbation is similar to what was discussed for the base flow in § 2.9.1. An implicitly restarted Arnoldi iteration method is used to solve the eigenvalue problem (equation 2.34) in which a standard orthogonal projection of the operator $\mathscr{A}$ to a low dimensional Krylov subspace is carried out. The sequence of the Krylov subspace is given by $[\boldsymbol{u}_0, \mathscr{A}\boldsymbol{u}_0, \mathscr{A}^2\boldsymbol{u}_0, ..., \mathscr{A}^{k-1}\boldsymbol{u}_0]$, where $\boldsymbol{u}_0$ is the initial guess of the perturbation field and k is the number of eigenvalues to be computed. The operator $\mathscr{A}$ is not explicitly constructed, instead the standard time-stepping scheme is used to integrate equation (2.28), (2.31) and (2.29), (2.32) to obtain the action of operator $\mathscr{A}$ on the perturbation field. Vectors spanning the Krylov subspace are orthonormalised using the Gram-Schmidt procedure to form the basis vector

$$\boldsymbol{V} = [\boldsymbol{v}_0, \boldsymbol{v}_2, \boldsymbol{v}_3, ...\boldsymbol{v}_k]. \tag{2.111}$$

Thereafter, a Hessenberg matrix (H_m) is constructed and diagonalised to obtain the eigenvalues and eigenvectors of H_m, where

$$H_m \equiv \boldsymbol{V}^T \mathscr{A} \boldsymbol{V}. \tag{2.112}$$

After each block of time stepping the eigenvalues (μ_{hi}) and eigenvectors (ψ_i) of H_m are computed. The iteration is repeated until the residual error which is given by

$$\varepsilon_i \equiv ||\mathscr{A}\psi_i - \mu_{hi}\psi_i|| \tag{2.113}$$

of the eigenpair of H_m is within the prescribed tolerance range which was set as 10^{-8}. The implicitly restarted Arnoldi iterations are implemented through the ARPACK package (Lehoucq *et al.*, 1998). Once converged, the eigenvalues and eigenvectors of H_m are the corresponding approximate (Ritz) eigenmodes of the linear operator $\mathscr{A}$. The maximum dimension of the Krylov subspace (K_e) used for constructing the orthogonal basis vector is a specifiable parameter in the present solver.

A similar technique is used to compute the leading eigenmodes of operator $\mathscr{A}^*\mathscr{A}$ for the transient growth analysis discussed in § 2.6, and of $\mathscr{A}^*$ to compute the adjoint eigenmodes for the sensitivity analysis discussed in § 2.4.

2.10 Three-dimensional direct numerical simulation (DNS)

In this section the discretisation technique used to perform 3D DNS is discussed. The solver uses a Fourier spectral method to discretize the z-direction, while to disretize the $x-y$ plane 2D nodal spectral element scheme discussed in § 2.9.1 is used. This scheme has found widespread applications since the work of Karniadakis & Triantafyllou (1992). The flow variables are represented using the Fourier expansion as

$$\begin{aligned} \boldsymbol{u}(x,y,z,t) &= \sum_{m=0}^{M-1} \boldsymbol{u}_m(x,y) e^{ikmz}, \\ p(x,y,z,t) &= \sum_{m=0}^{M-1} p_m(x,y) e^{ikmz}, \end{aligned} \tag{2.114}$$

where $k = 2\pi/l_z$ is the wavenumber of the Fourier mode m in the spanwise homogeneous direction z ensuring a spanwise periodicity, M is the number of

Fourier modes considered for the simulation and l_z is the spanwise periodic length of the flow domain. Substituting equation (2.114) into equation (2.5) and (2.6), the equations to be solved for each Fourier mode in the 2D dimensional plane ($x-y$ plane) is obtained

$$\boldsymbol{\nabla}_m \cdot \boldsymbol{u}_m = 0, \tag{2.115}$$

$$\frac{\partial \boldsymbol{u}_m}{\partial t} + \mathcal{F}_m\{(\boldsymbol{u}\cdot\boldsymbol{\nabla})\boldsymbol{u}\} = -\boldsymbol{\nabla}_m p_m + \frac{1}{Re}\nabla_m^2 \boldsymbol{u}_m,\ m = 0, ...M-1, \tag{2.116}$$

where $\mathcal{F}_m$ is the m^{th} Fourier mode of the Fourier transform operator $\mathcal{F}$ which is evaluated in physical, and not Fourier space. The operators $\boldsymbol{\nabla}_m$ and ∇_m^2 are given by

$$\begin{aligned} \boldsymbol{\nabla}_m &= \Big(\frac{\partial}{\partial x}, \frac{\partial}{\partial y}, imk\Big), \\ \nabla_m^2 &= \Big(\frac{\partial^2}{\partial x^2}, \frac{\partial^2}{\partial y^2}, -m^2k^2\Big). \end{aligned} \tag{2.117}$$

It is apparent from equation (2.116) that Fourier modes couple only through the advection term. Thus an efficient computation is possible whereby Fourier modes are distributed across parallel processes with inter-process communication only being required for evaluation of the advection term. In the present study this is implemented through the open message passing interface (MPI) library.

2.11 Grid resolution and validation

The numerical solver used in this study has been validated for both MHD and non-MHD flow simulations with focus on linear stability analysis (Sheard, 2011; Sapardi *et al.*, 2017; Ng *et al.*, 2018), transient growth analysis (Hussam *et al.*, 2012*b*; Cassells *et al.*, 2019), energetics analysis (Sheard *et al.*, 2016) and heat transfer analysis (Hussam & Sheard, 2013; Cassells *et al.*, 2016; Hamid *et al.*, 2016*a*). In this section, grid resolution is examined for each of the techniques which has been used to study the flow dynamics for the current system as described in § 2.1. Additionally, validation of the optimal energy growth obtained from transient growth analysis, the growth rate calculated from the different terms in the perturbation kinetic energy analysis, and from the different terms contributing to the endogeneity are also presented.

Initially, meshes with different number of elements were generated and for each of the cases, p-refinement was carried out considering polynomial orders ranging between $3 \leq n_p \leq 18$ for a case with $\beta = 0.25$, $\gamma = 2$ and $\tan(\phi) = 0.125$.

Considering a balance between computational error and computational time, the 594-element mesh with polynomial order $n_p = 15$ is adopted as the prototype for all the base flow computations carried out in this study. The 594-element mesh is shown in figure 2.4 along with the p-element refined meshes for $\beta = 0.25$, $\gamma = 2$ and $\tan(\phi) = 0.125$. For other β and γ cases, meshes were constructed such that the size of the smallest elements along the boundaries and largest elements remained the same as the mesh tested for grid resolution. The polynomial order for the base flow computations for all the cases was also preserved at $n_p = 15$. Examples of the grid used for a higher blockage ratio case $\beta = 0.8$, $\gamma = 2$, $\tan(\phi) = 0.125$ and for a longer pitch case $\beta = 0.25$, $\gamma = 8$, $\tan(\phi) = 0.125$ are shown in figures 2.5 and 2.6, respectively. The solution convergence with element polynomial order for the mesh adopted is shown in table 2.2 for a test case having $\beta = 0.25$, $\gamma = 2$, and $\tan(\phi) = 0.125$ at $Re = 400$ for the non-MHD cases, and at $H = 5$, $H = 200$ and $H = 500$ at $Re = 500$, $Re = 700$ and $Re = 1300$, respectively, for the quasi-2D MHD base flow simulations. The parameters tested for base flow convergence are the norm, $\mathscr{L}^2 = \int_\Omega |\boldsymbol{u}|^2 \, \mathrm{d}\Omega$ (an integral 2-norm or Euclidean norm of the velocity field), the friction factor f (equation 2.79) and the domain averaged Nusselt number $\langle Nu \rangle$ (equation 2.77). At the polynomial order selected for the base flow simulations all the tested parameters have a relative error of less than 0.007% with respective to the highest polynomial order.

The converged base flow solutions were used for conducting linear stability and transient growth analysis. Further grid convergence testing was conducted with respect to the polynomial order (n_p) used for the linear stability and transient growth studies to compute the eigenvalue and eigenvectors of the linearised operator $\mathscr{A}$ in equation (2.34) and the operator $\mathscr{A}^*\mathscr{A}$ in equation (2.66). The respective convergences are shown in tables 2.3 and 2.4. Convergence with respect to length of the eigenvector space used K_e (discussed in § 2.9.3) were also tested for both the non-MHD and quasi-2D MHD cases and $K_e = 20$ is chosen for all the cases. A spanwise wavenumber of $k = 1$ is used to check for the growth rate convergence at $Re = 400$ for the non-MHD cases, whereas a quasi-2D perturbation growth rate was tested at $H = 5$, 200 and 500 at different Reynolds number for the linear stability studies. For the transient growth analysis, the optimal energy growth of 2D perturbations at $Re = 400$ and quasi-2D perturbations considering different cases from the low to high-H range as used for the linear stability cases, all at a time horizon of $\tau = 1$, were used for the testing. The relative error of growth rate using $n_p = 15$ with respect to the highest polynomial order tested is within 0.07% and the relative error using $K_e = 20$ with respect the highest value

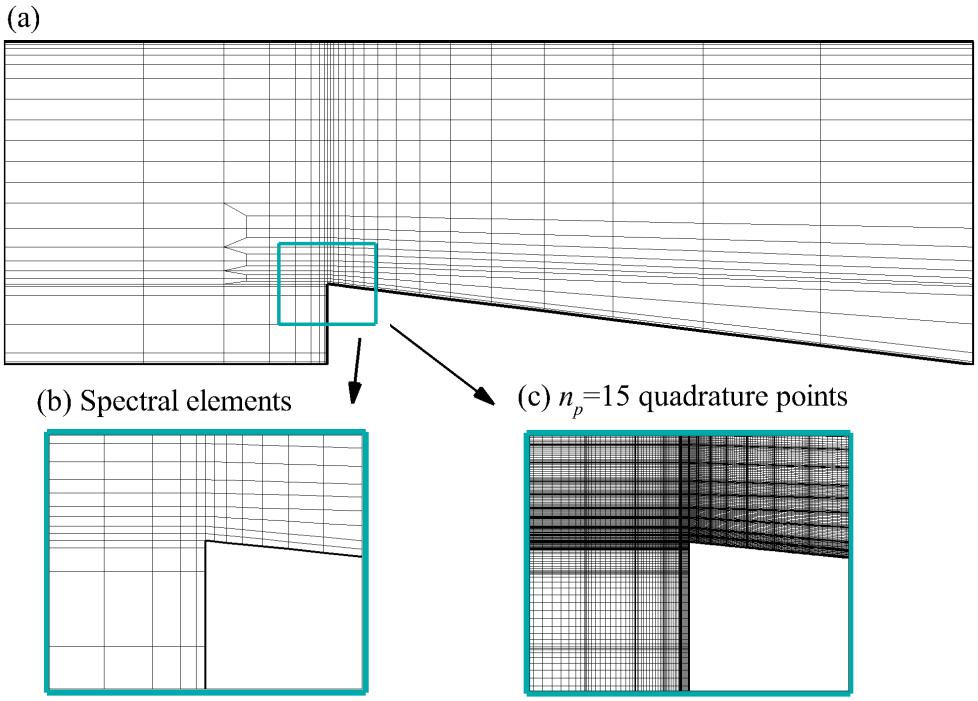

Figure 2.4: (a) Details of the spectral element mesh and (c) the overlay of a virtual grid through interior element quadrature points with $n_p = 15$. Close-up views of the mesh resolution near the wedge tip are shown in (b,c). The particular geometric parameters here are $\beta = 0.25$, $\gamma = 2$ and $\tan(\phi) = 0.125$.

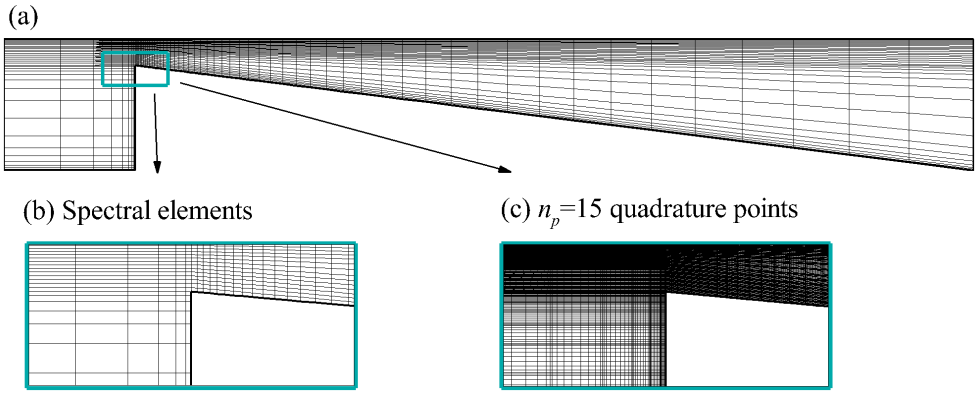

Figure 2.5: (a) Details of the spectral element mesh and (c) the overlay of a virtual grid through interior element quadrature points with $n_p = 15$. Close-up views of the mesh resolution near the wedge tip are shown in (b,c). The particular geometric parameters here are $\beta = 0.8$, $\gamma = 2$ and $\tan(\phi) = 0.125$.

tested is within $10^{-5}\%$ for all the cases tested. At the chosen polynomial order for the transient growth analysis, the relative error with respect to the highest polynomial order was found to be within 0.08% for all the cases tested.

Resolution testing was also conducted to decide the number of Fourier modes

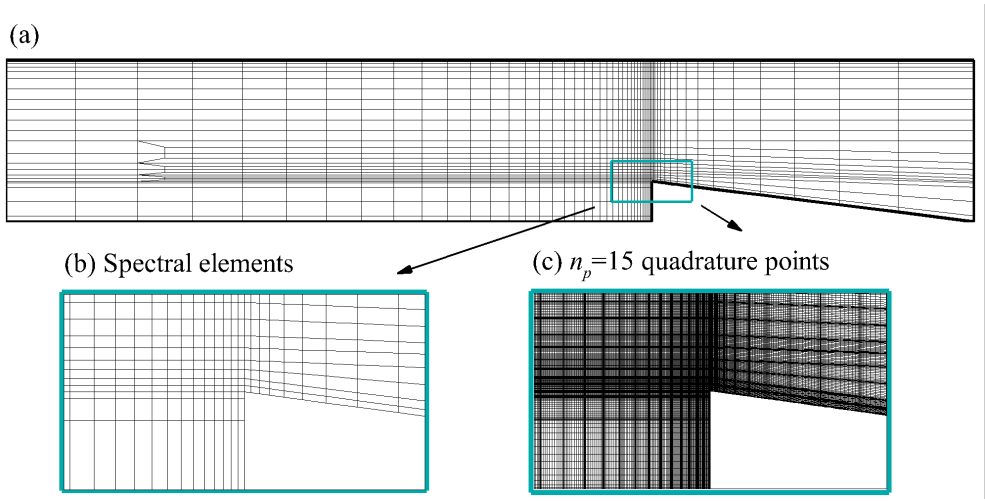

Figure 2.6: (a) Details of the spectral element mesh and (c) the overlay of a virtual grid through interior element quadrature points with $n_p = 15$. Close-up views of the mesh resolution near the wedge tip are shown in (b,c). The particular geometric parameters here are $\beta = 0.25$, $\gamma = 8$ and $\tan(\phi) = 0.125$.

(m) which are required to resolve the spectral element Fourier three-dimensional simulations with spanwise domain length matching the wavelength of the global instability mode predicted from a linear stability analysis (λ_{cr}). A blockage ratio of $\beta = 0.5$ was tested using Fourier modes between 4 and 32. It was found that for a λ_{cr} spanwise domain length, 16 Fourier modes could sufficiently resolve the flow. The parameters tested for convergence are shown in table 2.5.

For validating the optimal energy growth predicted by the linear transient growth solver, the optimal mode corresponding to some time horizon τ is used as an initial condition and linearly evolved to the same time using equations (2.28–2.29) for the non-MHD and equations (2.31–2.32) for the quasi-2D MHD cases. The energy of the evolved disturbance ($K(\tau)$) was then normalised by its initial energy ($K(0)$) and subsequently compared against the gain found from the transient growth analysis $G(\tau)$. Selected cases used to make this validation and a comparison of the corresponding normalised energy ratio and gain found from transient growth are shown in table 2.6 for validating the accuracy of the transient growth analysis implementation. The relative error of the normalised energy gain with respect the gain found from the transient growth analysis for each of these cases evaluated is less than 0.01%, thus verifying the accuracy of the transient growth analysis implementation.

For validating the energetics analysis used for the hydrodynamic cases, the computed individual components of equation (2.41) are summed, yielding an estimate of the growth rate that is compared with the growth rate computed from

$H = 0,\ Re = 400$				$H = 5, Re = 500$			
n_p	$\mathscr{L}^2$	f	$\langle Nu \rangle$	n_p	$\mathscr{L}^2$	f	$\langle Nu \rangle$
3	4.20119	0.02806	2.02691	3	4.14644	0.051614	
6	4.19953	0.02802	2.02691	6	4.14644	0.051614	1.92343
9	4.19951	0.02802	2.02771	9	4.14641	0.051613	1.92437
12	4.19951	0.02802	2.02979	12	4.14641	0.051613	1.92475
15	**4.19952**	**0.02802**	**2.03135**	**15**	**4.14642**	**0.051614**	**1.92494**
18	4.19952	0.02802	2.03144	18	4.14643	0.051614	1.92506
$H = 200, Re = 700$				$H = 500, Re = 1300$			
n_p	$\mathscr{L}^2$	f	$\langle Nu \rangle$	n_p	$\mathscr{L}^2$	f	$\langle Nu \rangle$
3	3.83711	0.737659	1.99195	3	3.81274	0.960569	2.01651
6	3.84009	0.738072	1.99544	6	3.81621	0.961437	2.01755
9	3.84003	0.738052	1.99605	9	3.81615	0.961410	2.01808
12	3.84003	0.738052	1.99629	12	3.81614	0.961404	2.01828
15	**3.84003**	**0.738058**	**1.99642**	**15**	**3.81614**	**0.961407**	**2.01839**
18	3.84007	0.738067	1.99648	18	3.81616	0.961414	2.01845

Table 2.2: Convergence of 2D solutions with increasing order of element polynomial (n_p) for mesh having 594 elements with $\beta = 0.25$, $\gamma = 2$, $\tan(\phi) = 0.125$ at $Re = 400$ for the non-MHD case ($H = 0$), and $H = 5$, 200 and 500 for the quasi-2D MHD cases. Quantities shown are the converged $\mathscr{L}^2$ norm, friction factor f and domain averaged Nusselt number $\langle Nu \rangle$.

the linear stability analysis. This was verified for all the enegretics computations conducted in this project. An example of such a validation is shown in table 2.7 for $\beta = 0.25$ at $Re = 400$. The relative error of growth rate from the energetics analysis is within 0.03% of that computed from linear stability analysis, thereby verifying the accuracy of the energetics analysis.

To validate the endogeneity analysis used for the hydrodynamic cases, the computed domain integrals of the individual components of equation (2.63) are summed, yielding an estimate of the growth rate. This growth rate is then compared with the growth rate computed from the linear stability analysis. Such comparisons were made for all the cases considered for endogeneity analysis. A sample case is shown in table 2.8 for $\beta = 0.25$ at $Re = 400$. The relative error of growth rate from the endogeneity analysis is within 0.03% of that computed from linear stability analysis, thus verifying the accuracy of the endogeneity analysis.

n_p	$H=0$, $Re=400$ σ	$H=5$, $Re=500$ σ	K_e	$H=0$, $Re=400$ σ	$H=5$, $Re=500$ σ
3	0.06808	-0.03368	10	0.06792	-0.03468
6	0.06791	-0.03083	20	0.06792	-0.03082
9	0.06791	-0.03472	**30**	**0.06792**	**-0.03082**
12	0.06792	-0.03084	50	0.06792	-0.03082
15	**0.06792**	**-0.03082**	80	0.06792	-0.03082
18	0.06792	-0.03080			
n_p	$H=200$, $Re=700$ σ	$H=500$, $Re=1300$ σ	K_e	$H=200$, $Re=700$ σ	$H=500$, $Re=1300$ σ
3	-0.150846		10	-0.11546	-0.15678
6	-0.13612	-0.15645	20	-0.11546	-0.15678
9	-0.11547	-0.15678	**30**	**-0.11546**	**-0.15678**
12	-0.11546	-0.15679	50	-0.11546	-0.15678
15	**-0.11546**	**-0.15678**	80	-0.11546	-0.15678
18	-0.11545	-0.15678			

Table 2.3: Convergence of growth rate of the leading eigenmode with increasing order of element polynomial (n_p) for $\beta = 0.25$, $\gamma = 2$, $\tan(\phi) = 0.125$ for the non-MHD case ($H = 0$), and $H = 5$, 200 and 500 for the quasi-2D MHD cases.

n_p	$H=0$, $Re=400$ $G(\tau=1)$	$H=5$, $Re=500$ $G(\tau=1)$	$H=200$, $Re=700$ $G(\tau=1)$	$H=500$, $Re=1450$ $G(\tau=1)$
3	4.75246	4.88346	16.74369	1740.28781
6	4.81973	4.99235	16.68156	1411.78958
9	4.82982	4.99275	16.68497	1417.27099
12	4.82981	4.99275	16.68512	1417.82221
15	**4.83095**	**4.99275**	**16.68475**	**1417.86138**
18	4.83095	4.99275	16.68430	1417.77350

Table 2.4: Convergence of optimal energy growth at $\tau = 1$ with increasing order of element polynomial (n_p) for $\beta = 0.25$, $\gamma = 2$, $\tan(\phi) = 0.125$ at $Re = 400$, $k = 0$ for the non-MHD and $H = 5$, $H = 200$ and $H = 500$ for the quasi-2D MHD cases.

m	$\overline{\overline{\langle E_k \rangle}}$	$\overline{\overline{\langle E_{k,0} \rangle}}$	$\overline{\overline{\langle E_{k,1} \rangle}}$	$\overline{\overline{\langle f \rangle}}$	$\overline{\overline{\langle Nu \rangle}}$
4	103.47576	97.73675	2.23070	0.32056	4.59831
8	103.33750	97.91335	2.14245	0.31866	4.70076
16	103.29384	97.87211	2.14143	0.31838	4.70237
32	103.24632	97.82569	2.14118	0.31824	4.70218

Table 2.5: Convergence of flow properties with increasing number of Fourier modes (m) using a test case of $\beta = 0.5$, $\gamma = 2$, $\tan(\phi) = 0.125$, $Re = 100$. Quantities shown are the time-averaged values of the volume integral of the kinetic energy of the flow $\overline{\overline{\langle E_k \rangle}}$, fundamental mode $\overline{\overline{\langle E_{k,0} \rangle}}$, dominant mode $\overline{\overline{\langle E_{k,1} \rangle}}$, the time-averaged friction factor and the time averaged Nusselt number, where the double-overline represents the time average.

$H = 0$, $Re = 400$			$H = 5$, $Re = 500$		
τ	$K(\tau)/K(0)$	$G(\tau)$	τ	$K(\tau)/K(0)$	$G(\tau)$
5.5	34.32694	34.33101	1.5	4.99275	4.99275

$H = 100$, $Re = 500$			$H = 500$, $Re = 1450$		
τ	$K(\tau)/K(0)$	$G(\tau)$	τ	$K(\tau)/K(0)$	$G(\tau)$
1	16.68434	16.68475	1	1417.80522	1417.86138

Table 2.6: Comparison of the normalised energy of the optimal disturbance ($K(\tau)/K(0)$) with the corresponding optimal energy growth found from transient growth analysis ($G(\tau)$) corresponding to time τ for the non-MHD and quasi-2D MHD cases.

	PKE	LSA	% relative difference in σ
$\langle \mathscr{T}_1 \rangle$	-0.0019117		
$\langle \mathscr{T}_2 \rangle$	0.0019111		
$\langle \mathscr{P}_1 \rangle$	-0.0016381		
$\langle \mathscr{P}_2 \rangle$	0.1448406		
$\langle \mathscr{P}_3 \rangle$	0.0021344		
$\langle \mathscr{P}_4 \rangle$	-0.0021662		
$\langle \mathscr{D} \rangle$	-0.0523740		
$\langle \sigma \rangle$	0.0907959	0.0907761	0.022

Table 2.7: Contribution of each term in equation (2.41) to the growth rate of the leading eigenmode and its comparison with the growth rate obtained from linear stability analysis for $\beta = 0.25$ and $Re = 400$.

	Endogeneity	LSA	% relative difference in σ
$\langle E_{\sigma,conv} \rangle$	0.012532		
$\langle E_{\sigma,prod} \rangle$	0.122446		
$\langle E_{\sigma,pres} \rangle$	0.000033		
$\langle E_{\sigma,diss} \rangle$	-0.044210		
$\langle E_\sigma \rangle$	0.090801	0.090776	0.027

Table 2.8: Contribution of the domain integral of each term in equation (2.63) to the growth rate of the leading eigenmode and its comparison with the growth rate obtained from linear stability analysis for $\beta = 0.25$ and $Re = 400$.

Chapter summary

In this chapter, the equations governing the fluid flow for both the non-MHD and MHD cases are discussed. Various techniques used to understand the dynamics of the flow such as the linear stability analysis, energetics analysis, sensitivity and receptivity analysis, endogeneity analysis, linear transient growth analysis and the Stuart–Landau analysis are presented. This is followed by a discussion of the parameters used to quantify the heat transfer effectiveness. Thereafter, the numerical method used to solve the governing equations and carry out three-dimensional simulations are elucidated. The grid resolution and validation testing conducted for different flow parameters are presented in the last section of this chapter.

The following chapters will discuss the results of the current work, starting from the linear stability characteristics of hydrodynamic channel flows with repeated wedge protrusions presented in the following chapter.

Chapter 3

Linear stability of two-dimensional hydrodynamic channel flow with repeated wedge protrusions

The two-dimensional hydrodynamic flow in the system under consideration is characterised in this chapter, starting with the identification of the general flow regimes and studying the influence of the associated temperature fields in the steady and unsteady states on the heat transfer ratio. Subsequently, regimes maps over a range of blockage ratios, pitch values and wedge angles are presented. This is followed by a discussion on the variation of separation and reattachment points of the different steady recirculation regions identified in the flow. The stability of the two-dimensional flow is studied via a global linear stability analysis. Both 2D and 3D stability boundaries are established and the dependence of various geometric parameters of the wedge on the stability boundaries are elucidated. Furthermore, the underlying eigenmodes destabilisng the base flow are elaborated and the mechanism through which the onset of instability occurs are explored through an energetics analysis of the dominant global mode. This chapter also explores the adjoint modes, the sensitivity of the eigenmodes as well the endogeneity to further understand the flow dynamics and elucidate the regions in the flow where placement of a flow control mechanism will be most effective. The last section explores the short-time dynamics of the system through the analysis of the linear transient growth behaviour. The optimal disturbance field structure associated with this flow and the corresponding energy gain are discussed. A comparison of the current streamwise periodic system to other confined channel

flow setups studied in the literature is also made. [1]

3.1 Two-dimensional flow

The focus of this section is to characterise the two-dimensional flow in the setup, which is carried out by classifying the flow regimes based on topological changes to the flow structure as Reynolds number is increased. Following this, the heat transfer behaviour in the identified steady and unsteady state of the flow is discussed. The flow regimes are further illustrated using regime maps, which are generated for different ranges of geometric parameters investigated. The steady separation and reattachment characteristics of the different recirculation zones are explained thereafter.

3.1.1 Flow regimes

This study begins with the acquisition of 2D flow solutions across a range of geometric parameters characterising the system. From these, the flows may be classified into five regimes based on the observed streamline patterns, in all cases, the results are shown at either a steady state or a statistically steady-state in cases reaching time-varying solutions. The identified flow regimes are shown in figure 3.1.

Regime-1 is characterised by a single recirculation region that develops in front of the wedge and is attached to the bottom boundary (figure 3.1a), occuring at low Re. The flow otherwise remains attached to the channel walls. The appearance of a recirculation region at a sharp concave corner is a ubiquitous feature of low-Reynolds number flows (Taneda, 1979). This is similar to the low Re flow over a FFS in which a primary recirculation region appears in front of the step (Mei & Plotkin, 1986; Stüer *et al.*, 1999).

With an increase in Re, an adverse pressure gradient compels the flow to separate from somewhere along the tapered surface of the wedge, subsequently reattaching to the bottom wall in the gap before the subsequent wedge. This results in a second recirculation region extending from the tapered wedge surface to the bottom surface between the current and the next wedge (regime-2, figure 3.1b). This is unlike the the flow over a FFS (Mei & Plotkin, 1986; Stüer *et al.*, 1999) where a secondary recirculation region forms immediately after the step.

[1] Some of the results contained in this chapter have been published in Murali, S, Ng, Z. Y. & Sheard, G. J. 2022 Stability of flow in a channel with repeated flow-facing wedge-shaped protrusions. *Journal of Fluid Mechanics.* **941**, A59.

In regime-3 (figure 3.1d), the recirculation region identified in regime-2 merges with the recirculation region in front of the next wedge forming a single recirculation region extending from the slanted wedge surface of the current wedge to the front of the next wedge. This effectively reduces the depth of the cavity between successive wedges, from the perspective of the through-flow. For higher blockage ratios of $\beta \gtrsim 0.5$, an additional steady secondary recirculation region is also observed immediately downstream of the wedge tip in regime-2 and regime-3 (figure 3.1c).

Further increasing Re produces a time dependent flow. In the unsteady regime-4, an instantaneous snapshot of which is shown in figure 3.1e, the steady recirculation region identified in regime-3 begins to shed, introducing vortices which sweep over the bottom wall, whereas the flow remains attached on the top wall of the channel. No vortex shedding from the wedge tip is observed in this regime. The last regime encountered, regime-5 (instantaneous snapshot in figure 3.1f), is characterised by vortex shedding occurring at the wedge tip along with entrainment of boundary layer vorticity into the core.

3.1.2 Heat transfer characteristics of the 2D flow

The heat transfer characteristics in the steady and unsteady regime of the two-dimensional flow identified in § 3.1.1 is briefly discussed in this section. The associated temperature fields in these flow regimes are shown in figure 3.2 for an example case with $\beta = 0.5$, $\gamma = 2$. A diffusive heat transfer behaviour can be observed in the steady state of the flow (figure 3.2a). In the unsteady regime, vortex shedding from the wedge tip engulfs the boundary layer vortices, thereby helping to achieve a better mixing between the hot fluid and cold fluid near the bottom wall and top walls, respectively, thereby resulting in a convection dominated heat transfer behaviour which can be noted from the temperature fields (figure 3.2b) in this state.

The heat transfer ratio HR as defined in equation (2.72) will be presented now to quantify the heat transfer enhancement that can be achieved by the presence of wedges in the channel. The value of HR above 1, indicates the improvement in heat transfer that could be achieved by the use of wedges. In figure 3.3, HR is plotted against $Re - Re_{cr,2\mathrm{D}}$ spanning the steady and unsteady flow regimes for different blockage ratios. In the steady flow regimes ($Re - Re_{cr,2\mathrm{D}} < 0$), HR remains very close to 1, irrespective of the blockage ratio considered. A rise in the value of HR can be seen as soon as the flow becomes unsteady ($Re - Re_{cr,2\mathrm{D}} > 0$) showing that the presence of the wedges can be effective in the unsteady regimes

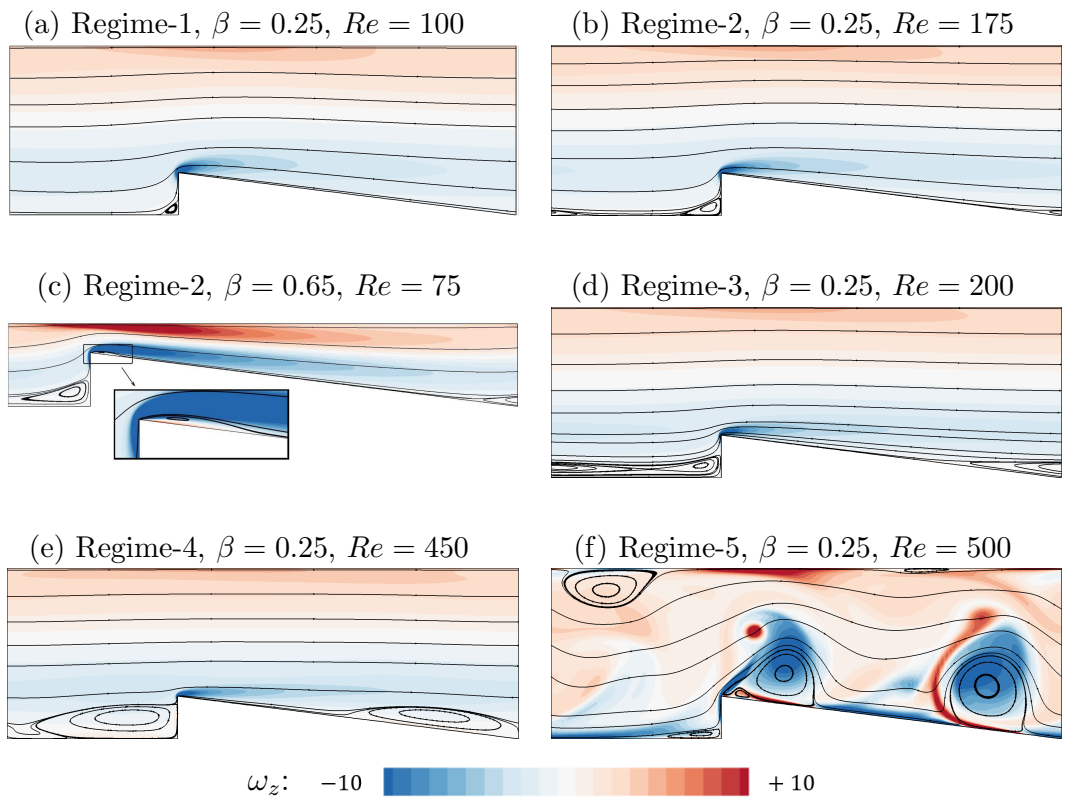

Figure 3.1: (a–f) Two-dimensional steady flow regimes 1–3 and (e–f) unsteady regimes 4–5. The flow streamlines and the spanwise vorticity field are shown for all cases. For the unsteady cases in (e–f) an instantaneous snapshot of the flow field is shown. For all the cases shown here, $\gamma = 2$ and $\tan(\phi) = 0.125$.

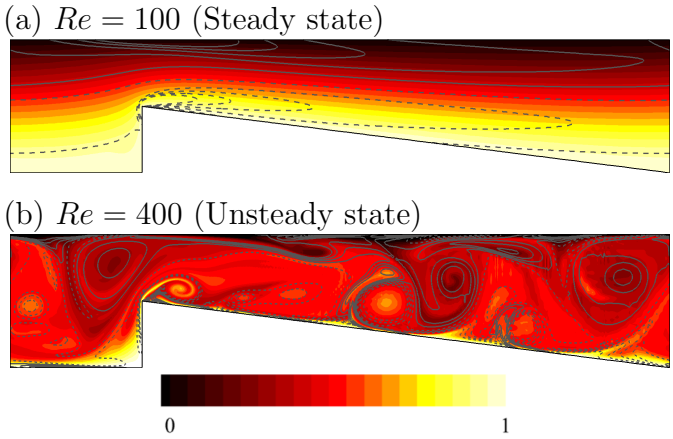

Figure 3.2: Temperature contours overlaid with the spanwise vorticity contours for a two-dimensional flow in the (a) steady state and (b) unsteady state. The parameter combination considered is $\beta = 0.5$, $\gamma = 2$ and $\tan(\phi) = 0.125$ at Reynolds number as indicated. The spanwise vorticity line contours are as per figure 3.1 with the solid and dashed lines indicating positive and negative values, respectively.

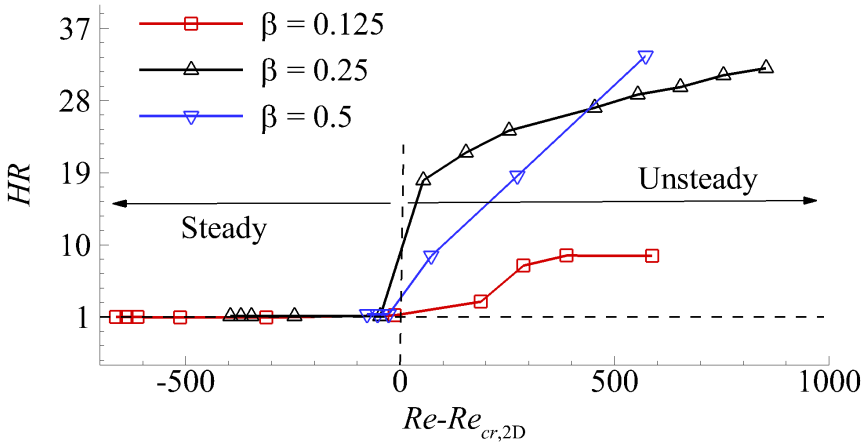

Figure 3.3: Heat transfer ratio HR plotted against $Re - Re_{cr,2D}$ for different β as indicated. The steady and unsteady flow regimes are on the left and right of the dashed vertical line, respectively.

of the flow, and a heat transfer increase as high as approximately 35 times that without the presence of wedges can be achieved.

3.1.3 Regime map

In this section, regime maps for a range of β, γ and ϕ are discussed. The Reynolds number for the onset of each regime identified in § 3.1.1 are termed Re_{Ri}, where $i = 2 - 5$ denotes the regime of the flow observed at $Re > Re_{Ri}$. $Re_{R5} = Re_{cr,2D}$ is the approximate critical Reynolds number for the onset of two-dimensional vortex shedding in the flow. These threshold Reynolds numbers for changes in the steady flow topology were determined visually, accurate to within $\Delta Re = \pm 10$. The critical Re for onset of the unsteady regime (Re_{R4} for some cases if it exists, Re_{R5} otherwise) is found through the linear stability analysis presented later in § 3.2.1.

$Re_{cr,2D}$ is found to decrease with increasing β, γ and ϕ. With increasing β, the range of Re for each regime decreases and at higher blockage ratios, vortex shedding starts after the flow passes through two steady regimes - regime 1 and 2. Regime-4 is not observed for $\beta \gtrsim 0.25$. Within $0.3 \lesssim \beta \lesssim 0.35$ regime-2 was not identified, whereas within $0.5 \lesssim \beta \lesssim 0.65$ regime-3 was not observed (figure 3.4a). A similar observation was made for $\gamma \gtrsim 5$ (figure 3.4b). Re_{Ri} appears to vary the most in the range $1 \lesssim \gamma \lesssim 5$, beyond $\gamma \gtrsim 5$, the different threshold values appears to plateau. In the range of wedge angles investigated, the flow passes through each of the flow regimes identified before becoming unsteady as shown in figure 3.4(c).

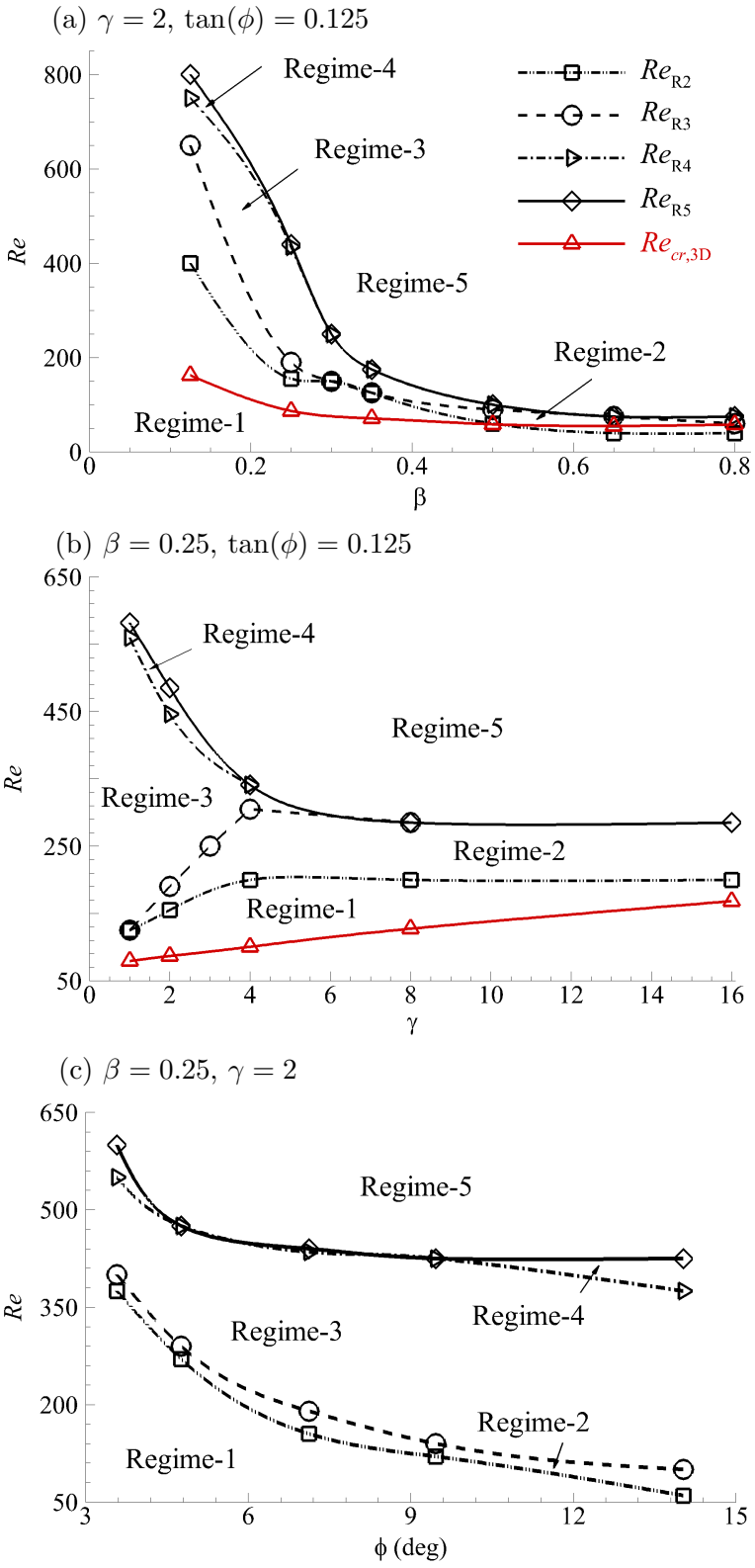

Figure 3.4: Regime maps as functions of Re and (a) β (b) γ and (c) ϕ. The threshold Reynolds numbers for onset of each two-dimensional flow regime shown in figure 3.1 are given by Re_{R2}, Re_{R3}, Re_{R4} and Re_{R5}. The critical Reynolds number for the onset of three-dimensional instability, $Re_{cr,3D}$ is also shown.

3.1.4 Steady separation and reattachment

The behaviour of different recirculation regions in the steady state flow are elucidated in this section by characterising the migration of their separation and reattachment points along the bottom wall for various blockage ratios, pitch values and wedge angles, which are shown in figure 3.5(b-g). The recirculation regions are places of accumulation of the fluid which does not interact with the bulk flow. From a heat transfer perspective, these are regions where high temperatures may develop, and, lacking convective transport and mixing, might lead to structural failure. A diagram illustrating the location of the recirculation zones and nomenclature of the separation and reattachment points is illustrated in figure 3.5(a). The recirculation region that forms in front of the wedge (denoted as 1) have separation and reattachment points x_{s1} and y_{r1} respectively. An increase in x_{s1} denotes its migration to the right whereas an increase in y_{r1} shows its movement upward on the vertical wall. For the recirculation region denoted as 3, closed and open circles respectively are used to denote the separation (x_{s3}) on the tapered wall and the corresponding reattachment (x_{r3}) on the bottom wall between the current and the subsequent wedge. An increase in either of these values denotes a shift to the right. For $\beta \gtrsim 0.5$, an additional recirculation region 2 starts forming with separation starting at the wedge tip and reattaching on the tapered wall (x_{r2}), represented by open triangle symbols. An increase in x_{r2} shows its movement to the right away from the wedge tip. Formation of recirculation region on the top wall was not observed in the steady regimes for the current setup differing from the observations made in flow over a backward-facing step (Armaly *et al.*, 1983; Ghia *et al.*, 1989; Lanzerstorfer & Kuhlmann, 2012*a*).

As an example, the trendlines showing the growth of the different recirculation regions are explained using $\beta = 0.25$. The growth of recirculation region 1 is shown by a decrease in x_{s1} and an increase in y_{r1} with increasing Re. Deviation from this trend is observed when recirculation region 3 emerges further downstream (represented by the first dash-dotted line from the bottom in figure 3.5b,c). Further, the growth of recirculation region 3 with Re is shown as an increase in x_{r3} and an approximately linear decrease in x_{s3}. A deviation in the trend of x_{s3} and y_{r1} is observed when recirculation regions 1 and 3 merge, shown by the second dash-dotted line from the bottom in figure 3.5(b,c). A similar trend is followed for all blockage ratios (figure 3.5b,c), pitch (figure 3.5d,e) and wedge angle variations (figure 3.5f,g). Comparable observations were also found for flows past a BFS (Erturk, 2008), FFS (Marino & Luchini, 2009) and in a 180-degree bend (Sapardi *et al.*, 2017), where a deviation from the growth trend

of a recirculation region was observed with the formation of a new recirculation region further downstream.

3.1.5 Unsteady flow

As discussed in § 3.1.1, there are two unsteady or time dependent flow regimes observed in the current setup. Regime-4 is characterisied by recirculation regions sweeping over the bottom wall with no vortex shedding observed. With increase in Re, vortex shedding starts from the tip of the wedge along with formation of recirculation regions on the top wall of the channel. The vortex shed from the wedge tip interacts with the secondary wall vortices formed on the walls. The Fourier spectra of the $\mathscr{L}^2$ signal in regime-4 ($Re = 480$) and 5 ($Re = 500$) for $\beta = 0.25$, $\gamma = 2$, and $\tan(\phi) = 0.125$ are shown in figure 3.6. The spectra of the signal reveals one dominant and two sub-dominant frequency peaks associated with the flow. The dominant frequency is found to be $f_1 \approx 0.27$, and the sub-dominant frequencies of relatively lower amplitude are its harmonics, $f_2 = 2f_1 \approx 0.53$ and $f_3 = 3f_1 \approx 0.79$. Further details on the onset of the two-dimensional unsteadiness in the flow are elucidated in the sections to follow.

3.2 Linear stability

This section investigates the linear stability of the steady two-dimensional flows reported earlier for a range of β and γ combinations. The stability of the flow to two-dimensional perturbations is investigated first and the global two-dimensional eigenmodes responsible for the onset of two-dimensional unsteadiness in the steady flow are discussed. Thereafter, the critical parameters, underlying eigenmodes and the mechanism responsible for the 3D bifurcation are elucidated.

3.2.1 2D instability

The two-dimensional stability of the flow is investigated in this section for a range of blockage ratios and pitch values by performing a linear stability analysis on the steady-state solutions. The resulting growth rates over a range of Re for selected β and γ combinations are shown in figure 3.7. Over the entire range of Reynolds numbers that produce steady flow solutions, the leading eigenmode has a real eigenvalue that remains stable. This mode is labelled as M1 here. As the unsteady Reynolds number regime is approached, evidence of a subdominant complex eigenmode is detected (labelled as M2 here). Using the `BoostConv` al-

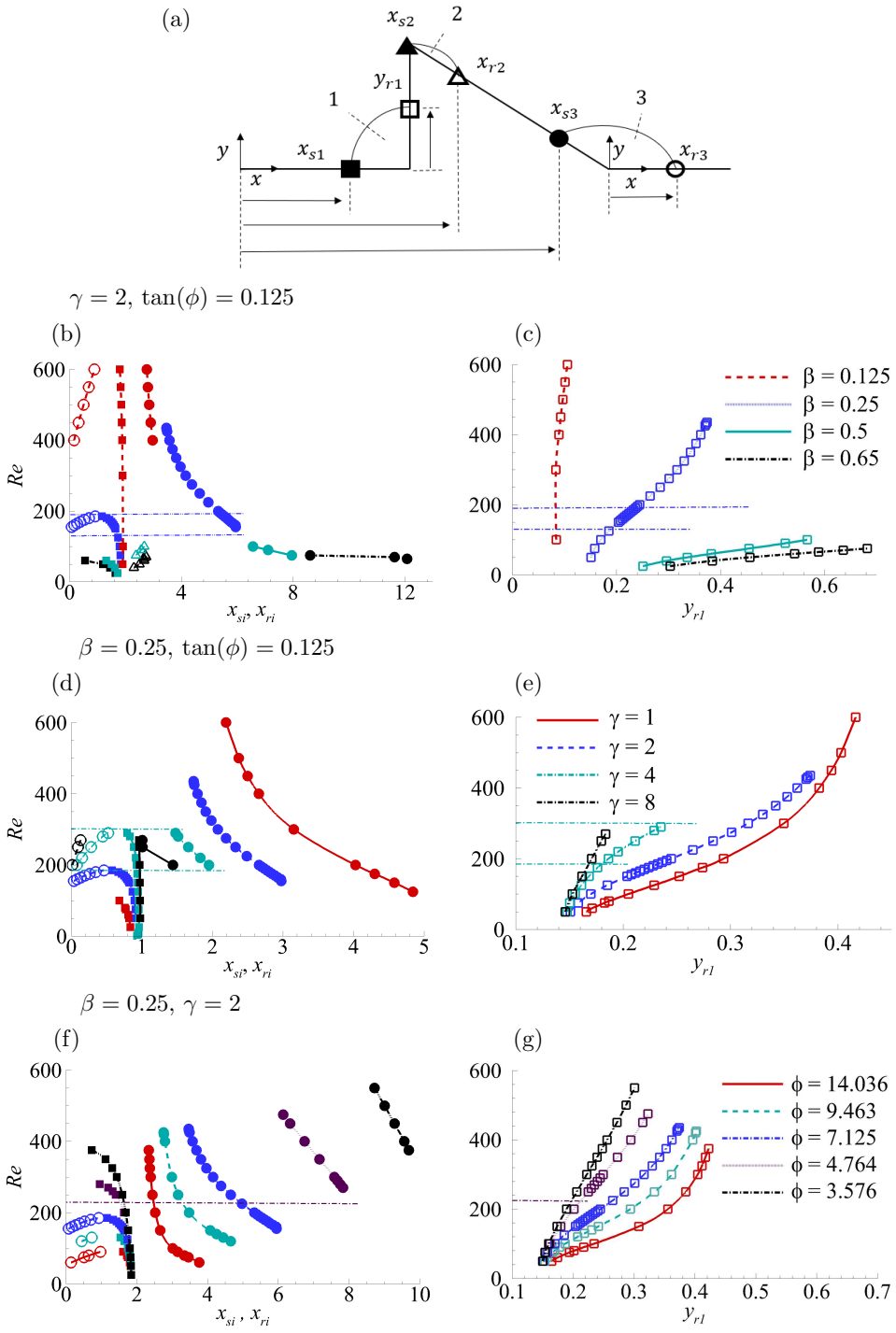

Figure 3.5: (a) Sketch showing the location of three identified recirculation zones and nomenclature of the separation (closed symbols) and reattachment points (open symbols) along with plots showing their dependence on Re and (b,c) β, (d,e) γ, (f,g) ϕ. Variation of the separation and reattachment points along bottom (b,d,f) horizontal & slanted wall and (c,e,g) vertical wall. Horizontal dash-dotted lines in (b-g) are used to represent the deviation from an existing trend due to the formation of a new recirculation region or merging of two existing recirculation regions for $\beta = 0.25$ in (b,c), $\gamma = 4$ in (d,e) and $\phi = 4.764$ in (f,g). x_{s3} and x_{r3} are normalised by γ in (d,e) for better visualisation.

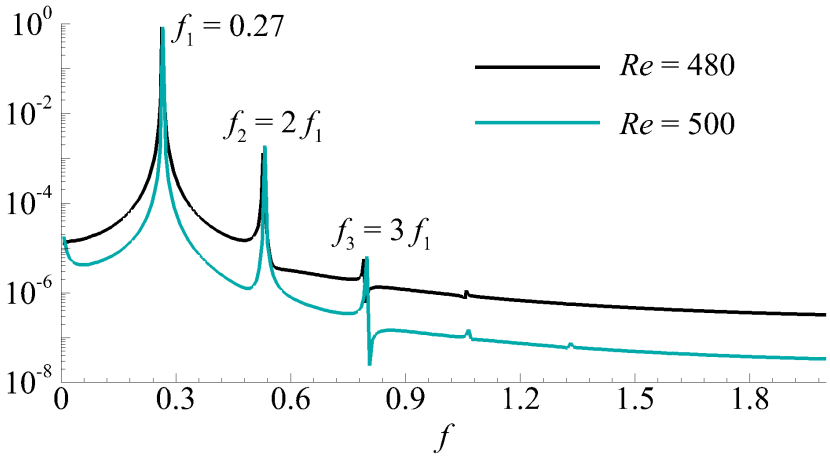

Figure 3.6: Fourier spectra of $\mathscr{L}^2$ signal for $\beta = 0.25$, $\gamma = 2$ and $\tan(\phi) = 0.125$ in regime-4 ($Re = 480$) and regime-5 ($Re = 500$).

$\gamma = 2$		$\beta = 0.25$		$\beta = 0.5$	
β	$Re_{cr,2D}$	γ	$Re_{cr,2D}$	γ	$Re_{cr,2D}$
0.125	712.10	1	582.23	2	126.92
0.25	445.93	2	445.93	16	110.87
0.50	126.92	4	340.83		
0.65	89.56	8	285.73		
0.80	80.25	16	285.07		

Table 3.1: Critical Reynolds number ($Re_{cr,2D}$) for different blockage ratio and pitch values.

gorithm (Citro *et al.*, 2017) steady-state solutions at higher Reynolds numbers are acquired, and analysis of these base flows reveals that this complex M2 mode grows rapidly over a small range of Reynolds numbers, quickly overtaking the M1 mode, before becoming unstable at Reynolds numbers consistent with the appearance of unsteady flow as described in § 3.1.3. The swift emergence of this mode shows that care must be taken when performing a linear stability analysis to include Reynolds number close to and where possible exceeding the critical Reynolds numbers. Techniques capable of recovering the steady 2D solutions at neutrally stable and unstable Reynolds numbers are key to this analysis, such as the `BoostConv` scheme (Citro *et al.*, 2017) used here, the recursive projection method (Shroff & Keller, 1993), the selective frequency damping (SFD) method (Akervik *et al.*, 2007) and the adaptive selective frequency damping method (Jordi *et al.*, 2015).

The perturbation fields of the complex eigenmode (M2) responsible for the onset of 2D unsteadiness is shown in figure 3.8. The eigenmode appears as a

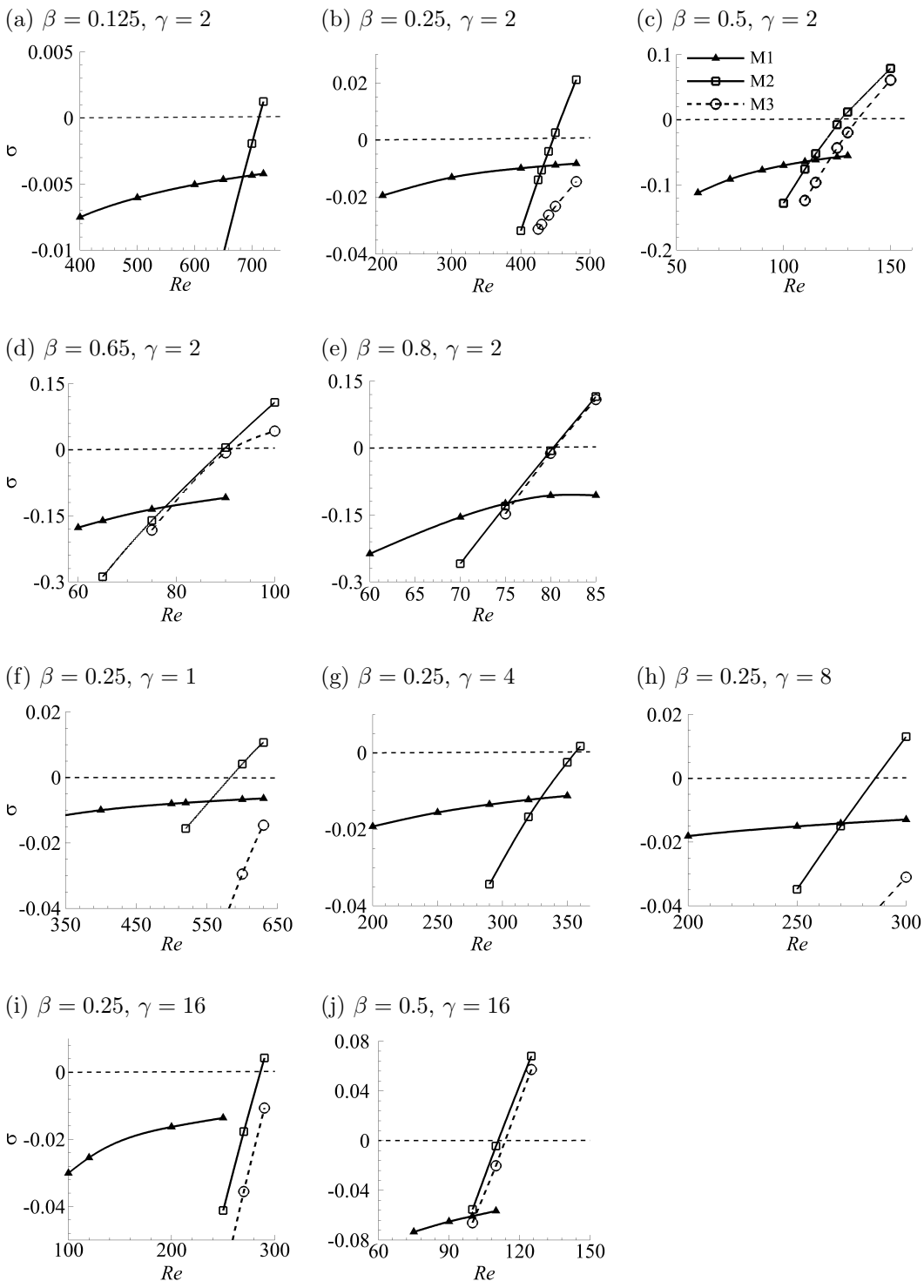

Figure 3.7: Plots of growth rate (σ) against Re. Real and complex eigenvalues are denoted by closed and open symbols respectively. Triangle, square and circle symbols represent mode M1, M2 and M3, respectively. All cases here have $\tan(\phi) = 0.125$.

wave extending over the flow domain destabilising the shear layers on the bottom and top wall of the channel. By contrast, these oscillatory structures are absent from the M1 eigenmodes, which instead exhibit elongated streamwise structures extending the length of the domain. The second subdominant mode (labelled M3 in figure 3.7) is similar to M2 but with a shorter streamwise wavenumber. Since the streamwise-periodic boundary conditions imposed on this system permit only an integer number of oscillatory waves within the domain, it is possible that disturbances featuring a non-integer number of waves over any one wedge unit could lead to a slightly lower critical Reynolds number. This may explain the decrease in $Re_{cr,\mathrm{2D}}$ observed in the flow with increasing γ for every fixed value of β. Beyond a certain γ where sufficiently wide bands of streamwise oscillation wavelengths are available, $Re_{cr,\mathrm{2D}}$ does not vary significantly with increase in γ (figure 3.4b). The critical Reynolds number ($Re_{cr,\mathrm{2D}}$ which corresponds to Re_{R4} or Re_{R5} shown in figure 3.4) corresponding to the onset of unsteadiness in the flow for different blockage ratio and pitch combinations are shown in table 3.1.

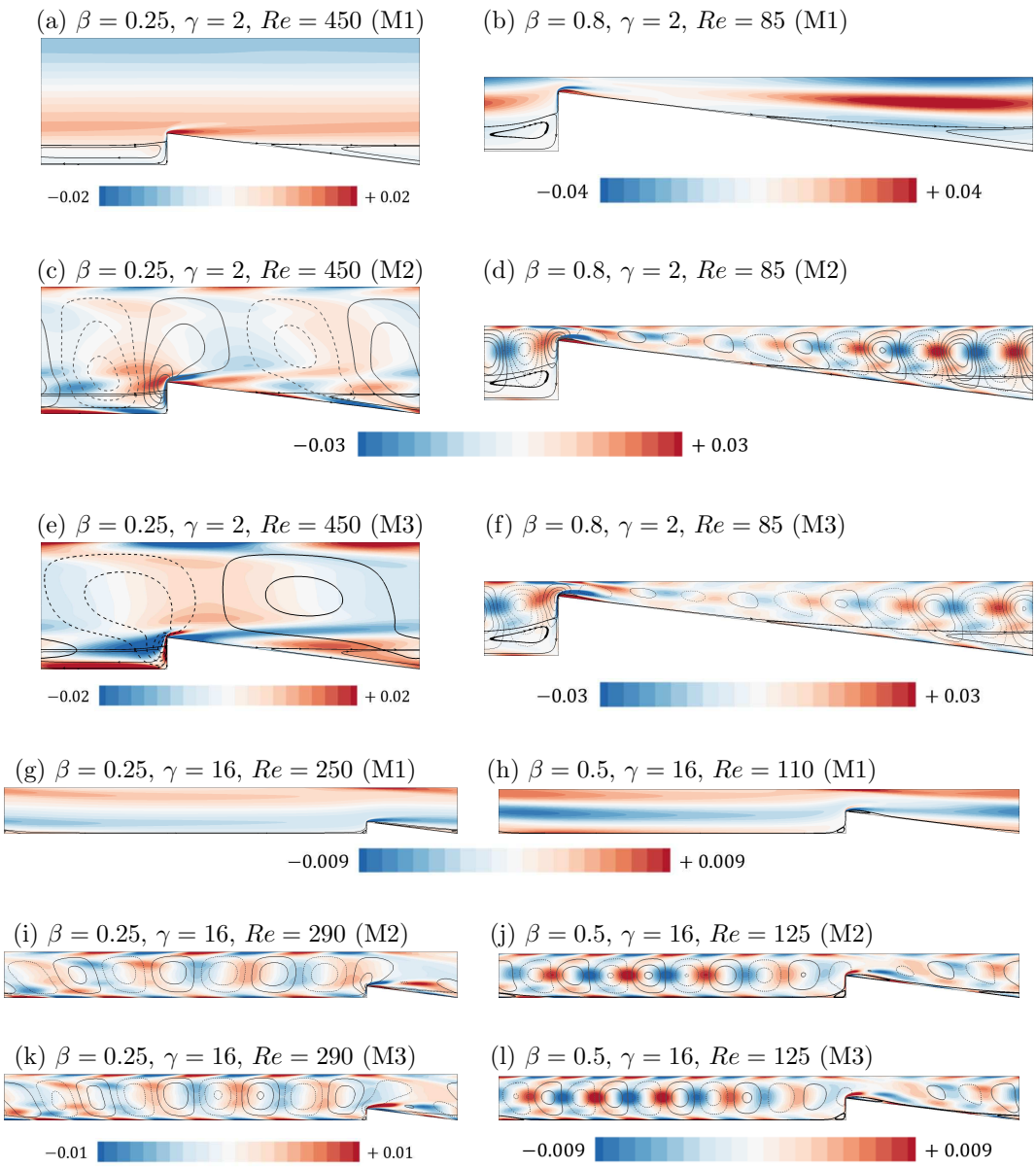

Figure 3.8: Contours of the real part of $\hat{\omega}_z$ for mode (a,b,g,h) M1, and $\hat{\omega}_z$ overlaid with the line contours of the real part of $\hat{v}$ for modes (c,d,i,j) M2 and (e,f,k,l) M3. Base flow streamlines are also shown for reference. All cases here have a wedge angle of $\tan(\phi) = 0.125$. Contours of $\hat{\omega}_z$ are shown in the linear scale at 20 equidistant levels, while line contours of $\hat{v}$ are shown at 10 equidistant levels with solid and dashed lines representing positive and negative values respectively between -0.004 to 0.004 for (c-e,j,l), between -0.005 to 0.005 for (f) and between -0.01 to 0.01 for (i,k).

3.2.2 3D instability - growth rate and marginal stability

The stability of the steady flow to 3D perturbations is investigated in this section. The growth rates of the leading eigenmode are shown in figure 3.9 as functions of Re and spanwise wavenumber, k for different β and $\gamma = 2$ combinations. The primary instability of the steady flow occurs through a real 3D eigenmode (having a real eigenvalue) for all β and γ investigated in this study. The Re and k at which the maximum growth rate of the perturbation is zero gives the critical Reynolds number ($Re_{cr,3D}$) and wavenumber (k_{cr}).

Inspection of the eigenvalue spectra for subcritical Reynolds numbers satisfying $|(Re - Re_{cr,3D})/Re_{cr,3D}| \lesssim 0.035$ for different cases indicate a single dominant mode to be responsible for the bifurcation. The full eigenvalue spectra near $Re_{cr,3D}$ are shown in figure 3.10 for selected cases. With increasing γ at a fixed blockage ratio, the number of subdominant complex eigenvalues (all stable) appear to increase and are spread across the complex plane. An increase in β at a fixed γ shows complex subdominant eigenvalues (all stable) with only a single real eigenvalue which corresponds to the dominant eigenmode. The first subdominant mode also appears to move closer to the neutral curve with an increase in β (figure 3.10a,d-f) and γ (figure 3.10a-c), although in the range of parameters investigated none of the subdominant eigenmodes become unstable. The dominant modes for different geometric parameter combinations are shown in figures 3.13 and 3.14 and the subdominant complex mode for $\beta = 0.8$, $\gamma = 2$ and $\beta = 0.25$, $\gamma = 16$ are shown in figure 3.10(g,h) as an example. They appear as a counter-rotating streamwise vorticity structure concentrated near the wedge tip along with other pairs near the top and bottom wall seen downstream, which appear as chevron structures in the 2D plane (figure 3.10i,j).

Marginal stability curves are constructed by polynomial interpolation to find the wavenumbers corresponding to zero growth rate for each respective Re and are shown for selected blockage ratios and pitch values in figure 3.11. The flow is unstable to infinitesimal perturbations of given wavenumbers to the right of these curves and stable to the left. With increasing blockage ratio, the curves shift to lower Re irrespective of the pitch and the unstable wavenumber range grows wider, indicating that higher blockages are more destabilising for the flow. At any fixed blockage ratio, decreasing γ causes the flow to become more unstable, which is observed as a shift in the neutral curves to the left. This is because the effect of the wedge on the flow becomes greater with increasing constriction and decreasing distance between the wedges.

In figure 3.4(a,b), $Re_{cr,3D}$ is overlaid on the regime maps of the two-dimensional

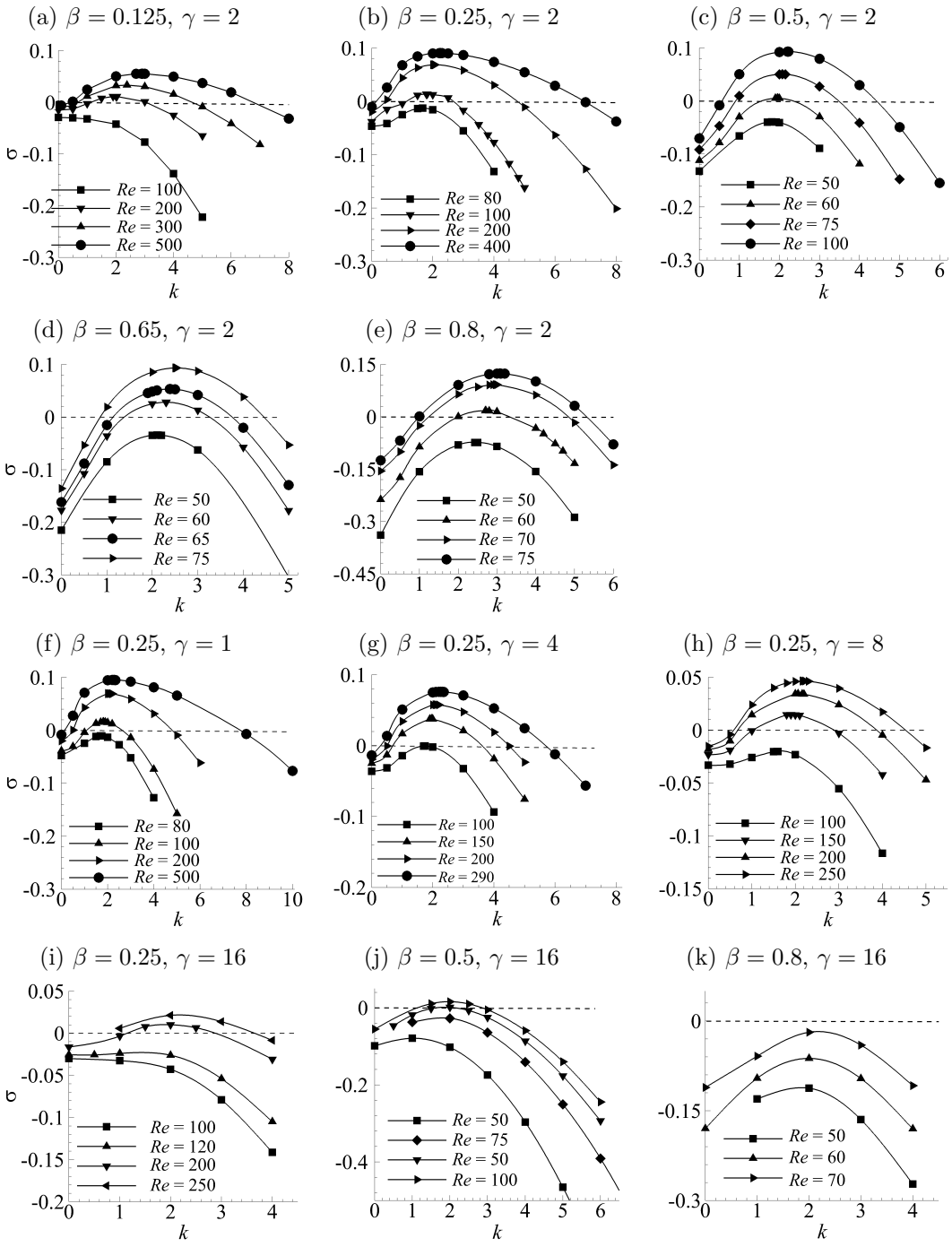

Figure 3.9: Plots of the growth rate (σ) against spanwise wavenumber k for different Re. The stability analysis was conducted for wavenumbers up to $k = 50$, but only a small range of interest is shown for clarity, the remaining modes always decayed monotonically with increasing wavenumber beyond the range shown.

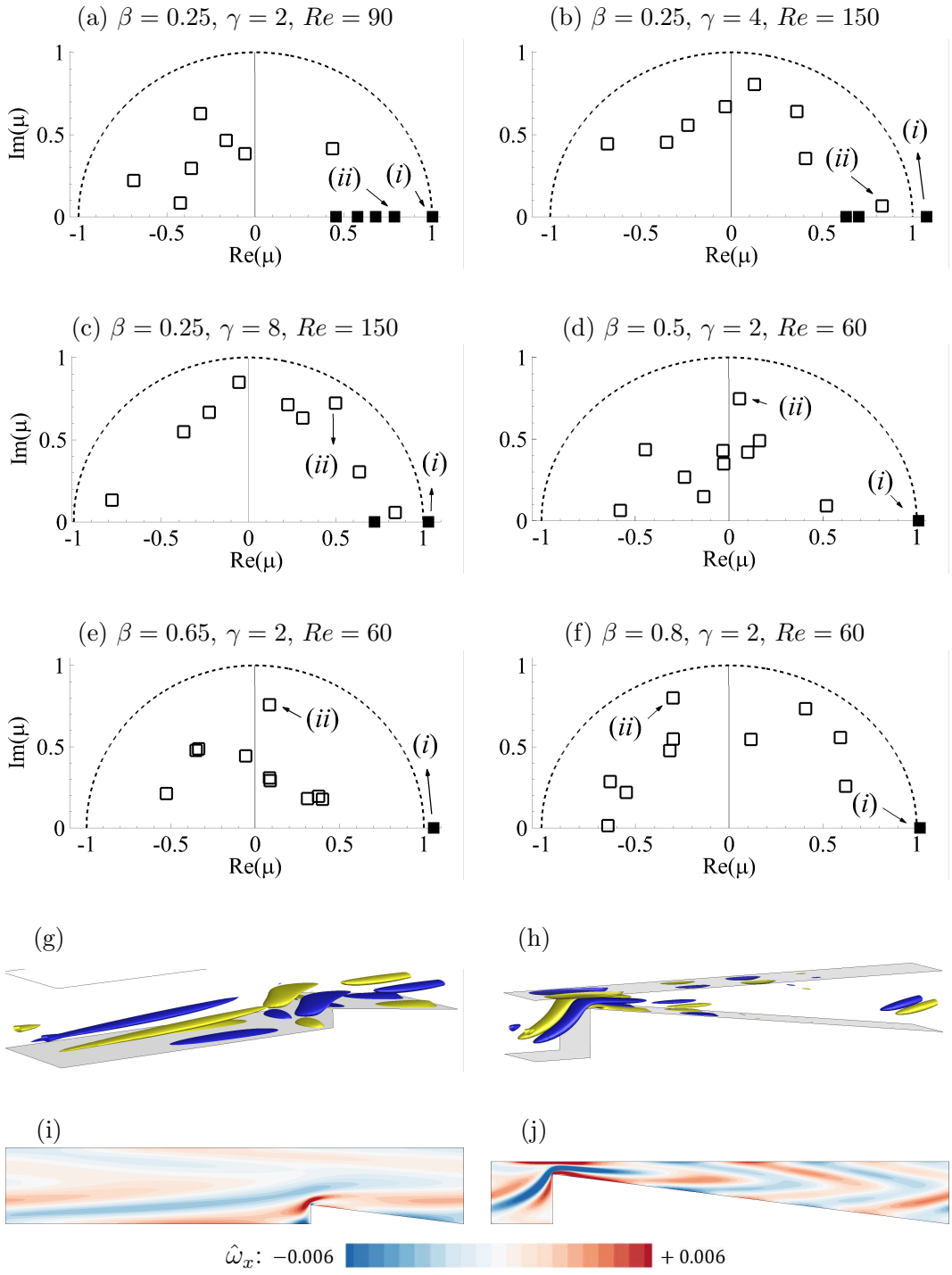

Figure 3.10: Eigenvalue spectra near the critical Reynolds number ($Re_{cr,3D}$). Only the positive imaginary plane is shown, as complex eigenmodes present as conjugate pairs. The leading and first subdominant eigenvalues are indicated as (i) and (ii). (g,h) Positive (blue) and negative (yellow) iso-surfaces of streamwise vorticity ($\hat{\omega}_x$) of the first subdominant eigenmode of (c,f), while the leading modes labelled (i) are shown in figures 3.13 and 3.14. (i,j) Streamwise vorticity contours on xy-plane showing formation of chevron structures for the same cases as in (g,h). The wedge angle $\tan(\phi) = 0.125$ for all cases.

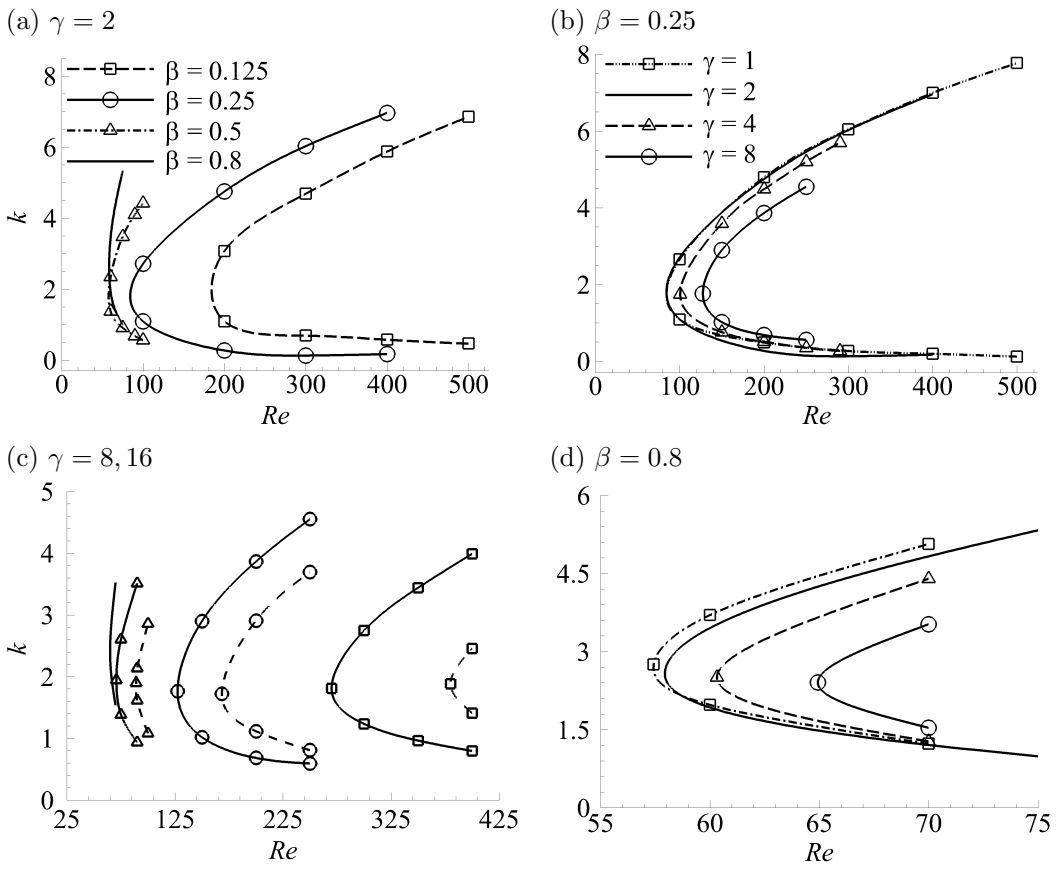

Figure 3.11: Neutral stability curves of the flow for different β and γ combinations. In (c) solid curves correspond to $\gamma = 8$ and dashed curves to $\gamma = 16$. Wedge angle $\tan(\phi) = 0.125$ for all the cases.

base flows as functions of β and γ. For all γ investigated here and for $\beta \lesssim 0.5$, $Re_{cr,3D}$ is within regime-1, where only a single recirculation region exists in front of the wedge. Beyond $\beta \approx 0.5$, onset of three-dimensionality occurs within regime-2 when another recirculation region is formed immediately after the wedge tip.

A summary of $Re_{cr,3D}$ and k_{cr} found for different β and γ combinations is shown in table 3.2. The resemblence of the wedge geometry to a FFS motivates a rescaling of $Re_{cr,3D}$ and k_{cr} by constriction gap height $(2L - h_w)$, consistent with the length scale based on the FFS downstream channel height used in Lanzerstorfer & Kuhlmann (2012*b*). The rescaled values are denoted as

$$Re_{cr,\beta} = 2Re_{cr,3D}(1-\beta), \quad k_{cr,\beta} = 2k_{cr}(1-\beta). \tag{3.1}$$

Similarly, to assess their variation with γ, they are rescaled based on the gap length l_p as

$$Re_{cr,\gamma} = \gamma Re_{cr,3D}, \quad k_{cr,\gamma} = \gamma k_{cr}. \tag{3.2}$$

The variation of these modified critical Reynolds number and wavenumber (3.1-3.2) with β at a fixed pitch of $\gamma = 2$ and $\gamma = 16$, as well as their variation with γ at a fixed blockage ratio of $\beta = 0.25$ and $\beta = 0.8$, are shown in figure 3.12. Both $Re_{cr,\beta}$, $k_{cr,\beta}$ and $Re_{cr,\gamma}$, $k_{cr,\gamma}$ show a monotonic decrease with increasing β and decreasing γ irrespective of the fixed parameter. From figure 3.11 and 3.12 it can be observed that the influence of β on the stability limit is greater at a larger pitch, whereas the influence of γ is more pronounced at smaller values of β. On the other hand, the variation of critical wavenumber is almost negligible when the fixed parameter is changed.

Dependence of $Re_{cr,\beta}$ and $k_{cr,\beta}$ on blockage ratio is qualitatively similar to those in a forward-facing step setup (Lanzerstorfer & Kuhlmann, 2012*b*), in which blockage ratio was termed as constriction ratio. For $\beta = 0.25$ and $\beta = 0.5$ at $\gamma = 2$ ($\gamma = 16$) the critical wavelength of the leading eigenmode λ_{cr} for the present flow domain is $6.9h_w$ ($7.85h_w$) and $3.2h_w$ ($3.31h_w$) respectively which falls between the corresponding λ_{cr} for FFS setup, $3h_s$ and $1.8h_s$ (Stüer *et al.*, 1999; Lanzerstorfer & Kuhlmann, 2012*b*) and BFS setup, $10h_s$ and $7.16h_s$ (Blackburn *et al.*, 2008*a*; Lanzerstorfer & Kuhlmann, 2012*a*). $Re_{cr,3D}$ in the present system is much lower than in those geometries. The disturbances from a leading wedge carry on to subsequent wedges in the present setup due to the streamwise periodic domain, therefore the flow is pre-disturbed at the inlet of a subsequent wedge, altering the stability characteristics. Figure 3.4(b) demonstrates that $Re_{cr,3D}$ increases with increasing pitch. This is likely because a larger pitch effectively

$\gamma = 2$			$\gamma = 16$		
β	$Re_{cr,3D}$	k_{cr}	β	$Re_{cr,3D}$	k_{cr}
0.125	162.22	1.82295	0.125	379.96	1.88670
0.25	86.85	1.72921	0.25	168.42	1.72233
0.50	58.59	1.95534	0.50	89.07	1.89777
0.65	55.15	2.21249	0.65	77.12	2.02639
0.80	57.98	2.65795	0.80	74.26	2.20345
0.95	70.82	3.76773			

$\beta = 0.25$			$\beta = 0.8$		
γ	$Re_{cr,3D}$	k_{cr}	γ	$Re_{cr,3D}$	k_{cr}
1	79.40	1.74095	1	57.43	2.75099
2	86.85	1.72921	2	57.96	2.65795
4	100.50	1.74665	4	59.88	2.49823
8	127.41	1.76608	8	64.73	2.49099
16	168.42	1.72233	16	74.26	2.20345

Table 3.2: Critical Reynolds number ($Re_{cr,3D}$) and wavenumber (k_{cr}) for different blockage ratio and pitch combinations.

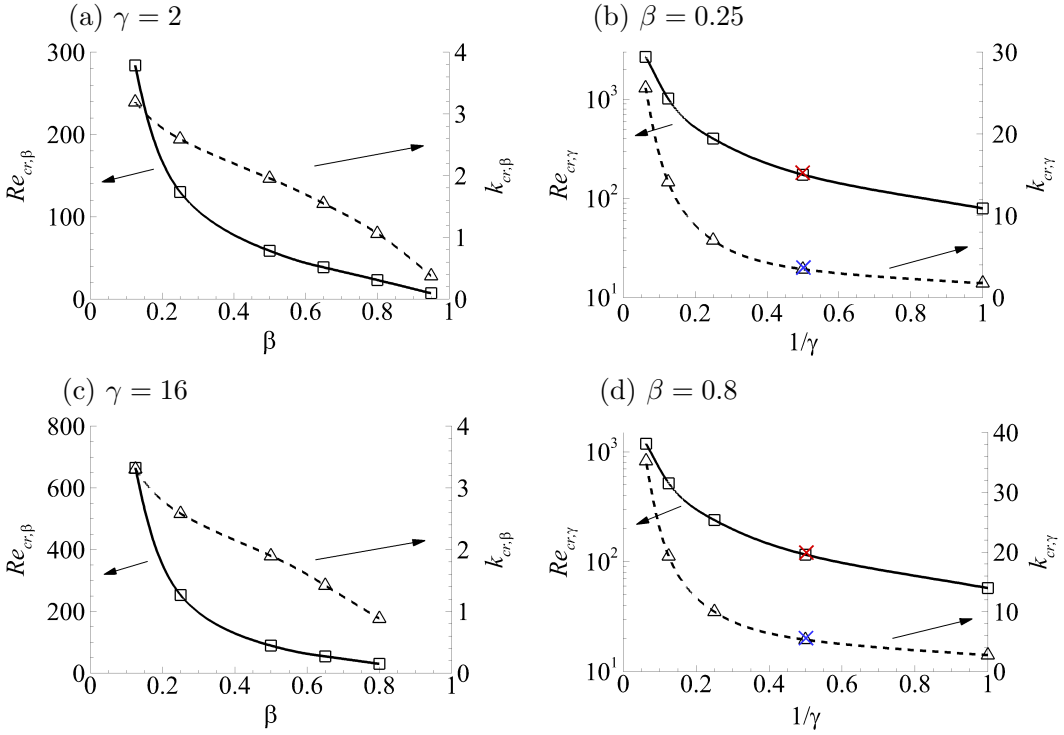

Figure 3.12: Dependence of $Re_{cr,\beta}$ and $k_{cr,\beta}$ on β at (a) $\gamma = 2$ and (c) $\gamma = 16$, and $Re_{cr,\gamma}$ and $k_{cr,\gamma}$ on γ at (b) $\beta = 0.25$ and (d) $\beta = 0.8$. The cross symbol in red and blue in (b) and (d) are the corresponding $Re_{cr,\gamma}$ and $k_{cr,\gamma}$ values for a double wedge case. All the cases have a wedge angle of $\tan(\phi) = 0.125$.

allows the disturbances to decay more before re-entering the domain to interact with a subsequent wedge, thereby increasing the stability. The increasing value of $Re_{cr,3D}$ with increasing γ and decreasing β can also be attributed to the fact that those changes direct the present setup towards a plane channel flow. These trends demonstrate that the periodic arrangement is favourable for promoting instability; as the distance between adjacent wedges increases, the flow becomes more stable.

3.2.3 3D eigenmodes and instability mechanism

In this section the three-dimensional eigenmodes through which instability manifests (eigenvector corresponding to the dominant eigenvalue in 3.2.2) are discussed first, following which the mechanism through which the linear instability mode destabilises the steady base flow are discussed.

The primary instability associated with this flow is a three-dimensional instability which manifests as a pair of counter-rotating streamwise vortices that extend over the wedge and induces streamwise velocity streaks extending through the length the flow domain. The structure of linear stability eigenmode is found to be qualitatively unaffected over the range of blockage ratio and pitch combinations investigated. Visualisation of these dominant eigenmodes through their fields of streamwise vorticity $\hat{\omega}_x$ and velocity $\hat{\boldsymbol{u}}$ for different β and γ values are shown in figures 3.13 and 3.14. For $\beta \gtrsim 0.5$, as the influence of the top wall becomes greater, an additional pair of streamwise vortices emerge near the top wall above the wedge. For $\beta = 0.8$, additional pair of streamwise perturbation velocity streaks also form after the constriction near the top wall. The region of non-zero spanwise velocity $\hat{w}$ of the eigenmode extends from the primary recirculation region over to the tip of the wedge and appears as counter-rotating spanwise rolls concentrated inside and outside the primary recirculation region (figure 3.15). For $\beta \gtrsim 0.5$, when a recirculation region is formed downstream of the wedge tip, the region of non-zero $\hat{w}$ extends over the separating streamline of that recirculation region, appearing as counter-rotating spanwise rolls located outside the secondary recirculation region (figure 3.15b,c).

The eigenmodes of the FFS (Lanzerstorfer & Kuhlmann, 2012*b*) and BFS setups for lower expansion ratios (Barkley *et al.*, 2002; Lanzerstorfer & Kuhlmann, 2012*a*) also appear as spanwise rolls, but are concentrated entirely inside the recirculation region formed after the step. The eigenmodes for the current setup shows resemblance to those modes, as elucidated in figure 3.15 in which $\hat{w}$ contours in the middle of the primary and secondary recirculation region and a subsequent

position further downstream in the flow domain are shown.

The imposition of streamwise periodicity over a single wedge in the present study raises the question as to whether this constraint excludes modes or flow features that would span multiple wedges. To test this, simulations have been performed in domains containing two successive wedges. Two distinct blockage ratios $\beta = 0.25$ and $\beta = 0.8$ were considered, both having $\gamma = 2$ and $\tan(\phi) = 0.125$. The critical Reynolds number and wavenumber for the double-wedge cases are found to match well with the corresponding values found using a single wedge. These are shown in figure 3.12(b,d). The global modes for the double-wedge cases also closely resemble the modes predicted using a single wedge, and are shown in figure 3.16. These results provide evidence in support of the periodic single-wedge results reported herein as being representative of multi-wedge duct flows.

The instability mechanism leading to the primary bifurcation of the flow is now discussed. Different instability mechanisms are examined with respect to the present system based on the eigenmode structure and their location.

Barkley *et al.* (2002) found the region of maximum net outward angular momentum decrease, based on a modified inviscid centrifugal instability criteria given by Rayleigh (Bayly, 1988), along the closed streamline of the recirculation region matching regions of peak three-dimensionality (spanwise velocity component) in a BFS setup. Hence, they argued that centrifugal instability of the primary recirculation region was responsible for destabilising the flow. The associated eigenmode appeared as two counter-rotating spanwise velocity component concentrated entirely inside the recirculation region. This, however, is not the case for the periodic wedge setup here, as the spanwise velocity component does not peak along the closed streamlines of the recirculation region. Another common vortex instability mechanism, elliptical instability arises in strained vortices where perturbations grow strongly in the core of the strained vortex in the direction of the principal strain (Thompson *et al.*, 2001; Bayly *et al.*, 1988; Lanzerstorfer & Kuhlmann, 2012*a*). No evidence of elliptic instability was detected in the eigenmodes in the present study.

For flow over a BFS, Ghia *et al.* (1989) argued that instability manifests as Taylor–Görtler vortices in the bulk flow, forming along curved streamlines induced by the strong recirculation regions on the top and bottom walls. They argue that until the appearance of the secondary recirculation region on the top wall, the dividing streamline at the point of separation of the primary recirculation region remains almost parallel to the flow direction, and has a convex curvature further downstream, and hence the flow remains stable. Destabilisation of the flow begins

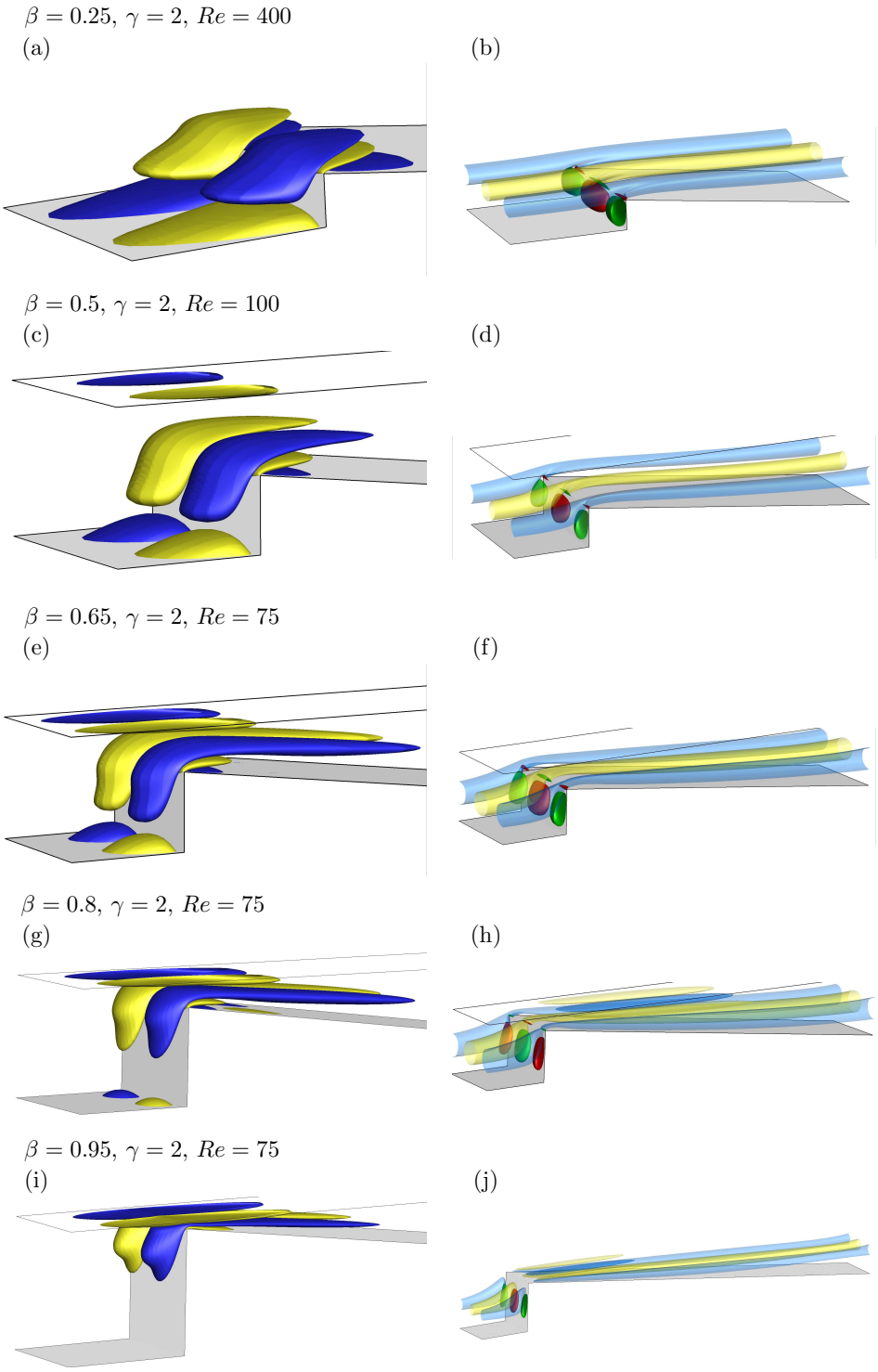

Figure 3.13: (a,c,e,g,i) Positive (blue) and negative (yellow) iso-surfaces of streamwise vorticity $\hat{\omega}_x$ of the leading eigenmodes, and (b,d,f,h,j) positive and negative iso-contours of streamwise velocity $\hat{u}$ (represented as translucent surfaces) and transverse velocity $\hat{v}$ (represented as opaque surfaces) of the leading mode at different blockage ratios. Levels equidistant from zero are chosen arbitarily to visualise the structures. All the cases have $\gamma = 2$ and a wedge angle of $\tan(\phi) = 0.125$.

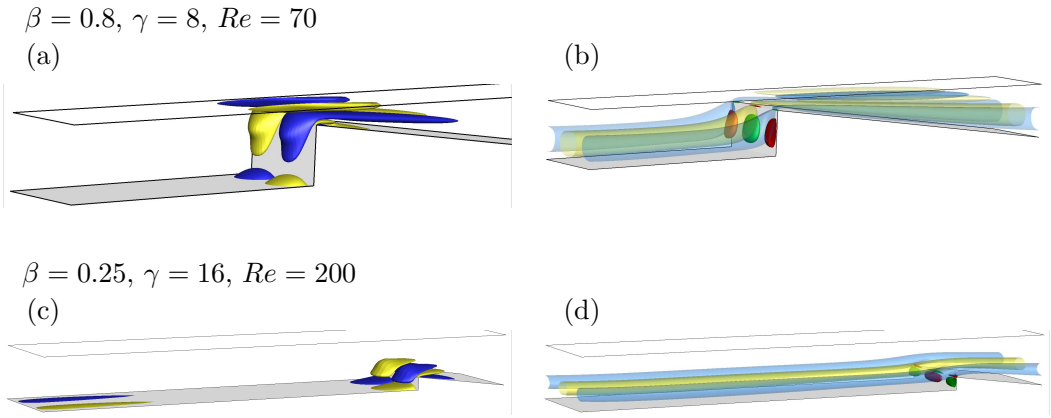

Figure 3.14: (a,c) Positive (blue) and negative (yellow) iso-surfaces of streamwise vorticity $\hat{\omega}_x$ of the leading eigenmodes and (b,d) positive and negative iso-contours of streamwise velocity $\hat{u}$ (represented as translucent surfaces) and transverse velocity $\hat{v}$ (represented as opaque surfaces) of the leading mode at larger pitch values. Levels equidistant from zero are chosen arbitarily to visualise the structures. All the cases have a wedge angle of $\tan(\phi) = 0.125$.

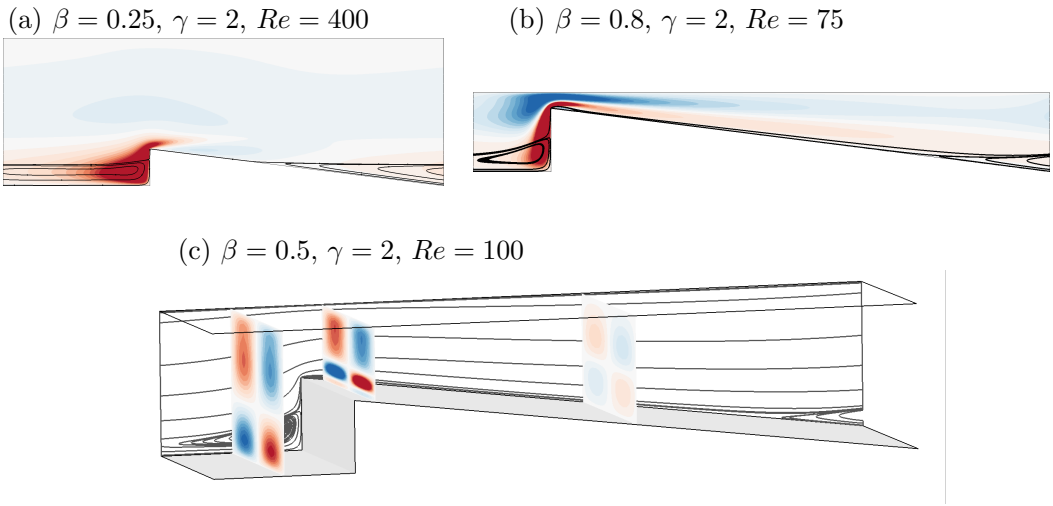

Figure 3.15: (a,b) Spanwise velocity ($\hat{w}$) contours overlaid with base flow streamlines (c) appearing as counter-rotating rolls, shown at $x = 1.0$ (middle of the primary recirculation region), $x = 2.3$ (middle of the secondary recirculation region) and $x = 6.0$. All cases here have $\gamma = 2$, $\tan(\phi) = 0.125$. Contours of $\hat{w}$ are shown in the linear scale at 20 equispaced levels between -0.001 (blue) and 0.001 (red).

with the formation of a secondary recirculation region on the top wall. Taylor–Görtler vortices appear as streamwise counter-rotating vortices. The formation of these vortices occurs in flow over concave curvature and also when the dividing streamline of the recirculation region separates at an angle to the main flow direction (Smith, 1955; Drazin & Reid, 2004). Unlike the flow topology in Ghia

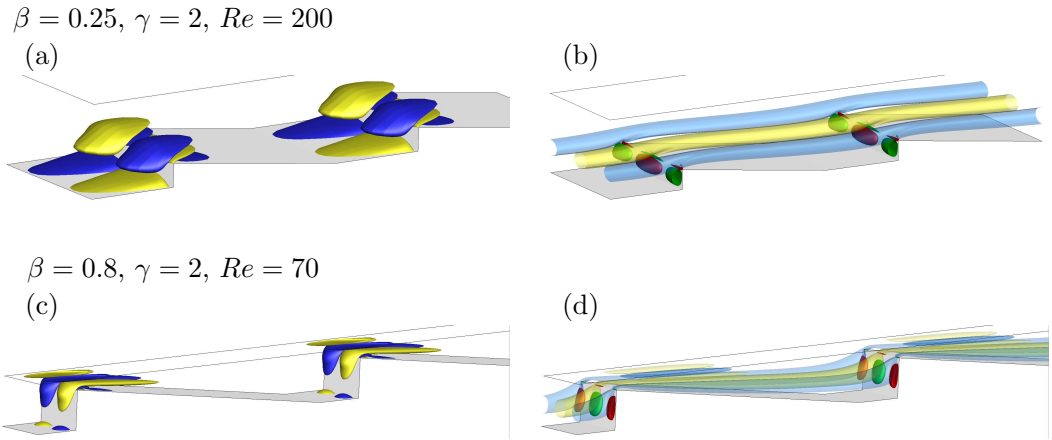

Figure 3.16: (a,c) Positive (blue) and negative (yellow) iso-surfaces of streamwise vorticity $\hat{\omega}_x$ of the leading eigenmodes and (b,d) positive and negative iso-contours of streamwise velocity $\hat{u}$ (represented as translucent surfaces) and transverse velocity $\hat{v}$ (represented as opaque surfaces) of the leading mode for double wedge cases. Levels equidistant from zero are chosen arbitarily to visualise the structures. All the cases have a wedge angle of $\tan(\phi) = 0.125$.

et al. (1989), in the present setup a secondary recirculation region on the top wall is absent in the steady base flow where instabilty occurs. The separating streamline of the recirculation region formed at the face of the wedge for higher blockage ratio has a concave curvature and the modes appear as counter-rotating streamwise vortices over this recirculation region. Since these modes persists even for lower blockage ratios, where the separating streamline is almost parallel to the flow direction, this mechanism might not be responsible for the onset of three-dimensionality in the flow. An assessment of the perturbation kinetic energy budget in § 3.3 will reinforce this point.

Formation of the streamwise velocity ($\hat{u}$) streaks extending through the flow domain as shown in figures 3.13(b,d,f,h,j,l) and 3.14(b,d) are characteristic of the lift-up mechanism (Landahl, 1975), where a small transverse velocity component moves the fluid to a high-velocity region leading to the formation of streaks. These streaks match with the experimental observation in a FFS setup (Stüer *et al.*, 1999). For FFS (Lanzerstorfer & Kuhlmann, 2012*b*) and BFS setups at lower expansion ratio (Lanzerstorfer & Kuhlmann, 2012*a*), this mechanism was found to be responsible for the instability. As a first step to check whether the lift-up mechanism underpins the instability here, the relative proportion of individual perturbation velocity components to its norm is quantified. In figure 3.17(a-d), ratios of integral of the different velocity components of the leading eigenmode are plotted along the streamwise direction (x) for blockage ratios ranging from $\beta = 0.25$ to $\beta = 0.8$ at $\gamma = 2$, along with the contours of absolute velocity of the leading eigenmode for each case. The plotted quantities are ratios of the integrals

$$I_i = \int_{y_{x,b}}^{2L} |\hat{u}_i| \, \mathrm{d}y, \quad I_{\text{total}} = \int_{y_{x,b}}^{2L} |\hat{\boldsymbol{u}}| \, \mathrm{d}y, \tag{3.3}$$

where $y_{x,b}$ is the y coordinate of the bottom wall at the corresponding x-position, and indices $i = 1 - 3$ correspond to the velocity components $\hat{u}$, $\hat{v}$ and $\hat{w}$, respectively.

For $\beta = 0.25$ and $\gamma = 2$, I_2 and I_3 are an order of magnitude smaller than I_1 and are limited to the free shear layers formed in front of the wedge near reattachment point y_{r1} (figure 3.17a). With increasing β, I_3 increases at the expense of I_1 near the vertical wedge wall, and for $\beta \gtrsim 0.65$ (figure 3.17c,d), I_3 exceeds I_1 locally before relaxing back to its pre-disturbed levels, indicative of the lift-up mechanism. Similar observations were made for other β and γ combinations. Flows in a setup with $\beta = 0.5$ when varying γ (figure 3.17e–f) is shown as an example to demonstrate that the contributions I_i remains similar when varying

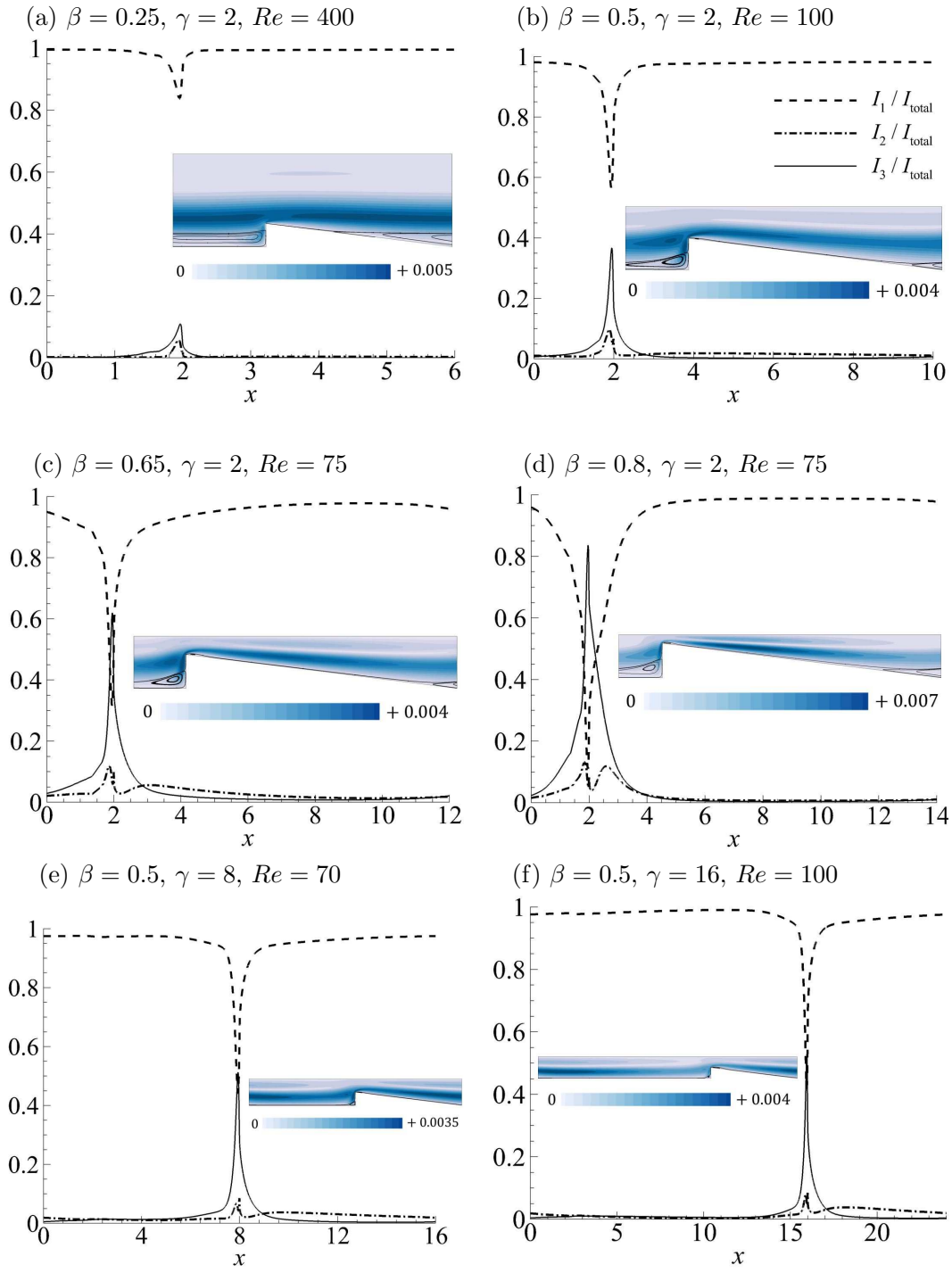

Figure 3.17: Variation of I_1/I_{total} (dashed line), I_2/I_{total} (dash-dotted line) and I_3/I_{total} (thin solid line) with streamwise coordinate x. Contours of absolute velocity ($|\hat{\boldsymbol{u}}|$) of the leading mode in the flow domain are also shown. The wedge angle for all cases here is $\tan(\phi) = 0.125$.

γ as it did with β variation, indicating that the instability mechanism is not influenced by changes in γ.

3.3 Energetics of the 3D instability modes

This section utilizes the energy analysis described in § 2.3 to investigate the factors that contribute to perturbation growth. Local changes in the base flow and their contribution to the growth rate of leading eigenmodes are discussed. Contribution of the production terms and the disipation term in equation (2.40) to the growth rate of the leading eigenmode for all the investigated cases are shown in table 3.3. The largest contribution (corresponding to the largest positive value) to the growth rate, and thus the instability, comes from the production term $\langle \mathscr{P}_2 \rangle = (1/2E_k) \int_\Omega \overline{u'v'} \partial U/\partial y \, \mathrm{d}\Omega$ for all cases investigated, whereas the most stabilising contribution (corresponding to the negative value having largest magnitude) comes from the dissipation term $\langle \mathscr{D} \rangle$. At $\gamma = 2$, the production term $\langle \mathscr{P}_1 \rangle$ has a net stabilising contribution for lower blockage ratios $\beta = 0.125$, 0.25 and the highest blockage ratio investigated here $\beta = 0.8$, whereas for intermediate blockage ratios $0.5 \lesssim \beta \lesssim 0.65$, its net contribution is positive, though an order of magnitude lower than the dominant production term $\langle \mathscr{P}_2 \rangle$. Terms $\langle \mathscr{P}_3 \rangle$ and $\langle \mathscr{P}_4 \rangle$ have net positive and negative contributions respectively, for all cases investigated, though they are typically more than an order of magnitude smaller than the dominant production term $\langle \mathscr{P}_2 \rangle$. The dominance of production term $\langle \mathscr{P}_2 \rangle$ for all the cases investigated shows that the mode gains energy predominantly through horizontal shear in the baseflow. The streamwise velocity dominance of the perturbations in the flow domain as shown in § 3.2.3, along with the fact that $\langle \mathscr{P}_2 \rangle$ is the largest contributor to σ, is compatable with the lift-up mechanism being responsible for the instability in the range of geometric parameters investigated. The transport terms $\langle \mathscr{T}_1 \rangle$ and $\langle \mathscr{T}_2 \rangle$ describe the transport of perturbation kinetic energy by the base flow within the domain. Owing to the wall confinement and streamwise periodicity of the flow domain, their sum is approximately zero, thus having no contribution to the growth rate of the eigenmode.

Spatial contours of the terms of equation (2.40) which are the integrands of equation (2.37) are shown in figures 3.18 and 3.19 for selected cases. These plots for various other β and γ combinations are visually similar to those already shown in figures 3.18(a) and 3.19(a). The regions in the flow domain where the respective streamwise and transverse velocities of the eigenmode grow due to strong streamwise and transverse velocity gradients in the base flow are shown

in the contours of $\overline{\mathscr{P}_1}$ and $\overline{\mathscr{P}_4}$. The streamwise velocity of the eigenmode grows predominantly in the region aft of the wedge tip (above the second recirculation region for $\beta \gtrsim 0.5$) and before the wedge. With increasing blockage ratio, the gain in the latter region is higher due to increasing streamwise velocity gradient in the baseflow, as seen from the contours of $\overline{\mathscr{P}_1}$. The transverse velocity growth magnitude is highest inside the recirculation region formed before the wedge, where $\overline{\mathscr{P}_4}$ is stabilising (negative contour levels in figures 3.18(a) and 3.19(a) for $\overline{\mathscr{P}_4}$). For higher β, due to the steeper transverse gradient in the constriction region above and after the wedge tip, a larger magnitude in $\hat{v}$ is observed in a similar region to where $\overline{\mathscr{P}_4}$ has a positive contribution to the growth rate (positive contour levels in figures 3.18(a) and 3.19(a) for $\overline{\mathscr{P}_4}$). The location in the flow domain having the largest contribution to the perturbation growth rate due to strong horizontal and vertical shear in the base flow are shown in the contour plots for $\overline{\mathscr{P}_2}$ and $\overline{\mathscr{P}_3}$, respectively. The dissipation $\overline{\mathscr{D}}$ is observed to be strongest about the wedge. This is expected due to the relatively large shear stresses in this vicinity. The bottom row for each case shows the combined contributions of the terms shown ($\overline{\sum}$) to the growth of the leading eigenmode, superimposed with line contours of $\hat{w}$. The region of maximum growth in $\hat{w}$ is where the the net contribution $\overline{\sum}$ has a highly stabilising contribution to the growth rate of the eigenmode, whereas the region dominated by the streamwise velocity contribution is where $\overline{\sum}$ has the highest positive contribution to the growth rate. This confirms the statement made in § 3.2.3, whereby Taylor–Görtler type instability is not responsible for the formation of streamwise counter-rotating vortices in these flows.

3.4 Adjoint modes, sensitivity and endogeneity analysis

In the previous sections, the global mode responsible for the bifurcation from the two-dimensional flow was discussed. It was also found that the primary bifurcation of the flow is three-dimensional and the associated global mode and instability mechanisms were elucidated. In this section, the adjoint eigenmodes and their structural senstivity for different geometric parameters both for the two-dimensional and three-dimensional perturbations are presented, shedding further light on the dynamics of the flow. This analysis is also useful from a flow control perspective. An endogeneity analysis is also considered to shed light on the local contributions to the growth of the destabilising three-dimensional eigenmode

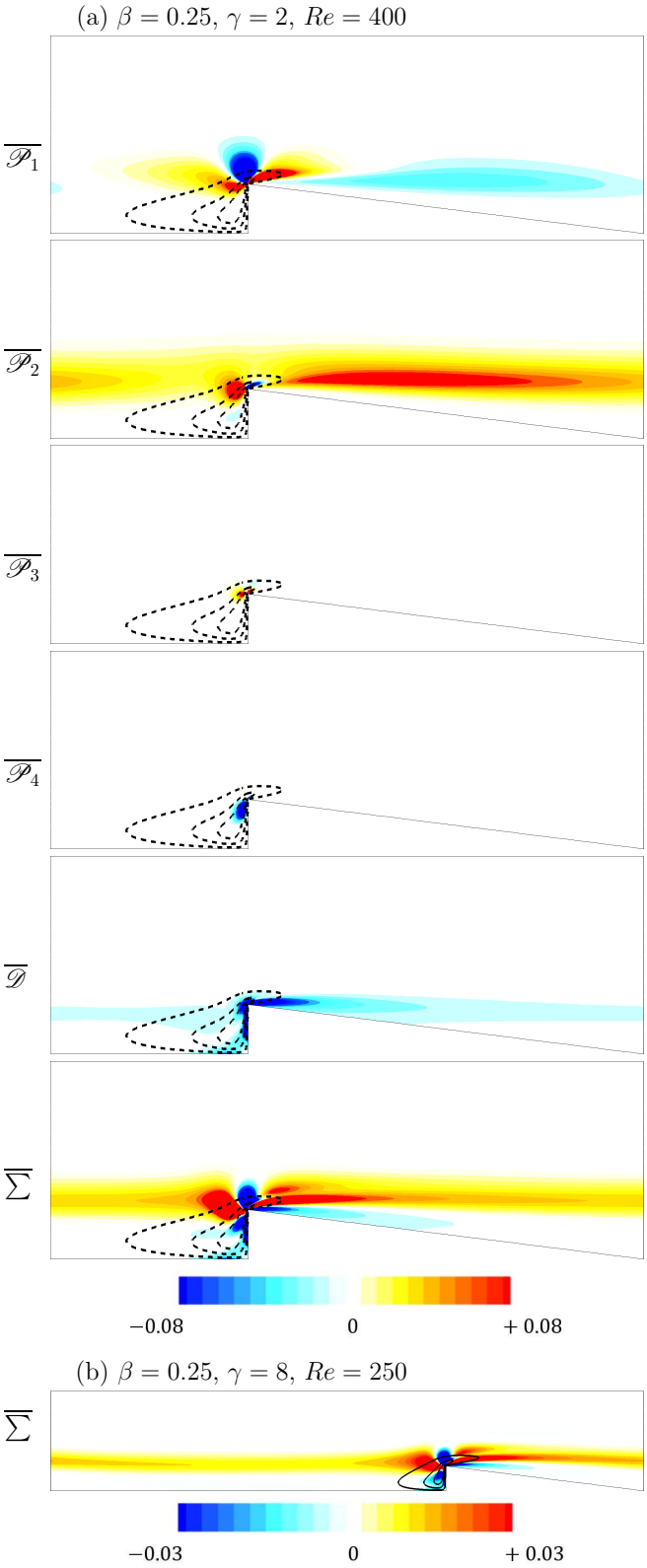

Figure 3.18: (a) Contours of terms from the spanwise averaged perturbation kinetic energy evolution equation (2.38) and their corresponding sum for the leading eigenmode overlaid with line contours of $\hat{w}$. (b) The contours of sum of terms in equation (2.38) shown at a larger γ. Wedge angle for these cases $\tan(\phi) = 0.125$. Positive (negative) contour levels indicate destabilising (stabilising) effect on the base flow.

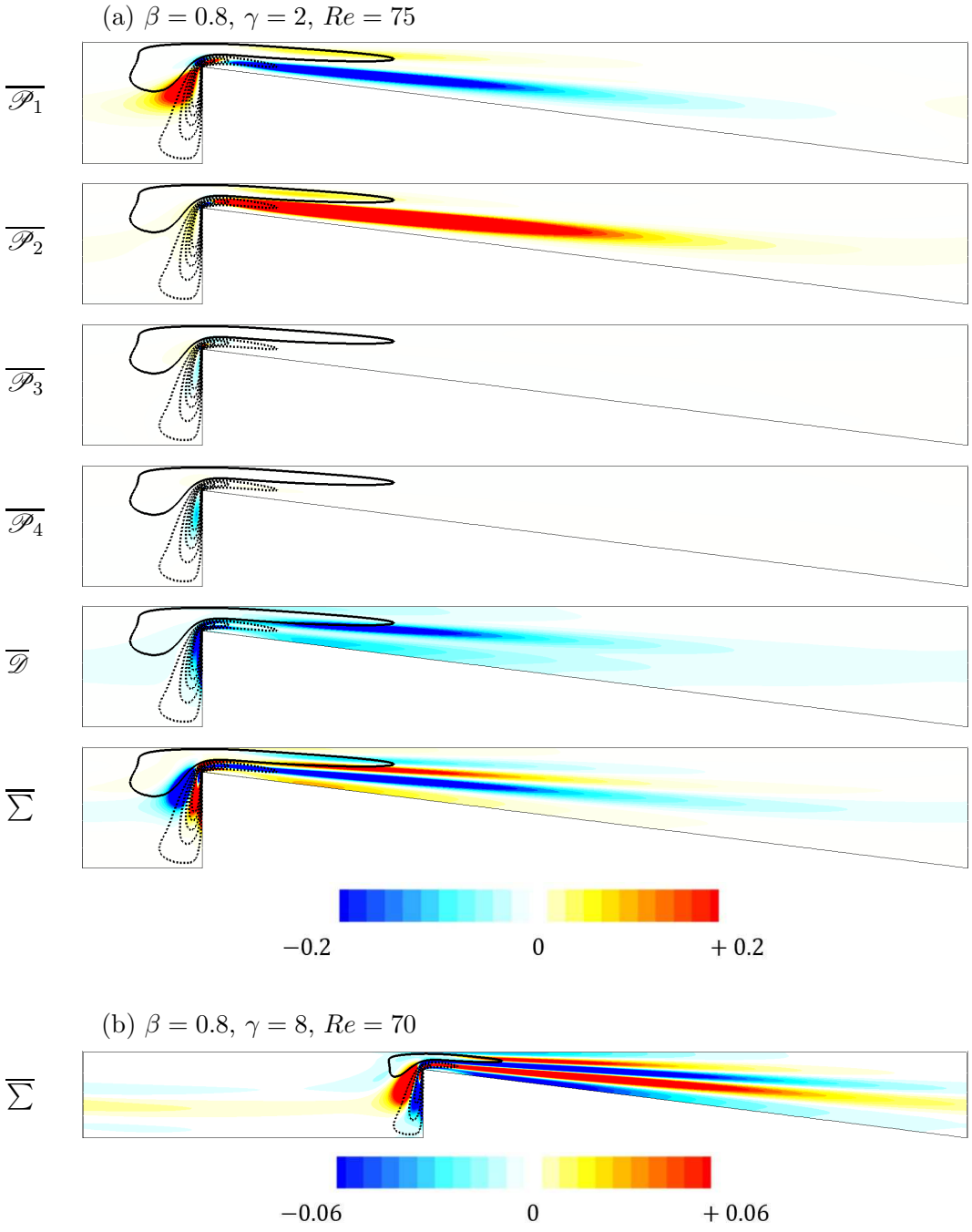

Figure 3.19: (a) Contours of terms from the spanwise averaged perturbation kinetic energy evolution equation (2.38) and their corresponding sum for the leading eigenmode overlaid with line contours of $\hat{w}$. (b) The contours of sum of terms in equation (2.38) shown at a larger γ. Wedge angle for these cases $\tan(\phi) = 0.125$. Positive (negative) contour levels indicate destabilising (stabilising) effect on the base flow.

$(\beta,\ \gamma,\ Re)$	$\langle\mathscr{P}_1\rangle$	$\langle\mathscr{P}_2\rangle$	$\langle\mathscr{P}_3\rangle$	$\langle\mathscr{P}_4\rangle$	$\langle\mathscr{D}\rangle$
(0.125, 2, 500)	-0.001295 (-2.33%)	**0.100159** (**180.10**%)	0.000712 (1.28%)	-0.000218 (-0.39%)	**-0.043747** (**-78.66**%)
(0.25, 2, 400)	-0.001638 (-1.80%)	**0.144841** (**159.52**%)	0.002134 (2.35%)	-0.002166 (-2.38%)	**-0.052374** (**-57.68**%)
(0.5, 2, 100)	0.021612 (23.08%)	**0.299900** (**320.31**%)	0.011426 (12.20%)	-0.012951 (-13.83%)	**-0.226354** (**-241.76**%)
(0.65, 2, 75)	0.011952 (12.75%)	**0.472378** (**503.79**%)	0.013503 (14.4%)	-0.016230 (-17.31%)	-0.387833 (**-413.63**%)
(0.8, 2, 75)	-0.129045 (-103.79%)	**0.870714** (**700.31**%)	0.006960 (5.6%)	-0.006641 (-5.34%)	**-0.617654** (**-496.78**%)
$(\gamma,\ \beta,\ Re)$					
(1, 0.25, 400)	-0.001087 (-1.18%)	**0.148284** (**161.04**%)	0.002294 (2.49%)	-0.002217 (-2.41%)	**-0.055197** (**-59.95**%)
(4, 0.25, 250)	-0.003434 (-4.92%)	**0.139211** (**199.43**%)	0.001973 (2.83%)	-0.001423 (-2.04%)	**-0.066520** (**-95.29**%)
(8, 0.25, 250)	-0.005087 (-10.91%)	**0.113144** (**242.69**%)	0.001351 (2.89%)	-0.001006 (-2.16%)	**-0.061782** (**-132.52**%)
(16, 0.25, 200)	-0.004909 (-48.24%)	**0.079200** (**778.18**%)	0.000755 (7.41%)	-0.000439 (-4.32%)	**-0.064428** (**-633.03**%)
(1, 0.8, 70)	-0.086481 (-84.11%)	**0.862769** (**839.07**%)	0.009527 (9.27%)	-0.011245 (-10.93%)	**-0.671733** (**-653.29**%)
(4, 0.8, 70)	-0.138681 (-199.02%)	**0.811758** (**1164.95**%)	0.007523 (10.79%)	-0.002556 (-3.67%)	**-0.608351** (**-873.04**%)
(8, 0.8, 70)	-0.118398 (-400.29%)	**0.604534** (**2043.85**%)	0.004802 (16.26%)	-0.002238 (-7.57%)	**-0.459115** (**-1552.21**%)

Table 3.3: Contribution of volume integrated values of production terms and dissipation term in equation (2.41) and their percentage relative contribution to the growth rate σ (enclosed in brackets) of the leading eigenmode for different β and γ at Re as indicated. The wedge angle is $\tan(\phi) = 0.125$ in all cases. The largest destabilising (positive terms) and stabilising (negative terms) contributions are shown in bold.

and comparisons are made with the growth rate contributions obtained from the pertubration kinetic energy analysis.

The power of adjoint analysis for flow control and sensitivity study was established for cylinder wakes by Giannetti & Luchini (2007). Similar analysis for FFS (Marino & Luchini, 2009) and smoothed BFS setups (Marquet *et al.*, 2009) have revealed regions for placement of active and passive flow control mechanisms. The region of largest magnitude of the adjoint modes is where the flow is most receptive to initial conditions or momentum forcing which an active flow control device could exploit to produce an optimal response in terms of amplification of the instability (Hill, 1995; Giannetti & Luchini, 2007; Akervik *et al.*, 2007). Hill (1995) and later Giannetti & Luchini (2007) have also shown that the overlap region of the largest global mode and adjoint mode velocity magnitude is most sensitive to any localised feedback as it has the most impact on the eigenvalue of the linearised operator. Physically, this could be by introduction of a passive structure in the flow (Strykowski & Sreenivasan, 1990). The sensitivity field hence shows the wavemaker region or the location of the origin of the instability (Chomaz, 2005).

3.4.1 Analysis of two-dimensional perturbations

The adjoint modes and the structural sensitivity of two-dimensional disturbances are presented in this section at $Re > Re_{cr,2\mathrm{D}}$. The 2D adjoint mode has a slanted structure against the base flow velocity gradient and is concentrated along the tapered wedge surface extending from the wedge tip to the separation point (x_{s3}) of the base flow, further downstream. With increasing blockage ratio the influence of the top wall increases, resulting in formation of additional receptive regions near the top wall along with the ones on the bottom wall. Increasing the pitch does not seem to significanly alter the adjoint mode (receptive locations in the flow). These are shown for different cases in the left column of figure 3.20. The most sensitive regions in the flow domain to 2D disturbances are seen as multiple patches spread along the tapered wedge surface in addition to the ones concentrated near the wedge tip. The top wall influence is also observed on the sensitivity field with increasing β. Similar to the receptive regions, increasing the pitch does not significanly alter the sensitive locations of the two-dimensional perturbations. The sensitive regions are concentrated near the wedge tip at all values of pitch at $\beta = 0.25$. The sensitivity field of two-dimensional perturbations are shown in the right column of figure 3.20.

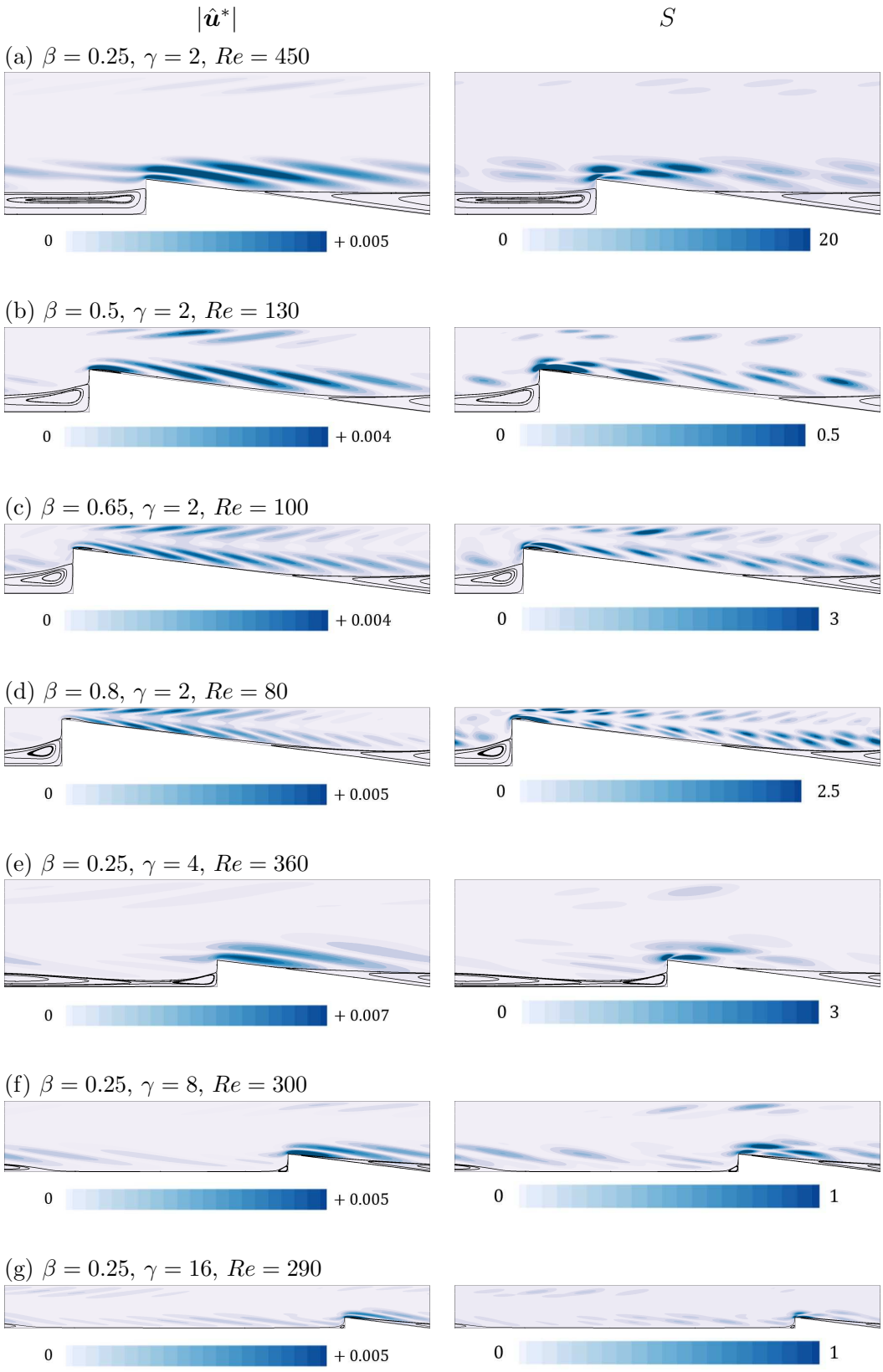

Figure 3.20: Receptivity to initial condition/momentum forcing (left column) and structural sensitivity (right column) of the unstable 2D eigenmodes overlaid with base flow streamlines.

3.4.2 Analysis of three-dimensional perturbations

An analysis of the receptivity and sensitivity of the flow to three-dimensional perturbations is carried out for a $Re > Re_{cr,3D}$ covering a range of blockage ratios and pitch values. The regions in the flow most receptive to momentum forcing is shown in the left column of figure 3.21. For $\gamma = 2$, the receptive region spans the incline of the wedge until the separation point and stretches further downstream with increasing β. For larger γ, additional receptive regions form in the gap between wedges (figure 3.21e,f left column), similar to what is observed in a FFS setup (Marino & Luchini, 2009; Lanzerstorfer & Kuhlmann, 2012*b*). The sensitive location given by the overlap region of the adjoint and direct mode's magnitude is shown for different β and γ in the right column of figure 3.21. The wavemaker is located in the region of strong base flow shear extending downstream of the wedge tip. At $\gamma = 2$ and with increasing blockage ratio ($\beta \geq 0.5$), a recirculation region forms immediately after the wedge tip causing a shift in the most sensitive region away from the wedge tip, to between the two recirculation regions on the tapered wedge surface. With increasing pitch, the sensitive locations appear to extend further downstream from the wedge tip to the gap between the wedges (figure 3.21e-i, right column). These sensitive regions strongly resemble the contours of $\overline{\mathscr{P}_2}$ in figures 3.18 and 3.19. These are regions in the flow that are expected to be important for the placement of a passive flow control mechanism in the flow (Giannetti & Luchini, 2007; Strykowski & Sreenivasan, 1990; Marquet *et al.*, 2009; Akervik *et al.*, 2007).

3.4.3 Endogeneity analysis of the three-dimensional global mode

In this section, the endogeneity distribution fields and the real parts of the individual contributions in equation (2.63) are examined to understand the local contributions to the growth rate of the destabilising eigenmode and to compare the integral values contributing to the growth rate found from the perturbation kinetic energy analysis in § 3.3.

The endogeneity analysis reveals that largest positive contribution to the growth rate of the global mode comes from the production due to base flow shear, whereas the largest negative contribution is from viscous dissipation of perturbation velocity; these findings are both consistent with the energetics analysis reported in § 3.3. However, a distinction from the PKE analysis is that there is also a destabilising contribution from convection of the perturbation by base

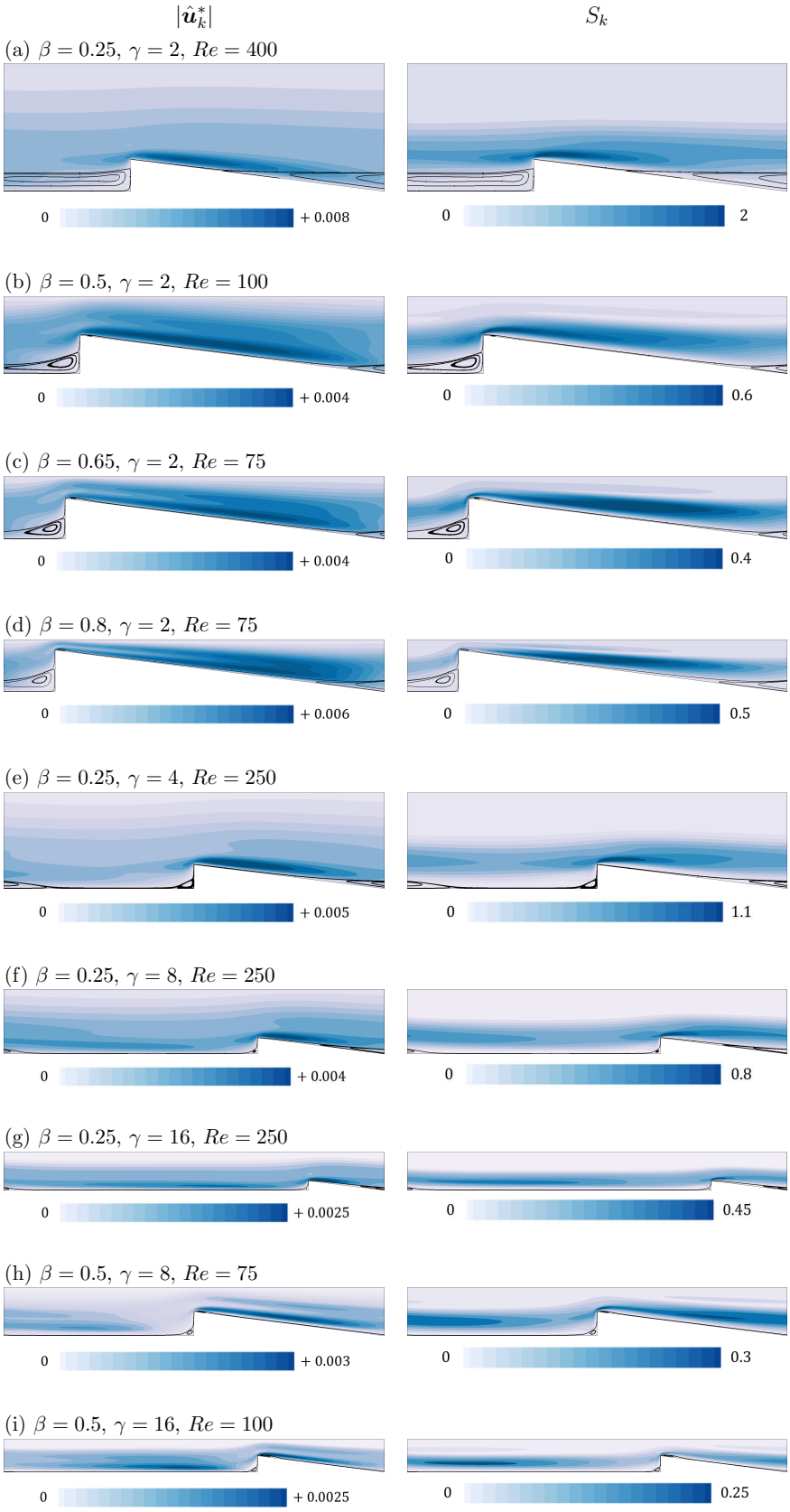

Figure 3.21: Receptivity to initial condition/momentum forcing (left column) and structural sensitivity (right column) of the unstable 3D eigenmodes overlaid with base flow streamlines.

flow velocity and the pressure forces. The convection contribution is modest, being almost an order of magnitude smaller than the production contribution. The pressure contribution should intrinsically integrate to zero (Marquet & Lesshafft, 2015), so its small finite values (being four to five orders of magnitude smaller than the production contributions) can be interpreted as an indication of the error level in the endogeneity calculations. These values are compared in table 3.4. When comparing the endogeneity analysis results to those of the energetics analysis, a point to note is that the energetics contributions are obtained from the eigenvector field of the linear instability eigenmode, whereas the endogeneity contributions emerge from the combination of the leading eigenmode and its adjoint.

The total endogeneity field shown in figure 3.22(e) shows a local stabilising contribution (negative values) around the wedge tip and a destabilising contribution (positive values) to the growth rate of the global mode in regions covering approximately half the constriction height. Similar observation was also made for blockage ratios up to $\beta = 0.8$ all with $\gamma = 2$ and $\beta = 0.5$, $\gamma = 8$, although the destabilising region occupied more of the constriction gap with increasing blockage ratio. The individual component contributions in figure 3.22(a-d) shown for $\beta = 0.25$, $\gamma = 2$ with $\tan(\phi) = 0.125$, reveal that the local contribution from the perturbation pressure gradient term swamps the total endogeneity, as E_σ closely resembles $E_{\sigma,\mathrm{pres}}$ for this case, and does not exhibit similarity to the wavemaker region obtained from the sensitivity analysis (figure 3.21b). This contrasts the case of 2D instability of the circular cylinder wake, in which the local endogeneity distribution exhibited qualitative similarity to the wavemaker region found from the sensitivity studies (Marquet & Lesshafft, 2015; Paladini *et al.*, 2019). However, the region contributing most strongly to the growth rate predicted from the spanwise averaged distribution of all contributions from the PKE analysis (figures 3.18 and 3.19) resembles more closely to the sum of contributions from $E_{\sigma,\mathrm{conv}}$, $E_{\sigma,\mathrm{prod}}$ and $E_{\sigma,\mathrm{diss}}$ as shown in figure 3.22(f). In contrast, the endogeneity for a longer pitch case of $\gamma = 16$ at $\beta = 0.5$ (figure 3.23e) showed a different distribution than the previous case, with a weaker distribution of the pressure contribution, which also shows a different distribution than in the aforementioned case. In this case, the endogeneity distribution matches with the wavemaker region predicted from an exogeneous approach (figure 3.21f) with a stronger distribution around the wedge tip for the endogeneity field. The fields showing the individual contributions for this case is shown in figure 3.23(a-d) and sum of contributions from $E_{\sigma,\mathrm{conv}}$, $E_{\sigma,\mathrm{prod}}$ and $E_{\sigma,\mathrm{diss}}$ in figure 3.23(e). The sudden constriction due to the

$\beta = 0.25$, $\gamma = 2$, $Re = 400$

Endogeneity	$E_{\sigma,\mathrm{conv}}$	$E_{\sigma,\mathrm{prod}}$	$E_{\sigma,\mathrm{pres}}$	$E_{\sigma,\mathrm{diss}}$	E_σ
	0.01253	0.12245	0.00003	-0.04421	0.09080
PKE		$\langle \mathscr{P} \rangle$		$\langle \mathscr{D} \rangle$	$\langle \sum \rangle$
		0.14317		-0.05237	0.09080

$\beta = 0.5$, $\gamma = 2$, $Re = 100$

Endogeneity	$E_{\sigma,\mathrm{conv}}$	$E_{\sigma,\mathrm{prod}}$	$E_{\sigma,\mathrm{pres}}$	$E_{\sigma,\mathrm{diss}}$	E_σ
	0.02824	0.22494	0.00012	-0.15967	0.09363
PKE		$\langle \mathscr{P} \rangle$		$\langle \mathscr{D} \rangle$	$\langle \sum \rangle$
		0.32008		-0.22635	0.09373

$\beta = 0.8$, $\gamma = 2$, $Re = 75$

Endogeneity	$E_{\sigma,\mathrm{conv}}$	$E_{\sigma,\mathrm{prod}}$	$E_{\sigma,\mathrm{pres}}$	$E_{\sigma,\mathrm{diss}}$	E_σ
	0.06163	0.46487	0.00063	-0.40230	0.12482
PKE		$\langle \mathscr{P} \rangle$		$\langle \mathscr{D} \rangle$	$\langle \sum \rangle$
		0.74199		-0.61765	0.12433

$\beta = 0.5$, $\gamma = 16$, $Re = 100$

Endogeneity	$E_{\sigma,\mathrm{conv}}$	$E_{\sigma,\mathrm{prod}}$	$E_{\sigma,\mathrm{pres}}$	$E_{\sigma,\mathrm{diss}}$	E_σ
	0.01424	0.12210	0.00000	-0.12036	0.01599
PKE		$\langle \mathscr{P} \rangle$		$\langle \mathscr{D} \rangle$	$\langle \sum \rangle$
		0.16041		-0.14440	0.01601

Table 3.4: Comparison of the contribution of volume integrated quantities of each term in equation (2.41) and the domain integral of the real part of individual terms in equation (2.63) to the growth rate σ of the leading eigenmode for different β and γ at Re as indicated. The wedge angle is $\tan(\phi) = 0.125$ in all cases. Positive (negative) terms have a destabilising (stabilising) contribution.

presence of the wedge might be one possible reason for the local pressure gradient to contribute significanly to the growth rate for all blockage ratios with a low pitch of $\gamma = 2$ investigated in this study. The impact of the subsequent wedge relaxes further with increasing γ, which may explain why the pressure term has a lesser influence on the endogeneity in the case of $\gamma = 16$, $\beta = 0.5$.

3.5 Linear transient growth

Thus far, the treatment of the stability of the flow has been confined to the asymptotic behaviour towards long times. Consideration is now given to the short time dynamics of the system. This is important because large transient

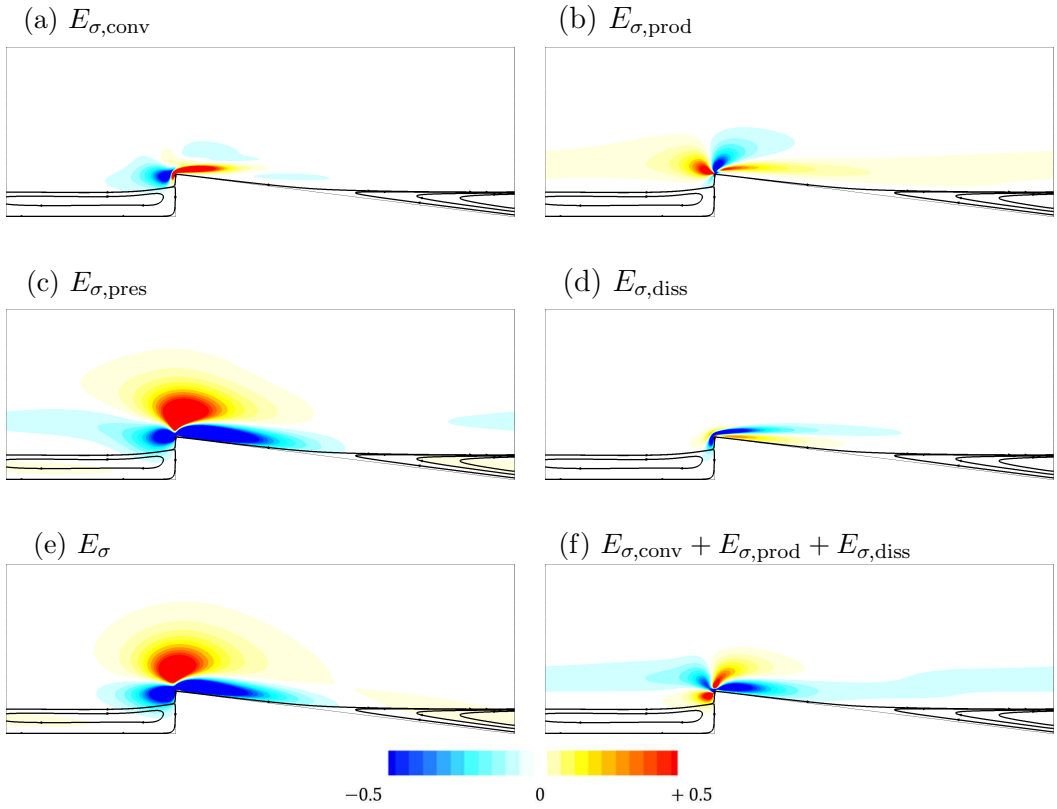

Figure 3.22: (a-d) Contribution of the real part of the individual endogeneity terms in equation (2.63) to the (e) endogeneity distribution and (f) sum of the convection, production and the dissipation contribution for $\beta = 0.25$, $\gamma = 2$ and $\tan(\phi) = 0.125$ at $Re = 400$. Note that $E = E_\sigma$ as the global mode has a real eigenvalue. Contours are shown in the linear scale at 20 equispaced levels.

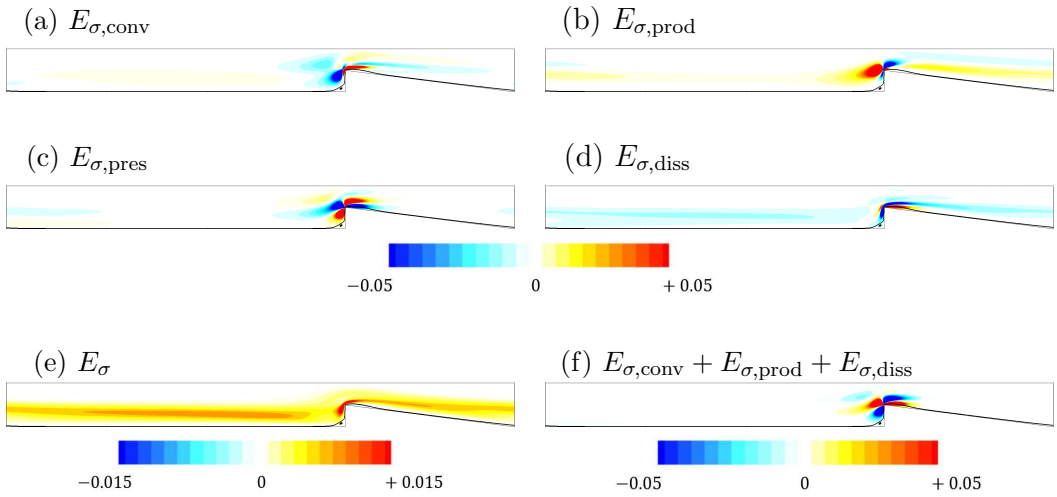

Figure 3.23: (a-d) Contribution of the real part of the individual endogeneity terms in equation (2.63) to the (e) endogeneity distribution and (f) sum of the convection, production and the dissipation contribution for $\beta = 0.5$, $\gamma = 16$ and $\tan(\phi) = 0.125$ at $Re = 100$. Note that $E = E_\sigma$ as the global mode has a real eigenvalue. Contours are shown in the linear scale at 20 equispaced levels.

amplification of disturbances over short time scales can occur in flows due to non-modal interactions between asymptotically decaying linear eigenmodes, possibility triggering a bypass transition. In similar channel flow setups such as BFS (Blackburn *et al.*, 2008*b*), rounded BFS (Marquet *et al.*, 2008) and stenotic flows (Blackburn *et al.*, 2008*b*; Griffith *et al.*, 2008), a large transient growth associated with convective instabilities have been found in the linearly stable region with amplifications exceeding 10^5 and 10^8 in some cases (Blackburn *et al.*, 2008*b*,*a*). Therefore, in this section the transient behaviour of the flow to both two-dimensional and three-dimensional perturbations are studied and the optimal mode associated with maximum energy amplification are discussed. Furthermore, the influence of varying the geometric parameters of the wedge on the transient energy amplification of the optimal disturbance are explained.

3.5.1 Optimal growth of two-dimensional disturbances

The two-dimensional optimal disturbances in the linearly stable two-dimensional regimes from § 3.2.1 are presented here for various combinations of β and γ over a range Reynolds numbers. In figures 3.24 and 3.25, optimal energy gain for a range of Re are shown as a function of time τ for different $\beta = 0.25$ and γ cases.

From the line plots and contours of $G(\tau)$, it can been seen that after a threshold Re, the optimal mode achieves a gain exceeding unity, reaching a maximum value G_{max} corresponding to an optimal time τ_{opt}, both of which increase with increasing Re. Eventually, the energy in the disturbance structure monotonically decrease with increasing time horizon for all Re in the range investigated which is in agreement with the observation from the linear stability analysis of 2D perturbations, where the two-dimensional perturbations are asymptotically stable. At a lower blockage ratio and pitch of $\beta = 0.25, \gamma = 2$, for $Re \gtrsim 400$, a second peak with lower gain than the first peak is observed, which is due to the interaction of the disturbance structure with the subsequent wedge and the free shear layers near the vertical wall of wedge. In the contour plot in figures 3.24(b,d,f) and 3.25(b,d), $\log_{10}G(\tau)$ is plotted on the $Re - \tau$ plane. The point on the Re axis where $\log_{10}G(\tau) = 0$ gives a Reynolds number Re_E below which all perturbations decay without any transient growth. At this Reynolds number, $G(\tau) \leq 1$ for all τ. Typically, this corresponds to the Reynolds number where $\mathrm{d}G/\mathrm{d}\tau = 0$ at $\tau = 0$, which becomes another way of determining Re_E. For the cases shown in figures 3.24 and 3.25, Re_E, $Re_{cr,\mathrm{2D}}$ and $Re_{cr,\mathrm{3D}}$ values are shown in table 3.5. The difference between Re_E and the critical Reynolds numbers indicates the subcritical range where transient amplification may excite disturbances to an absolute

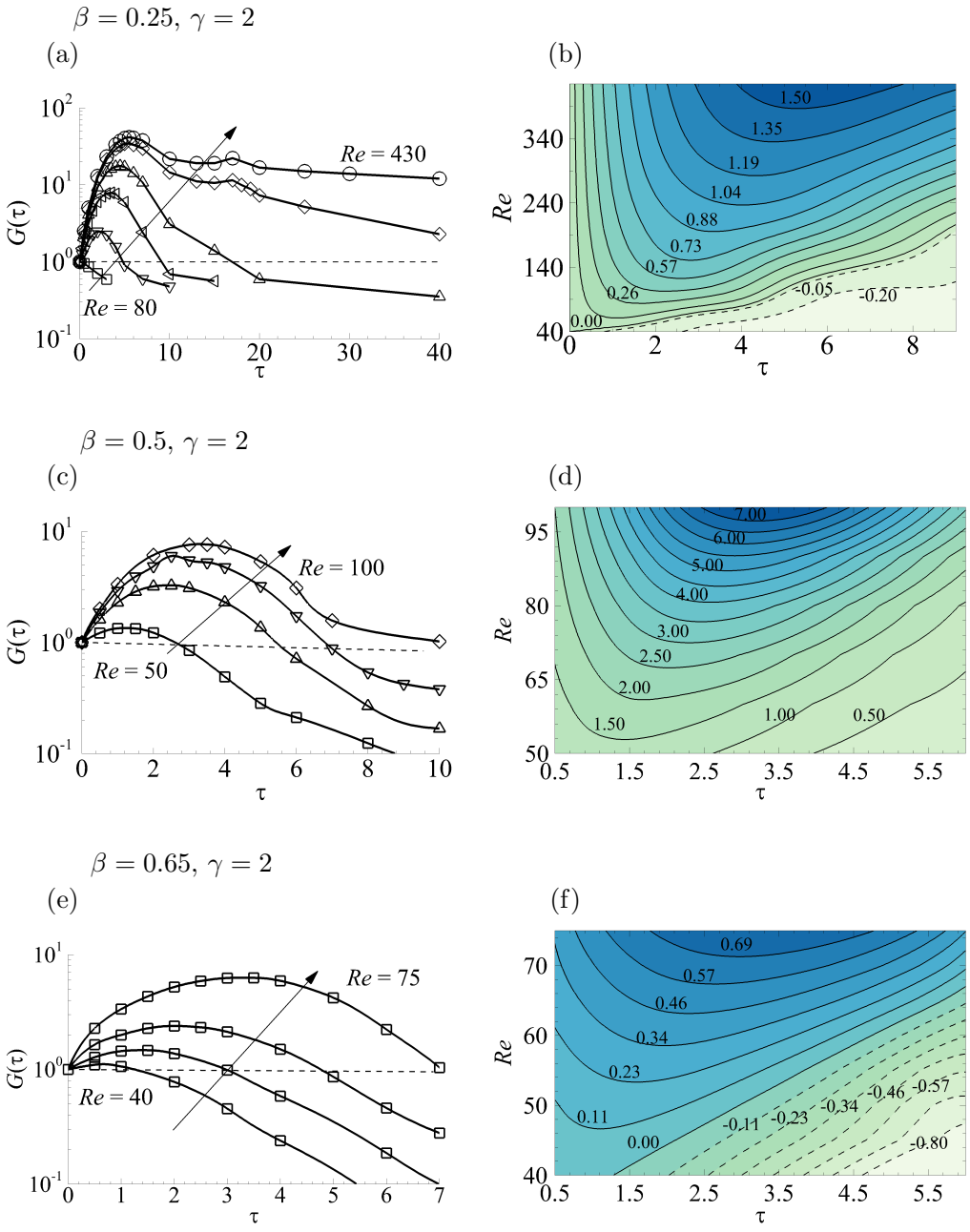

Figure 3.24: (a,c,e) Two dimensional optimal growth $G(\tau)$ curves for different Re at parameter combintions as shown. The dashed horizontal line represents the neutral line, and (b,d,f) contours of $\log_{10} G(\tau)$ (positive to negative shown as blue to green) plotted on $Re - \tau$ plane for different blockage ratios. Arrow indicates the direction of increasing Re with the first and the last Re as indicated. Wedge angle for all the cases here is $\tan(\phi) = 0.125$.

state depending on the disturbance shape and amplitude.

The 2D optimal modes (shown in panels corresponding to $t = 0$ in figures 3.26–3.28) are composed of narrow inclined structures of alternate sign, opposing the mean flow direction that are concentrated before the first separation point

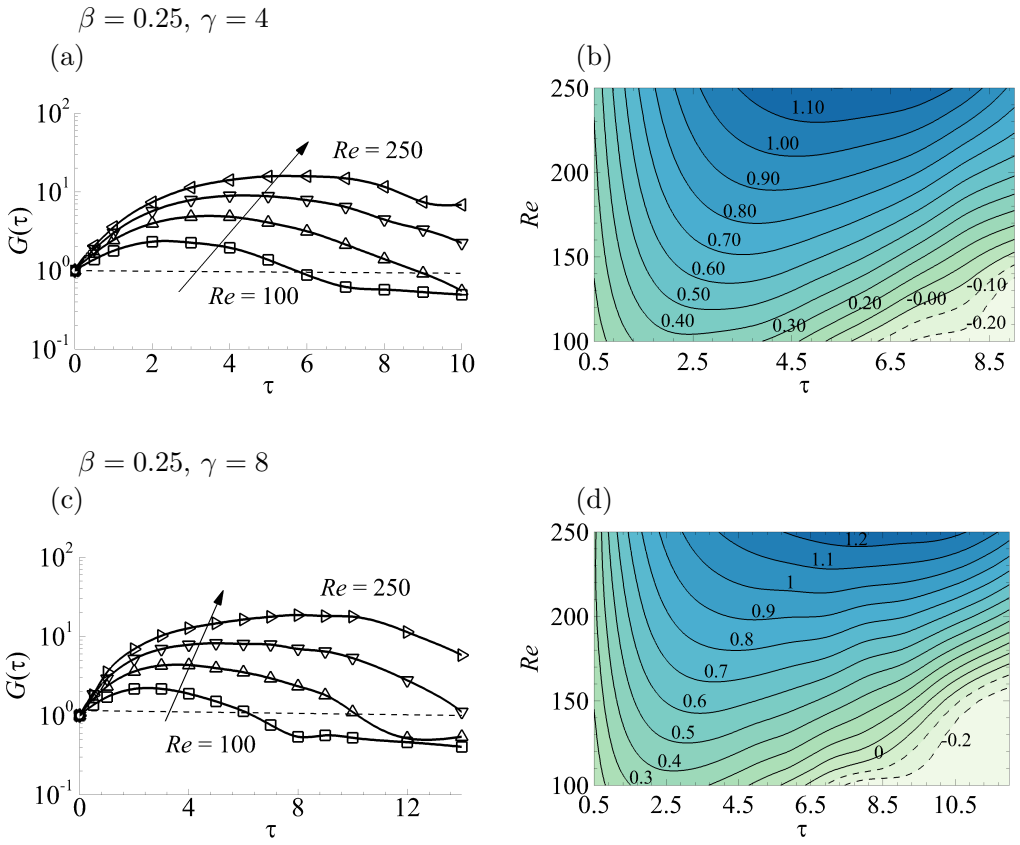

Figure 3.25: (a,c) Two dimensional optimal growth $G(\tau)$ curves for different Re at parameter combinations as shown. The dashed horizontal line represent the neutral line, and (b,d) contours of $\log_{10} G(\tau)$ (positive to negative shown as blue to green) plotted on $Re - \tau$ plane for two different pitch values. Arrow indicates the direction of increasing Re with the first and the last Re as indicated. Wedge angle for all the cases here is $\tan(\phi) = 0.125$.

β, γ	Re_E	$Re_{cr,2D}$	$Re_{cr,3D}$
0.25, 2	42.09	445.93	86.85
0.50, 2	31.88	126.92	58.59
0.65, 2	28.80	89.56	55.15
0.25, 4	33.13	340.83	100.50
0.25, 8	24.85	285.07	127.41

Table 3.5: Critical values of Reynolds number found from linear transient growth analysis and linear stability analysis. Wedge angle for the cases here is $\tan(\phi) = 0.125$.

of the base flow after the wedge tip (x_{s3} in figure 3.5a). The linear evolution of the optimal mode is elucidated for selected β and γ combinations in figures 3.26–3.28. It is observed that over time, the disturbance structures are advected downstream by the base flow, and the slanted structures are slowly rotated to

an upright orientation by the background shear, suggesting the energy gain in the disturbance structure is via the two-dimensional Orr mechanism (Orr, 1907). On interaction with the subsequent wedge, the disturbance structure also gains energy from the free shear layers about the wedge tip. This can be observed from the increased density of line contours of perturbation kinetic energy carried by the disturbances as it impinges on the subsequent wedge (panels corresponding to τ_{opt}). A similar observation can be made from the energy contours corresponding to the subsequent peaks observed in $\beta = 0.25$, $\gamma = 2$ labelled as $T2$ and $T3$ and $T4$ in figure 3.29(a), suggesting a contribution to the energy growth of the disturbance on impingement on the wedge wall. The lower energy gain in the subsequent peaks indicate that the optimal mode gains energy predominantly through its tilting in the base flow direction (the Orr mechanism), as this feature is only present through the primary $K(t)/K(0)$ maximum. A significant decay in the energy of the disturbance structure after the optimal time τ_{opt} at a higher blockage ratio of $\beta = 0.5$ ($\gamma = 2$) and larger pitch of $\gamma = 8$ ($\beta = 0.25$), relative to the lower blockage ratio and shorter pitch case of $\beta = 0.25$, $\gamma = 2$ can also be noted from the corresponding contours for these cases.

In figure 3.29, the influence of γ and β on the energy of the disturbance on linear evolution starting from the optimal mode is shown at selected Reynolds numbers. A decrease in the peak energy growth of the optimal disturbance with increase in pitch at $\beta = 0.25$ is observed from figure 3.29(a). At $\beta = 0.25$ and larger pitch $\gamma \gtrsim 5$, the base flow reattaches to the channel bottom wall well before the subsequent wedge (base flow streamlines shown in figure 3.28) unlike at $\gamma \lesssim 2$ where the recirculation region extends the entire gap between wedges (base flow streamlines shown in figure 3.26). The energy gain from the larger extent of free shear layer near the wedge wall at lower γ could possibly be the reason for a higher optimal energy gain in those cases. The energy in successive peaks is also observed to be lower at higher γ (figure 3.29a) since the disturbances decay much more in the gap before reaching the subsequent wedge as illustrated in figure 3.28. At a low pitch of $\gamma = 2$, increasing the blockage ratio also results in a lower optimal growth (shown for $\beta = 0.5$ in figure 3.29b). This could be due to the channel wall interactions at large blockage ratios which limit the tilting of the optimal disturbances, and hence its energy gain (panels until τ_{opt} in figure 3.27).

From the variation of G_{max} and τ_{opt} with Re obtained for various combinations of β and γ, the corresponding values for Reynolds numbers at $\varepsilon_{2\mathrm{D}} = Re/Re_{cr,2D} = 0.85$ and 0.95 were interpolated. These values are shown in figure 3.30. In the

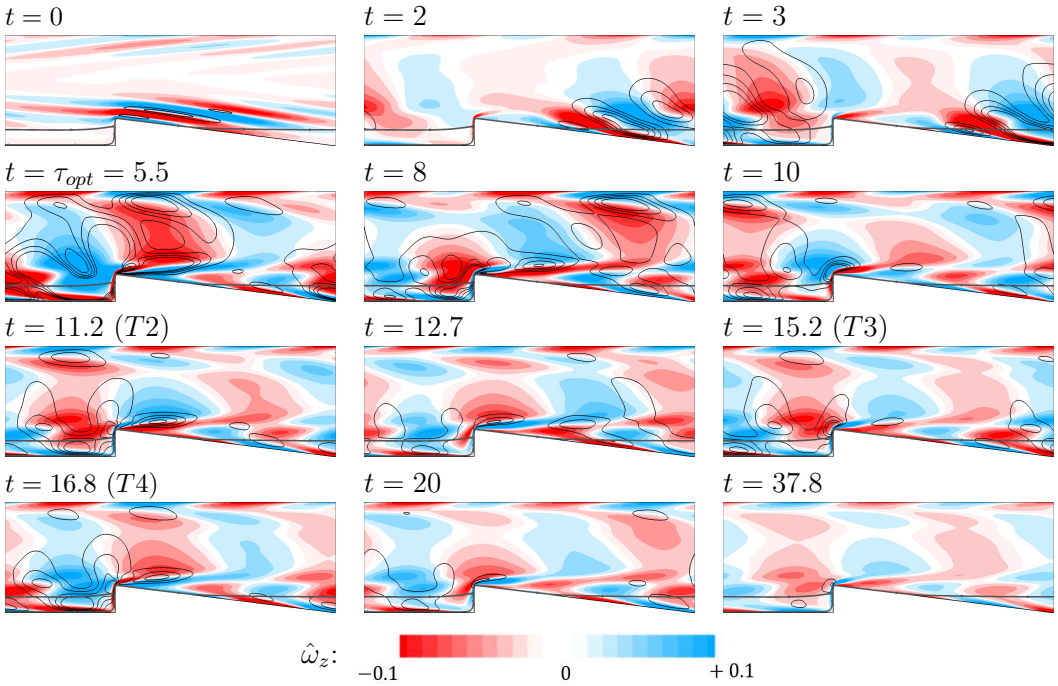

Figure 3.26: Snapshots of the evolution of the spanwise perturbation vorticity ($\hat{\omega}_z$) flooded contours overlaid by perturbation kinetic energy contour lines for $\beta = 0.25$, $\gamma = 2$ at $Re = 400$. The initial condition at $t = 0$ corresponds to the optimal mode, and the subsequent time instants of each frame correspond to the square marker position for this case shown in figure 3.29(a). The dividing streamline of the base flow is also shown. Energy iso-contours are shown at 5 equispaced levels between 0 and 0.0006.

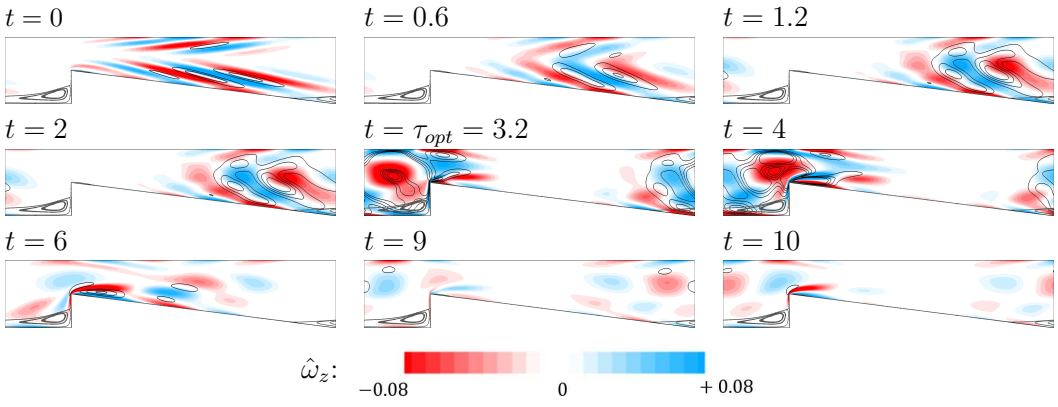

Figure 3.27: Snapshots of the evolution of the spanwise perturbation vorticity ($\hat{\omega}_z$) flooded contours overlaid by perturbation kinetic energy contour lines for $\beta = 0.5$, $\gamma = 2$ at $Re = 100$. The initial condition at $t = 0$ corresponds to the optimal mode, and the subsequent time instants of each frame correspond to the triangle marker positions for this case shown in figure 3.29(b). The dividing streamline of the base flow is also shown. Energy iso-contours are shown at 5 equispaced levels between 0 and 0.0003.

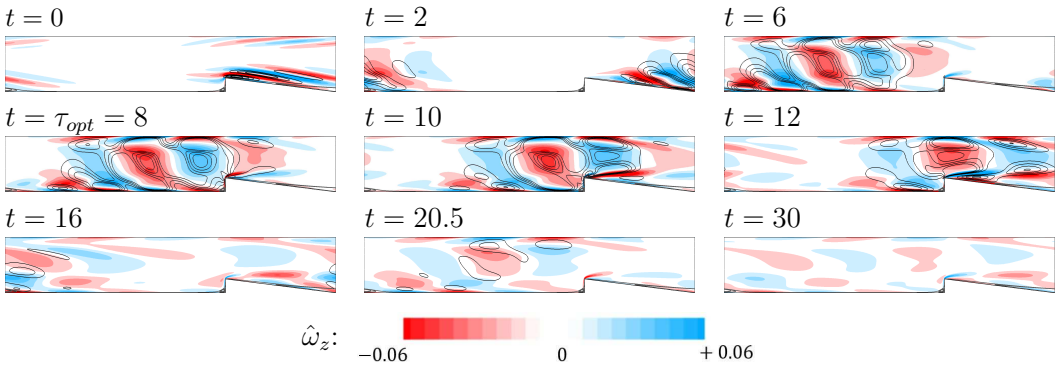

Figure 3.28: Snapshots of the evolution of the spanwise perturbation vorticity ($\hat{\omega}_z$) flooded contours overlaid by perturbation kinetic energy contour lines for $\beta = 0.25$, $\gamma = 8$ at $Re = 400$. The initial condition at $t = 0$ corresponds to the optimal mode, and the subsequent time instants of each frame correspond to the inverted triangle marker positions for this case shown in figure 3.29(a). The dividing streamline of the base flow is also shown. Energy iso-contours are shown at 5 equispaced levels between 0 and 0.00008.

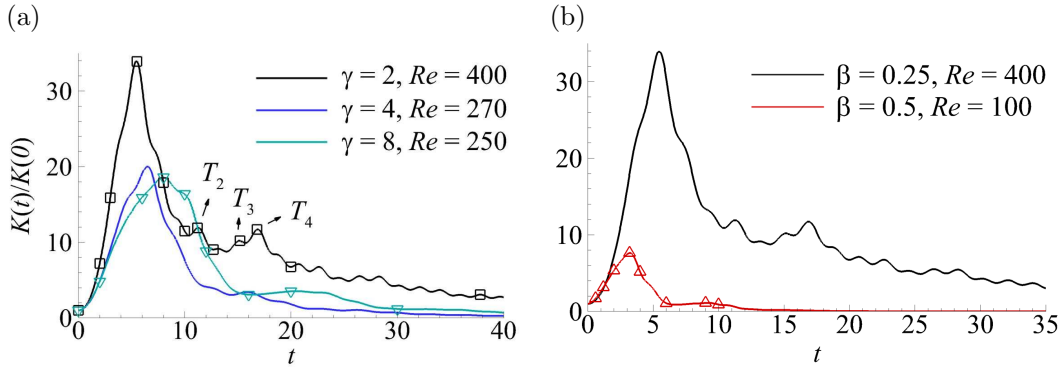

Figure 3.29: Comparison of perturbation kinetic energy time histories obtained by linear evolution of 2D optimal mode for different (a) γ at $\beta = 0.25$ and (b) β at $\gamma = 2$. Wedge angle $\tan(\phi) = 0.125$ for all the cases.

range of parameters investigated, G_{max} is highest between $1 \lesssim \gamma \lesssim 4$ for $\beta = 0.25$, whereas for $\beta = 0.5$, G_{max} decreases monotonically until $\gamma \approx 8$ and a slightly higher value is found at $\gamma = 16$. The optimal time horizon (τ_{opt}) appears to increase with γ in the low range for both $\beta = 0.25$ and 0.5, and decreases slowly at higher $\gamma \gtrsim 8$ for $\beta = 0.25$, whereas it appears to plateau for $\beta = 0.5$. The largest energy gain possible (G_{max}) is consistently lower at a higher blockage ratio of $\beta = 0.5$ than those obtained at $\beta = 0.25$ for all γ in this study due to the limited tilting of the disturbances explained in the previous paragraphs.

Although the energy gains observed in the current setup are lower than in the BFS flow (Blackburn *et al.*, 2008*a*), rounded BFS flow (Marquet *et al.*, 2008) and constricted flow (Blackburn *et al.*, 2008*b*), the energy gain mechanism remains

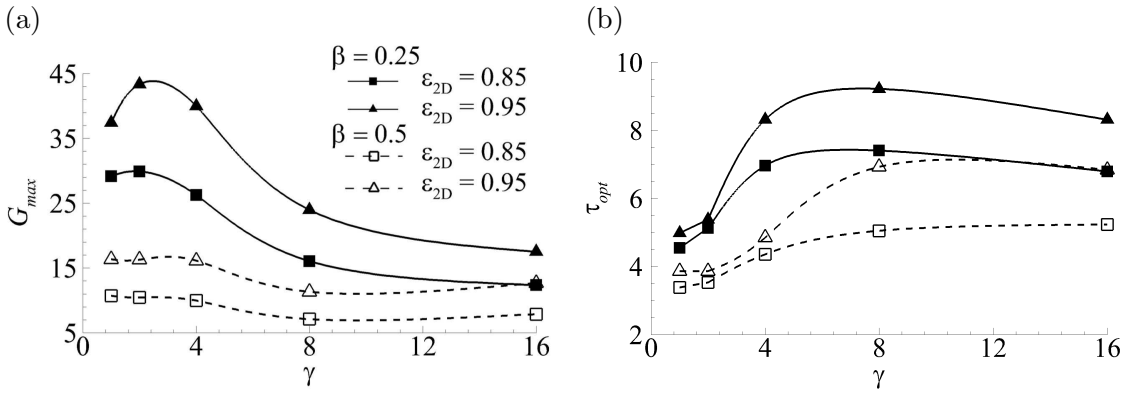

Figure 3.30: Variation of (a) G_{max} and (b) τ_{opt} with γ for $\beta = 0.25$ (filled symbols, solid line) and $\beta = 0.5$ (open symbols, dashed line). Square symbols are interpolated at $\varepsilon_{2\mathrm{D}} = Re/Re_{cr,2\mathrm{D}} = 0.85$ and triangle symbols at $\varepsilon_{2\mathrm{D}} = Re/Re_{cr,2\mathrm{D}} = 0.95$.

similar. The subsequent energy gains due to the streamwise periodic setup in this study is, however, novel. The low algebraic energy growth found here implies that a two-dimensional bypass transition via a linear transient growth mechanism is unlikely to occur. For comparison, G_{max} for the BFS (Blackburn *et al.*, 2008*a*) and constricted flow setups (Blackburn *et al.*, 2008*b*) at $Re = 500$ and $Re = 400$ were $G_{max} \sim \mathcal{O}(10^4)$, that for a slanted BFS at $Re = 800$ was $G_{max} \sim \mathcal{O}(10^2)$, while for the present setup maximum value of $G_{max} \sim \mathcal{O}(10^1)$.

3.5.2 Optimal growth of three-dimensional disturbances

In this section, attention is turned to the optimal growth of three-dimensional disturbances in the linearly stable regimes found from § 3.2.3, i.e. at subcritical Reynolds numbers, $Re < Re_{cr,3\mathrm{D}}$. Transient growth amplification factors are determined for various spanwise wavenumber k and time horizon τ at different $\varepsilon_{3\mathrm{D}}$ values. For each τ, optimal energy growth increases to maximum, before decreasing with increasing k as shown in figure 3.31(a-f), where $\varepsilon_{3\mathrm{D}} = Re/Re_{cr,3\mathrm{D}}$. For every k, a maximum energy amplification $G_{max,k}$ exists, corresponding to a finite time $\tau_{opt,k}$, and the optimal energy of the disturbance eventually decreases at large time horizons as they are in the subcritical regime. The variation of $G_{max,k}$ with k is shown in figure 3.32 for a case with $\beta = 0.25$, $\gamma = 2$ at different $\varepsilon_{3\mathrm{D}}$ values, showing how $G_{max,k}$ increases on approaching the critical Reynolds number. Note that $G_{max,k} \to 1$ as $k \to \infty$. At larger k, viscous dissipation increasingly damps.

At a given $\varepsilon_{3\mathrm{D}}$, the maximum of $G_{max,k}$ over all k, then gives the maximum optimal energy growth G_{max} and corresponding wavenumber is the optimal

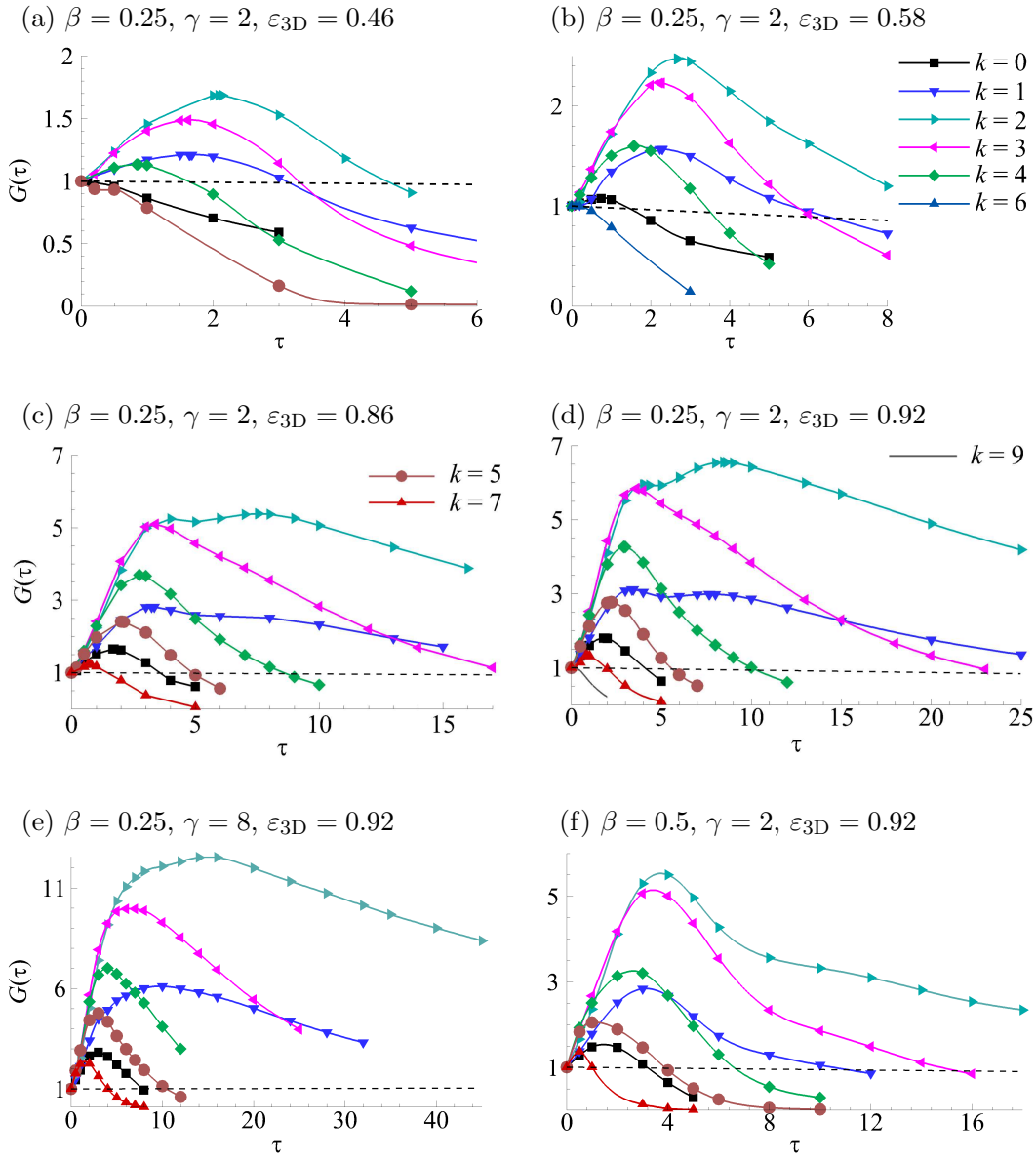

Figure 3.31: Three-dimensional optimal growth curves at various spanwise wavenumber k as shown. Wedge angle $\tan(\phi) = 0.125$ for all the cases here.

wavenumber k_{opt}. The variation of G_{max} with ε_{3D} is shown in figure 3.33. These also demonstrate how the optimal energy growth varies on changing the blockage ratio and pitch. An exponential increase in the maximum optimal growth was found for the three different cases investgated, with $G_{max} \sim e^{2.76\varepsilon_{3D}}$ for $\beta = 0.25$ at $\gamma = 2$, $G_{max} \sim e^{3.09\varepsilon_{3D}}$ for a larger pitch case of $\gamma = 8$ at the same blockage ratio of $\beta = 0.25$, and $G_{max} \sim e^{4.5\varepsilon_{3D}}$ at a higher blockage ratio of $\beta = 0.8$ at $\gamma = 2$. However, the maximum growth remained a very modest $G_{max} \sim 10$ even on approaching the critical Reynolds number for 3D transition. The implication of the modest amplifications found here is that subcritical routes to instability ig-

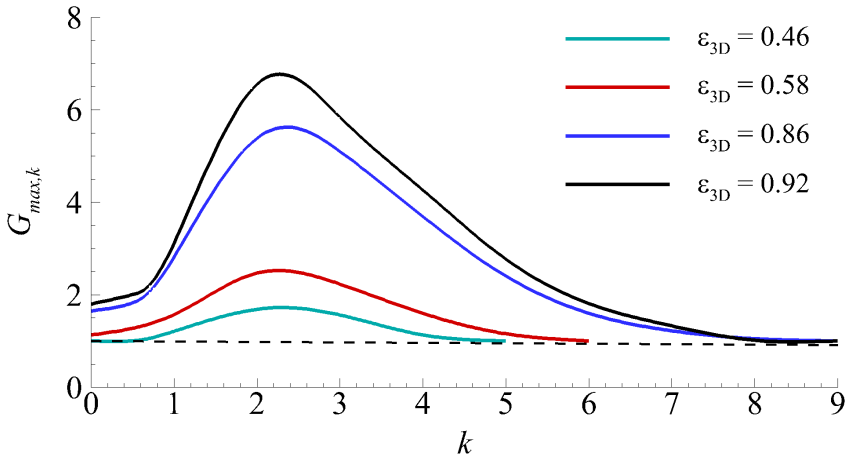

Figure 3.32: Maximum optimal growth ($G_{max,k}$) plotted against spanwise wavenumber k for different Re represented by $\varepsilon_{3D} = Re/Re_{cr,3D}$. Geometric parameter used here are $\beta = 0.25$, $\gamma = 2$, $\tan(\phi) = 0.125$.

nited by strong transient growth are unlikely in this system. The optimal growth and the wavenumber for the different cases investigated are also summarised in table 3.6.

The maximum three-dimensional optimal growth for each of these cases investigated has a relatively higher value that the corresponding two-dimensional optimal growth, although it is still only of very modest amplitude of ~ 10. With an increase in blockage ratio, the range of Re over which a transient amplification is possible reduces for both the 2D and 3D perturbations (table 3.5) and the maximum optimal growth (2D and 3D) is also found to decrease with increasing β. Whereas, when increasing pitch, the range of Re over which a transient amplification is possible reduces for 2D disturbances and increases for 3D disturbances. This could be the reason for a contradicting effect of increasing γ on the 2D optimal growth and 3D optimal growth.

The 3D optimal initial disturbance field for all the investigated parameters take the form of inclined streamwise opposite-signed structures lying along the inclined wedge surface and are shown in figure 3.34 for selected cases. On linear evolution of these optimal modes, the disturbance quickly morphs into the form of the linear global mode before decaying due to the subcritical Reynolds numbers.

A direct comparison with the energy growth in other reported confined shearing flows at similar Reynolds numbers cannot be made as the subcritical Reynolds number range here is relatively lower than in those cases, due to the lower $Re_{cr,3D}$ value for the current setup. Hence, a comparison of the 3D optimal energy growth with respect to the $\varepsilon_{3D} = Re/Re_{cr,3D}$ values is made here. For flow over a BFS (Blackburn *et al.*, 2008*a*), the three-dimensional optimal growth at $\varepsilon_{3D} \approx 0.7$

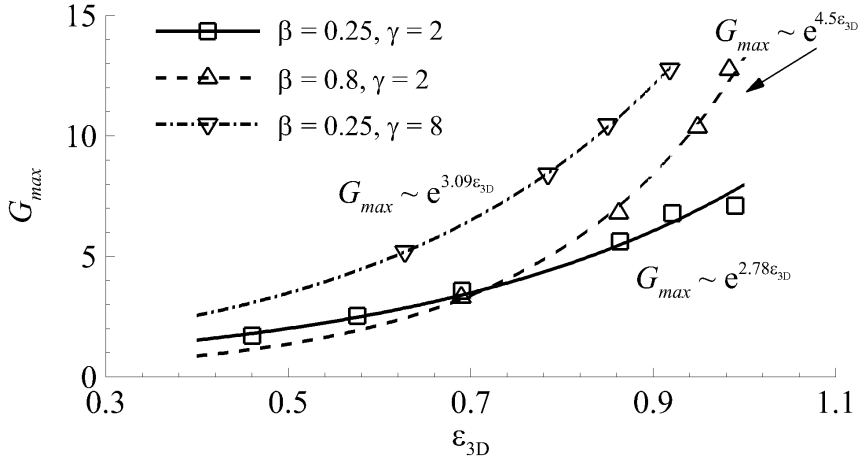

Figure 3.33: Maximum optimal energy growth G_{max} plotted against $\varepsilon_{3D} = Re/Re_{cr,3D}$ at different β and γ as indicated. For all the cases wedge angle $\tan(\phi) = 0.125$. Lines are exponential fits to the respecive data set.

$\beta = 0.25,\ \gamma = 2$			$\beta = 0.25,\ \gamma = 8$		
ε_{3D}	G_{max}	k_{opt}	ε_{3D}	G_{max}	k_{opt}
0.46	1.71185	2.29539	0.63	5.18957	2.27124
0.58	2.51773	2.29008	0.78	8.41842	2.28713
0.69	3.56045	2.34744	0.92	12.76438	2.21425
0.86	5.61308	2.40049			
0.92	6.77576	2.32896			
0.99	7.10266	2.40164			
$\beta = 0.5,\ \gamma = 2$			$\beta = 0.8,\ \gamma = 2$		
ε_{3D}	G_{max}	k_{opt}	ε_{3D}	G_{max}	k_{opt}
0.92	5.74020	2.38166	0.69	3.30084	2.23941
0.99	7.10266	2.40164	0.86	6.78134	2.54493
			0.95	10.35171	2.83490
			0.98	12.74046	3.10047

Table 3.6: Maximum three-dimensional optimal energy and the corresponding optimal spanwise wavenumber k_{opt} at different $\varepsilon_{3D} = Re/Re_{cr,3D}$ and geometric parameter setting. Wedge angle for the cases here is $\tan(\phi) = 0.125$.

(a) $\beta = 0.25$, $\varepsilon_{3D} = 0.99$ (b) $\beta = 0.8$, $\varepsilon_{3D} = 0.98$

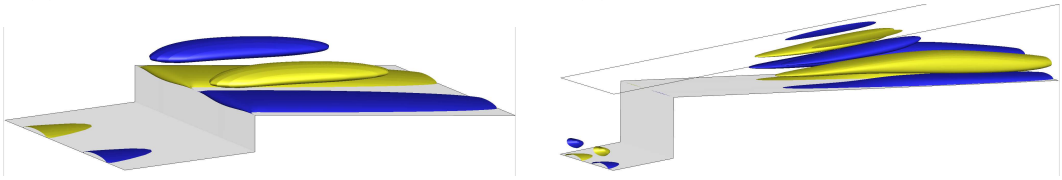

Figure 3.34: Positive (blue) and negative (yellow) iso-contours of streamwise vorticity of the three-dimensional optimal mode at different β. Wedge angle $\tan(\phi) = 0.125$ and $\gamma = 2$ for the cases shown here.

was $G_{max} \sim \mathcal{O}(10^4)$, whereas for flow over a rounded BFS at $\varepsilon_{3D} \approx 0.95$ was lower than the former case with $G_{max} \sim \mathcal{O}(10^2)$. Similar to the observation made for the two-dimensional optimal growth, for the current setup, maximum three-dimensional optimal growth is found to be $G_{max} \sim \mathcal{O}(10)$ at $\varepsilon_{3D} \approx 0.92$ lower than in similar flow setups. The reason for the lower energy growth in the present setup remains an open question.

Chapter summary

The kinematic and stability characteristics of the hydrodynamic flow in a channel with repeated flow-facing wedge shaped protrusions is presented in this chapter. Linear stability analysis was conducted to establish the various bifurcation branches of the two-dimensional flow solution. The transition to a two-dimensional unsteady state is found to occur through a global complex mode appearing as a wave spanning the streamwise domain length. It is observed that increasing the blockage ratio, pitch and wedge angle prepones this transition to a lower Re. The primary bifurcation of the two-dimensional flow solution is three-dimensional and occurs through a real mode, well before the threshold for 2D instability. This holds for the range of blockage ratios and pitch values covered in this study. Increasing the blockage ratio and decreasing the pitch results in a decrease in the critical Reynolds number $Re_{cr,3D}$, i.e. causes the flow to become more unstable three-dimensionally. The onset of three-dimensional effects in the flow is observed mostly near the wedge. The instability is characterised by the formation of streamwise velocity streak induced by the counter-rotating streamwise vortices near the wedge tip. The lift-up mechanism is found to be responsible for this instability. A perturbation kinetic energy budget of the instability modes shows that the production due to horizontal shear in the base flow is responsible for most of the energy gain in all cases. The corresponding locations of maximum shear are in the region ahead and after the wedge tip.

The wavemaker region in the flow found though sensitivity analysis is similarly located, further supporting the previous finding from the energetics analysis. The significant regions in the flow for the placement of an active or passive control mechanism were also identified through receptivity and sensitivity analysis for both two- and three-dimensional disturbances. For most of the cases considered, the local pressure gradient component of the endogeneity distribution was found to feature prominently in the total endogeneity field, the sum of which retrieves the growth rate of the global eigenmode, despite its net contribution being intrinsically zero. This emphasizes its role in the local endogeneous eigendynamics in this system. Studies were also carried out to understand the optimal growth of two- and three-dimensional disturbance. The optimal disturbance structure is presented, and the influence of the subsequent wedge and geometric parameter change on the energy growth of the optimal mode is elaborated. It is found that the flow does not aid a significant transient energy growth, unlike similar confined flow setups (Blackburn *et al.*, 2008*a*,*b*; Marquet *et al.*, 2008) over the different range of geometric parameters considered, thereby being unlikely to support a bypass transition via transient energy amplifications.

In the next chapter, the non-linear interactions in hydrodynamic channel flows with repeated wedges are discussed to verify the findings from the linear analyses, and to illustrate how non-linear interactions modify the flow structures and the associated temperature fields.

Chapter 4

Non-linear interactions in hydrodynamic channel flow with wedge-shaped protrusions

In the previous chapter, both two- and three-dimensional global linear instability modes associated with the two-dimensional solution branch, and the primary 3D bifurcation, respectively, were elucidated. The associated temperature fields in the 2D steady and unsteady state of the flow and its influence on the heat transfer behaviour were considered. Optimal modes associated with the linear transient amplication of disturbance energy were also discussed, and it was found that the maximum optimal energy growth was likely insufficient to incite a bypass transition in the current flow system. The objectives of this chapter are hence threefold. First, the influence of non-linear effects on the transient growth of the optimal mode structures is discussed and used as support to show that these interactions cannot lead to amplification of the energy in optimal disturbance structures and trigger an early transition in these flows. Second, the findings from the linear stability analysis are verified by carrying out non-linear simulations and comparing the underlying disturbance structure leading to the unstable state for the 2D cases. This is followed by a comparison of the flow structure in the linear and weakly non-linear stages to that predicted from the linear analysis for the 3D cases, which further strengthens the findings from the linear analysis about the route to transition. The non-linear simulations also highlight how non-linearity influences the flow structures and the associated temperature fields. Lastly, the nature of the primary bifurcation of the 2D steady flow is identified via a weakly non-linear analysis using the Stuart–Landau equation.

4.1 Influence of non-linear interactions on transient growth of the optimal modes

In this section the influence of non-linearity on the transient energy growth of the two-dimensional optimal modes found from the linear analysis in § 3.5.1 is discussed. To study the effect of non-linearity on the evolution of the two-dimensional optimal modes, a 2D initial condition is applied as a superposition of the base flow and the 2D optimal mode, scaled to different energy levels. The expectation is that as the initial energy level of the disturbance approaches zero, the evolution of the disturbance will approach the evolution of the optimal mode using the linearised equations, and non-linear effects will increasingly modify the evolution as the initial energy is increased. The unknown is whether finite-amplitude seeding can invoke an enhancement of growth via non-linear means. The normalised energy of the disturbance (equation 2.65) is monitored and compared with that of the linear evolution case.

Three same cases considered in the linear transient growth analysis in § 3.5.1 are used here. The time histories of the disturbance energy are shown in figure 4.1 for different cases. For the cases considered, at relatively smaller seeding ($K(0)= 10^{-}9$) of the 2D optima to the baseflow, energy growth in the non-linear evolves matches with the linear evolution curve through the first peak. For $\beta = 0.25$, $\gamma = 2$ (figure 4.1a), these curves lie approximately on top of one another and has the same decay rate as the linear case at low seeding, whereas for the other two cases considered (figure 4.1b,c), the curves at lower seeding have a relatively lower energy growth at the subsequent peaks and a slightly lower decay rate compared to the linear evolution curves. With further increases in the amplitude of the perturbation seeding, the normalised energy growth curves falls below the linear growth curve, with the peak growth remaining lower, and occuring earlier than the linear evolution case. Thus, the effect of non-linearity has a stabilising effect on the transient growth of the predicted optimals.

4.2 Non-linear interactions in two- and three-dimensional transition

The linearised analysis is predicated on the assumption that perturbations are infinitesimally small, thus rendering nonlinear effects negligible. In this section, consideration is given to the the non-linear effects. Initially, the underlying disturbance structure leading to the 2D unsteady states found from the non-linear

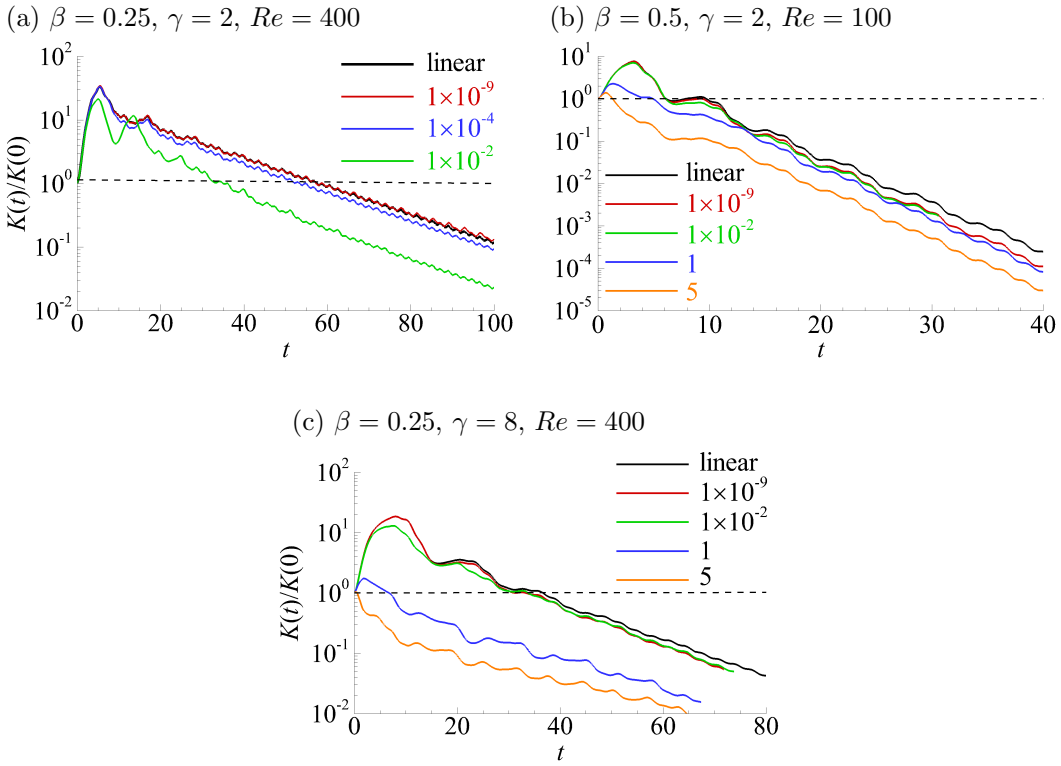

Figure 4.1: Normalised energy of 2D disturbance plotted against time for different geometric parameter combinations as indicated. Thick solid black line represents the linear energy evolution of the optimal modes, whereas the other lines shows the non-linear evolution by seeding the base flow with the initial disturbance scaled to specific kinetic energy levels as indicated.

simulations is discussed, and used to verify the predictions made from the two-dimensional linear stability study in § 3.2.1. Thereafter, the change in the flow structure on the onset of non-linear effects are elucidated for the three-dimensional cases. The flow structure in the linear and weakly non-linear stages are also compared with the corresponding three-dimensional linear stability mode found in § 3.2.3, thereby verifying the predictions made from the linear analysis. A longer spanwise extent of the flow domain is also studied and briefly discussed.

4.2.1 Non-linear interactions in two-dimensional unsteadiness

The disturbance structure leading to 2D unsteadiness in the flow is discussed in this section to verify the findings from the 2D linear stability analysis. The flow is evolved naturally (without the addition of white noise) from the steady solution obtained from the `BoostConv` algorithm. At each time step, the underlying disturbance structures are acquired by subtracting the flow solution from

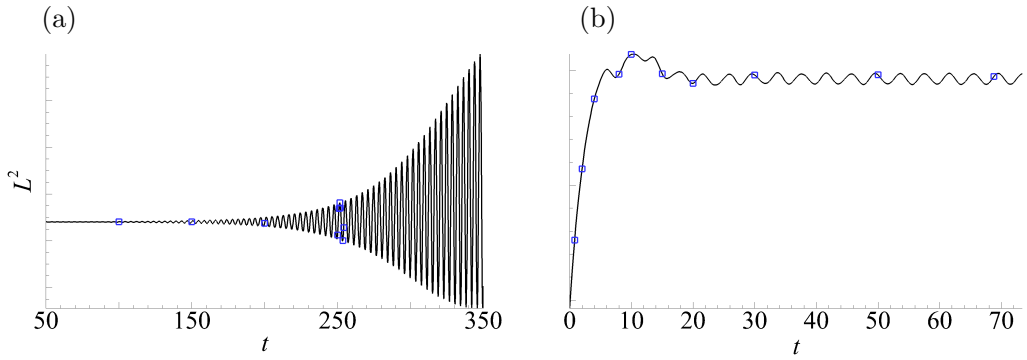

Figure 4.2: Time history of $\mathscr{L}^2$ amplitude on naturally evolving the flow from the steady state solution for (a) $\beta = 0.25$ at $Re = 480$ ($\varepsilon_{2D} = 1.08$) and (b) $\beta = 0.5$ at $Re = 130$ ($\varepsilon_{2D} = 1.02$). The cases here have $\gamma = 2$, $\tan(\phi) = 0.125$. The marker positions in (a) and (b) corresponds to the time at which the snapshots of the underlying disturbance field are shown in figures 4.3 and 4.4, respectively.

the steady-state solution. Reynolds number shortly beyond $Re_{cr,2D}$ is considered for this analysis for $\beta = 0.25$ and $\beta = 0.5$. The 2-norm of the velocity field, $\mathscr{L}^2$ of the flow is monitored during its evolution, which shows the growth and saturation of the $\mathscr{L}^2$ amplitude of the flow. These are shown in figure 4.2 for the cases considered. Snapshots of the underlying disturbance structure at a few time instances, corresponding to the marker positions in figure 4.2(a) and (b) are visualised in figures 4.3 and 4.4, respectively. It is observed that the underlying disturbance structure matches with the dominant mode (M2) found from linear stability analysis in § 3.2.1 at longer times when the amplitude of $\mathscr{L}^2$ has reached a saturated state. The close match between mode M2 and the underlying disturbance structure verifies the findings from the linear analysis.

Additionally, the frequency of oscillation (f_{linear}) obtained from linear evolution of the unstable mode M2 is compared with the corresponding frequency of oscillation (f) of the unsteady 2D flow upon saturation for selected cases. The corresponding frequencies are shown in table 4.1. It is found that f_{linear} matches closely to f, thereby further supporting the previous finding that the onset of 2D unsteadiness is due to the linear instability mode M2.

4.2.2 Non-linear interactions in three-dimensional transition

In this section, results from three-dimensional simulations are discussed and the onset of non-linear effects in the flow is explained for selected cases by capturing the flow structures that emerge from the linear through the weakly non-linear

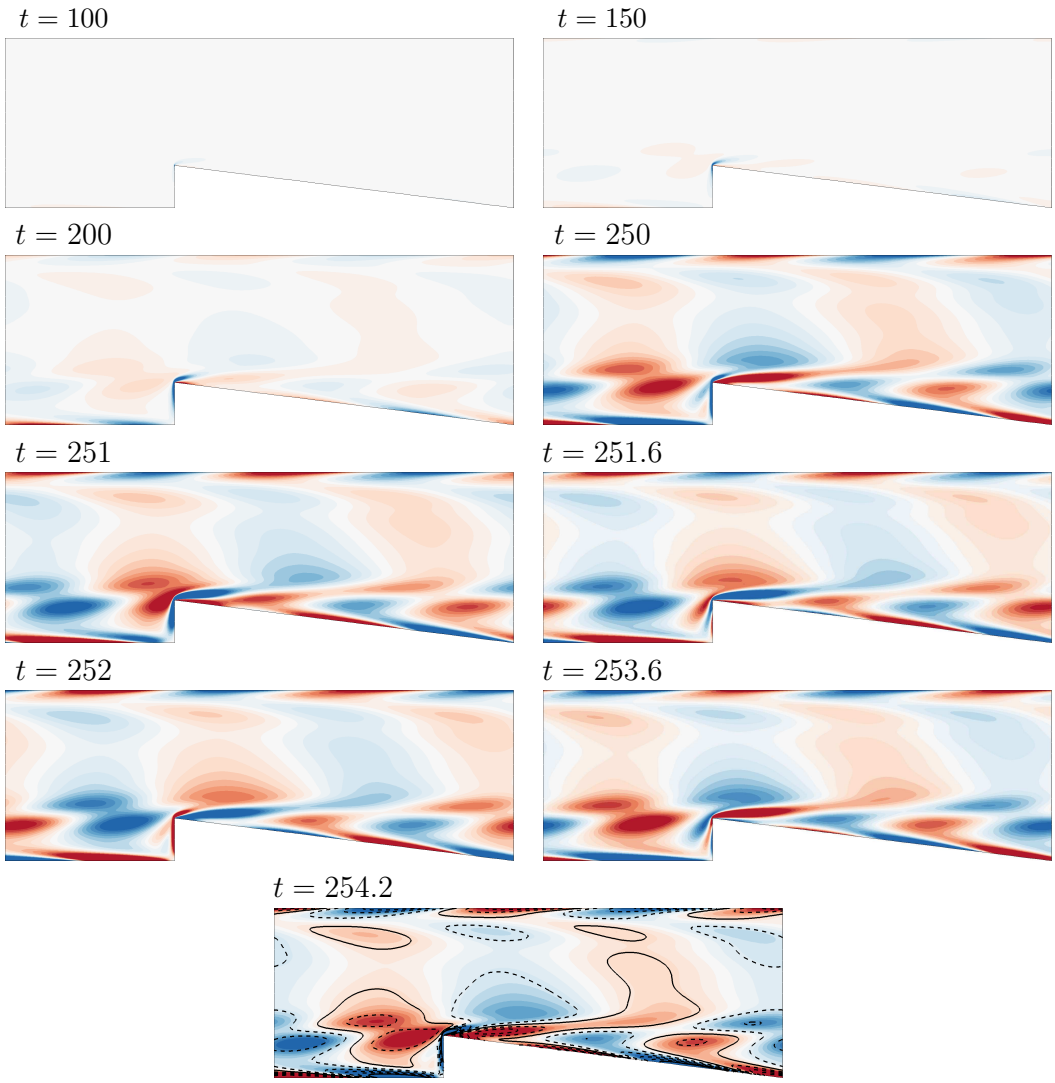

Figure 4.3: Snapshots of spanwise vorticity ($\hat{\omega}_z$) contours of the underlying disturbance field upon naturally evolving the flow from the steady-state solution for $\beta = 0.25$, $\gamma = 2$, $\tan(\phi) = 0.125$ at $Re = 480$ ($\varepsilon_{2D} = 1.08$). The line contours of spanwise vorticity of the corresponding linear instability mode (M2) is shown at $t = 254.2$. Contours of $\hat{\omega}_z$ of the disturbance field are shown at 20 equispaced levels between -0.05 (blue) to 0.05 (red), whereas the line contours of $\hat{\omega}_z$ for M2 are spaced at 10 equispaced levels in the same range with solid and dashed lines representing positive and negative values, respectively. The time instance of each frame correspond to the marker positions in figure 4.2(a).

stage. Verification of the findings from the linear stability analysis is made by comparing the flow structures in the linear and weakly non-linear stage to the corresponding 3D linear mode. For the three-dimensional simulations, the out-of-plane domain length is selected to match the wavelength of the dominant eigenmode predicted in § 3.2.2 (λ_{cr}). The flow is initialised with the 2D base flow solution superimposed with a small random 3D perturbation. A longer spanwise

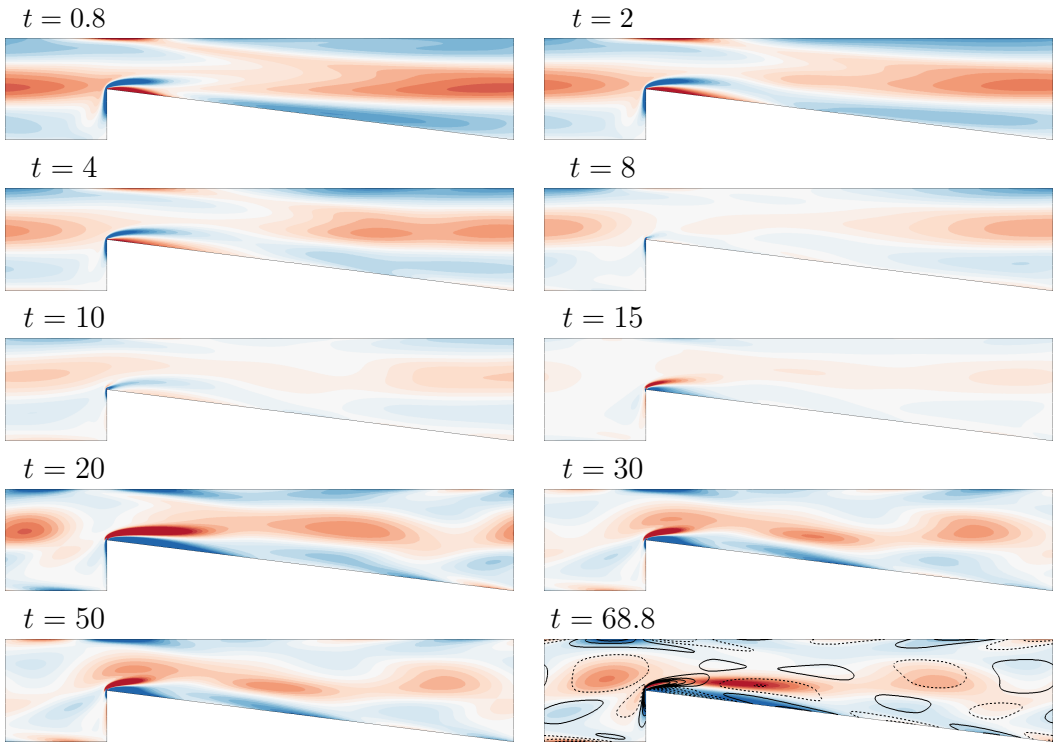

Figure 4.4: Snapshots of spanwise vorticity ($\hat{\omega}_z$) contours of the underlying disturbance field upon naturally evolving the flow from the steady-state solution for $\beta = 0.5$, $\gamma = 2$, $\tan(\phi) = 0.125$ at $Re = 130$ ($\varepsilon_{2D} = 1.02$). The line contours of spanwise vorticity of the corresponding linear instability mode (M2) is shown at $t = 68.8$. Contours of $\hat{\omega}_z$ of the disturbance field are shown at 20 equispaced levels between -0.1 (blue) to 0.1 (red) for $t = 0.8$ to 15, and between -0.02 (blue) to 0.02 (red) for $t = 20$ to 68.8. The line contours of $\hat{\omega}_z$ for M2 are spaced at 10 equispaced levels between -0.05 (dashed line) to 0.05 (solid line). The time instance of each frame correspond to the marker positions in figure 4.2(b).

extent of the domain, approximately four ($4\lambda_{cr}$) and eight times ($8\lambda_{cr}$) the dominant wavelength from linear analysis are also considered for selected cases in order to capture any longer wavelength structures that might manifest and to determine how these structures influence the flow and the temperature distribution.

The onset of weakly non-linear effects in the flow are discussed at Re beyond the critical Reynolds number $Re_{cr,3D}$ predicted in § 3.2.2. The closeness of Re to $Re_{cr,3D}$ is quantified through the term $\varepsilon_{3D} = Re/Re_{cr,3D}$. Plots showing the time evolution of kinetic energy of each Fourier mode along with iso-contours capturing the effect of non-linearity in the flow are shown for two different blockage ratios in figures 4.5 and 4.6. The evolution of the Fourier mode's energy, in general, may be divided into three regions. These are explained using an example of the kinetic energy plot shown in figure 4.5 for $\beta = 0.25$. The initial stage (*1*) represents the short-term dynamics of the flow where a transient rise in the energy of first three

Parameters	ε_{2D}	f_{linear}	f
$\beta = 0.25,\ \gamma = 2$	1.08	0.260	0.261
$\beta = 0.50,\ \gamma = 2$	1.02	0.253	0.252
$\beta = 0.65,\ \gamma = 2$	1.01	0.454	0.451
$\beta = 0.25,\ \gamma = 1$	1.08	0.111	0.113
$\beta = 0.25,\ \gamma = 4$	1.06	0.140	0.138
$\beta = 0.25,\ \gamma = 16$	1.02	0.156	0.156

Table 4.1: Comparison of the frequency of oscillation of the unsteady 2D flow upon saturation (f) with the frequency on linear evolution from the 2D linear mode (f_{linear}) at $\varepsilon_{2D} = Re/Re_{cr,2D}$ as indicated.

Fourier modes can be observed. This is followed by a linear growth stage (*2*). The growth rate of the leading Fourier mode here ($\mathrm{d}\langle E_{k,1}/2\rangle/\mathrm{d}t = 0.09080$) matches well with the growth rate predicted from linear stability analysis ($\sigma = 0.09077$). Stage *3* is where non-linear effects dominate the flow dynamics.

For $\beta = 0.25$, $\gamma = 2$ with $\varepsilon_{3D} \approx 4.6$, figure 4.5 captures the flow structures as the flow evolves from linear stage *2* to the non-linear saturation in *3*. The flow structures in the linear stage at $t = 243$ match with the eigenmodes found from linear stability analysis (figure 3.13a), and even through the weakly non-linear stage. The lift-up mechanism becomes evident by $t = 260$ and $t = 265$, where the deformation of the streamwise vortices can be observed as an extension of the counter-rotating vortices downstream, decrease in its spanwise extent, along with the structure's non-linear distortion. Eventually, these primary streamwise vortices interact with the top wall, distorting and then breaking down ($t = 267$ and $t = 275$). The deformation of the spanwise vorticity contours with the flow evolution can also be observed from the translucent isocontours shown in figure 4.5. This process repeats itself with newly formed streamwise vortices at the wedge induced by the lift-up. The flow structures in a saturated stage at $t = 477$ is also shown.

At a higher blockage ratio of $\beta = 0.5$, the flow structures in the non-linear 3D simulations shows resemblance to the linear mode, and it persists even when non-linear effects become dominant (figure 4.6). The streamwise vortices are observed to elongate and shrink with time as the flow evolves, and no breakdown of these structures is observed. This is likely due the Reynolds number being closer to the critical $Re_{\mathrm{cr,3D}}$ ($\varepsilon_{3D} \approx 1.7$) considered for this case.

Longer spanwise extents of the flow domain, approximately four and eight times the wavelength of the global eigenmode found from linear stability analysis is now considered for two blockage ratio cases. This permits the growth of longer

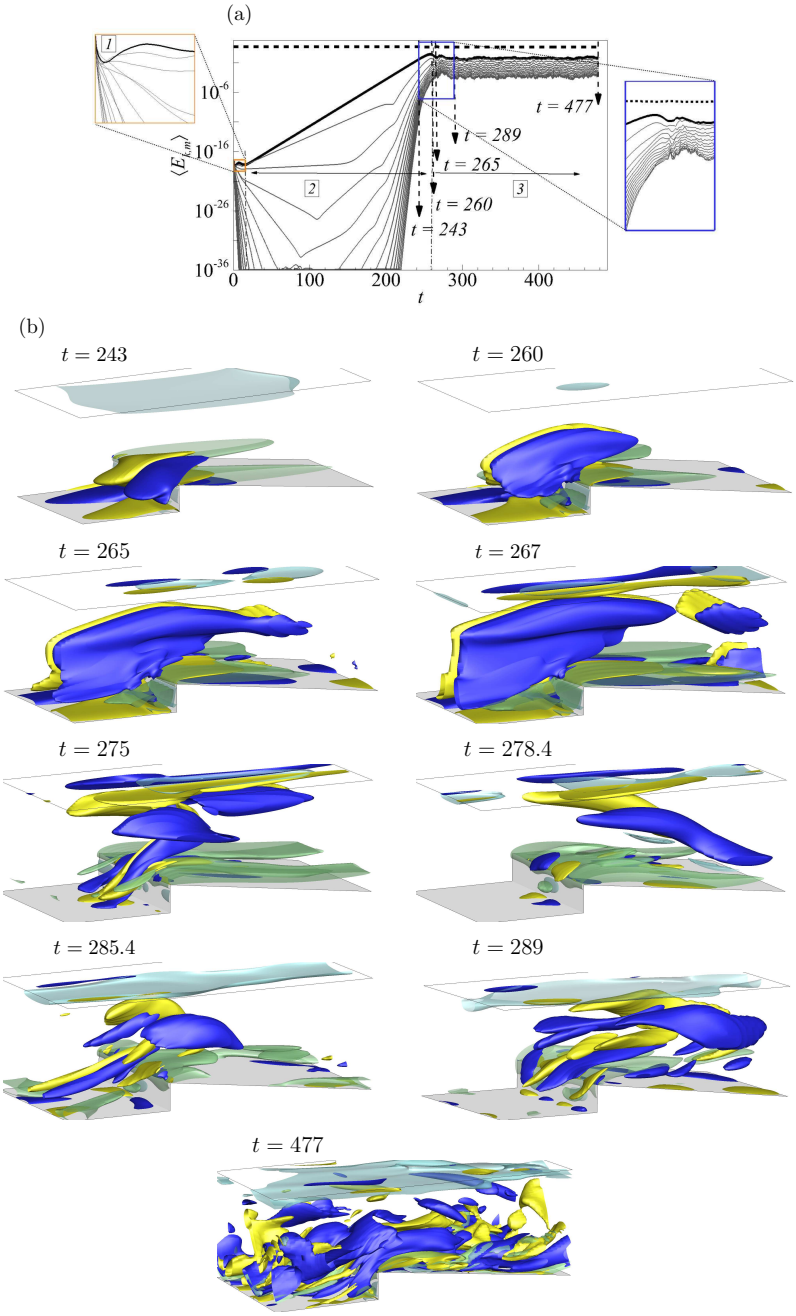

Figure 4.5: (a) Line plot showing the time evolution of domain integral of kinetic energy ($\langle E_{k,m} \rangle$) in 16 Fourier modes along with (b) iso-surface plots of positive (blue) and negative (yellow) streamwise vorticity, and positive (translucent blue) and negative (translucent green) spanwise vorticity of the flow capturing the onset of non-linear effects for $\beta = 0.25$, $\gamma = 2$, $\tan(\phi) = 0.125$ at $Re = 400$ ($\varepsilon_{3D} \approx 4.6$). In (a) the dashed bold line represents the energy in the fundamental mode ($\langle E_{k,0} \rangle$), while energy in the dominant mode ($\langle E_{k,1} \rangle$) is given by the solid bold line. The other thin lines represent the energy evolution in the subdominant modes. The transient, linear and non-linear saturation regions are identified as *1* (the section shown in orange), *2* and *3* respectively. A section showing the time interval between the linear regime and the fully saturated non-linear regime is also shown (in blue) along with time stamps of the iso-contours, for reference.

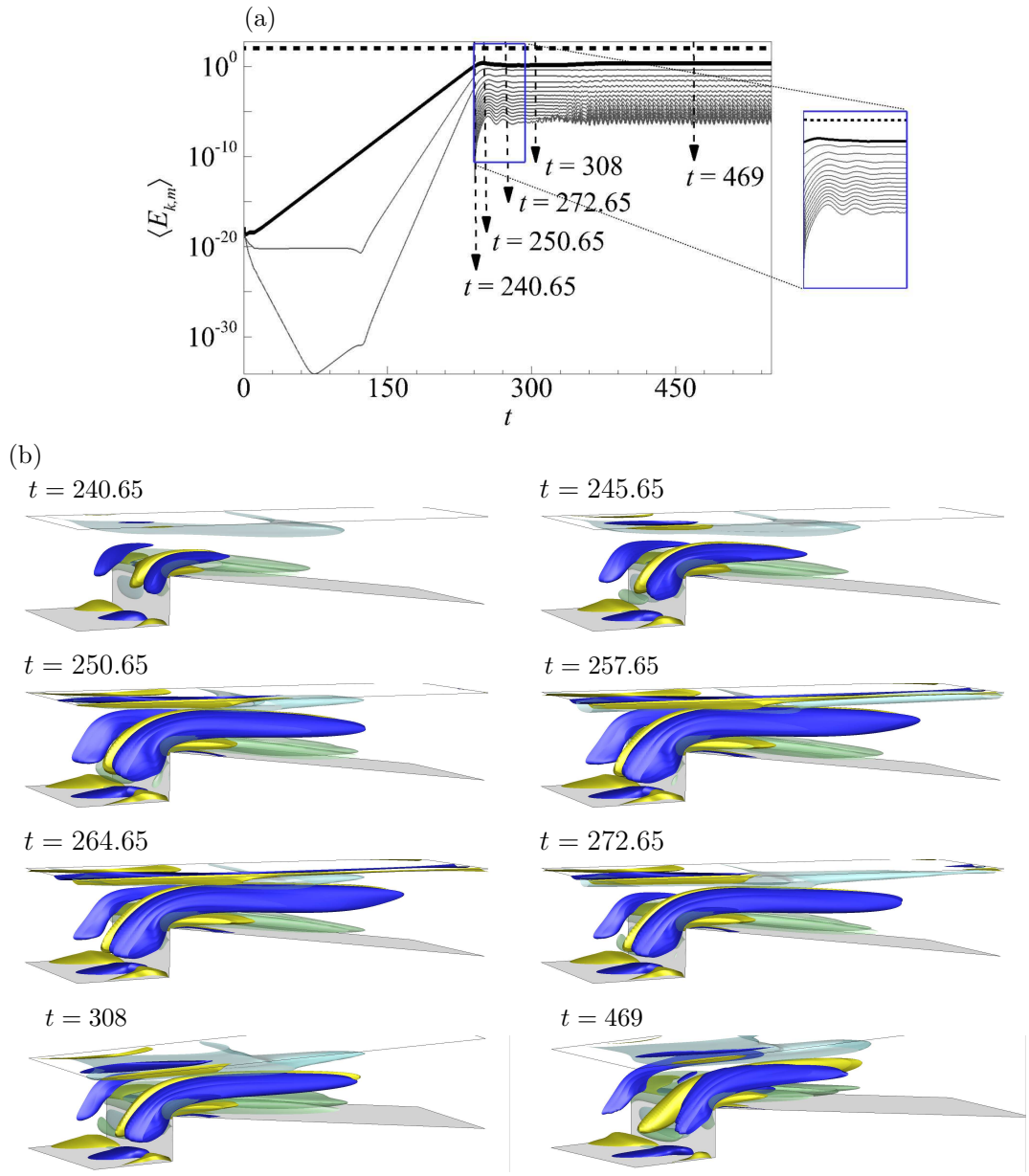

Figure 4.6: (a) Line plot showing the time evolution of domain integral of kinetic energy ($\langle E_{k,m} \rangle$) in 16 Fourier modes along with (b) iso-surface plots of positive (blue) and negative (yellow) streamwise vorticity, and positive (translucent blue) and negative (translucent green) spanwise vorticity of the flow capturing the onset of non-linear effects for $\beta = 0.5$, $\gamma = 2$, $\tan(\phi) = 0.125$ at $Re = 100$ ($\varepsilon_{3D} \approx 1.7$). In (a) the line labels are same as in figure 4.5(a). A section showing the time interval between the linear regime and the fully saturated non-linear regimes is also shown (in blue) along with time stamps of the iso-contours, for reference.

wavelength Fourier modes. For $\beta = 0.125$, the flow structures on non-linear saturation is shown at different Reynolds numbers in figure 4.7 for a domain with four times the spanwise length of the global mode. Deformation of the spanwise vorticity sheets by the streamwise vorticity structures which is more prevelant near the bottom wall can be observed from the three-dimensional iso-contours shown in figure 4.7. The passive temperature field forms alternate streaks of hot and cold temperature fluids extending the streamwise length of the flow domain and seems to follow the streamwise vorticity field's pattern. These streaks are strong support of the lift-up mechanism; the cold streaks being where the fluid is pushed down by the streamwise rollers, the hot streaks are where they are lifting the hot fluid from near the surface into the interior of the duct. The spanwise velocity fields which appeared as purely spanwise rolls in the linear and weakly non-linear stage can be seen to be deformed further, resulting in a much extensive mixing of the hot and the cold fluids near the top and bottom walls of the channel, respectively. This is evident from the plume structures formed between the deformed alternate spanwise velocity rolls. A more vigorous deformation is found with increasing Reynolds number with the formation of much small scale structures in the flow. For the largest spanwise length investigated (eight times the spanwise length of the global mode) the flow structures are observed to have a similar structure as the $4\lambda_{cr}$ case with more small scale structures being captured as shown in figure 4.8.

Comparison of the flow fields for a smaller spanwise domain length (λ_{cr}) with the $4\lambda_{cr}$ domain is made in figures 4.9 and 4.10 for $\beta = 0.25$. The visualisation clearly shows how small scale structures are captured in the $4\lambda_{cr}$ domain allowing for its effect to be captured in the temperature fields as well. At similar Reynolds number the streamwise vorticity fields seems to have a more coherent repeating pattern at a lower blockage ratio of $\beta = 0.125$ which is lost for the $\beta = 0.25$ case. Instead, swirling of the alternate streamwise vorticity streaks downstream of the wedge tip is observed for this case. The effect of this swirling can be visualised through the temperature fields which no longer has the alternate streak pattern extending the streamwise extent of the flow domain as observed for $\beta = 0.125$, thereby increasing the mixing of the hot fluid to the bulk at a higher blockage ratio.

A qualitative illustration of the three-dimensional flow structures and the effect of spanwise domain length was provided in figures 4.5-4.10. A quantitative consideration will now be given. In table 4.2 a comparison of the time averaged bulk flow properties of the flow per unit spanwise length of the domain is made

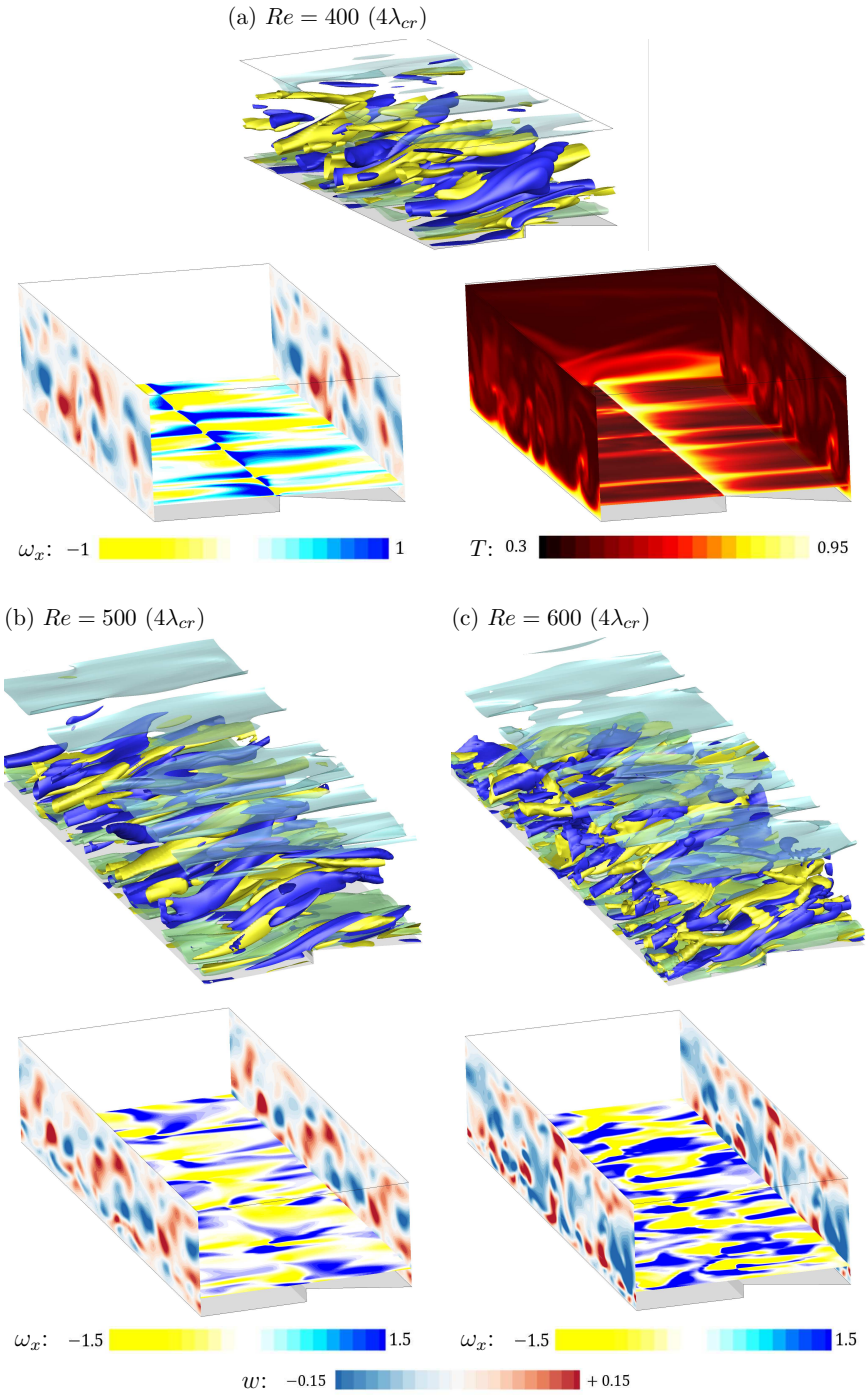

Figure 4.7: Visualisations of a snapshot of the saturated three-dimensional flow in domains with spanwise length four times $(4\lambda_{cr})$ the dominant wavelength predicted from the linear stability analysis. In (a-c), the top frame plots the isosurfaces of streamwise vorticity with opaque blue and yellow showing positive and negative values, respectively, and isosurfaces of spanwise vorticity with translucent blue and green showing positive and negative values, respectively. In (a) the temperature distribution is shown (bottom right), while in (a-c) the bottom frames also plot the contours of streamwise vorticity ω_x and spanwise velocity w. Parameters for the case shown are $\beta = 0.125$, $\gamma = 2$ and $\tan(\phi) = 0.125$ at (a) $Re = 400$, (b) $Re = 500$ and (c) $Re = 600$.

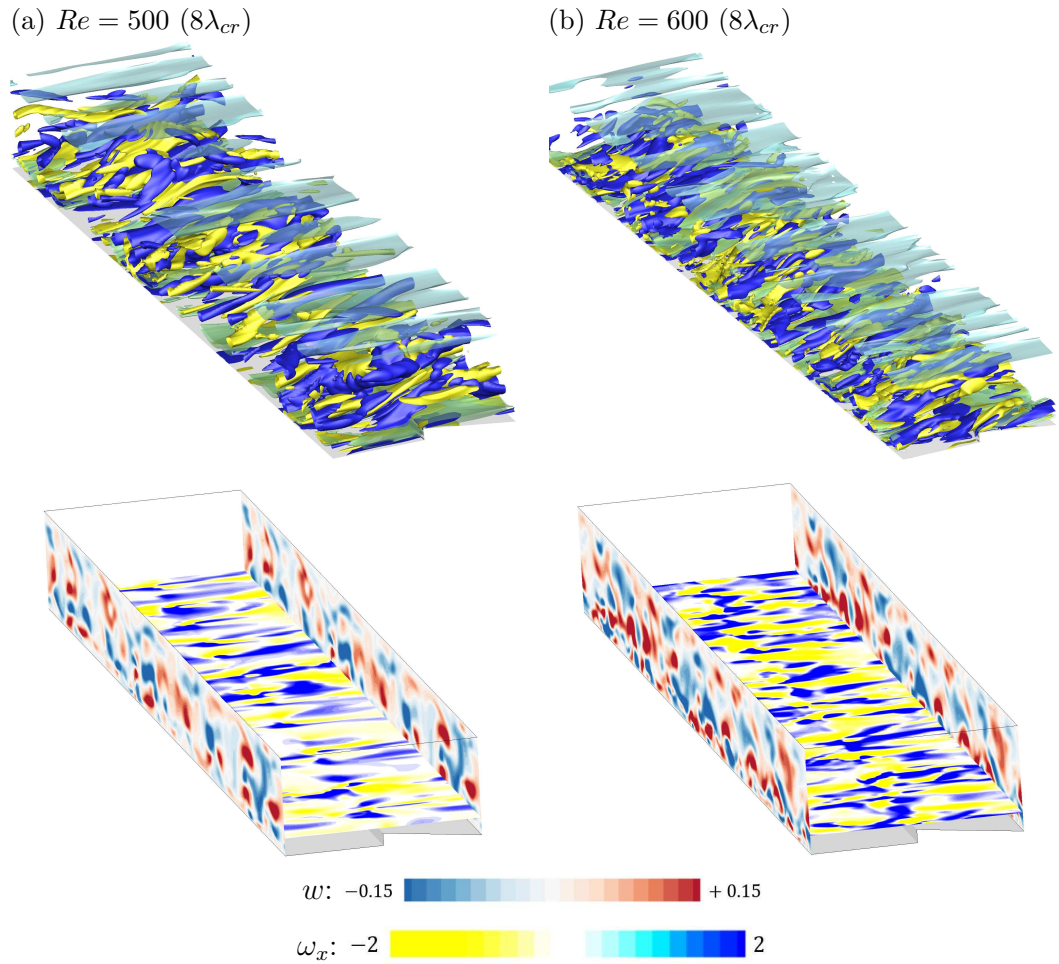

Figure 4.8: Visualisations of a snapshot of the saturated three-dimensional flow in domains with spanwise length eight times $(8\lambda_{cr})$ the dominant wavelength predicted from the linear stability analysis. In (a,b), the top frame plots the isosurfaces of streamwise vorticity with opaque blue and yellow showing positive and negative values, respectively, and isosurfaces of spanwise vorticity with translucent blue and green showing positive and negative values, respectively. The bottom frame plots the contours of streamwise vorticity (ω_x) and spanwise velocity (w). Parameters for the case shown are $\beta = 0.125$, $\gamma = 2$ and $\tan(\phi) = 0.125$ at (a) $Re = 500$ and (b) $Re = 600$.

for selected cases. Although, the larger spanwise length flow domain can capture the small scale flow structures than the λ_{cr} domain, the bulk properties of the flow calculated from the λ_{cr} domain matches closely with those calculated from the larger spanwise domain length cases. The effect of swirls observed in the streamwise vorticity contours for $\beta = 0.25$ case which resulted in a better mixing between the hot and cold fluid downstream of the wedge tip could be observed as an enhancement in Nusselt number for this case than at lower blockage ratio of $\beta = 0.125$. However, these are also associated with a much higher pressure drop

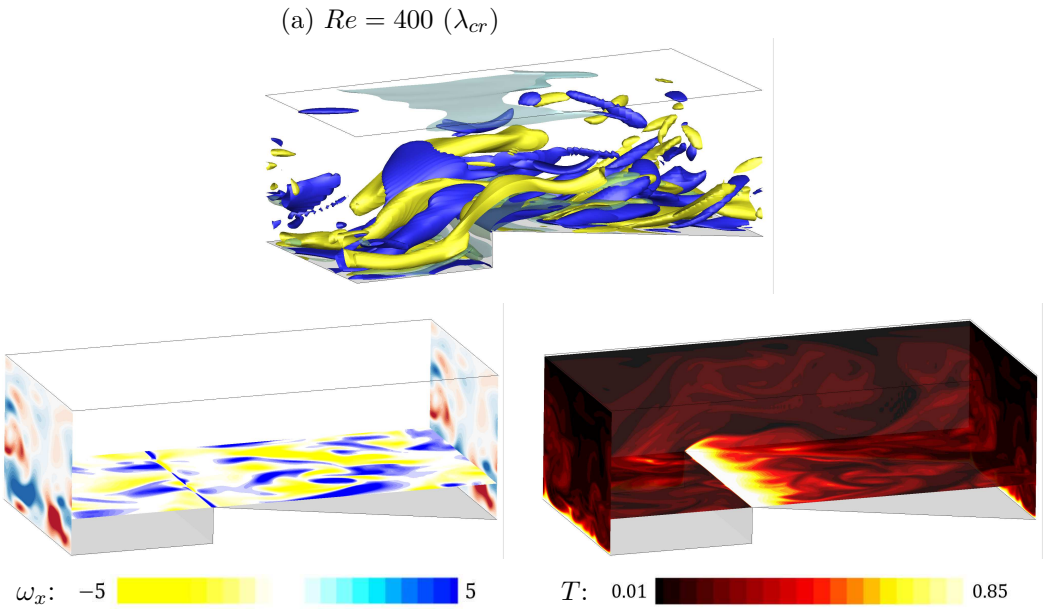

Figure 4.9: Visualisations of a snapshot of the saturated three-dimensional flow in domains with spanwise length equal to (λ_{cr}) the dominant wavelength predicted from the linear stability analysis. The top frame plots the isosurfaces of streamwise vorticity with opaque blue and yellow showing positive and negative values, respectively, and isosurfaces of spanwise vorticity with translucent blue and green showing positive and negative values, respectively. The bottom right frame plots the temperature distribution, while the contours of streamwise vorticity ω_x and spanwise velocity w are shown in the bottom left frame. Parameters for the case shown are $\beta = 0.25$, $\gamma = 2$ and $\tan(\phi) = 0.25$.

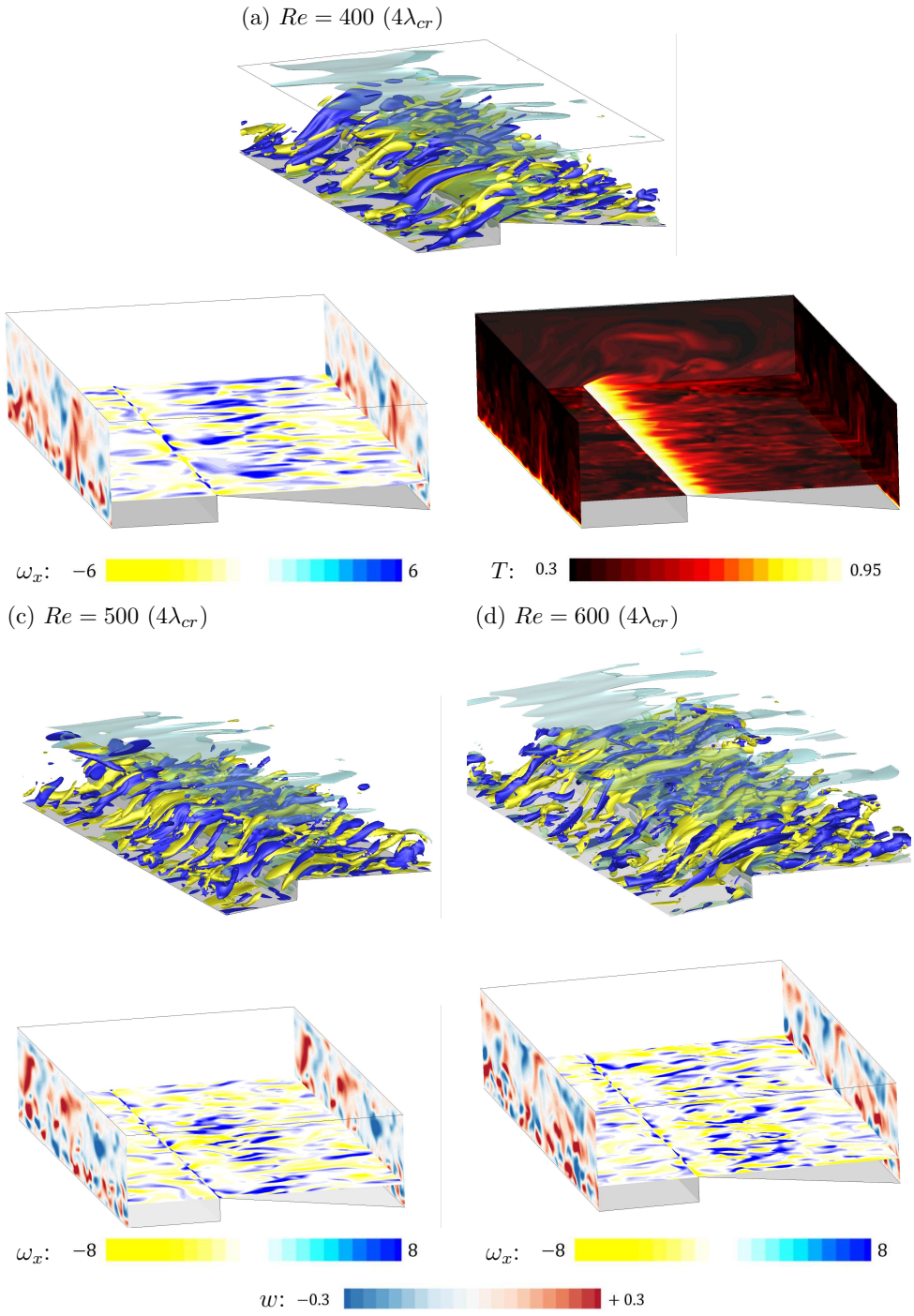

Figure 4.10: Visualisations of a snapshot of the saturated three-dimensional flow in domains with spanwise length equal to four times $(4\lambda_{cr})$ the dominant wavelength predicted from the linear stability analysis. In (a-c), the top frame plots the isosurfaces of streamwise vorticity with opaque blue and yellow showing positive and negative values, respectively, and isosurfaces of spanwise vorticity with translucent blue and green showing positive and negative values, respectively. In (a) the temperature distribution (bottom right) is shown, while in (a-c) the bottom frame also plots the contours of streamwise vorticity ω_x and spanwise velocity w. Parameters for the case shown are $\beta = 0.25$, $\gamma = 2$ and $\tan(\phi) = 0.25$.

$\beta = 0.125$, $\gamma = 2$				
Time averaged flow parameter per unit spanwise length	Re	λ_{cr}	$4\lambda_{cr}$	$8\lambda_{cr}$
Flow kinetic energy	400	22.28102	23.68234	
	500		23.40327	23.44405
	600		23.45281	23.43449
Friction factor	400	0.03277	0.03391	
	500		0.03299	0.03348
Nusselt number	400	8.20288		
$\beta = 0.25$, $\gamma = 2$				
Time averaged flow parameter per unit spanwise length	Re	λ_{cr}	$4\lambda_{cr}$	
Flow kinetic energy	400	43.62923	43.29894	
	500		38.60451	
	600		38.32449	
Friction factor	400	0.07538	0.07407	
	500		0.07337	
	600		0.07252	
Nusselt number	400	55.60261	55.61804	
	500		59.03361	
	600		75.80818	

Table 4.2: Comparison of various bulk flow parameters per unit spanwise width for cases with spanwise width equal to (λ_{cr}), four times ($4\lambda_{cr}$) and eight times ($8\lambda_{cr}$) the wavelength of the global mode found from linear stability analysis. Quantities shown are the time averaged kinetic energy of the flow, friction factor f and domain averaged Nusselt number $\langle Nu \rangle$.

as can be noted from the friction factor values for these cases.

4.3 Weakly non-linear Stuart–Landau analysis

The last aim of this chapter is addressed in this section, which is to understand the nature of the primary bifurcation from 2D steady state to 3D state using the Stuart–Landau equation as described in § 2.7.

The nature of the primary bifurcation from the two-dimensional steady state to a three-dimensional state is discussed in this section. The mode amplitude measure (A in equation 2.67) used for this analysis is the time history of kinetic energy contained in the leading Fourier mode. The mode amplitude variation with time for various cases considered here are shown in figure 4.11. The mode amplitude time history is then used to obtain plots of $\mathrm{d}(\log|A|)/\mathrm{d}t$ against $|A|^2$ which are shown in figure 4.12 for the same cases as in figure 4.11. For all these cases, it can be observed that the slope is negative at $|A|^2 \approx 0$ (corresponding to $l > 0$ in equation 2.68). Hence, the primary bifurcation of the flow is found to be supercritical for all the parameter combinations tested. This is notable as a wide range of blockage ratios ($0.125 \leq \beta \leq 0.8$) and pitch ($2 \leq \gamma \leq 4$) are captured. The underlying eigenmodes for each of these cases all have positive real eigenvalues (§ 3.2.2). These two findings combine to suggest that the flow undergoes a change to the 3D state via a supercritical pitchfork bifurcation. The supercritical nature of the bifurcation (or absence of subcriticality) is consistent with the weak transient growth at subcritical Reynolds numbers, and indicates the difficulty in promoting unstable states or turbulence at subcritical Re in this system (Reddy & Henningson, 1993; Trefethen *et al.*, 1993; Krasnov *et al.*, 2004; Camobreco *et al.*, 2020).

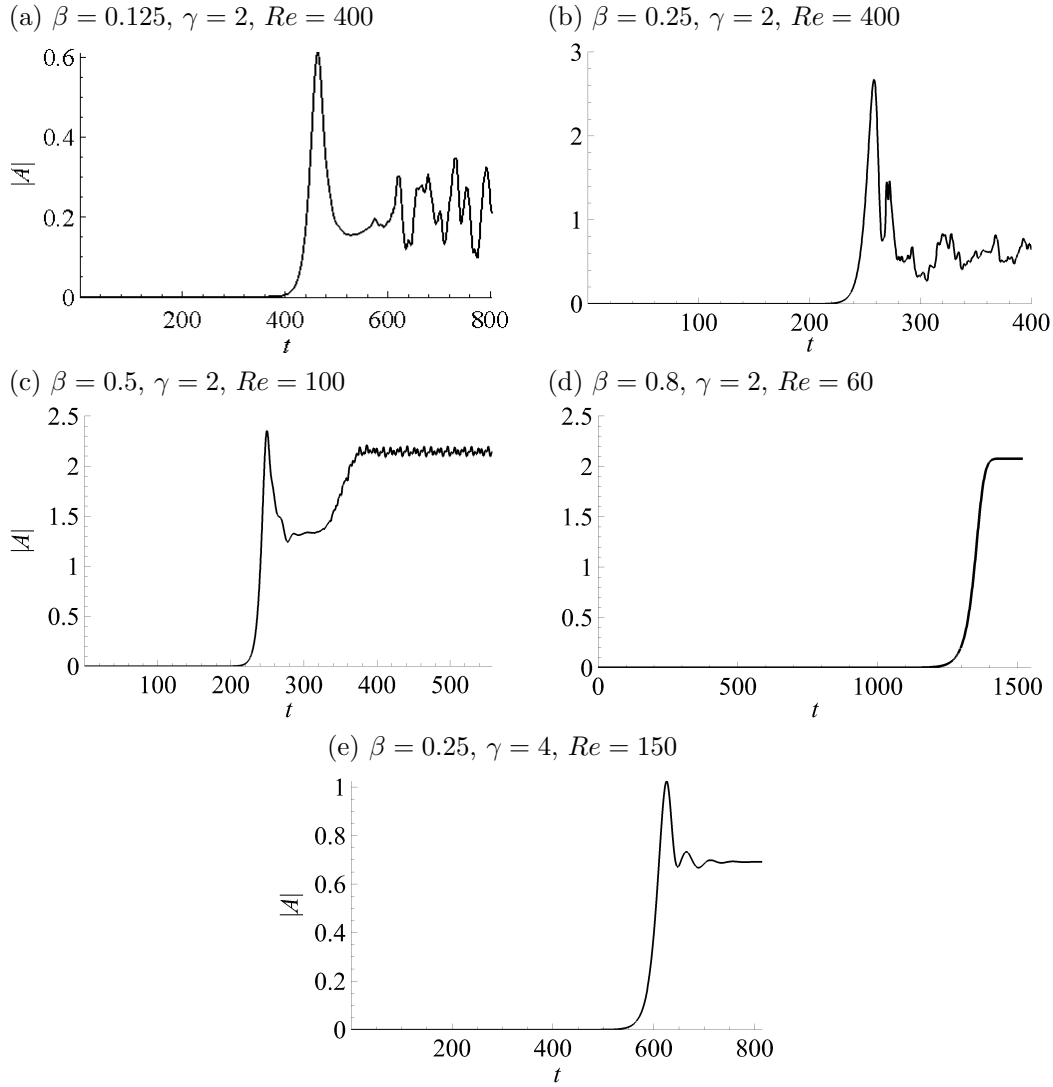

Figure 4.11: Time history of $|A|$ showing the exponential growth and non-linear saturation. The cases here have fixed parameter $\gamma = 2$ and $\tan(\phi) = 0.125$.

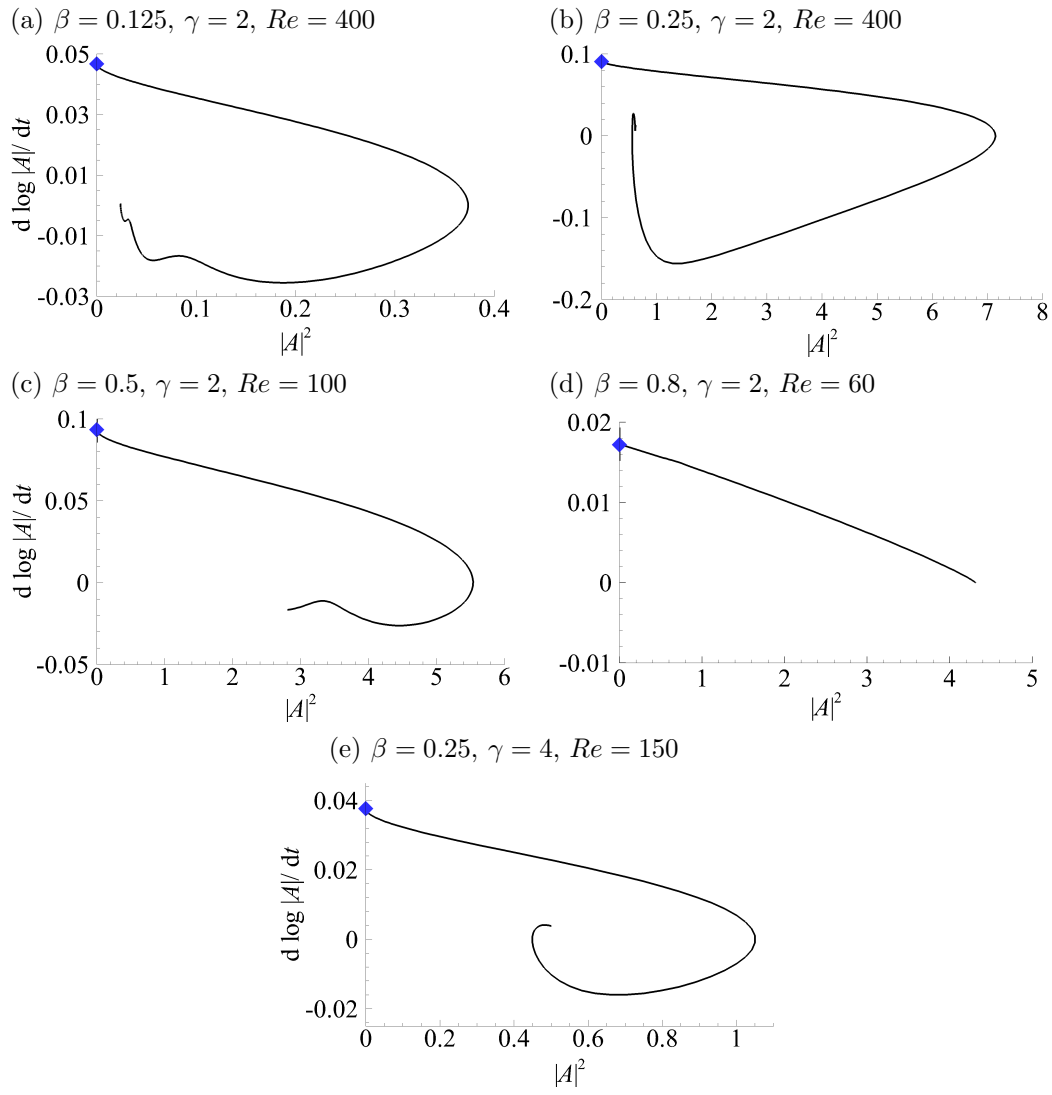

Figure 4.12: Plots of $\mathrm{d}\log|A|/\mathrm{d}t$ against $|A|^2$ with a negative slope ($l > 0$) showing a supercritical bifurcation of the 2D flow to a 3D state. The growth rate of the corresponding critical eigenmode is represented as a diamond symbol. The cases here have fixed parameter $\gamma = 2$ and $\tan(\phi) = 0.125$.

Chapter Summary

Non-linear interactions in the flow evolution in hydrodynamic channel flows with repeated wedge protrusions are explored in this chapter. Investigation of the influence of non-linearity on the transient growth of linear optimal modes shows that non-linearity has a stabilising effect on the growth of the optimal modes. Through monitoring the underlying disturbance structure on naturally evolving the steady state solution of two-dimensional flows, it is verified that the onset of two-dimensional unsteadiness manifests through the global 2D eigenmodes obtained from the linear analysis. Three-dimensional simulations are carried out to verify that the primary three-dimensional bifurcation occurs through the linear global 3D mode obtained from the linear stability analysis. The change in the flow structures as non-linear effects dominates is explained, followed by a dicussion of the effect of selecting the spanwise extent of the domain on the flow structures, temperature field and the bulk flow properties. The nature of the primary bifurcation is found to be a supercritical, supporting the low transient growth observed in the system under consideration.

In the following chapter, the stability characteristics of quasi-two-dimensional MHD flows in ducts with repeated wedge-protrusions are presented.

Chapter 5

Stability of quasi-2D magnetohydrodynamic duct flow with repeated wedge protrusions

The second main objective of this project is addressed in this chapter by considering a quasi-two-dimensional magnetohydrodynamic (MHD) flow though a duct with repeated flow-facing wedge protrusions on the bottom wall. The flow regimes associated with this flow are identified by considering a range of Hartmann friction parameters and Reynolds numbers. A comparison of the flow structure (streamline patterns) is made to the hydrodynamic channel flow case discussed in § 3.1.1. The dominant steady recirculation region identified from the flow regimes are further characterised by describing how the length of this recirculation region varies over a range of Hartmann friction parameters covering low to high values and its dependence on the geometric parameters of the wedge is discussed. Thereafter, the primary bifurcation of the steady quasi-2D flow is elucidated though a linear stability analysis of the flow to quasi-2D perturbations. The quasi-2D modes leading to the primary bifurcation are visualised. Following this, the transient growth of quasi-2D perturbations is described and the possibility of a sub-critical route to transition is examined. A study on the influence of non-linear interactions on the optimal energy growth of quasi-2D disturbances is presented. Lastly, three-dimensional simulations under the low-R_m assumption describing the flow transition are presented as a further validation of the findings from the linear stability analysis.

5.1 Quasi-2D magnetohydrodynamic flow

The flow regimes associated with the quasi-two-dimensional MHD flow through the flow setup described in the introduction (figure 4) are discussed in this section by considering a range of Hartmann friction parameters ($0.5 \leq H \leq 1000$) and blockage ratios ($0.125 \leq \beta \leq 0.65$). Comparison is made with the corresponding hydrodynamic channel flow case from § 3.1. Regime maps are presented and the critical Reynolds number ($Re_{cr,\mathrm{Q2D}}$) for the onset of quasi-2D vortex shedding are identified as a function of H and β. This is followed by a discussion of the characteristics of the dominant recirculation region.

5.1.1 Flow regimes

For flow through the current setup, four different regimes are identified in the range of Harmann friction parameters investigated, based on the flow structure (visualisation of streamline pattern) and the variation of $Re_{cr,\mathrm{Q2D}}$ with H.

The first three regimes produce steady flows, whereas the last identified regime adopts an unsteady state. The features of the flow in each identified regime are shown in figure 5.1, and are described here:

1. Regime-1: This regime manifests at low-H, with the flow features being similar to those of regime-3 in the hydrodynamic channel flow case. Figure 5.1(a-d) shows the streamlines at $H = 0$ and $H = 0.3$, corresponding to regime-1 for $\beta = 0.25$ and $\beta = 0.5$. In this regime, the critical Reynolds number $Re_{cr,\mathrm{Q2D}}$ for the onset of quasi-2D vortex shedding remains almost independent of H at very low H values, and is followed by an increase with further increase in H. This characteristics is the same for all blockage ratios investigated and is shown in figure 5.2.

2. Regime-2: This regime exists only for lower blockage ratios ($\beta \lesssim 0.5$) and intermediate Hartmann friction parameters. Figure 5.1(e,f) shows the streamlines at $H = 40$ and $H = 10$ corresponding to regime-2 for $\beta = 0.125$ and $\beta = 0.25$, respectively. Here, the flow exhibits a change with the formation of a recirculation region immediately after the wedge tip, and splitting of the recirculation region identified in regime-1 into a small recirculation zone in front of the wedge and one extending from the tapered wedge surface of the current wedge to the the gap between the current and the next wedge. The latter recirculation regions still remain dominant in the flow in this regime. An interesting feature of this regime is that $Re_{cr,\mathrm{Q2D}}$ decreases with

increasing H (right of H_{R2} in figure 5.2). Increasing β prepones the onset of this regime and also decreases the range of H over which this regime exists. This can be observed in figure 5.2 with the first and the second dashed lines from the left, corresponding to H_{R2} and H_{R3}, respectively shifting towards lower H. Regime-2 is not observed for $\beta = 0.5$ and $\beta = 0.65$.

3. Regime-3: This regime features only a dominant recirculation region immediately after the wedge tip with all other recirculation regions suppressed in the flow. This holds for all blockage ratios under investigation. The flow streamlines for this regime are shown in figure 5.1(g,h) at $H = 200$ for $\beta = 0.25$ and $\beta = 0.5$. Unlike regime-2, in this regime, $Re_{cr,\mathrm{Q2D}}$ increases monotonically with H (right of H_{R3} in figure 5.2) and appears to converge to a similar $Re_{cr,\mathrm{Q2D}}$ value at very high H for the different β cases considered here. This may be due to the very thin boundary and shear layers formed at very high-H, possibly making the influence of blockage ratio less effective. The discussion of the quasi-2D mode through which instability manifests in these flows in § 5.2.2 will further explain this behaviour.

4. Regime-4: In this regime an unsteady quasi-2D state persists for $Re > Re_{cr,\mathrm{Q2D}}$, with quasi-2D vortex shedding in the flow. This happens when the steady recirculation region identified in the previous (steady) regime breaks up. For the low and intermediate values of H, this is associated with vortices sweeping over the bottom and top walls of the duct for all blockage ratios with $\beta \gtrsim 0.25$ considered in this study. For $\beta = 0.125$, however, two unsteady states are observed similar to that for the non-MHD cases discussed in § 3.1.3. At higher values of H, the unsteady state is associated with vortex shedding starting from the wedge tip and vortices sweeping over the botom wall of the duct at lower blockage ratios ($\beta \lesssim 0.5$), while additional recirculation regions are observed to sweep over the top wall at higher blockage ratios ($\beta \gtrsim 0.5$). These flow features are visualised through an instantaneous spanshot of the spanwise vorticity contours and are shown in figure 5.1(i,j) for a lower and higher bloackge ratio case, respectively.

The Hartmann friction parameter H models the influence of the Hartmann layer on the walls perpendicular to the magnetic field direction. For the current system, $H = r^2(Ha/2)$, where $r = 2L/a$ is the aspect ratio of the duct cross-section and takes into account both the Hartmann number and the aspect ratio of the duct. Increasing H has a stabilising effect on the flow as the perturbations are dissipated by increased Harmann damping. In regime-2, an opposite behaviour

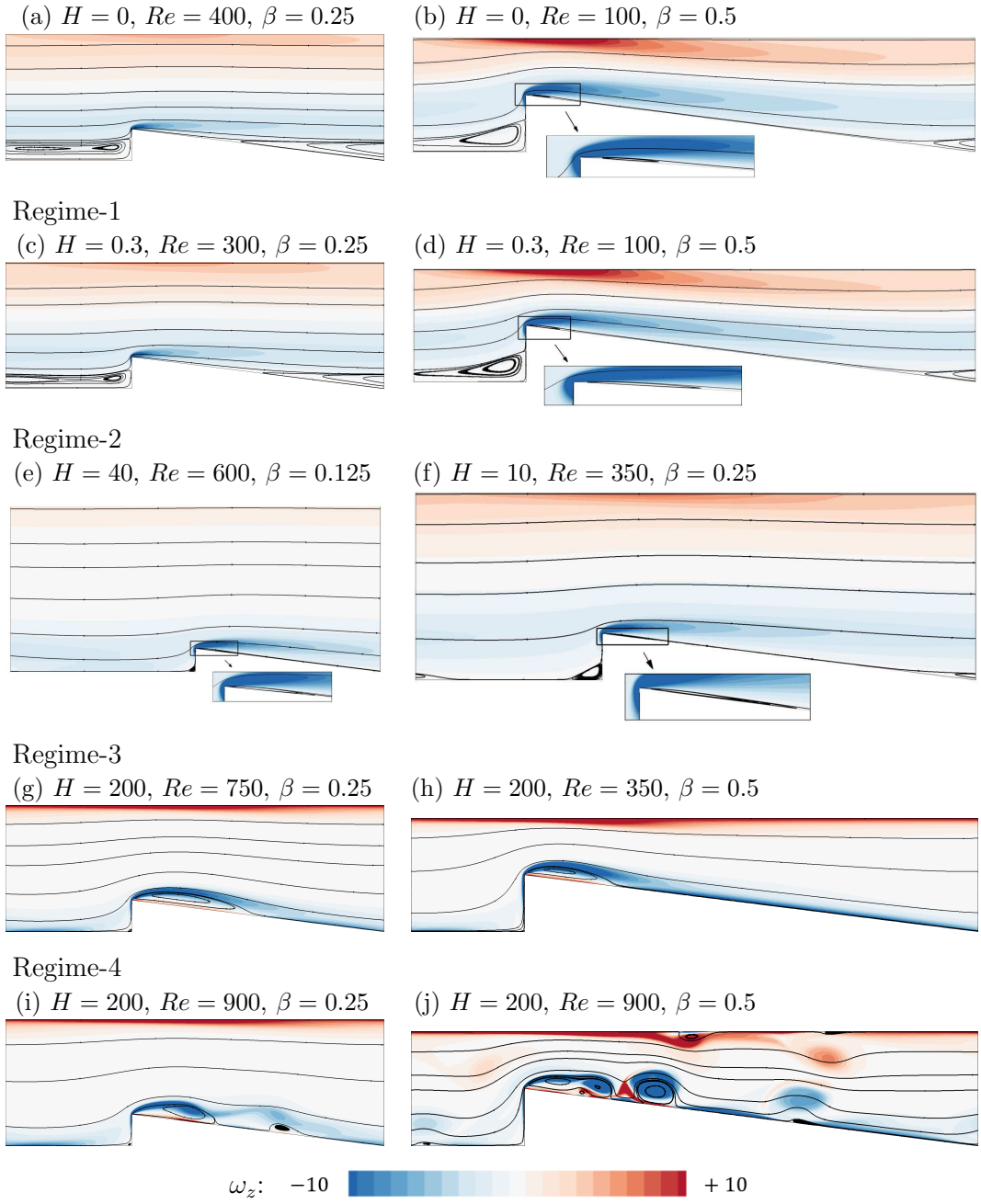

Figure 5.1: Flow regimes associated with change in H shown for different blockage ratios. Shown are the base flow streamlines and spanwise vorticity contours for (a,b) hydrodynamic channel flow cases (c-h) steady quasi-2D MHD regimes 1 to 3 and (i,j) the unsteady quasi-2D MHD regime-4. Instantaneous spanwise vorticity contours are shown for the unsteady regimes in (i,j).

of decreasing critical Reynolds number $Re_{cr,\mathrm{Q2D}}$ with H is observed for cases with $\beta \lesssim 0.5$. This can be explained by considering the change in the flow feature observed in this regime. As discussed earlier, this regime is characterised with the formation of a new recirculation region after the wedge tip, which has the effect of

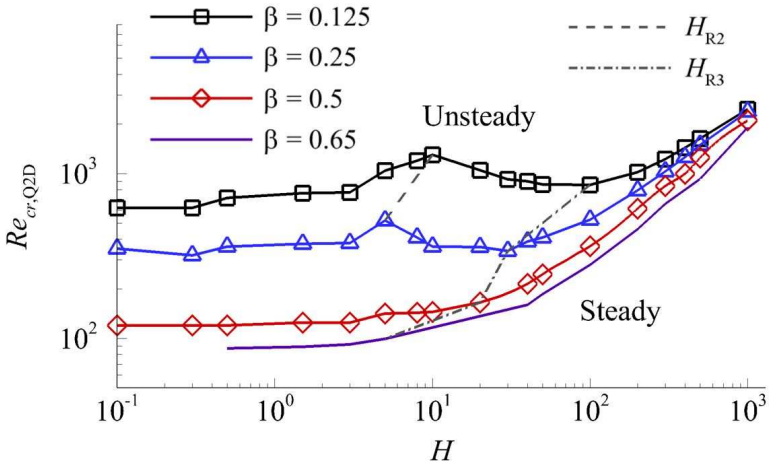

Figure 5.2: Variation of critical Reynolds number ($Re_{cr,\mathrm{Q2D}}$) for the onset of vortex shedding as a function of Hartmann friction parameter H for different blockage ratios β with $\gamma = 2$ and $\tan(\phi) = 0.125$. The approximate critical H for the onset of regime-2 and regime-3 are shown respectively as H_{R2} and H_{R3}. Regime-4 starts beyond $Re_{cr,\mathrm{Q2D}}$.

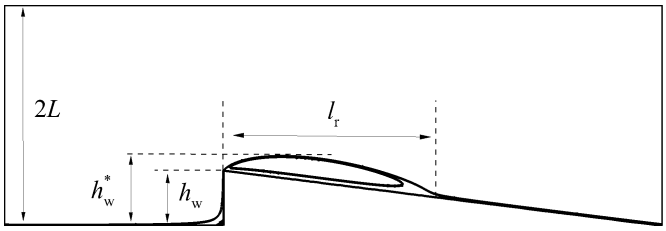

Figure 5.3: Increase in the effective height of the wedge from h_w to h_w^* with the formation of recirculation region of length l_r in the streamwise direction after the wedge tip.

increasing the effective height of the wedge from h_w to h_w^* as shown in figure 5.3, which in turn increases the blockage from $\beta = h_w/2L$ to $\beta^* = h_w^*/2L$ (effective blockage ratio). Increasing blockage ratio is observed to have a destabilising effect on the flow, which can be noted from the lower $Re_{cr,\mathrm{Q2D}}$ value with increasing β in figure 5.2, in the low and intermediate values of H. The decreasing influence of blockage ratio on $Re_{cr,\mathrm{Q2D}}$ can also be observed with the converging values of $Re_{cr,\mathrm{Q2D}}$ at higher H. Owing to the dominant influence of increased blockage ratio relative to the stabilising effect of H, $Re_{cr,\mathrm{Q2D}}$ decreases with H in regime-2. In regime-3, the effect of Hartmann damping dominates the decreasing influence of blockage ratio on the flow and hence $Re_{cr,\mathrm{Q2D}}$ increases with H as expected.

5.1.2 Recirculation length characteristics

As elucidated in § 5.1.1, the recirculation region after the wedge tip starts forming for $\beta \lesssim 0.5$ in the intermediate range of H, whereas it is already present at higher blockage ratio $\beta \gtrsim 0.5$, and becomes the dominant feature of the flow in regime-3 (corresponding to high-H range) for all cases. The characteristics of this dominant steady recirculation region formed immediately after the wedge tip are discussed in this section and compared to similar regions found in other confined quasi-2D flow setups. Figure 5.4(a-d) shows the variation of the length L_r of this recirculation zone with Re for a range of H in the high H-range at different blockage ratios. The dimensionless length of the recirculation region is given by $L_r = l_r/L$, where l_r is the distance in the streamwise direction from the separation point to the reattachment point of the recirculation bubble on the tapered wedge surface and L is half-duct height (figure 5.3). L_r varies approximately linearly with Re for all the H investigated with the rate of increase of L_r with Re decreasing with H. Similar behaviour was also observed for all the β investigated. The characteristics of this recirculation region exhibits similarity to that of a steady recirculation region formed behind cylindrical bluff body in a confined quasi-2D MHD flow (Hussam *et al.*, 2012*b*). For a similar setup as in Hussam *et al.* (2012*b*), Dousset & Pothérat (2008) showed a collapse in L_r curves at higher Hartmann numbers Ha ($H = 40$ for a duct with aspect ratio 1 in their case) and found that L_r followed the relationship $L_r \sim Re/Ha^{0.8}$. A similar collapse is found in the present setup only for $H \gtrsim 300$. In the range of Hartmann paramaters $100 \leq H \leq 2000$, it is found that the change of L_r with Re follows a correlation of $\mathrm{d}L_r/\mathrm{d}Re \approx 0.8(H/\beta)^{-0.8}$ for blockage ratios $0.125 \leq \beta \leq 0.65$. A collapse of the curve $\mathrm{d}L_r/\mathrm{d}Re$ is shown in figure 5.4(e,f). A linear fit to the logarithm of these values follows $\log_{10}(\mathrm{d}L_r/\mathrm{d}Re) \approx -0.8\log_{10}(H/\beta) - 0.1$ accurate to R^2=0.98.

5.2 Linear stability of quasi-two-dimensional flow

The quasi-2D flow regimes were mapped in § 5.1.1 and the recirculation length variation of the dominant recirculation region was quantified in § 5.1.2. In this section, the linear stability of the steady quasi-2D MHD flow ranging over the different regimes identified, and spanning over a range of H, blockage ratio and pitch is elucidated. The focus is on the possible scenario of bifurcation from the steady to the unsteady state through quasi-2D modes found through a global instability mode. For these cases, the growth rate of the quasi-2D modes and

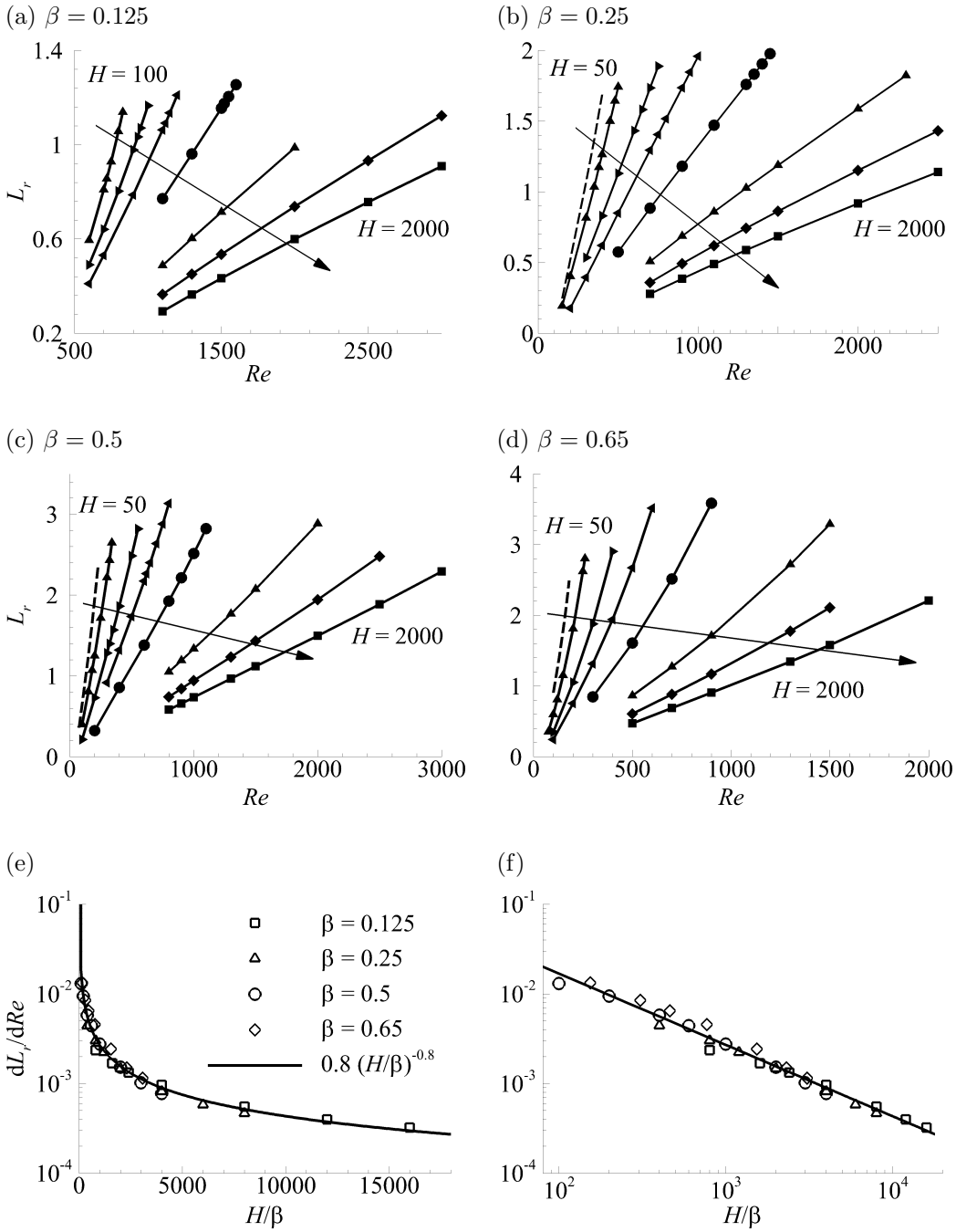

Figure 5.4: (a-d) Variation of recirculation length L_r as a function of Re and H (arrow indicates the direction of increasing H with first and the last H as indicated) and (e,f) collapse of $\mathrm{d}L_r/\mathrm{d}Re$ when plotted against H/β in the range $100 \leq H \leq 2000$ and $0.125 \leq \beta \leq 0.65$.

the critical Reynolds number $Re_{cr,\mathrm{Q2D}}$ are obtained for different blockage ratios and pitch values. Comparison of the MHD cases to the corresponding non-MHD case ($H = 0$) is also made. Following the discussion of the critical parameters and their dependence on H, β and γ, the global quasi-2D eigenmodes associated

with these flows and the mode responsible for the onset of the instability are elaborated.

5.2.1 Growth rate and critical parameters of quasi-2D perturbations

Linear stability analysis (§ 2.2) is performed on the steady state solutions of the quasi-2D flow (Citro *et al.*, 2017). The growth rate of quasi-2D perturbations is presented here for different H covering the low, intermediate and high-H range, and considering various β and γ values. In figure 5.5, the growth rate curves as a function of Re are shown for $H = 5$, and compared with the corresponding hydrodynamic channel flow case at $H = 0$. Similar curves for the intermediate and high-H ranges are also shown in figures 5.6 and 5.7, respectively. For all these cases, it is observed that the steady quasi-2D flow is associated with a dominant eigenmode associated with a real eigenvalue (labelled QM1), which remains stable to quasi-2D perturbations over a range of Re. On approaching the Reynolds number where the flow is unsteady, a subdominant eigenmode associated with complex eigenvalue (labelled QM2) is observed. The growth rate of QM2 shows a rapid rise and ultimately becomes responsible for the quasi-2D vortex shedding. A second subdominant mode associated with complex eigenvalue (labelled QM3) is also observed whose growth rate remains closely behind that of QM2. The growth rate trends are similar to what is observed for the 2D disturbance in the hydrodynamic channel flow case (figure 5.5), although for the quasi-2D MHD cases, this is associated with the primary bifurcation of the flow to a quasi-2D unsteady state, because three-dimensional modes are excluded by the two-dimensionality of the model.

The critical Reynolds number $Re_{cr,\mathrm{Q2D}}$ for the onset of quasi-2D vortex shedding found though linear stability analysis for the different cases studied are given in table 5.1. Irrespective of the value of H, increasing the blockage ratio always results in a destabilisation of the flow, which can be noticed as a decrease in the critical Reynolds number (both $Re_{cr,\mathrm{Q2D}}$ and $Re_{cr,\mathrm{2D}}$) with increasing β. In the low and intermediate ranges of H investigated, the quasi-2D flow becomes more unstable with increasing pitch. This trend matches the observation made for the hydrodynamic cases. However, in the higher range of H considered in this study, the quasi-2D flow becomes increasing stable to quasi-2D disturbances when increasing the pitch. The streamwise wavenumber of the quasi-2D unstable mode is seen to increase with increasing H, and it is possible that the lower pitch cases at higher H, already captures the unstable wavenumbers, contrasting the

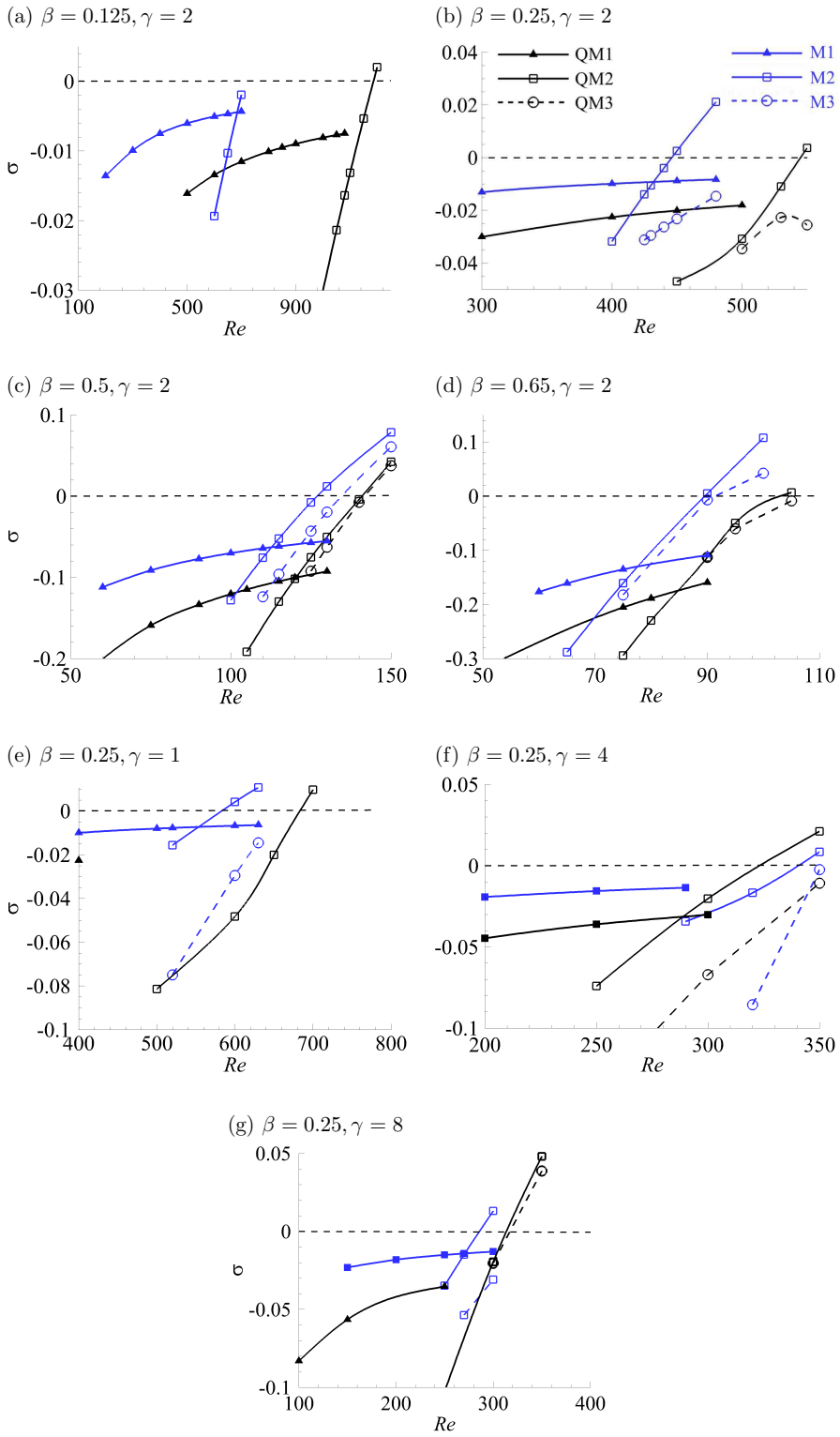

Figure 5.5: Plots of growth rate against Re in the low-H range ($H = 5$) for different geometric parameter combinations. Real and complex eigenvalues are denoted by closed and open symbols, respectively. Triangle, square and circle symbols represent mode QM1, QM2 and QM3, respectively. The growth rate of the corresponding hydrodynamic channel flow case ($H = 0$) is shown in blue for comparison. The symbols for $H = 0$ cases are as in figure 3.7. All cases here have $\tan(\phi) = 0.125$.

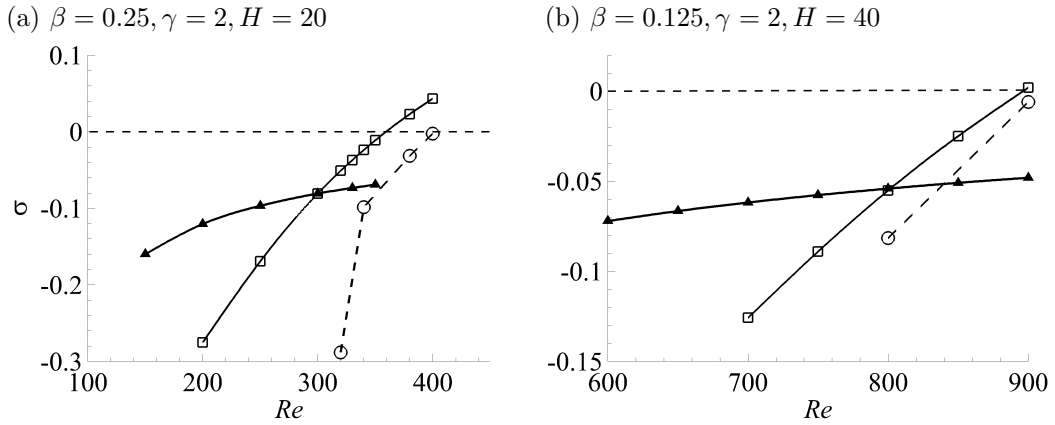

Figure 5.6: Plots of growth rate against Re at (a) $H = 20$ and (b) $H = 40$ range for different geometric parameter combinations as indicated. Line labels are as per figure 5.5. All cases here have $\tan(\phi) = 0.125$.

β, γ	$H = 0$	$H = 5$	$H = 200$
0.125, 2	712.16	1185.93	1021.85
0.25, 2	445.93	545.14	788.91
0.5, 2	126.92	141.39	612.27
0.65, 2	89.56	99.27	460.39
0.25, 1	582.23	684.03	724.51
0.25, 4	340.83	322.62	927.81
0.25, 8	285.73	313.35	1150.20

Table 5.1: Critical Reynolds number $Re_{cr,\text{2D}}$ for the onset of 2D vortex shedding and, $Re_{cr,\text{Q2D}}$ for the onset of quasi-2D vortex shedding over a range of Hartmann parameters H for different blockage ratios and pitch. Wedge angle for the cases here is $\tan(\phi) = 0.125$.

findings for the lower-H regimes. Hence, any further increase in pitch results in an increased stability of the quasi-2D flow in this regime.

5.2.2 Quasi-2D eigenmodes

From § 5.2.1 it was found that the flow eigenspectrum contains three significant quasi-2D eigenmodes QM1, QM2 and QM3, and the onset of quasi-2D vortex shedding is consistently associated with a complex quasi-2D mode (QM2) over a range of H. In this section, these eigenmode structures are discussed. The unstable complex mode QM2, the stable subdominant real mode QM1 and complex mode QM3 are shown for different cases in the low, intermediate and high-H regimes in figures 5.8-5.10. Over the range of H, the destabilising mode QM2 appears as a wave extending over the flow domain observable in the $\hat{v}$ contours. In the low-H range, the opposite signed vorticity structures appear over the bot-

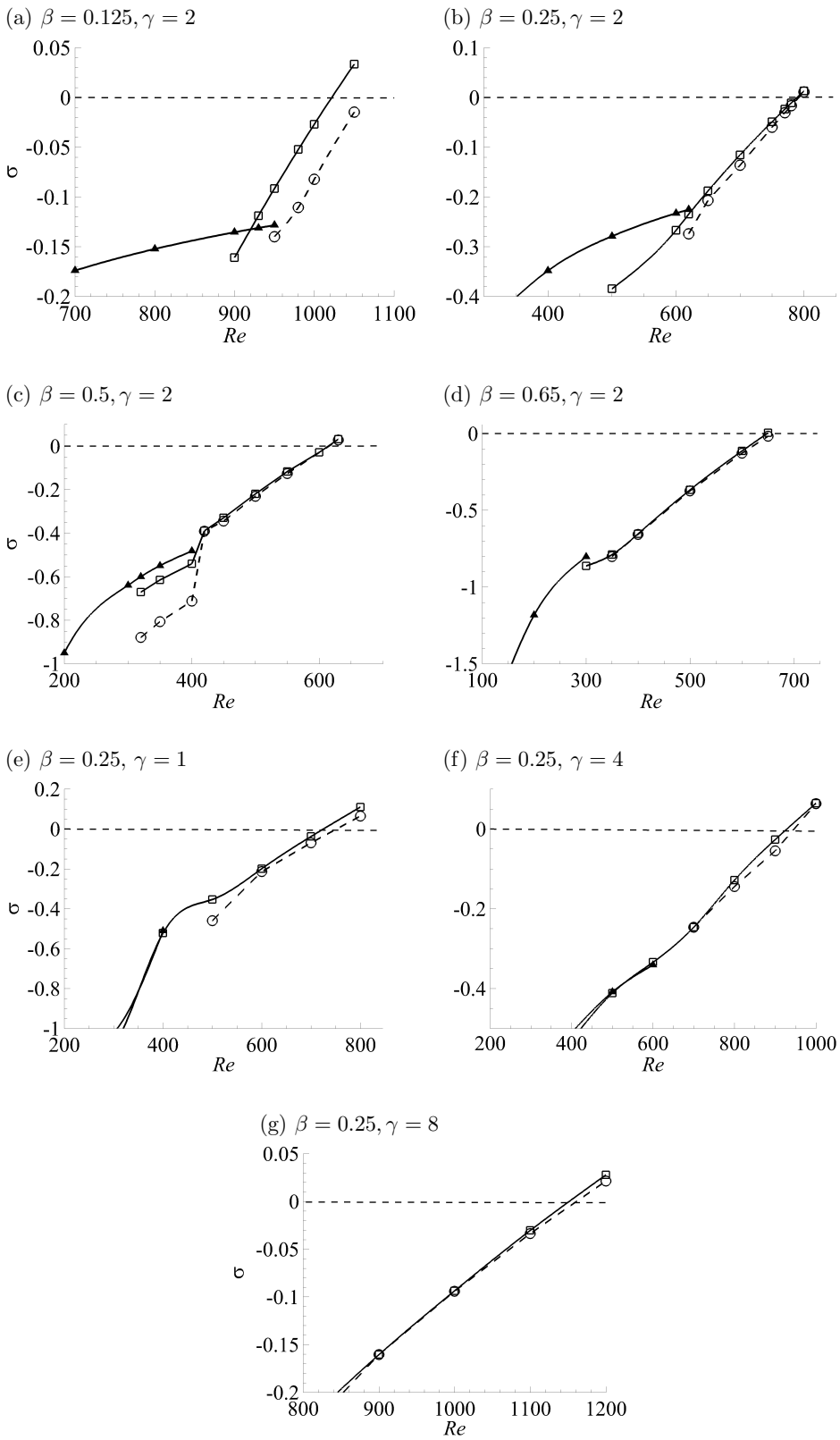

Figure 5.7: Plots of growth rate against Re in the high-H range ($H = 200$ for (a-c) and (e-g) and $H = 300$ for d) for different geometric parameter combinations. Line labels are as per figure 5.5. All cases here have $\tan(\phi) = 0.125$.

tom and top walls, extending over the streamwise length of the flow domain, suggesting an instability of the bottom and top wall boundary layers. QM3 is a similar mode to QM2, with a smaller streamwise wavenumber. These modes have a similar structure as the 2D modes found in the corresponding hydrodynamic channel flow cases (figure 3.8) and are the quasi-2D equivalent of the 2D modes M1, M2 and M3.

In the intermediate range of H, as the base flow structure changes (figure 5.1e,f), the vortical structures of QM2 appear to become concentrated near the newly formed recirculation region immediately after the wedge tip. At a higher H, although the eigenmode structure seems similar, they are now more intense around the dominant recirculation region (figure 5.1g,h) formed after the wedge tip and concentrated in the much thinner Shercliff boundary layer on the walls. This reinforces the point that there is a lesser influence of blockage ratio on the flow instability at higher values of H as raised in § 5.1.1. The vortices in the subdominant complex mode QM3 in these cases are more closely spaced than those of mode QM2. The eigenmodes in MHD duct flows were found to be the quasi-2D MHD equivalent of the Tollmien–Schlichting waves (Pothérat, 2007) lying entirely within the Shercliff layers. In the present setup, although the mode structures lie within the Shercliff layers, the presence of the wedge causes the modes to be concentrated along the free shear layer formed over the recirculation region and along the subsequent slanted wedge surface. The instability in these high-H regimes appears to manifests due to the combined effects of the instability of the free shear layer and the boundary layer on the tapered wedge surface.

5.3 Linear transient growth

It was found from the the linear stability analysis in § 5.2 that, over a range of Hartmann friction parameters, the quasi-2D MHD flow bifurcates to a quasi-2D unsteady state via a global quasi-2D modal instability. The corresponding mode shapes and locations were identified and discussed. In this section, the corresponding linear transient growth behaviour of quasi-2D perturbations are studied. For MHD channel flows and duct flows in the presence of a spanwise magnetic field, there has been strong disagreement between the critical Reynolds number predicted by linear stability analysis (Ting *et al.*, 1991) to those observed in experimental studies (Reed & Picologlou, 1989). Later studies (Pothérat, 2007; Krasnov *et al.*, 2008, 2010) have found that the reason for the strong disagreement is because these flows undergo a bypass transition by large transient amplication

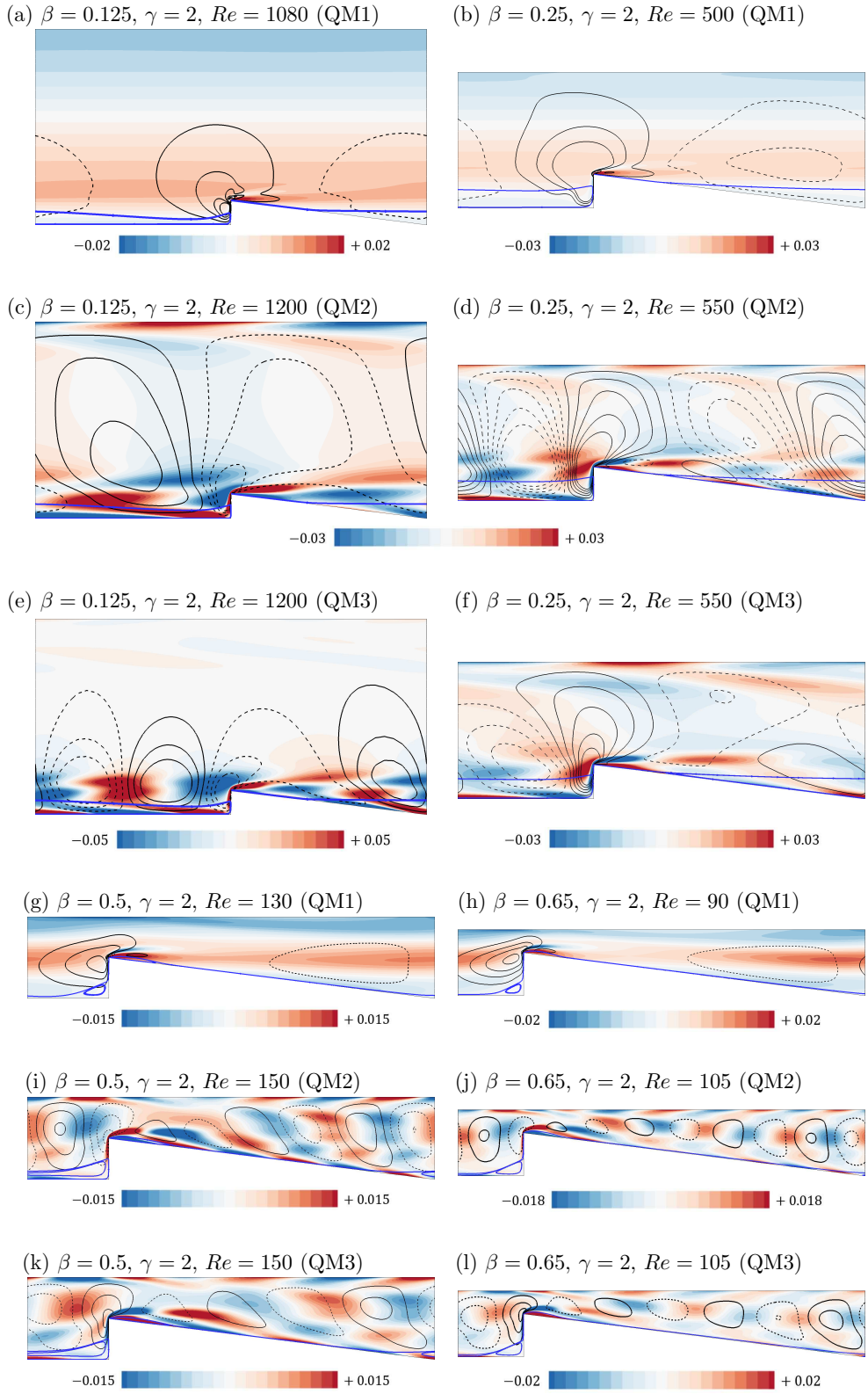

Figure 5.8: Flooded contours of z-vorticity ($\hat{\omega}_z$) superimposed by line contours of transverse velocity $\hat{v}$ of the dominant (QM2) and sub-dominant quasi-2D eigenmodes (QM1, QM3) at $Re > Re_{cr,\mathrm{Q2D}}$ in the low-H range ($H = 5$). The quasi-2D base flow streamlines are overlaid in blue. Line contour levels equidistant from zero are chosen arbitarity to visualise the structures.

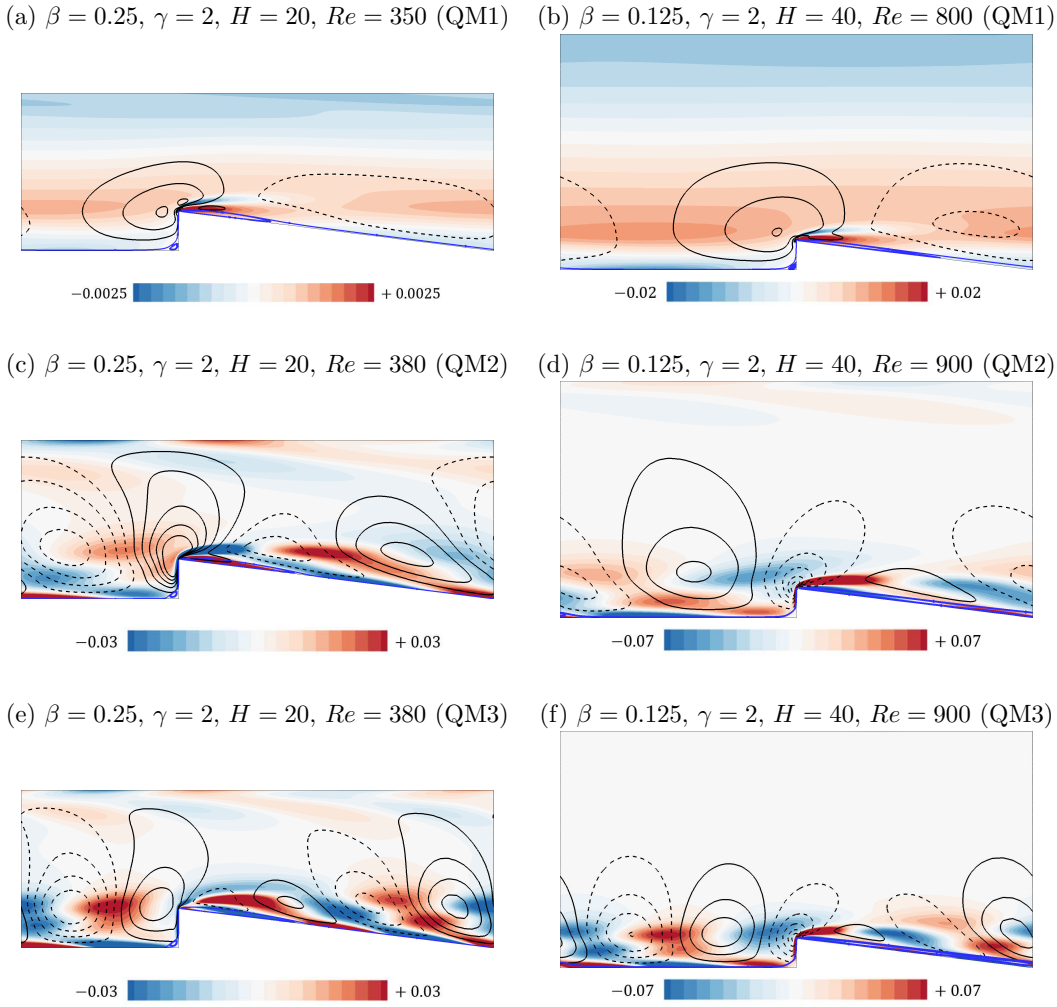

Figure 5.9: Flooded contours of z-vorticity ($\hat{\omega}_z$) superimposed by line contours of transverse velocity $\hat{v}$ of the dominant (QM2) and sub-dominant quasi-2D eigenmodes (QM1, QM3) at $Re > Re_{cr,\mathrm{Q2D}}$ in the intermediate-H range. The quasi-2D base flow streamlines are overlaid in blue. Line contour levels equidistant from zero are chosen arbitarity to visualise the structures.

of non-modal perturbations. Therefore, understanding the transient growth is important to completely understand the nature of transitions in the system under consideration. In duct flows, the SM82 model has been found to predict transient energy amplification with excellent agreement against three-dimensional analysis in the limit of high Hartmann number, $Ha \gtrsim 100$ (Cassells *et al.*, 2019). Thus, analysis of the transient behaviour of quasi-2D perturbations has been considered extensively. Here the optimal growth and the corresponding quasi-2D initial disturbances are discussed. The possibility of a sub-critical route to transition is also explored by studying the non-linear interactions in the transient energy growth of the quasi-2D optimal modes.

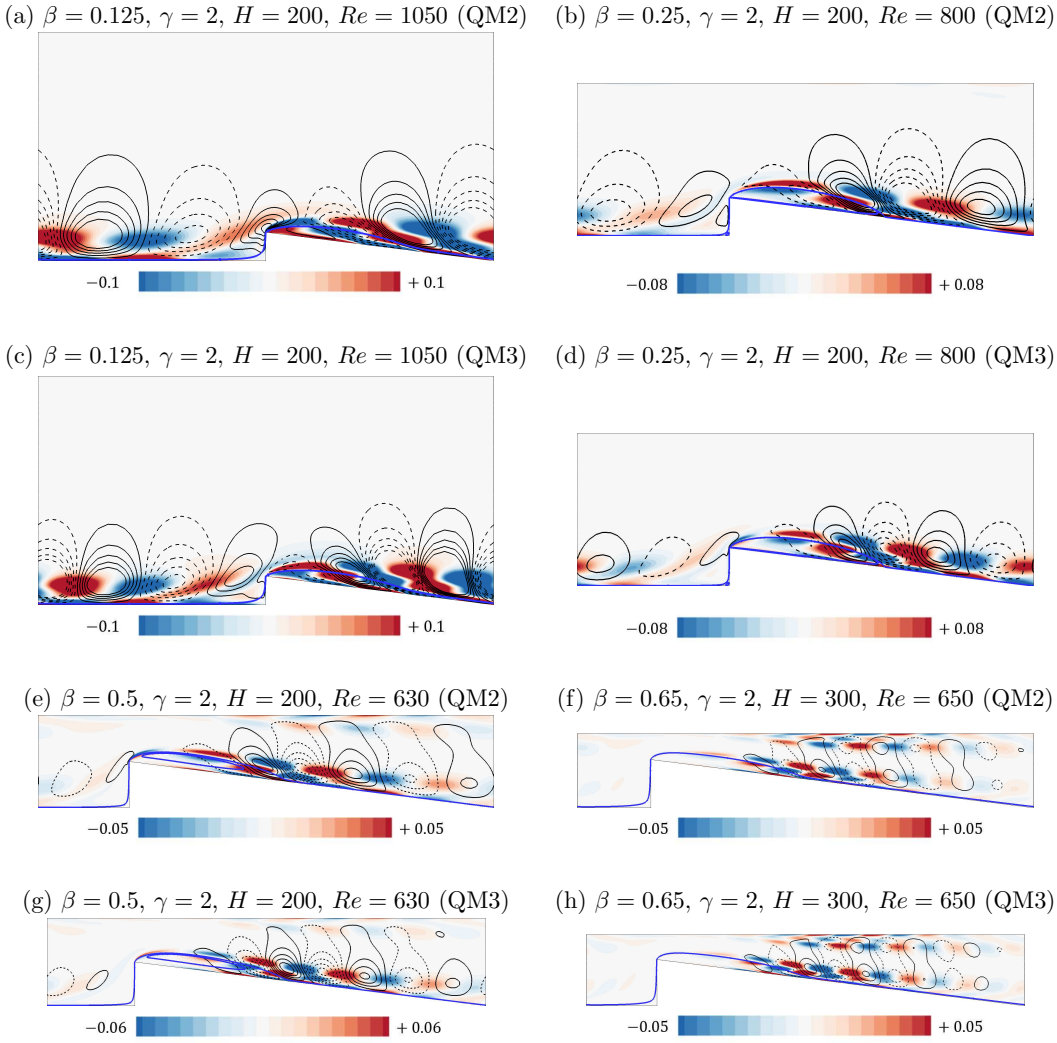

Figure 5.10: Flooded contours of z-vorticity ($\hat{\omega}_z$) superimposed by line contours of transverse velocity $\hat{v}$ of the dominant (QM2) and sub-dominant quasi-2D eigenmode (QM3) at $Re > Re_{cr,\mathrm{Q2D}}$ in the high-H range. The quasi-2D base flow streamlines are overlaid in blue. Line contour levels equidistant from zero are chosen arbitarity to visualise the structures.

5.3.1 Optimal growth of quasi-2D perturbations

The linear transient growth of quasi-2D perturbations is discussed in this section for a range of Hartmann friction parameters $5 \leq H \leq 1000$, and Reynolds number in the linearly stable range ($Re < Re_{cr,\mathrm{Q2D}}$). The optimal energy growth curves of quasi-2D perturbations are shown in figure 5.11 for different H and Re for a case with $\beta = 0.25$, $\gamma = 2$ and $\tan(\phi) = 0.125$. In the range of Reynolds number considered (maximum $Re \approx 0.95 Re_{cr,Q2D}$), the optimal energy of quasi-2D disturbances rises monotonically to a peak and subsequently exhibits an undulating decay with increasing time horizon. Unlike the hydrodynamic cases (figures

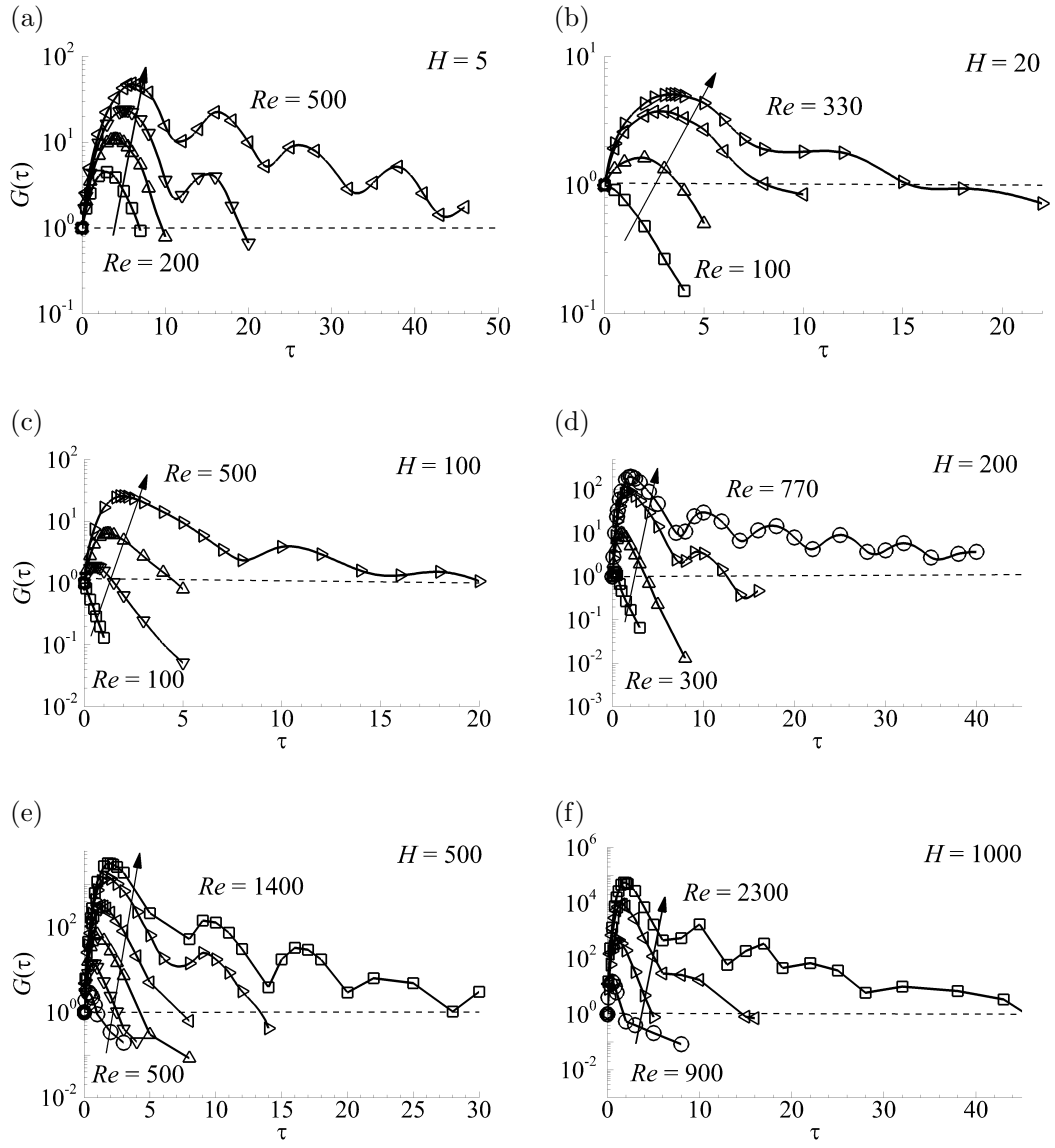

Figure 5.11: Plots showing the optimal energy growth of quasi-2D perturbations plotted against time horizon τ for $5 \leq H \leq 1000$ at different Reynolds numbers in the linearly stable range $Re < Re_{cr,\mathrm{Q2D}}$. Arrow indicates the direction of increasing Re with the first and the last Re as indicated.

3.24 and 3.25), multiple subsequent smaller peaks can be observed in the optimal growth curves during the decay of the perturbation optimal energy. It will be shown in the results to follow that in the low-H regimes, the subsequent peaks are associated with the disturbance structure impinging on the subsequent wedges, however, for the intermediate and high-H cases the subsequent peaks during decay are associated with the energy gain from the free shear layer at the time when the disturbance structure passes over the recirculation region formed immediately after the wedge tip.

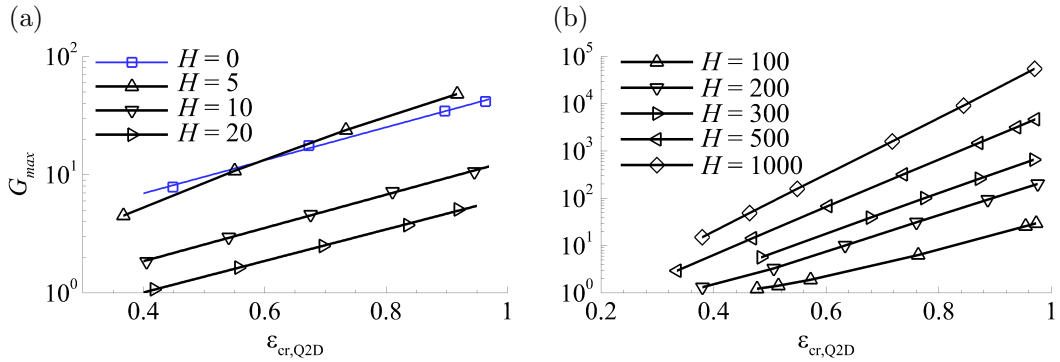

Figure 5.12: Plot showing G_{max} against $\varepsilon_{\text{Q2D}} = Re/Re_{cr,\text{Q2D}}$ in the (a) low ($H = 5$) and intermediate-H ranges ($H = 10$, $H = 20$) along with a comparison of the non-MHD case ($H = 0$), and (b) the high-H range ($100 \leq H \leq 1000$).

Maximum optimal growth G_{max} is obtained for the various cases and its variation with Re is further interrogated here. Observation made from figure 5.12(a) shows that for the low-H case ($H = 5$), G_{max} variation with $\varepsilon_{\text{Q2D}} = Re/Re_{cr,\text{Q2D}}$ is comparable to the $H = 0$ case, with a maximum growth between $\mathcal{O}(10) - \mathcal{O}(10^2)$, whereas in the intermediate range of Hartmann friction parameters ($H = 10, 20$), G_{max} remains lower than the former cases (maximum $G_{max} \sim \mathcal{O}(10)$). This deflation of maximum transient amplification may be attributed to the increasing Hartmann friction damping as H increases. In the low-H cases, the range of Re over which the flow remains linearly stable is almost comparable to $H = 0$ case, whereas in the intermediate-H range, this range of Re slightly decreases. This can be noted from the flow regime map in figure 5.2 for $\beta = 0.25$. On the other hand, in the high-H range of parameters, the flow remains linearly stable over a wider range of Re, increasing the horizon of Re over which transient growth is possible. An exponential increase in the maximum optimal energy gain can be seen with Re approaching $Re_{cr,\text{Q2D}}$ (ε_{Q2D} approaching 1) in the high-H cases (figure 5.12b), with the maximum growth achieving a much higher value with increasing H. In the case of a plane duct without wedges, G_{max} near $\varepsilon_{\text{Q2D}} \sim 1$ was found to be $\mathcal{O}(10^2)$ at $H = 1000$ (Pothérat, 2007). For the present setup $G_{max} \sim \mathcal{O}(10^5)$ is achieved at similar parameters. Thus, the presence of wedges can be more effective to achieve higher transient amplification of perturbation energy at higher H, contrasting the corresponding non-MHD case and the low and intermediate-H range. This is particularly appealing in the context of fusion blanket applications, where the Hartmann numbers are inevitably very high due to the intense confining magnetic fields (Sommeria & Moreau, 1982; Barleon *et al.*, 1991; Kirillov *et al.*, 1995; Abdou *et al.*, 2015).

At Reynolds numbers close to the critical value for the onset of quasi-2D vortex

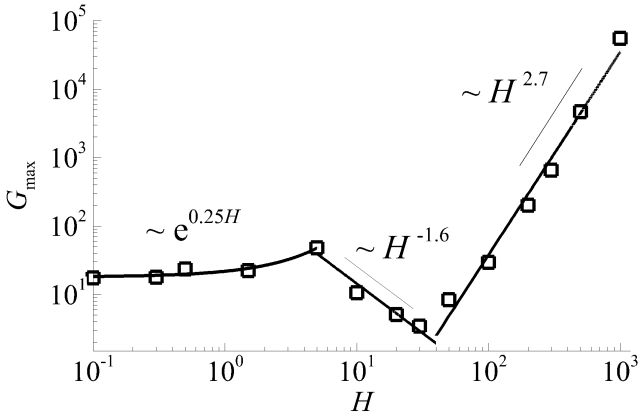

Figure 5.13: Variation of G_{max} with H at Re close to neutral stability, in the range $0.97 \lesssim \varepsilon_{\text{Q2D}} \lesssim 0.99$.

shedding ($0.97 \lesssim \varepsilon_{\text{Q2D}} \lesssim 0.99$), the dependence of G_{max} and its scaling with Hartmann friction parameter is shown in figure 5.13. A clear switch in the scaling with H is observed when the flow structure of the quasi-2D base flow changes. Across these almost neutrally stable Reynolds numbers, the maximum optimal energy gain increases approximately exponentially with H in the low-H range, with G_{max} increasing from approximately $20-50$ up to $H = 5$. With an observable change in the flow structure of the quasi-2D base flow in the intermediate-H range, G_{max} decreases approximately as $H^{-1.6}$. With the recirculation region after the wedge tip becoming dominant in the high-H range, the maximum optimal energy growth of the quasi-2D modes increases almost as $H^{2.7}$ and is found to be $G_{max} \sim 10^5$ at the highest H value investigated. Investigation of the optimal modes associated with each of the three regimes and their evolution in the domain will help further understand the energy gain mechanism of the optimal modes and are discussed in the following section.

5.3.2 Quasi-2D optimal mode

In this section, the quasi-2D optimal mode corresponding to the maximum optimal growth in the low, intermediate and high-H ranges as identified in figure 5.13 is elucidated and compared with the corresponding non-MHD case ($H = 0$). In the low-H range, the quasi-2D base flow structure is found to remain similar to the hydrodynamic channel flow case shown in § 5.1.1. The quasi-2D optimal mode for the low-H cases also has a similar structure as the 2D optimal mode (figures 3.26-3.28 at $t = 0$) and appears as slanted counter-rotating vorticity bands stacked against one another just in front of the separation point on the slanted surface of the wedge. This is shown in figure 5.14(a) for a low Hartmann friction

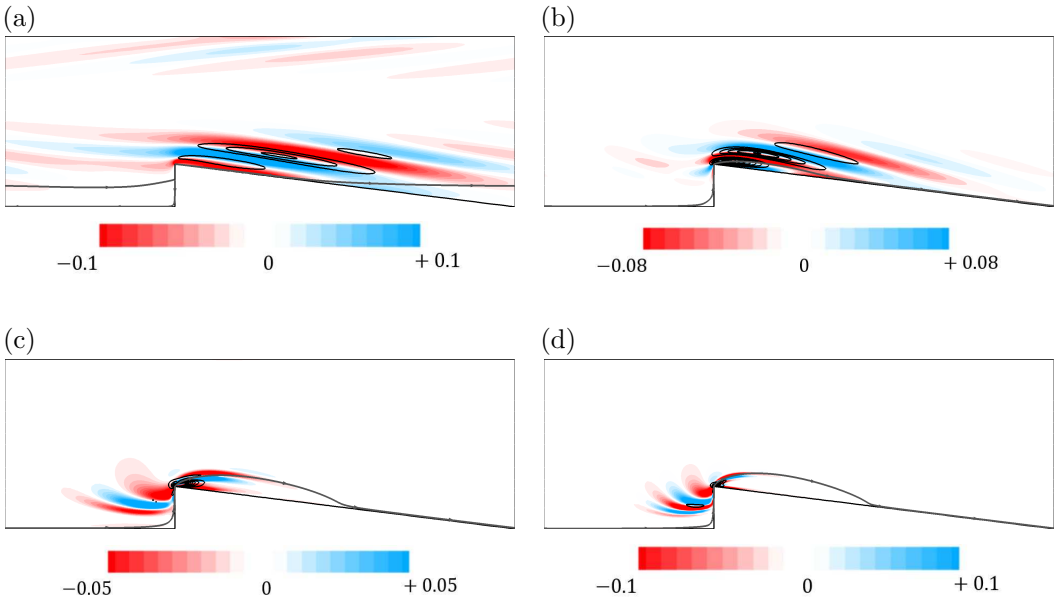

Figure 5.14: Spanwise vorticity ($\hat{\omega}_z$) contours of the initial quasi-2D optimal mode shape for the (a) low ($H = 1.5$ at $Re = 360$), (b) intermediate ($H = 30$ at $Re = 330$) and (c,d) high-H ($H = 200$ at $Re = 770$ and $H = 1000$ at $Re = 2300$) regimes overlaid by the perturbation kinetic energy contours (black line contours). The dividing steamline of the base flow is also shown. Energy iso-contours are shown at 10 equispaced levels between 0 and 0.0002 for (a-c), and between 0 and 0.0005 for (d). The parameter combination considered for these cases is $\beta = 0.25$, $\gamma = 2$ and $\tan(\phi) = 0.125$.

parameter of $H = 1.5$. The quasi-2D optimal mode maintains a similar structure in the intermediate range of H, where a change in the the base flow structure as formation of a recirculation region just after the wedge tip is observed. However, the spanwise extent of mode structure is slightly lower, and the stacked optimal disturbance structures are concentrated on top of the newly formed recircualtion region after the wedge tip shown in figure 5.14(b). The spatial location of quasi-2D optimal modes in the high-H regime shifts further upstream, with the disturbance structure appearing as counter-rotating structures concentrated about the wedge tip, extending from the vertical wall of the wedge slightly over to the separating streamline of the recirculation region after the wedge tip which is the dominant feature in the high-H range (figures 5.14c,d).

For a range of H covering the three regimes, the linear evolution of the quasi-2D optimal mode structures in the quasi-2D base flow and the mechanism through which the disturbance energy are amplified is compared and presented next. In figure 5.15 the normalised energy of the disturbance structure during the linear evolution is compared for different H over the three regimes. The peak energy growth and the corresponding time with the presence of Hartmann damping is

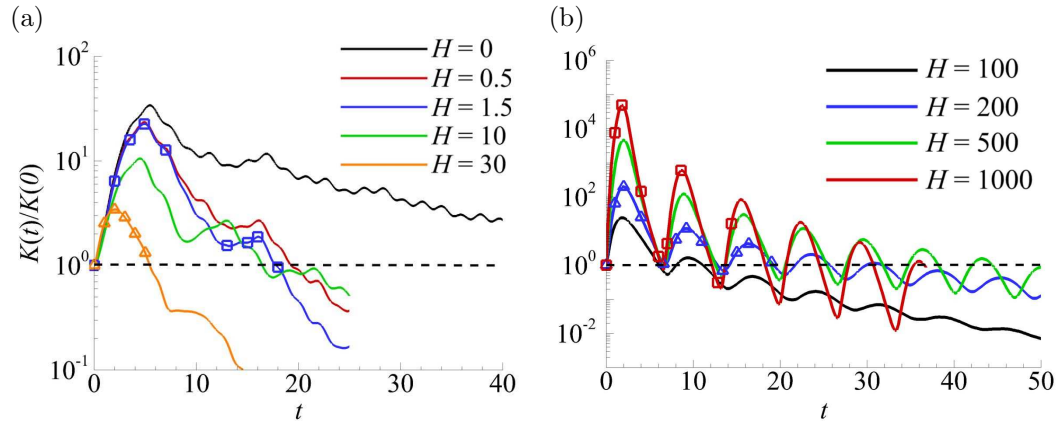

Figure 5.15: Time evolution of normalised kinetic energy of quasi-2D disturbances starting from the optimal quasi-2D mode for (a) $0 \leq H \leq 30$ and (b) $100 \leq H \leq 1000$ in the range $0.92 \lesssim \varepsilon_{\text{Q2D}} \lesssim 0.97$. The parameter combination considered for these cases is $\beta = 0.25$, $\gamma = 2$ and $\tan(\phi) = 0.125$.

lower than the hydrodynamic case ($H = 0$) and decreases with increasing effect of Hartmann friction over the low and intermediate-H range as shown in figure 5.15(a). A much faster rate of energy dissipation can also be noted from the energy curves for these cases. Contour plots illustrating the linear evolution of the optimal mode structures are shown in figures 5.16 and 5.17 for a low ($H = 1.5$) and intermediate-H ($H = 30$) case respectively. In both of these cases, the energy gain of the quasi-2D optimal mode is through tilting upright by the background shear suggesting an Orr mechanism (Orr, 1907), similar to the energy amplification mechanism in 2D optimal modes in $H = 0$ discussed in § 3.5.1. The time for the structures to tilt upright decreases with H, due to the shorter streamwise extent of the structures with increasing H, until the intermediate-H range. The enhanced dissipation of the energy contained in the disturbance structure at a higher H can also be visualised and compared in the low and intermediate-H cases, from the frames corresponding to times after τ_{opt} in figures 5.16 and 5.17. The subsequent smaller peak observed for the low-H cases correspond to the time when the disturbance structure impinge on the subsequent wedge (observed as a small energy gain about the wedge tip at $t = 15$ and $= 16$ in figure 5.16). This behaviour is also similar to the corresponding non-MHD cases discussed in § 3.5.1.

Unlike the low and intermediate-H cases, the peak energy growth of the disturbance shows a rise with increasing H in the high-H cases as shown in the normalised energy curves in figure 5.15(b). Another distinguishing feature that can be noticed from these curves is the multiple peaks of progressively smaller

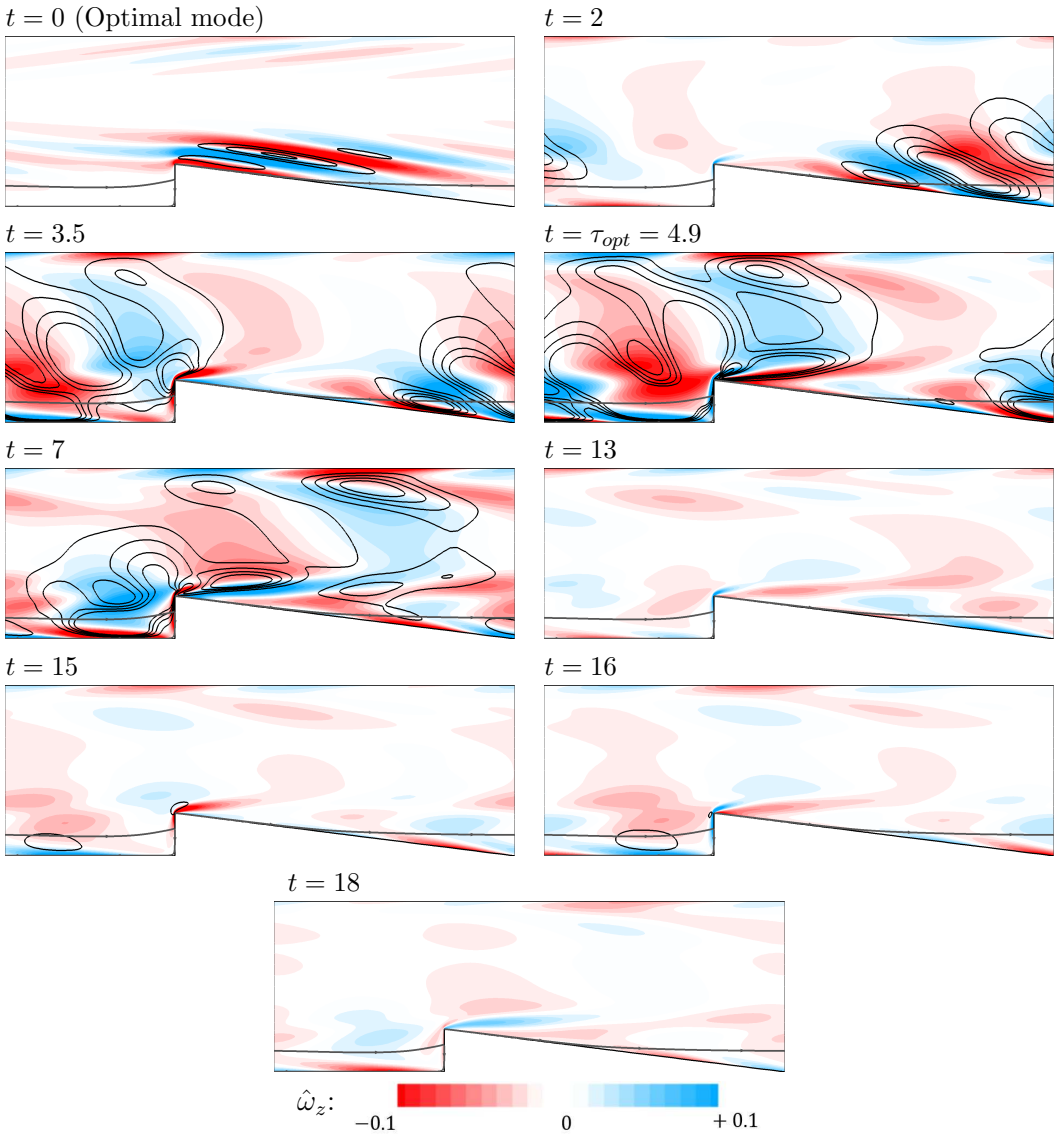

Figure 5.16: Spanwise quasi-2D perturbation vorticity ($\hat{\omega}_z$) contours overlaid by perturbation kinetic energy contours (black line contours) for $\beta = 0.25$, $\gamma = 2$ at $H = 1.5$, $Re = 360$, and its linear evolution over time. The initial condition at $t = 0$ is the optimal mode, and the subsequent times correspond to the square marker positions for this case shown in figure 5.15(a). The dividing streamline of the base flow is also shown. Energy iso-contours are shown at 10 equispaced levels between 0 and 0.0002.

amplification for these cases. The decay rate of the disturbance energy, though, increases as H is increased as in the previous regimes. These are discussed further with the aid of contour plots capturing the linear evolution of the quasi-2D optimal modes shown in figures 5.18 and 5.19 for $H = 200$ and $H = 1000$, respectively. The higher energy growth in the high-H cases may be associated with a difference in the energy gain mechanism in this regime. The quasi-2D optimal

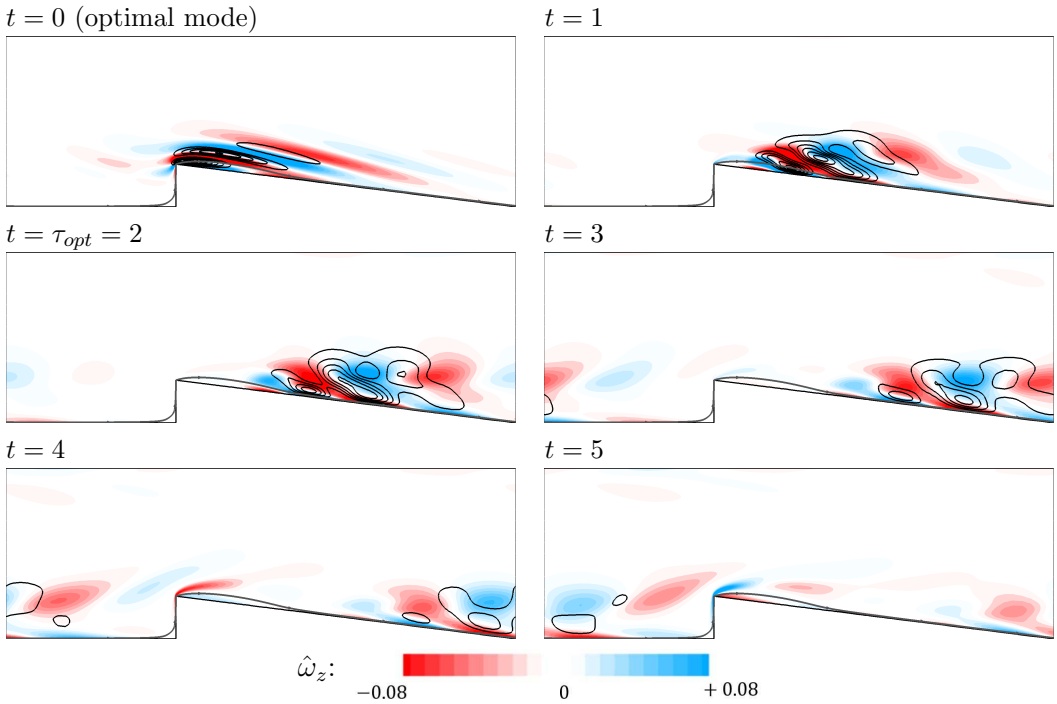

Figure 5.17: Spanwise quasi-2D perturbation vorticity ($\hat{\omega}_z$) contours overlaid by perturbation kinetic energy contours (black line contours) for $\beta = 0.25$, $\gamma = 2$ at $H = 30$, $Re = 330$, and its linear evolution over time. The initial condition at $t = 0$ is the optimal mode, and the subsequent times correspond to the triangle marker positions for this case shown in figure 5.15(a). The dividing streamline of the base flow is also shown. Energy iso-contours are shown at 10 equispaced levels between 0 and 0.0002.

modes gain energy when passing over the free shear layer formed after the wedge tip and attains maximum growth when it reaches the reattachment point of the recirculation region. This can be observed from the panels corresponding to $t = 0$ until $t = \tau_{opt}$ in figures 5.18 and 5.19. Thereafter, the disturbance structure's energy decays drastically until it reaches the subsequent wedge and rises again as it passes over the recirculation region, forming the second peak observed in the energy curves.

In figure 5.20, the quasi-2D disturbance structure and their kinetic energy contours are shown, zoomed over the recirculation region, at times when the disturbance structure experiences an energy gain (panels at $t = 1$ and 8 in figure 5.18) for a high-H case ($H = 200$, $Re = 770$). The opposite-signed disturbance structures are concentrated on either side of the inflection line (shown as a dashed line) with the maximum energy gain of the disturbance lying about the inflection line. This is an indication of an inflectional mechanism being associated with the energy gain in these cases. Similar observation was also made for $H = 1000$,

$Re = 2300$. The energy gain mechanism of the quasi-2D disturbance in the high-H range holds similarity to the energy gain in flow over a backward-facing (Blackburn *et al.*, 2008*a*) and a rounded backward-facing step (Marquet *et al.*, 2008), where two-dimensional disturbances gain energy when convecting over the recirculation region formed behind the step. In the current setup, however, the inflectional mechanism seems to play the predominant role in the energy growth of the quasi-2D disturbance in the high-H range, distinct from the other confined flow setups.

5.3.3 Influence of non-linear interaction on optimal energy growth

The non-linear evolution of the quasi-2D optimal modes in the quasi-2D base flow is investigated in this section. The aim is to study the influence of non-linear interactions of the quasi-2D optimal modes in the energy amplification, compare it with the corresponding linear evolution case discussed in § 5.3.2, and study the possibility of a sub-critical route to transition in these flows. For this analysis, the quasi-2D base flow is superimposed with the quasi-2D optimal mode at different initial energy levels relative to the base flow and the normalised disturbance energy (disturbance energy relative to its initial energy level in the domain) for each of these cases on non-linear evolution is monitored. In figure 5.21 the normalised energy of the disturbance on non-linear evolution is shown at different initial energy seeding in the low, intermediate and high-H ranges. As discussed in § 4.1, it is expected that as the inital energy level of the disturbance approaches zero, the evolution of the disturbance will approach the linearised evolution of the optimal mode. At very low initial energy seeding ($E(0) = 10^{-9}$), the normalised energy curve match with the linear evolution curve for all the H values considered and is almost indistinguishable from one another.

For the low and intermediate range of H considered it is observed that with increasing initial energy seeding of the optimal mode the peak energy amplification and the associated time of growth decreases, and beyond a certain threshold non-linear interactions results in a monotonic decay in the normalised disturbance energy as shown in figure 5.21(a,b). Hence, in this range of H, non-linear effects have a stabilising effect on the transient growth of the predicted optimal. The low energy growth, and the negligible effect of non-linearity at a range of different energy seeding, can be used as an indicator that a sub-critical route to transition in this range of H is unlikely (Camobreco *et al.*, 2020). This is similar to the findings in the corresponding hydrodynamic channel flow cases discussed in § 4.1.

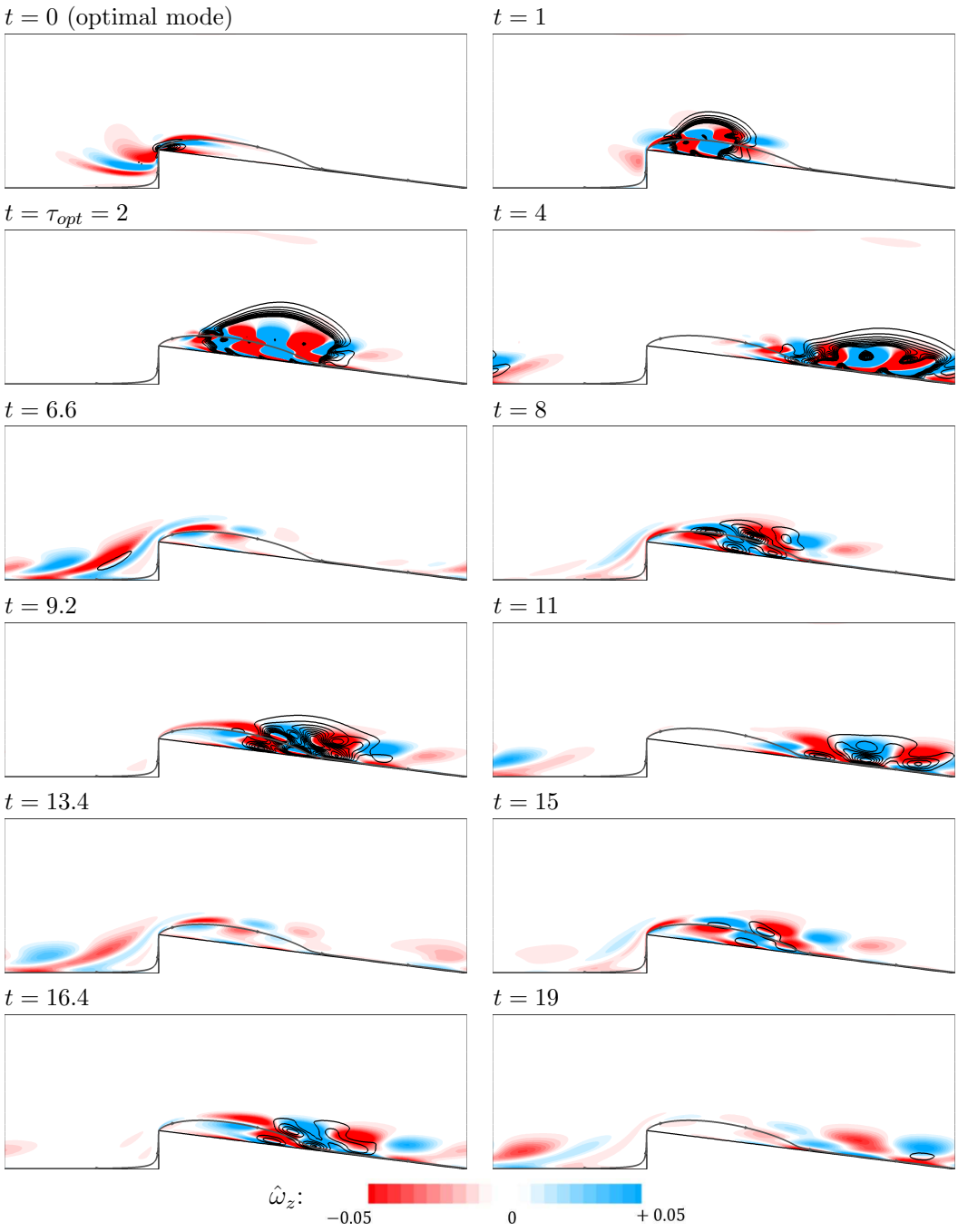

Figure 5.18: Spanwise quasi-2D perturbation vorticity ($\hat{\omega}_z$) contours overlaid by perturbation kinetic energy contours (black line contours) for $\beta = 0.25$, $\gamma = 2$ at $H = 200$, $Re = 770$, and its linear evolution over time. The initial condition at $t = 0$ is the optimal mode, and the subsequent times correspond to the triangle marker positions for this case shown in figure 5.15(b). The dividing streamline of the base flow is also shown. Energy iso-contours are shown at 10 equispaced levels between 0 and 0.0002.

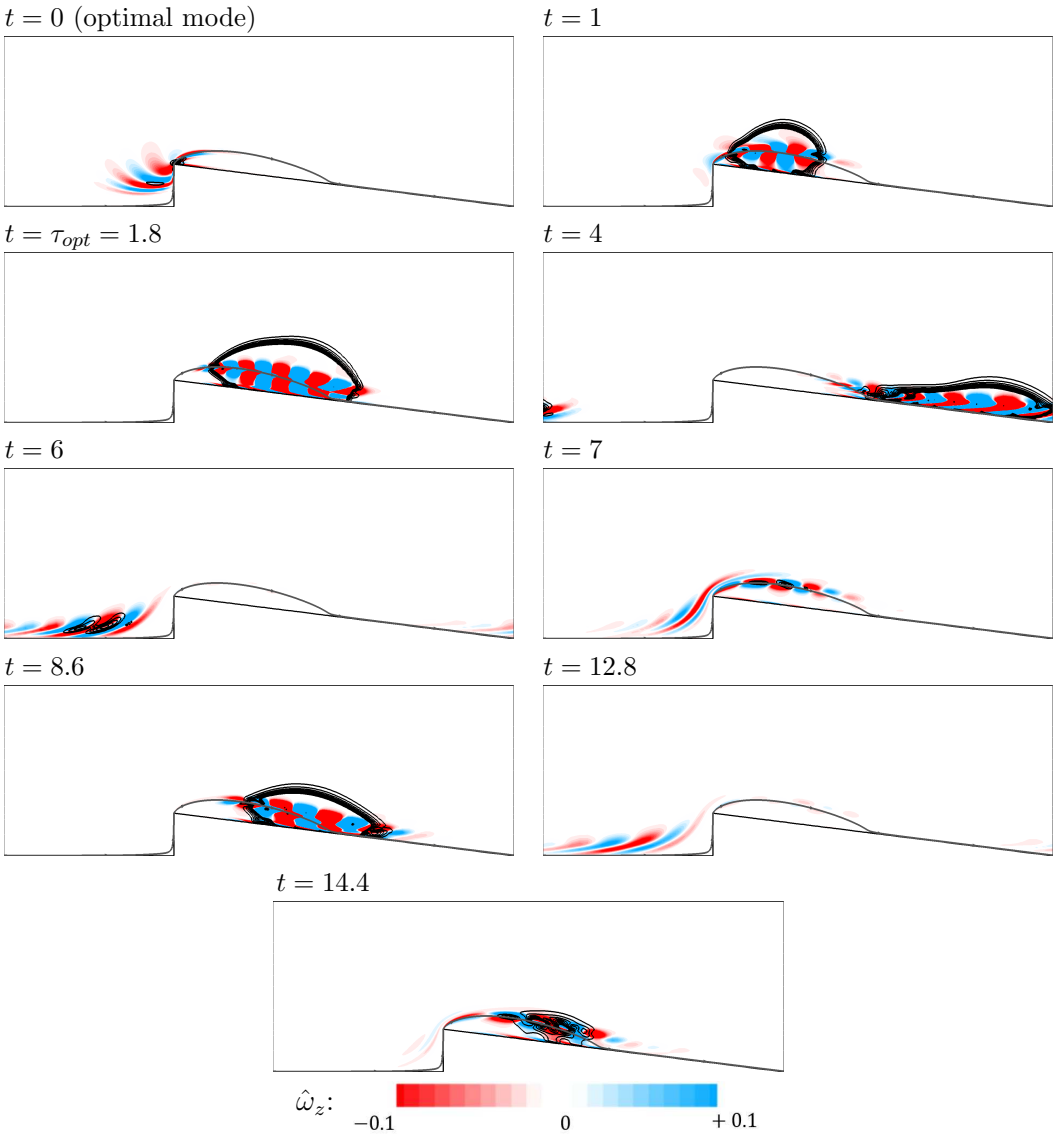

Figure 5.19: Spanwise quasi-2D perturbation vorticity ($\hat{\omega}_z$) contours overlaid by perturbation kinetic energy contours (black line contours) for $\beta = 0.25$, $\gamma = 2$ at $H = 1000$, $Re = 2300$, and its linear evolution over time. The initial condition at $t = 0$ is the optimal mode, and the subsequent times correspond to the square marker positions for this case shown in figure 5.15(b). The dividing streamline of the base flow is also shown. Energy iso-contours are shown at 10 equispaced levels between 0 and 0.0005.

Interestingly, in the high-H range, non-linear interactions have a different effect on the energy amplification, contrary to the previous regimes of H. The variation of the normalised disturbance energy with time at different initial energy seeding of the optimal mode is shown in figure 5.21(e,f). Up to a certain threshold of initial energy level, non-linear interactions play the role of delaying the time for energy dissipation of the disturbance. However, beyond the threshold

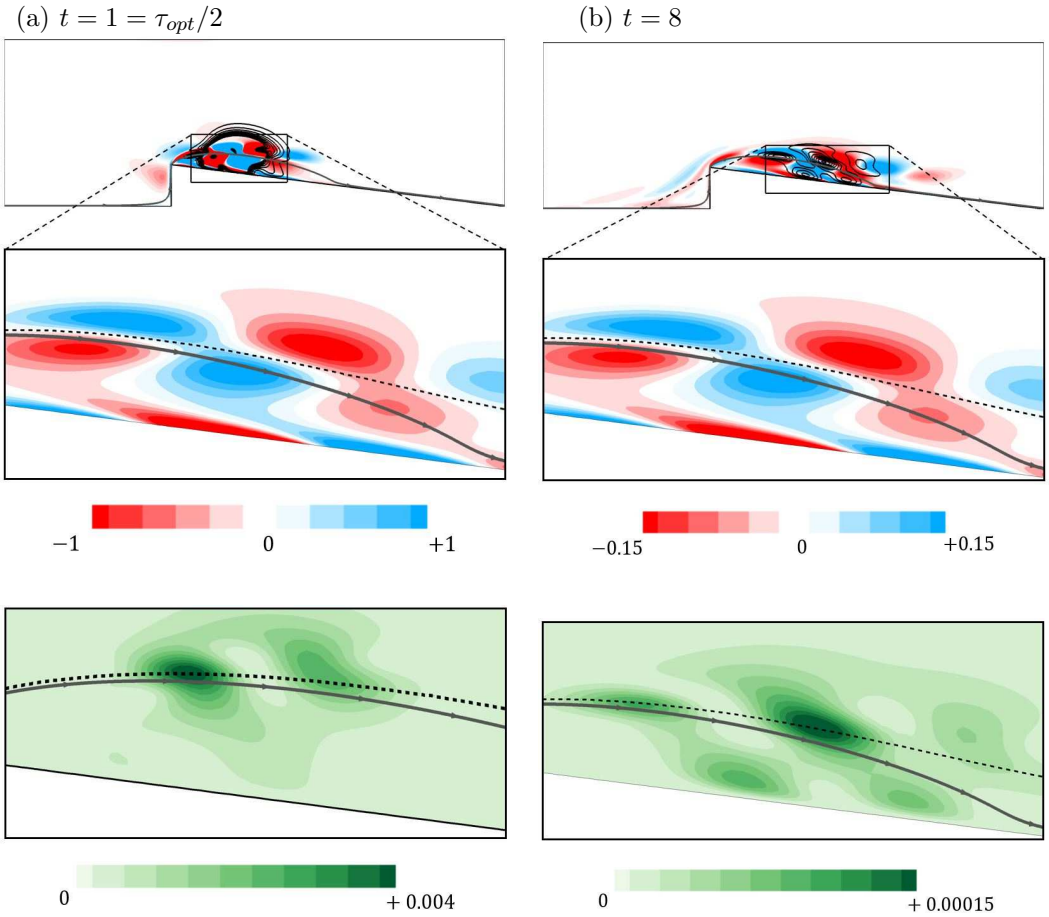

Figure 5.20: The spanwise vorticity contours (top and middle row) and the energy contours (bottom row) of the quasi-2D perturbation for the case shown in figure 5.18. Figures are zoomed over the recirculation region as indicated in the top row, and shows the separating streamline (solid line) and the locus of the inflection points of the base flow velocity (dashed lines) at (a) $\tau_{opt}/2$ and (b) at half the time to reach the second peak as shown in figure 5.15(b) for this case.

initial energy, non-linear interactions results in higher energy dissipation decreasing the peak energy growth and increasing the energy decay rate than the linear cases. The peak energy growth at the lowest initial energy seeding matches with the linear evolution case for both the cases tested, however with increasing seeding energy, the peak growth is found to be slightly higher that the linear peak energy growth and beyond a certain threshold falls below that value for $H = 200$ (zoomed section in figure 5.21c), and decreases monotonically with increasing seeding energy for $H = 1000$ (zoomed section in figure 5.21d). No subcritical excursions to an unstable or turbulent state were observed in the range of H investigated, even though the optimal mode could attain an energy amplication exceeding 10^4 at the highest H investigated ($H = 1000$).

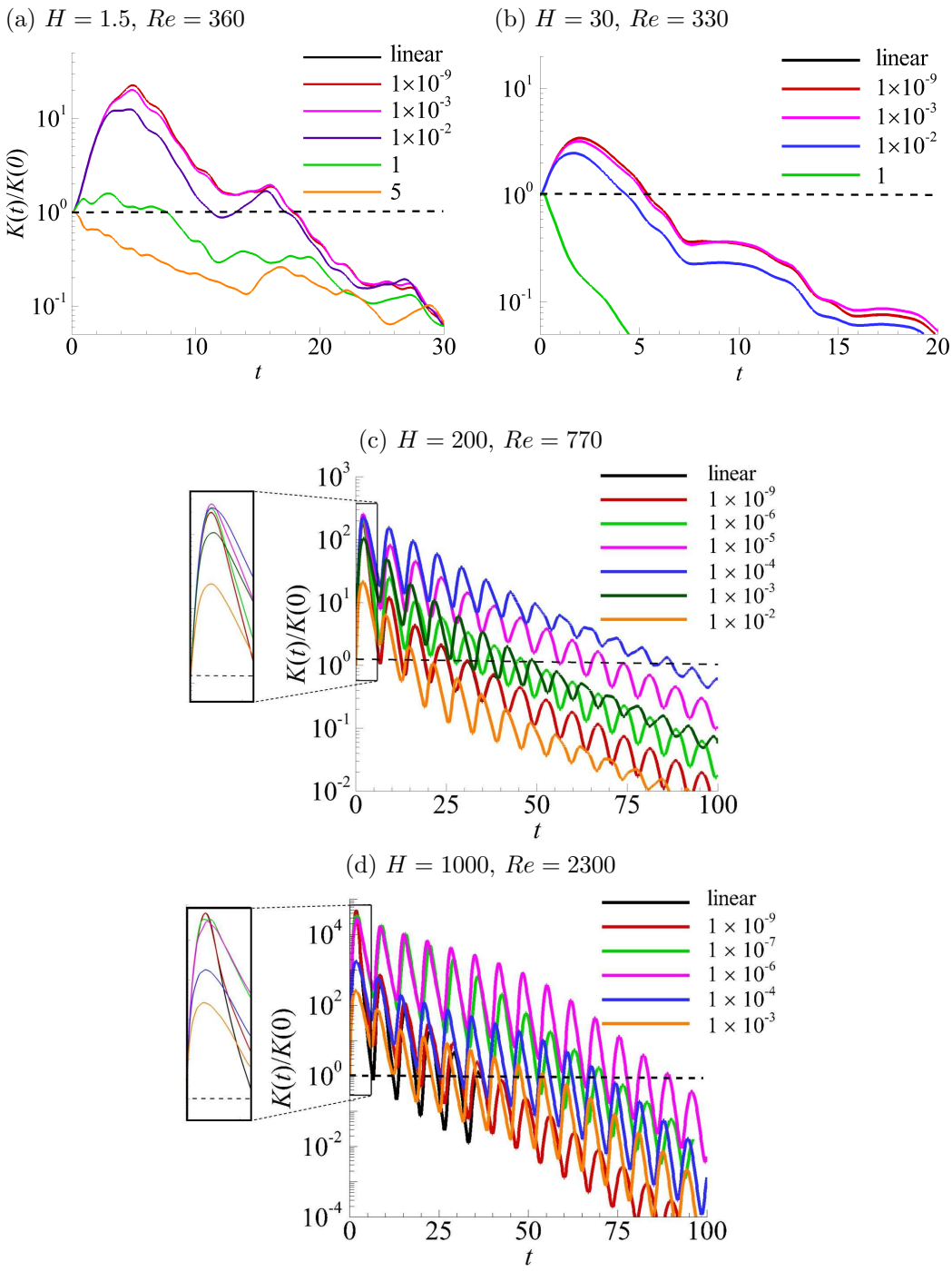

Figure 5.21: Comparison of linear and non-linear evolution of the quasi-2D optimal mode in the (a) low, (b) intermediate and (c,d) high-H ranges for $\beta = 0.25$, $\gamma = 2$.

Chapter Summary

The stability and characteristics of quasi-2D magnetohydrodynamic duct flows having wedge protrusions were discussed in this chapter. Four quasi-2D flow regimes were identified, considering a range of Hartmann friction parameters and a change in the flow structure in the high-H range was elucidated. The primary bifurcation of the flow was found to occur through quasi-2D eigenmodes. In the low-H range, the quasi-2D mode had a similar structure and spatial location as 2D perturbations associated with vortex shedding in the corresponding hydrodynamic channel flow setup. The eigenmodes were increasingly localised in the thin Shercliff layers on the bottom wall with increasing H. A shift in the spatial location of the quasi-2D eigenmode was also observed with a change in the base flow structure at higher H. The optimal energy growth of quasi-2D disturbances were comparable with the corresponding hydrodynamic optimal modes in the low-H range of parameters. However, maximum optimal energy growth of approximately 10^5 was found at the highest H investigated in this study, as opposed to approximately 10^1 to 10^2 in the low and intermediate ranges of H. Even though non-linear interactions of the optimal modes at an optimal initial energy seeding could delay the decay rate of the disturbance energy, a sub-critical transition via transient energy amplification was not observed in the range of parameters studied.

In the next chapter, heat transfer enhancement by the use of repeated wedges in a quasi-2D MHD duct flow and the optimal geometric parameters to achieve maximum heat transfer efficiency are presented.

Chapter 6

Heat transfer enhancement in quasi-2D magnetohydrodynamic duct flow using repeated wedge protrusions

In this chapter, the heat transfer enhancement in a quasi-2D magnetohydrodynamic duct flow achieved by using repeated wedges is discussed. The flow field, vortex evolution in the unsteady state or the quasi-2D turbulent state, and its influence on the local Nusselt number are elucidated, following which the influence of each geometric parameter of the wedge on the heat transfer ratio and overall efficiency are explained for a range of Hartmann friction parameters and Reynolds numbers. The optimal geometric parameters for achieving maximum heat transfer ratio and overall efficiency are also presented. The effectiveness of the wedges is further supported by a net power analysis. A comparison of the heat transfer ratio and efficiency achieved by using wedges with other heat transfer enhancement strategies used in quasi-2D magnetohydrodynamic duct flows is also made . [1]

[1]Some of the results contained in this chapter have been published in Murali, S., Hussam, W. K. & Sheard, G. J. 2021 Heat transfer enhancement in quasi-two-dimensional magnetohydrodynamic duct flows using repeated flow-facing wedge-shaped protrusions. *Int. J. Heat Mass Trans.* **171**, 121066.

6.1 Flow field and influence on local Nusselt number

In § 5.1.1 it was found that the unsteady regime of a quasi-2D magnetohydrodynamic flow in a duct is associated with vortex shedding starting from the wedge tip. The associated flow field and the vortex dynamics in these unsteady state plays an essential role in influencing the local heat transfer behaviour and thereby the overall heat transfer to the fluid. To understand this influence, in this section, the variation of local intensity of a vortex (ω_{zxp}) from its formation at the wedge tip until it reaches the subsequent wedge tip are elucidated along with its influence on the local instantaneous Nusselt number $Nu_x(x,t)$ for a quasi-2D unsteady flow using a case with $Re = 1300$, $H = 50$, $\beta = 0.25$, $\gamma = 4$ and $\phi = 7.125$. At a given time instance, the net circulation is used to represent the intensity of a vortex at any streamwise location x and is calculated by the local vortex flux crossing a given cross section, given by

$$\omega_{zxp} = \frac{1}{(2L - y_{b,x})} \int_{y_{b,x}}^{2L} \omega_{zx} \, \mathrm{d}y, \tag{6.1}$$

where, $y_{b,x}$ is the y-coordinate of the bottom wall, and ω_{zx} is the spanwise vorticity at streamwise location x.

The presence of the wedge results in vortex formation (represented as 1) starting at the wedge tip as shown in figure 6.1(a). This vortex extends downstream remaining attached to the wedge tip, while a second smaller vortex (represented as 2) starts forming behind it (figure 6.1b). The strength of the vortex increases with x and achieves a maximum value when attached to the tip. A corresponding increase in Nu_x is also observed, which is associated with the forming vortex interacting with the wall vortices. With the growth of vortex 2, the larger vortex 1 deattaches itself from the wedge tip, which is associated with a drop in its strength (figure 6.1c). Similar behaviour of a second vortex formation and dettachment of the primary vortex was also observed in Hamid *et al.* (2015), where a point electrode was used as vortex generator. After dettachment from the wedge tip, vortex 1 convects downstream along the wedge taper with its strength decaying, during its evolution as can be seen from figure 6.1(c-e). An associated peak in Nu_x is due to the interaction of the convecting vortex with the wall vortices which disrupts the thermal boundary layer thickness. Further downstream, vortex 1 interacts and merges with a vortex convecting from upstream represented as vortex 3 (figure 6.1f,g), resulting in increase in the strength of vortex 1. The rise in

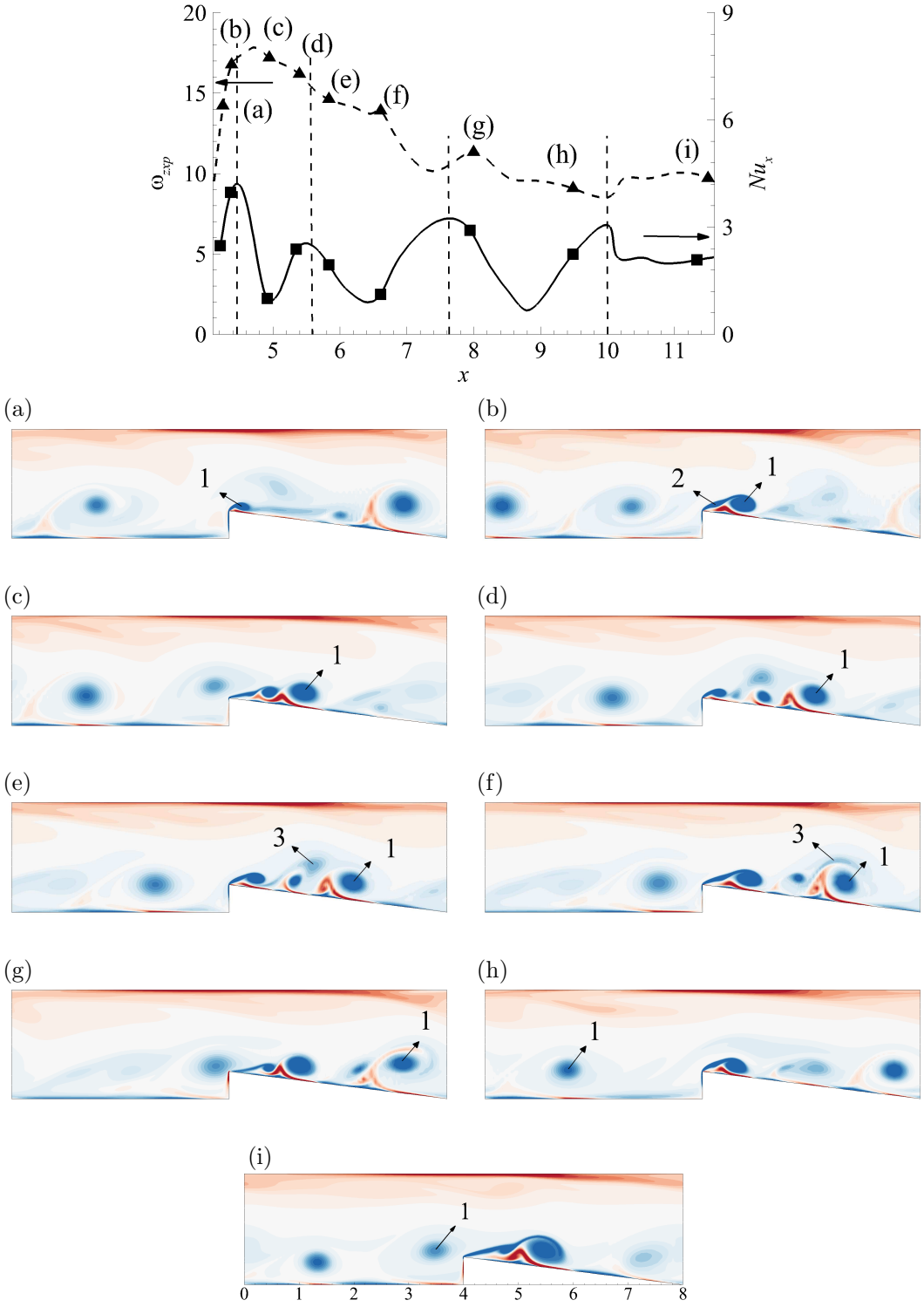

Figure 6.1: Plot showing the evolution of vortex strength (ω_{zxp}, dashed line) and local instantaneous Nusselt number ($Nu_x(x,t)$, solid line) plotted against its streamwise position x for a case with $\beta = 0.25$, $\gamma = 4$, $\phi = 7.125$, $Re = 1300$ and $H = 50$. Values of ω_{zxp} and Nu_x are obtained from the trajectory of vortex labelled "1" in the accompanying sequence of vorticity contour plots (a)–(i) also shown in the curve as ▲ and ■, respectively. Twenty equispaced vorticity contour levels are plotted between -10 (blue) and 10 (red).

intensity on vortex merging depends on the intensity of the two merging vortices. The third peak in Nu_x corresponds to the vortex merging thereby illustrating the favourable effect of vortex interactions and merging on Nu_x. The strength of the vortex drops further when convecting in the gap between the wedges (figure 6.1h) with an associated decrease in Nu_x. On approaching the wedge, vortex 1 accelerates over the wedge, sweeping with it the secondary wall vortices, which explains the increasing Nu_x and the jump in vortex strength in that region (figure 6.1i). Thereafter, vortex 1 interacts with the new vortex forming at the next wedge tip. The interplay of vortex formation at the wedge tip, its intensity at formation, interaction of the convecting vortices with the wall vortices, and interaction and merging with the incoming vortices plays a key role in the heat transfer behaviour of the system which are in turn dictated by

1. flow parameters: such as the Reynolds number and the Hartmann number with respect to their roles in the dissipation of the vortex strength;

2. geometric parameter setting of the wedge: such as blockage ratio, pitch and wedge angle, with respect to controlling the number of merging, interaction with the thermal and Shercliff boundary layers.

In the subsequent sections, the influence of each of these parameters on the heat transfer rate and overall efficiency are discussed in detail.

6.2 Heat transfer ratio, *HR*

In this section, the heat transfer ratio (HR), which quantifies the heat transfer enhancement achieved using wedges, relative to using a plane duct without wedges, and its dependence on different geometric parameters of the wedge β, γ and ϕ, and flow parameters, H and Re for each case is elaborated in detail.

6.2.1 Effect of blockage ratio (β)

The influence of β is discussed here for a reference case with $H = 50$ and $Re = 1300$. In figure 6.2, variation of HR and the maximum strength of the vortex at its formation at the wedge tip (ω_{zp}) with β are shown.

Both HR and ω_{zp} increase monotonically with β. Up to $\beta \approx 0.3$, HR increases at a lower rate with β, whereas a relatively higher rate of increase in HR is observed for $\beta \gtrsim 0.3$. An instantaneous snapshot of the flow field and the temperature field for $\beta = 0.125$, 0.25, 0.35 and 0.5 are shown in figure 6.3. It can be

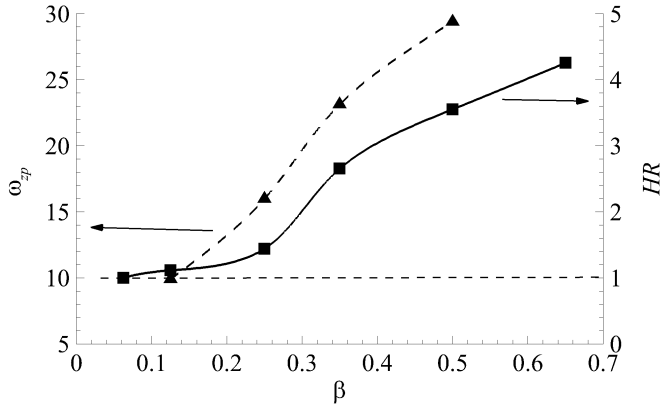

Figure 6.2: Plot of variation of *HR* (■; solid spline) and the maximum intensity of the vortex formed at the wedge tip before deattachment (▲; dashed spline) against β for $Re = 1300$, $H = 50$ and $\beta = 0.25$. The dashed horizontal line represents *HR* for a duct with no wedges.

observed that the size of the vortex formed at the wedge tip scales approximately with the height of the wedge. Thus, with increasing β, the vortices formed at the wedge tip are more intense and of larger size, both of which are favourable for achieving a higher Nu_x as discussed in § 6.1. The vortices formed at the wedge tip roll up and are cast further away from the tapered wall with increasing β, before deattaching themselves from the tip and convecting downstream, which results in an increase in intensity of the vortex at formation. At higher blockage $\beta \gtrsim 0.35$, in addition to its interaction with the secondary wall vortices on the bottom wall, convecting vortices interacts with the secondary wall vortices on the top wall of the duct resulting in better mixing of the hot fluid near the bottom wall and the cold fluid near the top wall of the duct. This is evident from the temperature field, where more dominant plume structures are observed with increasing β. For example, for $\beta = 0.5$, the convecting vortices engulf the vortices on the top wall resulting in counter-rotating vortex pairs forming on the wedge taper surface evident from the spanwise vorticity field shown in figure 6.3(d). These interactions disrupt the thermal boundary layer more severely, sweeping hot fluid into the interior and, helping to achieve higher *HR*.

6.2.2 Effect of pitch (γ)

The effect of pitch on *HR* is discussed in this section for $\beta = 0.25$ at the same Re and H as in § 6.2.1. For a fixed blockage ratio, *HR* achieves a peak value followed by a decrease with γ in the range of γ investigated. The dependence of *HR* and ω_{zp} on γ are shown in figure 6.4.

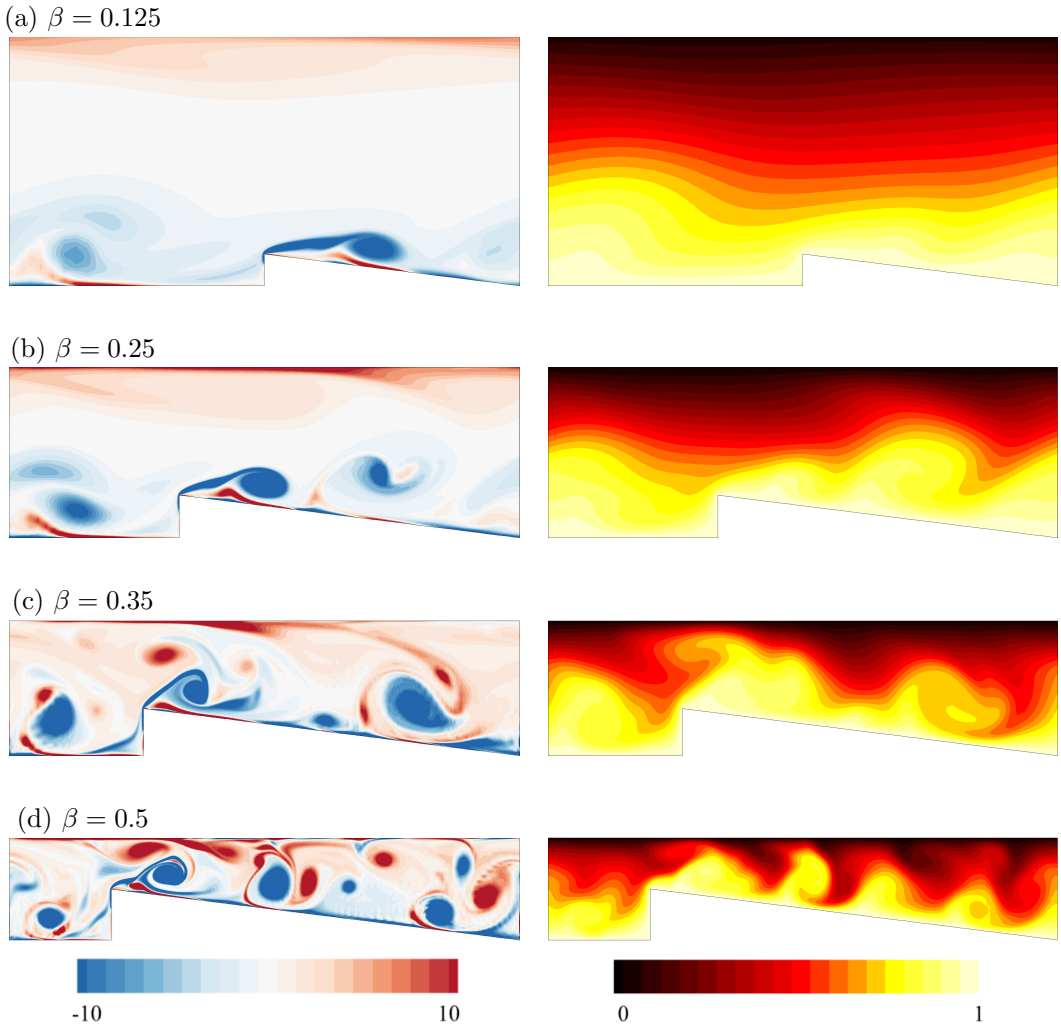

Figure 6.3: Contours of (left) spanwise vorticity (ω_z) and (right) temperature field for blockage ratios (a) $\beta = 0.125$, (b) $\beta = 0.25$ (c) $\beta = 0.35$ and (d) $\beta = 0.5$ at $Re = 1300$ and $H = 50$. Twenty equispaced contour levels are plotted between $-10 \leq \omega_z \leq 10$, while temperature contours are shown in the range $T_h \leq T \leq T_c$ with the dark and light shading representing cold and hot fluid, respectively.

The pitch corresponding to the maximum HR is the optimal pitch, $\gamma_{\text{opt},HR}$. It can be observed that ω_{zp} also attains a peak value close to $\gamma_{\text{opt},HR}$. For $\gamma < \gamma_{\text{opt},HR}$, ω_{zp} is lower than the optimal case and the domain length is short, and hence does not allow for more vortex merging and interactions with the wall vortices in the gap between the wedges, thereby lowering HR. Although $\gamma > \gamma_{\text{opt},HR}$ allows for multiple vortex merging events and interactions with the wall vortices, the vortex formed at the wedge tip now has to travel a larger distance before reaching the subsequent wedge. Since the Hartmann damping effect dissipates energy from these vortices (Kanaris *et al.*, 2013; Hamid *et al.*, 2015), their interaction with the wall vortices has a weaker impact on the thermal boundary layers leading to

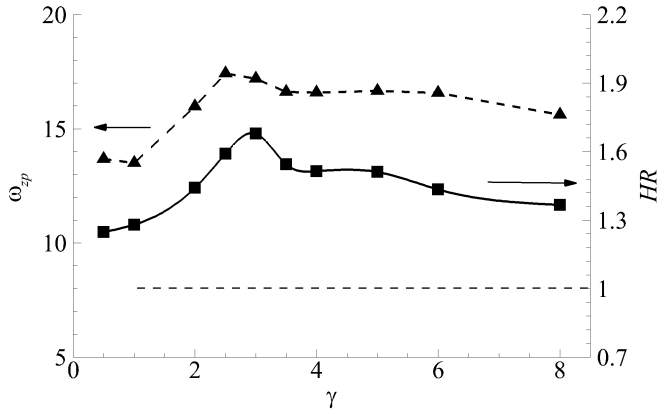

Figure 6.4: Plot of variation of *HR* (■; solid spline) and the maximum intensity of the vortex formed at the wedge tip before deattachment (▲; dashed spline) against γ for $Re = 1300$, $H = 50$ and $\beta = 0.25$. The dashed horizontal line represents *HR* for a duct with no wedges.

a lower Nu_x. A visualisation of an instantaneous flow and temperature field for $\gamma = 1$, 2, 3, 4 and 8, covering values less than and greater than $\gamma_{\text{opt},HR}$, are shown in figure 6.5.

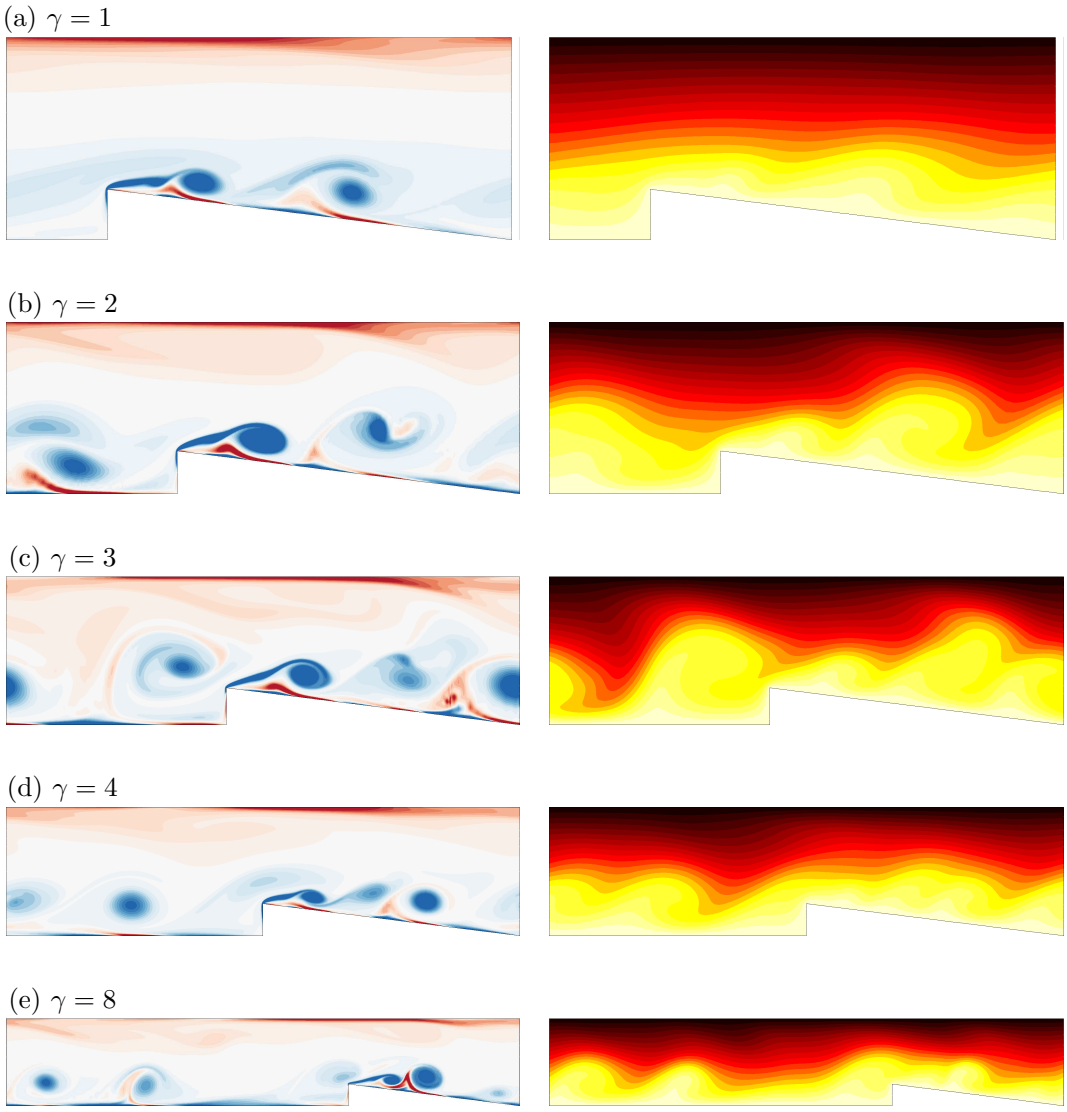

Figure 6.5: Contours of (left) spanwise vorticity (ω_z) and (right) temperature field for pitch values (a) $\gamma = 1$, (b) $\gamma = 2$, (c) $\gamma = 3$, (d) $\gamma = 4$ and (e) $\gamma = 8$ at $Re = 1300$ and $H = 50$. The contour levels are as per figure 6.3.

6.2.3 Effect of wedge angle (ϕ)

Variation of HR with wedge angle is discussed in this section for the same H and Re as in § 6.2.1. Similarly to the existence of an optimal pitch, there also exists an optimal wedge angle $\phi_{\text{opt},HR}$ at which a maximum HR can be attained. The dependence of HR and ω_{zp} on ϕ are shown in figure 6.6. For a fixed β and γ, increasing ϕ not only increases the inclination of the tapered surface of the wedge, but also decreases the streamwise length of the wedge or shortening the distance to the next wedge. With a steepest inclination of the wedges investigated, $\phi = 14.036^o$, the vortices are cast away from the taper wall during its formation, resulting in lesser interaction with the wall vortices. The shorter

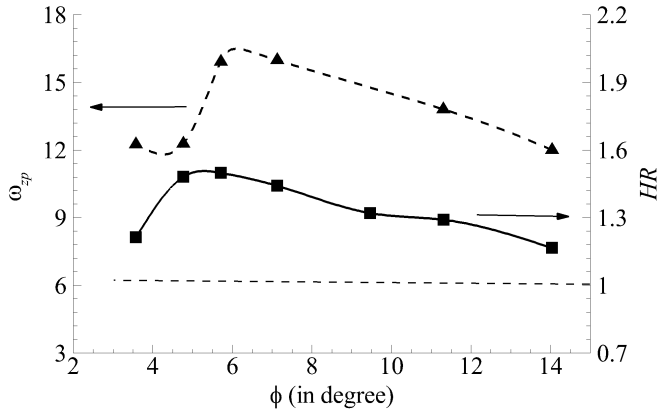

Figure 6.6: Plot of variation of *HR* (■; solid spline) and the maximum intensity of the vortex formed at the wedge tip before deattachment (▲; dashed spline) against ϕ for $Re = 1300$ and $H = 50$. The dashed horizontal line represents *HR* for a duct with no wedges.

wedge length is also not favorable for interactions with convecting vortices. This can be visualised in the spanwise vorticity and temperature contours shown in figure 6.7(a). With decreasing ϕ, until $\phi_{\text{opt},HR}$, the vortices formed at the tip are cast relatively closer to the wedge walls, allowing for better interactions with the wall vortices and a wedge length allowing for interaction of convecting vortices. With further decrease beyond $\phi_{\text{opt},HR}$, the vortices formed are less intense and the interacting convecting vortices are weaker, resulting in weaker interaction with wall vortices and a lower *HR*. The temperature contours for wedge angles above, near and below the optimal angle limit shown in figure 6.7 (a), (c) and (e) shows a diffusively dominated flow at smaller and larger wedge angles and the plume structures at intermediate wedge angle close to $\phi_{\text{opt},HR}$, which is an indication of a convectively dominant heat transfer mechanism with enhanced mixing between the hot and cold fluids near the bottom wall and top walls respectively. Similar behaviour was also observed in Hussam & Sheard (2013), in which the influence of varying gap height (measure of distance of a cylinder from the hot wall of the duct) on the *HR* was studied. They found that, the vortices generated by the cylinder could be cast on the hot wall at different angles by varying the gap height. Decreasing gap height helped better interaction with wall vortices and after an optimal distance, further movement closer to the wall suppressed the vortices due to interaction with Shercliff layers, similar to the effect of decreasing the wedge angle in the present setup.

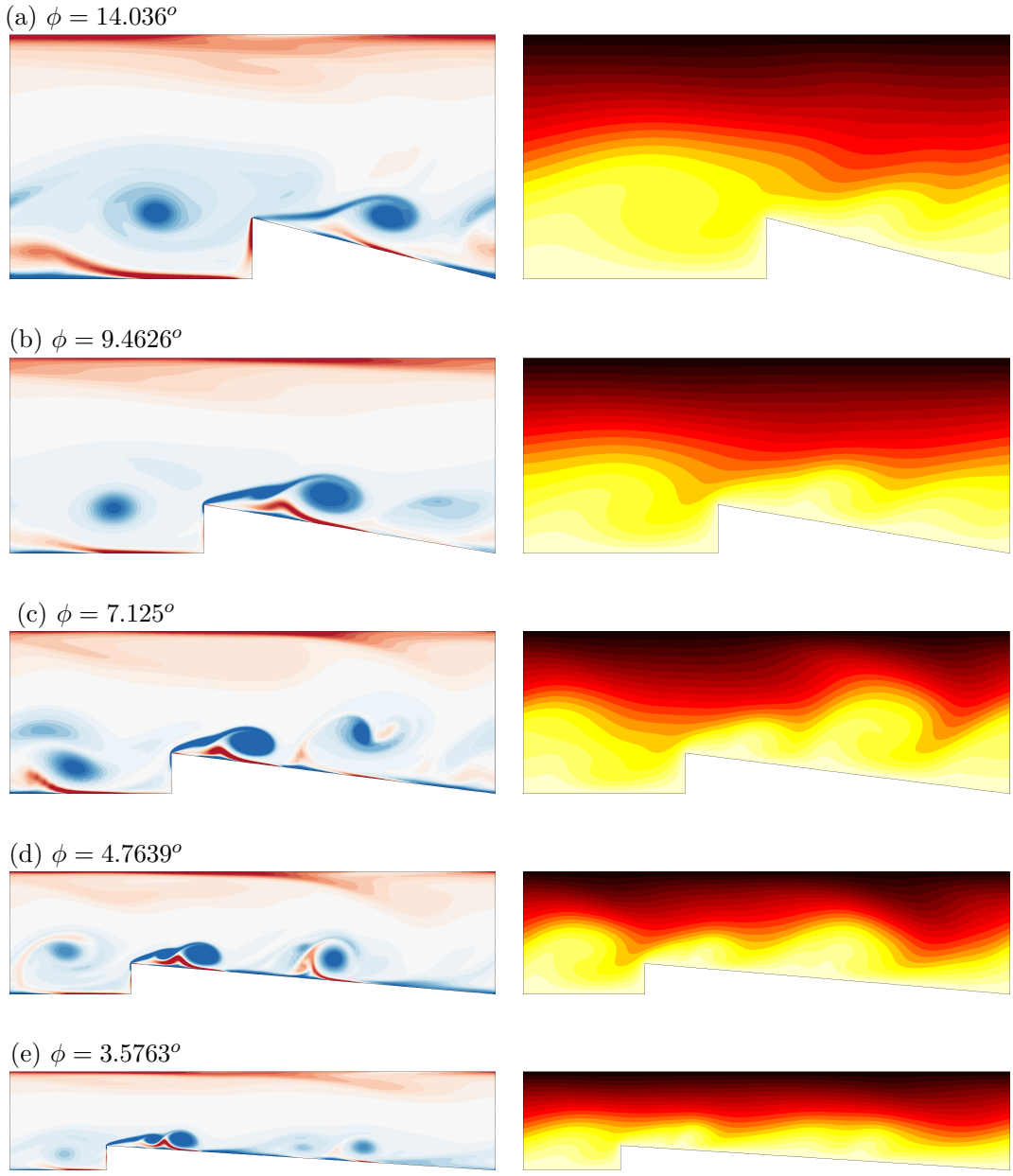

Figure 6.7: Contours of (left) spanwise vorticity (ω_z) and (right) temperature field for wedge angles (a) $\phi = 14.036^o$, (b) $\phi = 9.4626^o$, (c) $\phi = 7.125^o$, (d) $\phi = 4.7639^o$ and (e) $\phi = 3.5763^o$ at $Re = 1300$ and $H = 50$. The contour levels are as per figure 6.3.

6.2.4 Effect of Hartmann friction (H)

In the previous sub-sections, the influence of each of the identified geometric parameter of the wedge on HR was explained by considering a single H and Re. In this section, the effect of varying H for a range of these geometric parameters will be discussed for a case with $Re = 1300$. Hartmann friction plays the role of dissipating the kinetic energy of the quasi-2D vortices formed at the wedge and

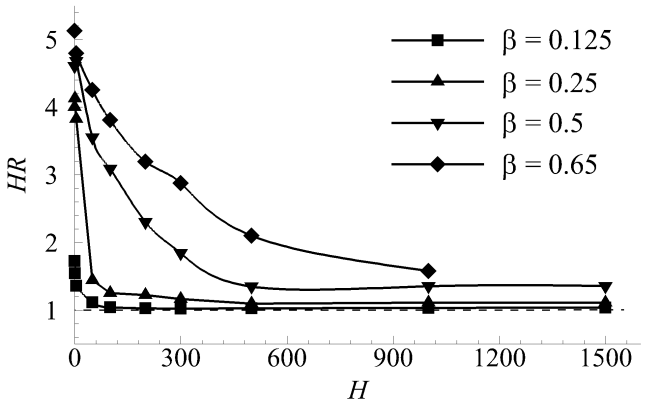

Figure 6.8: A plot of variation of HR against H for different β as indicated at $Re = 1300$, $\gamma = 2$, $\tan(\phi) = 0.125$. Dashed horizontal line represents HR for a duct with no wedges.

convecting in the flow domain. Therefore at a higher H, the vortices lose energy more swiftly and are lower in strength when convecting the same distance in the flow domain, thereby decreasing their impact on the rise in Nu_x and in turn on HR. In figure 6.8, the influence of H on HR is depicted for a range of β. As expected, a monotonic decrease in HR with H is observed for all β, with HR asymptoting to a constant value a bit above unity at higher H. By increasing the blockage ratio, a broader range of H, producing $HR > 1$ can be achieved. This is because increasing β lowers the critical Re for the onset of unsteadiness in the flow (§ 5.2). For a fixed β, a further improvement in HR can be achieved by setting the wedge at an optimal pitch $\gamma_{\text{opt},HR}$ and wedge angle $\phi_{\text{opt},HR}$ corresponding to each H. Heat transfer ratio HR as a function of γ and ϕ are shown in figure 6.9(a) and (b), respectively for a range of H for a wedge with $\beta = 0.25$. With increasing H, both $\gamma_{\text{opt},HR}$ and $\phi_{\text{opt},HR}$ has a non-monotonic trend showing an increase followed by a decrease in its value, in the parameter range investigated. At higher H, a wedge with lower γ is more destabilising, lowering the Re for the onset of vortex shedding. A wedge with shorter distance also seems to be more favorable due to the increased dissipation of the vortex strength with H, which explains the shift in $\gamma_{\text{opt},HR}$ to lower values with H.

6.2.5 Dependence on Reynolds number (Re)

The focus of this section is on the dependence of HR on Re. A case with $H = 500$ is considered for ranges of the geometric parameters. In the quasi-2D steady state regime, HR remains almost constant with increasing Re and higher β cases are found to be more effective for enhancing HR. Similar to its positive effect in the

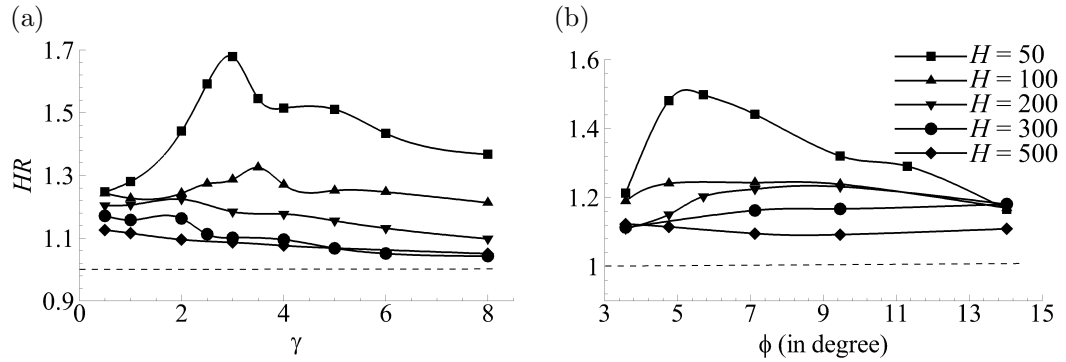

Figure 6.9: Plots of HR against (a) γ, and (b) ϕ at $\beta = 0.25$ and $Re = 1300$ at Hartmann friction values as indicated.

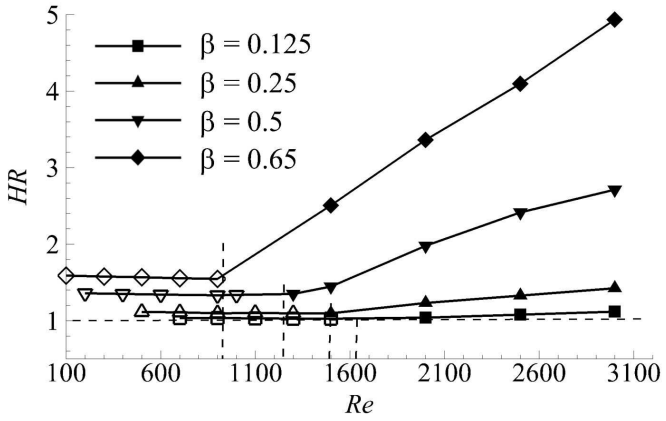

Figure 6.10: A plot of HR against Re for different β as indicated at $H = 500$, $\gamma = 2$ and $\tan(\phi) = 0.125$. Dashed horizontal line represents HR for a duct with no wedges. The dashed vertical lines from right to left indicate $Re_{cr,\mathrm{Q2D}}$ for lower to higher β. Open and closed symbols represent the HR values corresponding to the steady and unsteady states of the flow, respectively.

steady state regime, increasing β is also favorable to promote HR in the unsteady regime with HR increasing almost linearly with Re for all the cases investigated. The variation of HR with Re for a few β cases investigated is shown in figure 6.10 for $H = 500$. In addition to preponing the onset of quasi-2D vortex shedding to lower Re, the rate of HR rise with Re is also higher at higher β.

Similar to its dependence on H, for a fixed blockage an optimal γ and ϕ exists for different Re (figure 6.11). At $Re = 1500$, the flow remains in the steady state for $\gamma \gtrsim 2$. Decreasing γ further triggers unsteadiness, causing HR to rise for $\gamma < 2$. In this case, consecutive wedges with no gap between them are most favourable for heat transfer increase. With increasing Re, a shift to higher optimal γ is observed. The higher wedge angle gives maximum HR at $Re = 1500$. With increasing Re, wedge angle giving maximum HR shifts to lower values.

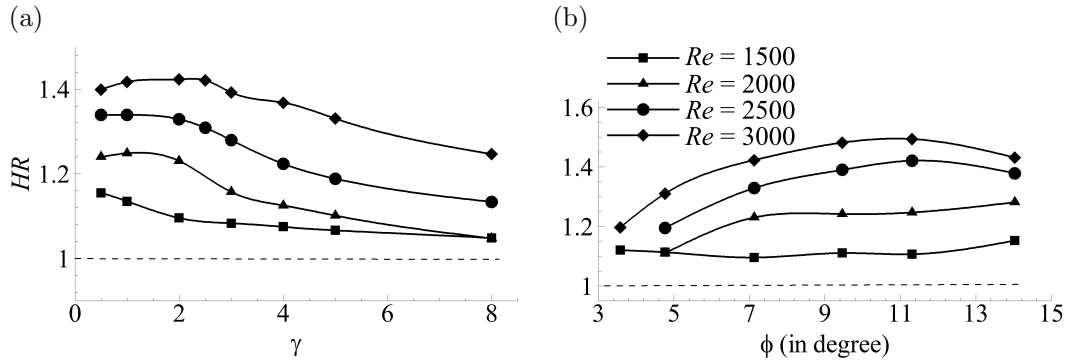

Figure 6.11: Plots of HR against (a) γ, and (b) ϕ at $\beta = 0.25$ and $H = 500$ at Reynolds numbers as indicated.

6.3 Heat transfer efficiency, η

The heat transfer rate from the heated wall to the fluid flowing through the duct with repeated wedge-shaped protrusions and the optimal geometric parameters to achieve maximum HR for a range of H and Re were discussed in § 6.2. It is important to consider the frictional losses and the associated pressure penalties with the use of these wedges to evaluate the overall efficiency of heat transfer as discussed in § 2.8.1. This section will concentrate on the overall efficiency of heat transfer with presence of wedges in the duct and the optimal design of the wedge geometric parameters for $50 \leq H \leq 500$ at $Re = 1300$ and $Re = 2000$ to achieve maximum efficiency, $\eta_{\max}$. Recalling that the overall efficiency accounts for the heat transfer enhancement achieved over the pressure drop losses in the duct, and is given by $\eta = HR/PR$.

Unlike HR, which showed an unvarying increase with β, an optimal blockage ($\beta_{\text{opt},\eta}$) setting of the wedge achieves $\eta_{\max}$ as shown in figure 6.12. With increasing H, a higher blockage is required to achieve $\eta_{\max}$. All cases with $\eta > 1$ are favourable for heat transfer enhancement whereas $\eta < 1$ corresponds to cases which are not effective as the pressure drop dominates the heat transfer improvement achieved. Figure 6.12 shows that heat transfer efficiency increases of beyond 40% are achievable, though there is a significant dependence on the blockage ratio at which maximum efficiency is achieved, increasing as H increases. The variation of the heat transfer efficiency along with HR and PR as a function of blockage ratio is illustrated in figure 6.13 for a case with $\gamma = 2$ at $H = 200$, $Re = 2000$. Maximum efficiency $\eta_{\max}$ is achieved when the separation between HR and PR is maximum.

An optimal setting of pitch $\gamma_{\text{opt},\eta}$ and wedge angle $\phi_{\text{opt},\eta}$ exists for a fixed blockage, where $\eta_{\max}$ could be attained. In figure 6.14, variation of η with γ

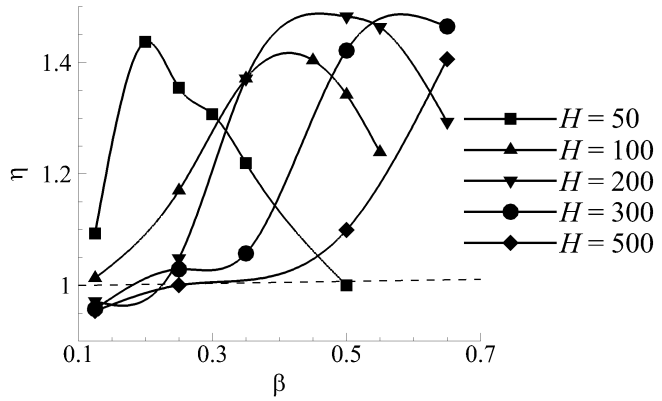

Figure 6.12: A plot of η against β at $Re = 2000$ for friction parameters as indicated. The fixed parameters used for these cases are $\gamma = 2$ and $\tan(\phi) = 0.125$.

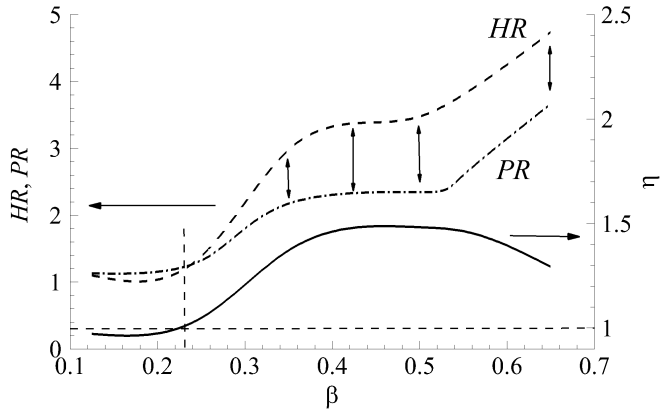

Figure 6.13: A plot of HR, PR and η as a function of β at $H = 200$, $Re = 2000$. To the left of the dashed vertical line PR dominates HR whereas on its right, HR takes over PR thereby making $\eta > 1$. Maximum area between the HR and PR curve corresponds to the maximum in η. The fixed parameters used for these cases are $\gamma = 2$ and $\tan(\phi) = 0.125$.

and ϕ are shown for $50 \leq H \leq 500$ at $Re = 2000$. The maximum possible efficiency at a given H and Re could be achieved by designing the wedge with a combination of the three optimal geometric parameters ($\beta_{\text{opt},\eta}$, $\gamma_{\text{opt},\eta}$ and $\gamma_{\text{opt},\eta}$). Both $\gamma_{\text{opt},\eta}$ and $\phi_{\text{opt},\eta}$ show a non-monotonic trend with H as shown in figure 6.15(a). Beyond $H \approx 200$ a reversal in trend in the optimal values is observed. For every geometric setting of the wedge, there exists a critical Hartmann friction parameter H_{cr} associated with $\eta_{\max}$. Beyond H_{cr}, η decreases monotonically with H. In figure 6.15(b), η is shown as a function of H. For $0.25 \lesssim \beta \lesssim 0.65$, the critical Hartmann friction parameter moves towards higher values. It can also be observed that higher β has a wider range of H over which efficiency increases of $\gtrsim 25\%$ are achievable. The lowest blockage, $\beta = 0.125$ does not show an optimal

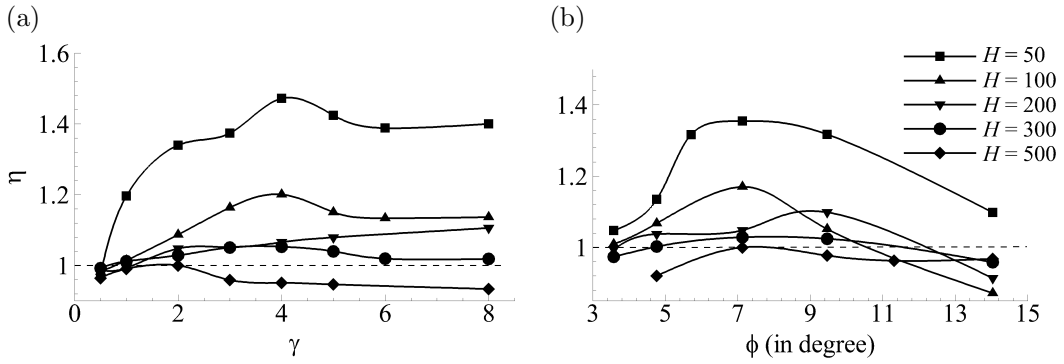

Figure 6.14: Plots of η as functions (a) γ, and (b) ϕ at $Re = 2000$ for friction parameters as indicated.

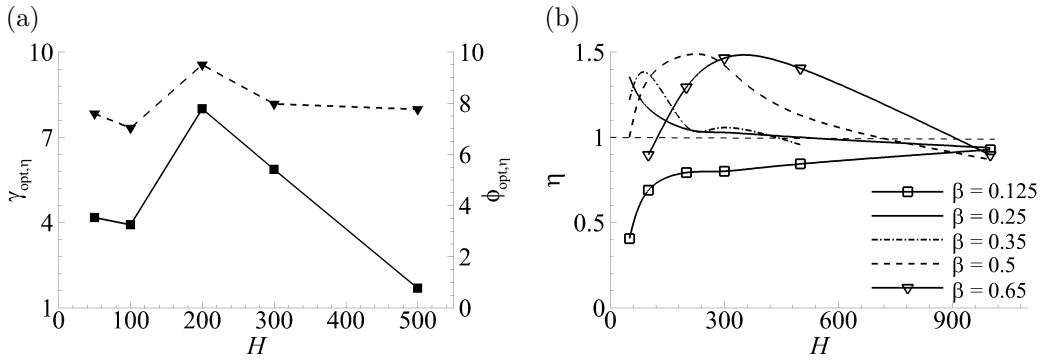

Figure 6.15: Plots showing (a) $\gamma_{\text{opt},\eta}$ and $\phi_{\text{opt},\eta}$ against H for $\beta = 0.25$ and (b) η against H for different blockage ratios at $Re = 2000$, $\gamma = 2$.

value in the range of H investigated. The best design in terms of maximising the heat transfer efficiency could also be considered as the geometric setting which has H_{cr} close to the operating conditions under which it is going to be used.

To further illustrate how selecting a combination of parameters at a given H and Re can help maximise the achievable efficiency, $H = 50$, $Re = 1300$ is considered as an example, and η attained at a combination of β and γ are shown in figure 6.16. In this case, a wedge with $\beta \approx 0.35$ and $\gamma \approx 6$ achieves an efficiency exceeding that of other combinations, $\eta_{\max} \approx 20\%$.

6.4 Net power analysis

In the previous section § 6.3, the effectiveness of wedges for heat transfer enhancement were evaluated using heat transfer efficiency η. Another useful measure of the effectiveness of protrusions which has found utility in the literature (Cassells *et al.*, 2016; Hamid *et al.*, 2016*b*) is the net power gained or lost by the system ΔP_{net}. The net power ΔP_{net} offsets the rate of heat energy transferred by the

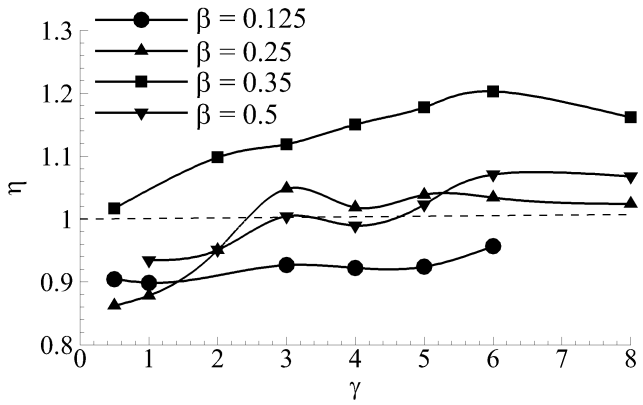

Figure 6.16: A plot of η against γ at $Re = 1300$, $H = 50$ and blockage ratios as indicated.

rate of work required to overcome duct friction when maintaining the flow. The system here refers to the setup under investigation (figure 4), for which ΔP_{net} is calculated using equation (2.86). In this section, the effectiveness of the wedges are evaluated using ΔP_{net}.

For a fixed Re and H, ΔP_{net} is calculated by considering a range of Eckert numbers Ec. As discussed in § 2.8.2, a positive value of ΔP_{net} represents a net power gain by the system and vice-versa, and Ec_{cr} gives the critical Eckert number where ΔP_{net} changes from positive to negative. The wedges are hence effective in terms of a net power gain to the system for all $Ec < Ec_{cr}$. Figure 6.17 shows Ec_{cr} as a function of H for $Re = 1300$ for two representative blockage ratios, $\beta = 0.25$ and 0.65. For fusion relevant conditions, $Ec \approx 4.838 \times 10^{-9}$, considering a mean velocity through the duct as $U_0 = 0.015$ m/s (Smolentsev *et al.*, 2010*b*), the specific heat capacity of the liquid-Lithium at fusion relevant temperature as $C_p \approx 186$ J/kgK (Schulz, 1991; de les Valls *et al.*, 2008) and the temperature difference of the the fluid from inlet to outlet to be $\Delta T \approx 250$ K (Smolentsev *et al.*, 2010*b*). The lowest Ec_{cr} for the current setup is around 2.928×10^{-2} indicating that there is always a net positive power gain for the current setup not just for fusion relevant conditions but also for a large range of Ec below Ec_{cr}.

6.5 Comparison with other enhancement techniques

In this section, a comparison of the performance of using repeated wedge protrusions for heat transfer enhancement in a quasi-two-dimensional MHD duct is made with other techniques which are available in the literature. While the efficiency of

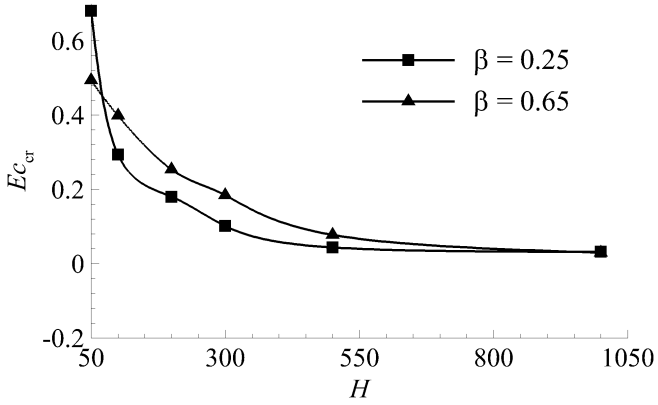

Figure 6.17: A plot of Ec_{cr} against H for $Re = 1300$ comparing $\beta = 0.25$ and 0.65 with $\gamma = 2$.

other wall protrusion strategies is not reported in the literature, the performance of the current approach can be compared against methods incorporating either immersed physical obstacles or electrically driven vortices. In a previous study considering the use of a cylindrical bluff body for vortex generation (Hussam & Sheard, 2013), with a parameter setting of $H = 100$ and $Re = 2000$, $\eta \approx 2.2$ was obtained for the best case. At similar H and Re, the current setup achieves $\eta \approx 1.5$ for the highest β investigated. A further increase can be achieved by setting the wedge pitch and angle at $\gamma_{\text{opt},\eta}$ and $\phi_{\text{opt},\eta}$ respectively. The present setup is effective at higher H cases up to $H \approx 500$ (§ 6.3), whereas the previous study did not consider cases with higher H, where there is a possibility of drastic reduction in η. The current configuration at an optimal blockage ratio gives an approximate three-fold increase in the heat transfer ratio than the use of square cylinder bluff bodies (Chatterjee & Gupta, 2015; Farahi & Hossein, 2017) at similar Hartmann numbers (corresponding to $H = 300$ and 500) at $Re = 2000$. Use of protrusions on the wall for vortex generation also seems to be more favourable for cases with lower H/Re compared to vortex generation using point electrodes in the duct (Hamid *et al.*, 2016*b*), which achieves relatively more η at higher H/Re. For similar flow parameters as in Hussam *et al.* (2012*a*), where a torsionally ocsillating cylinder was used as turbulent generator, the current setup can reach much higher $Nu \approx 6.39$ than the best case reported in their study which was about $Nu \approx 2.6$. Additionally, designing the current setup needs only a modification on the wall and no additional power requirement and mounting arrangements which may be required for other vortex generation strategies.

Chapter summary

In this chapter, the use of repeated wedge protrusions on the side walls of an MHD duct as a means to generate quasi-two-dimensional vortices and its influence on heat transfer characteristics from the side wall to the fluid flowing through the duct were discussed. The influence of both Hartmann friction parameter and Reynolds number on the heat transfer ratio and efficiency achieved was considered. The rise in H increases the dissipation rate of the quasi-2D vortices generated by the presence of wedges and convecting in the flow domain, whereas a rise in Re decreases the viscous dissipation rate, thereby having a negative and positive impact on heat transfer improvement, respectively. It was found that along with the flow parameters, geometric parameter settings of the wedge influences the strength of formation of the quasi-2D vortices generated, the way they interact with the Shercliff layers and the thermal boundary layers, thereby playing an important role in the achievable heat transfer efficiency. The optimal setting to achieve maximum efficiency was also identified for a range of H and Re. For the highest H investigated, an approximately five-fold improvement in the heat transfer ratio and approximately 50% increase in efficiency was obtained over a plane duct without wedges. A discussion in the final section compared the current setup to other techniques in the literature used for heat transfer enhancement. The use of wedges was found to be the most effective at lower H/Re and also achieved high performance at higher values of H relative to other cases.

Chapter 7

Conclusions and directions for future work

This study has explored the flow dynamics in hydrodynamic channel flows and magnetohydrodynamic duct flows with repeated wedge-shaped protrusions on one of the walls, and how these wall modifications could help improve the heat transfer rate and the overall heat transfer efficiency in magnetohydrodynamic duct flows. The studies in the literature which have used surface modifications for heat transfer enhancement are scarce for magnetohydrodynamic flows. The current study provides insight into the flow transitions in quasi-2D magnetohydrodynamic flows, and reports on enhancement in heat transition efficiency that could be achieved using wedge protrusions on the duct walls. Most studies on hydrodynamic cases have focused on high-Re turbulent flows. Few studies have explored the transitional regimes which are relevant for the application motivating the current study. This work therefore contributes to the understanding of the onset of instabilities and the route to turbulence in hydrodynamic wall-bounded flows with repeated protrusions.

This work consists of three broad parts. Firstly, hydrodynamic channel flows with repeated wedge protrusions were investigated, thereafter the quasi-2D magnetohydrodynamic counterpart was considered. Lastly, heat transfer studies were conducted for the quasi-2D magnetohydrodynamic flows. In this chapter, the conclusions drawn from these phases of the work are presented. The chapter is closed by discussing possible directions for future work.

7.1 Linear stability and non-linear interactions in hydrodynamic channel flows with repeated wedge-shaped protrusions

For the hydrodynamic channel flows with repeated wedge-shaped protrusions, three steady-state regimes are identified. These begin with the formation of a single recirculation region in front of the wedge, followed by the formation of a recirculation region further downstream of the wedge, extending between the current and subsequent wedge. Lastly, a merging of the two recirculation regions identified from the previous two-regimes is observed. In the first of the two unsteady flow regimes, a breakdown of the recirculation region formed in the last steady-state regime is observed. The final (unsteady) regime is associated with two-dimensional vortex shedding incepted at the wedge tip. The temperature fields associated with the steady and unsteady states of the flow are obtained and the enhancement in heat transfer with the onset of unsteadiness is discussed. A regime map is obtained for a range of blockage ratios, pitch and wedge angle values.

The onset of two-dimensional unsteadiness in the flow is found to occur through a global complex mode appearing as a wave spanning the streamwise domain length. The critical Reynolds number marking the onset of two-dimensional vortex shedding is preponed with increasing blockage ratio, pitch and wedge angle. However, the primary bifurcation of the two-dimensional flow is found to be three-dimensional, and occurs through a stationary mode well before the onset of the 2D instability. A similar mode is associated with the three-dimensional instability for a range of blockage ratios and pitch values that are considered in this study. Increasing blockage ratio and decreasing pitch both results in a decrease in the critical Reynolds number $Re_{cr,3\mathrm{D}}$. The global mode through which three-dimensional effects manifests in the flow appear as streamwise velocity streaks and are induced by the counter-rotating streamwise vortices concentrated near the wedge tip.

The analysis of the perturbation velocity components and their variation in the flow shows that the lift-up mechanism is responsible for the three-dimensional instability. The investigation of the perturbation kinetic energy budget of the instability modes shows that most of the the energy gain is through production due to horizontal shear in the base flow. The corresponding locations of maximum shear are in the region ahead and after the wedge tip. This finding is consistent through the range of blockage ratios and pitch values covered in this

study. The location of the wavemaker region in the flow found though sensitivity analysis matches with the locations of maximum shear, further supporting the previous finding from energetics analysis. The receptivity and structural sensitivity of the instability is also investigated to identify regions in the flow which are significant from a flow control perspective for placement of an active or passive control mechanism. Further, an endogeneity analysis is performed to understand the local contributions of the different terms in the momentum equation to the growth rate of the global eigenmode. The endogeneous approach shows that the local endogeneity contribution associated with the pressure gradient term features prominently in the total endogeneity fields for most of the cases considered, emphasizing its role in the local endogeneous eigendynamics in this system, despite its net contribution being identically zero.

To understand the short-time dynamics of the flow, the optimal linear growth of two- and three-dimensional disturbances was studied. The optimal modes are counter-signed inclined structures stacked adjacent to one another and concentrated near the first separation point of the recirculation region of the base flow formed after the wedge tip. The two-dimensional energy gain of the optimal mode structures as they convect downstream is predominantly through the Orr mechanism. There is also a brief period of energy gain when the disturbance structure impinges on the subsequent wedge. However, in contrast to similar confined flow setups (Blackburn *et al.*, 2008*a*,*b*; Marquet *et al.*, 2008), the current flow setup does not aid a significant transient energy growth over the range of geometric parameters considered in this study, thereby being an unlikely candidate for bypass transition.

In order to verify the two-dimensional and three-dimensional transition routes predicted by the linear analysis, firstly, non-linear two-dimensional simulations are conducted starting from the steady state two-dimensional flow solution allowing it to evolve naturally. It was found that the underlying disturbance fields evolve into the two-dimensional global mode found from the linear analysis, verifying the two-dimensional linear stability predictions. Thereafter, spectral element-Fourier three-dimensional simulations verify the predictions from the three-dimensional linear stability analysis, showing that the flow is unstable through a global linear mode. The influence of non-linear effects on the three-dimensional flow structures and on the corresponding temperature fields was discussed, highlighting how these could promote the heat transfer rate to the fluid. The Stuart–Landau model was used to study the nature of the primary three-dimensional instability which was consistently found to occur via a supercritical pitchfork bifurcation.

7.2 Stability of quasi-2D magnetohydrodynamic duct flows with repeated wedge protrusions

Three different steady flow regimes were identified for the quasi-2D magnetohydrodynamic duct flows under the SM82 model with repeated wedge protrusions over a range of Hartmann friction parameters. The flow streamline patterns in the low-H regime were similar to the corresponding non-MHD cases. A new recirculation region was observed immediately after the wedge tip in the intermediate range of H for blockage ratios $\beta \lesssim 0.5$, with the other recirculations being reduced in size. This second regime is absent for blockage ratios $\beta \gtrsim 0.5$. The last regime corresponds to the high-H cases, where the only dominant feature is a recirculation region immediately after the wedge tip for all the cases. Unlike the non-MHD cases, the primary bifurcation for the MHD cases occurs through a quasi-2D eigenmode leading to quasi-2D vortex shedding in the flow. The global modes are quasi-2D equivalent of the 2D global modes and are increasingly localised in the thin Shercliff layers on the bottom wall with increasing values of H. At a higher blockage ratio, the modes are concentrated near the reattachment point of the dominant recirculation region of the base flow.

The transient energy growth of quasi-2D perturbations is modest in the low and intermediate ranges of H, similar to the non-MHD cases. However, in the high-H regime a maximum optimal energy growth factor of approximately 10^5 was found at the highest H investigated in this study. In this range of H, both the optimal mode shape and their spatial location differ from the low, intermediate -H and non-MHD cases, with the optimal quasi-2D mode concentrated about the wedge tip for these cases. This is associated with the change in the base flow structure at higher H. The optimal mode gains energy while convecting over the free shear layer behind the wedge tip in this range of H, differing from the energy gain mechanism for the other cases. Despite the high energy amplification of the optimal modes, non-linear interactions of the quasi-2D optimal modes did not lead to a sub-critical transition. However, an optimal initial energy seeding of the optimal mode can delay the decay rate of the disturbance energy.

7.3 Heat transfer enhancement in quasi-2D magnetohydrodynamic duct flows using repeated wedge protrusions

The use of repeated wedge protrusions on one of the walls of an MHD duct was explored as a means to generate quasi-two-dimensional vortices and thus aid heat transfer from a hot wall to the fluid flowing through the duct. The study of the influence of vortex dynamics on the local Nusselt number was initially carried out. It showed that an interplay of the intensity of vortex formation at the wedge tip, the number of vortex merging with the convecting vortices, their intensities during merging, and interaction of the generated vortices with the Shercliff layer and the thermal boundary layer each influence the local Nusselt number distribution in the flow.

All of these features depend on the flow parameters and could be controlled to a certain extent with the variation of the geometric parameters of the wedge. Hence, the influence of each of the identified geometric parameters of the wedge on the heat transfer rate is explored at Hartmann numbers in the high-H range, considering a range of Re. The heat transfer ratio increases monotonically with increasing blockage ratio. At a higher blockage ratio, a wider range of H exists where the heat transfer ratio remains high.

Unlike the blockage ratio, an optimal value of pitch and wedge angle exists where maximum heat transfer rate could be achieved. An optimal pitch has a high intensity of vortex formation and is a favourable condition for a balance between increasing the number of vortex merging and the Hartmann dissipation of the convecting vortices. An optimal wedge angle allows for the vortices generated at the wedge tip to be cast at a favourable angle so as to neither sweep over the hot walls nor be cast away from them. A rise in H increases the dissipation rate of the quasi-2D vortices generated by the presence of wedges and convecting in the flow domain, whereas a rise in Re decreases the viscous dissipation rate, thereby having a negative and positive impact on heat transfer improvement, respectively.

The optimal geometric setting of the wedge to achieve maximum heat transfer efficiency is also identified for a range of H and Re. For the highest H investigated, an approximate five-fold improvement in the heat transfer ratio and an approximate 50% increase in heat transfer efficiency were obtained over a plane duct without wedges.

Besides the heat transfer efficiency, a net power analysis was also used as a quantifying parameter to calculate the effectiveness of using repeated wedge for

heat transfer enhancement. The current configuration was found to be effective over a range of Eckert numbers, and the critical Eckert number up to which the wedges could be effective is identified. The fusion blanket relevant Eckert number is well below the critical value identified, and hence these wedges are shown to be effective in those conditions. A comparison was made with other quasi-2D vortex generation techniques for heat transfer enhancement in MHD ducts, which shows that the technique of surface modification of the duct wall using wedge protrusions could be most effective at lower H/Re values and also achieves a high performance at higher H values relative to the alternative approaches.

7.4 Directions for future work

The current study investigated the flow dynamics in hydrodynamic channel flow with repeated wedge protrusions covering a wide range of geometric parameter variation. The focus has been mainly on understanding the linear dynamics of the flow. The non-linear simulations were conducted to verify the findings from the linear analysis. It also showed how the flow structures change when non-linear effects become dominant. Further investigations could be conducted on understanding the non-linear dynamics in these flows.

The study also investigated the quasi-2D dynamics of magnetohydrodynamic duct flows with repeated wedge protrusions covering a range of Hartmann friction parameters. Studies on the short-time dynamics showed a high energy amplification of quasi-2D optimal modes in the high-H range. Non-linear evolution of the quasi-2D optimal modes was found to delay the decay time of the disturbance energy. These non-linear evolutions considered only the quasi-2D disturbances. Further understanding on how the presence of three-dimensional disturbances could affect the flow dynamics can be a possible avenue for future studies. The study focused only on the quasi-2D dynamics, full three-dimensional simulations including the Hartmann layers can be carried out to understand the three-dimensional dynamics of these flows.

The heat transfer enhancement achieved in MHD duct flows using repeated wedge-shaped protrusions were investigated and optimal geometric settings to achieve maximum efficiency was obtained. The study showed that surface modification of the wall could be an effective way to increase heat transfer efficiency in MHD ducts. The current study did not take into account the radiative heat transfer and the volumetric heating which are important in the cooling blanket modules in magnetic confinement fusion reactors. Future studies can consider

these factors to get a more realistic picture on the heat transfer efficiency changes with surface modifications in MHD duct walls.

References

Abdou, M., Morley, N. B., Smolentsev, S., Ying, A., Malang, S., Rowcliffe, A. & Ulrickson, M. 2015 Blanket/first wall challenges and required R&D on the pathway to DEMO. *Fusion Eng. Des.* **100**, 2–43.

Airiau, C. & Castets, M. 2004 On the amplification of small disturbances in a channel flow with a normal magnetic field. *Phys. Fluids* **16** (8), 2991–3005.

Akervik, E., Hœpffner, J., Ehrenstein, U. & Henningson, D.S. 2007 Optimal growth, model reduction and control in a separated boundary-layer flow using global eigenmodes. *J. Fluid Mech.* **579**, 305–314.

Alam, T., Saini, R. P. & Saini, J. S. 2014 Use of turbulators for heat transfer augmentation in an air duct–A review. *Renew. Energ.* **62**, 689–715.

Alemany, A., Moreau, R., Sulem, P. L. & Frisch, U. 1979 Influence of an external magnetic field on homogeneous MHD turbulence. *J. de. Mec.* **18** (2), 277–313.

Armaly, B. F., Durst, F., Pereira, J. C. F. & Schönung, B. 1983 Experimental and theoretical investigation of backward-facing step flow. *J. Fluid Mech.* **127**, 473–496.

Baker, N. T., Pothérat, A. & Davoust, L. 2015 Dimensionality, secondary flows and helicity in low-Rm MHD vortices. *J. Fluid Mech.* **779**, 325–350.

Barkley, D., Blackburn, H. M. & Sherwin, S. J. 2008 Direct optimal growth analysis for timesteppers. *Int. J. Numer. Meth. Fl.* **57** (9), 1435–1458.

Barkley, D., Gomes, M.G. M. & Henderson, R. D. 2002 Three-dimensional instability in flow over a backward-facing step. *J. Fluid Mech.* **473**, 167–190.

Barleon, L., Burr, U., Mack, K. J. & Stieglitz, R. 2000 Heat transfer in liquid metal cooled fusion blankets. *Fusion Eng. Des.* **51–52**, 723–733.

Barleon, L., Casal, V. & Lenhart, L. 1991 MHD flow in liquid-metal-cooled blankets. *Fusion Eng. Des.* **14** (3–4), 401–412.

Bayly, B. J. 1988 Three-dimensional centrifugal-type instabilities in inviscid two-dimensional flows. *Phys. Fluids* **31** (1), 56–64.

Bayly, B. J., Orszag, S. A. & Herbert, T. 1988 Instability mechanisms in shear-flow transition. *Annu. Rev. Fluid Mech.* **20**, 359–391.

Bergman, T. L., Lavine, A. S., Incropera, F. P. & DeWitt, D. P. 2007 *Fundamentals of Heat and Mass Transfer*. USA: John Wiley & Sons.

Bhagoria, J. L., Saini, J. S. & Solanki, S. C. 2002 Heat transfer coefficient and friction factor correlations for rectangular solar air heater duct having transverse wedge shaped rib roughness on the absorber plate. *Renew. Energ.* **25** (3), 341–369.

Blackburn, H. M., Barkley, D. & Sherwin, S. J. 2008*a* Convective instability and transient growth in flow over a backward-facing step. *J. Fluid Mech.* **603**, 271–304.

Blackburn, H. M. & Sherwin, S. J. 2004 Formulation of a Galerkin spectral element–Fourier method for three-dimensional incompressible flows in cylindrical geometries. *J. Comput. Phys.* **197** (2), 759–778.

Blackburn, H. M., Sherwin, S. J. & Barkley, D. 2008*b* Convective instability and transient growth in steady and pulsatile stenotic flows. *J. Fluid Mech.* **607**, 267–277.

Branover, H., Eidelman, A. & Nagorny, M. 1995 Use of turbulence modification for heat transfer enhancement in liquid metal blankets. *Fusion Eng. Des.* **27**, 719–724.

Burr, U., Barleon, L., Mack, K. & Müller, U. 1999 *The effect of horizontal magnetic field on liquid metal Rayleigh–Benard convection*. Karlruhe: FZKA-Report No. 6277.

Camobreco, C. J., Pothérat, A. & Sheard, G. J. 2020 Subcritical route to turbulence via the Orr mechanism in a quasi-two-dimensional boundary layer. *Phys. Rev. Fluids* **5** (11), 113902.

Carlson, D. R., Widnall, S. E. & Peeters, M. F. 1982 A flow-visualization study of transition in plane poiseuille flow. *J. Fluid Mech.* **121**, 487–505.

Carvalho, M. G., Durst, F. & Pereira, J. C. F. 1987 Predictions and measurements of laminar flow over two-dimensional obstacles. *Appl. Math. Model.* **11** (1), 23–34.

Cassells, O. G. W., Hussam, W. K. & Sheard, G. J. 2016 Heat transfer enhancement using rectangular vortex promoters in confined quasi-two-dimensional magnetohydrodynamic flows. *Int. J. Heat Mass Trans.* **93**, 186–199.

Cassells, O. G. W., Vo, T., Pothérat, A. & Sheard, G. J. 2019 From three-dimensional to quasi-two-dimensional: transient growth in magnetohydrodynamic duct flows. *J. Fluid Mech.* **861**, 382–406.

Chatterjee, D. & Gupta, S. K. 2015 MHD flow and heat transfer behind a square cylinder in a duct under strong axial magnetic field. *Int. J. Heat Mass Trans.* **88**, 1–13.

Chaube, A., Sahoo, P. K. & Solanki, S. C. 2006 Analysis of heat transfer augmentation and flow characteristics due to rib roughness over absorber plate of a solar air heater. *Renew. Energ.* **31** (3), 317–331.

Chen, Y.T, Nie, J.H., Hsieh, H-T & Sun, L.J. 2006 Three-dimensional convection flow adjacent to inclined backward-facing step. *Int. J. Heat Mass Trans.* **49** (25–26), 4795–4803.

Chiba, K., Ishida, R. & Nakamura, K. 1995 Mechanism for entry flow instability through a forward-facing step channel. *J. Non Newton. Fluid Mech.* **57** (2–3), 271–282.

Chilcott, R. E. 1967 A review of separated and reattaching flows with heat transfer. *Int. J. Heat Mass Trans.* **10** (6), 783–797.

Chomaz, J.-M. 2005 Global instabilities in spatially developing flows: non-normality and nonlinearity. *Annu. Rev. Fluid Mech.* **37**, 357–392.

Citro, V., Luchini, P., Giannetti, F. & Auteri, F. 2017 Efficient stabilization and acceleration of numerical simulation of fluid flows by residual recombination. *J. Comput. Phys.* **344**, 234–246.

Davidson, P.A. 1997 The role of angular momentum in the magnetic damping of turbulence. *J. Fluid Mech.* **336**, 123–150.

Davidson, P. A. 2002 *An introduction to magnetohydrodynamics*. American Association of Physics Teachers.

Dennis, S. C. R. & Smith, F. T. 1980 Steady flow through a channel with a symmetrical constriction in the form of a step. *Proc. R. Soc. Lond. A Math. Phys. Sci.* **372** (1750), 393–414.

Dousset, V. & Pothérat, A. 2008 Numerical simulations of a cylinder wake under a strong axial magnetic field. *Phys. Fluids* **20** (1), 017104.

Drazin, P. G. & Reid, W. H. 2004 *Hydrodynamic Stability*, 2nd edn. UK: Cambridge University Press.

Dušek, J., Gal, P. Le & Frauniè, P. 1994 A numerical and theoretical study of the first Hopf bifurcation in a cylinder wake. *J. Fluid Mech.* **264**, 59–80.

Edwards, F. J. 1961 The heat transfer and friction characteristic for forced convention air flow over a particular type of rough surface. *Int. Dev. Heat Trans.* pp. 415–425.

Emerson, W. H. 1966 Heat transfer in a duct in regions of separated flow. In *International Heat Transfer Conference Digital Library*. Begel House Inc.

Erturk, E. 2008 Numerical solutions of 2-D steady incompressible flow over a backward-facing step, Part I: High Reynolds number solutions. *Comput. Fluids* **37** (6), 633–655.

Farahi, S. M. & Hossein, N. A. 2017 Investigation of magnetohydrodynamics flow and heat transfer in the presence of a confined square cylinder using SM82 equations. *Therm. Sci.* **21** (2), 889–899.

Frank, M., Barleon, L. & Müller, U. 2001 Visual analysis of two-dimensional magnetohydrodynamics. *Phys. Fluids* **13** (8), 2287–2295.

Gallaire, F., Marquillie, M. & Ehrenstein, U. 2007 Three-dimensional transverse instabilities in detached boundary layers. *J. Fluid Mech.* **571**, 221–233.

Garimella, S. V. & Eibeck, P. A. 1990 Heat transfer characteristics of an array of protruding elements in single phase forced convection. *Int. J. Heat Mass Trans.* **33** (12), 2659–2669.

Gartling, D. K. 1990 A test problem for outflow boundary conditions - flow over a backward-facing step. *Int. J. Numer. Meth. Fl.* **11** (7), 953–967.

Gerard-Varet, D. 2002 Amplification of small perturbations in a Hartmann layer. *Phys. Fluids* **14** (4), 1458–1467.

Ghia, K. N., Osswald, G. A. & Ghia, U. 1989 Analysis of incompressible massively separated viscous flows using unsteady Navier–Stokes equations. *Int. J. Numer. Meth. Fl.* **9** (8), 1025–1050.

Giannetti, F. & Luchini, P. 2007 Structural sensitivity of the first instability of the cylinder wake. *J. Fluid Mech.* **581**, 167–197.

Gresho, P. M., Gartling, D. K., Torczynski, J. R., Cliffe, K. A., Winters, K. H., Garratt, T. J., Spence, A. & Goodrich, J. W. 1993 Is the steady viscous incompressible two–dimensional flow over a backward–facing step at Re= 800 stable? *Int. J. Numer. Meth. Fl.* **17** (6), 501–541.

Griffith, M. D., Leweke, T., Thompson, M. C. & Hourigan, K. 2008 Steady inlet flow in stenotic geometries: convective and absolute instabilities. *J. Fluid Mech.* **616**, 111–133.

Gschwendtner, M. A. 2004 The Eckert number phenomenon: Experimental investigations on the heat transfer from a moving wall in the case of a rotating cylinder. *Heat Mass Transf.* **40** (6), 551–559.

Hamid, A. H. A., Hussam, W. K., Pothérat, A. & Sheard, G. J. 2015 Spatial evolution of a quasi-two-dimensional Kármán vortex street subjected to a strong uniform magnetic field. *Phys. Fluids* **27** (5), 053602.

Hamid, A. H. A, Hussam, W. K. & Sheard, G. J. 2016*a* Combining an obstacle and electrically driven vortices to enhance heat transfer in a quasi-two-dimensional MHD duct flow. *J. Fluid Mech.* **792**, 364–396.

Hamid, A. H. A., Hussam, W. K. & Sheard, G. J. 2016*b* Heat transfer augmentation of a quasi-two-dimensional MHD duct flow via electrically driven vortices. *Numer. Heat Transf.* **70** (8), 847–869.

Han, J. C. & Park, J. S. 1988 Developing heat transfer in rectangular channels with rib turbulators. *Int. J. Heat Mass Trans.* **31** (1), 183–195.

Hartmann, J. & Lazarus, F. 1937 *Hg-dynamics*. Levin & Munksgaard Copenhagen.

Henderson, R. D. & Barkley, D. 1996 Secondary instability in the wake of a circular cylinder. *Phys. Fluids* **8** (6), 1683–1685.

Henningson, D. S. & Reddy, S. C. 1994 On the role of linear mechanisms in transition to turbulence. *Phys. Fluids* **6** (3), 1396–1398.

Hill, D. C. 1995 Adjoint systems and their role in the receptivity problem for boundary layers. *J. Fluid Mech.* **292**, 183–204.

Holman, J. P. 2010 *Heat transfer*. McGraw-Hill.

Hossain, M. A. 1992 Viscous and Joule heating effects on MHD free convection flow with variable plate temperature. *Int. J. Heat Mass Trans.* **35** (12), 3485–3487.

Huang, H. & Li, B. 2011 Heat transfer enhancement of MHD flow by conducting strips on the insulating wall. *J. Heat Trans.* **133** (2), 021902.

Hussam, W. K., Hamid, A. H. A., Ng, Z. Y. & Sheard, G. J. 2018 Effect of vortex promoter shape on heat transfer in MHD duct flow with axial magnetic field. *Int. J. Thermal Sci.* **134**, 453–464.

Hussam, W. K. & Sheard, G. J. 2013 Heat transfer in a high Hartmann number MHD duct flow with a circular cylinder placed near the heated sidewall. *Int. J. Heat Mass Trans.* **67**, 944–954.

Hussam, W. K., Thompson, M. C. & Sheard, G. J. 2011 Dynamics and heat transfer in a quasi-two-dimensional MHD flow past a circular cylinder in a duct at high Hartmann number. *Int. J. Heat Mass Trans.* **54** (5–6), 1091–1100.

Hussam, W. K., Thompson, M. C. & Sheard, G. J. 2012*a* Enhancing heat transfer in a high Hartmann number magnetohydrodynamic channel flow via torsional oscillation of a cylindrical obstacle. *Phys. Fluids* **24** (11), 113601.

Hussam, W. K., Thompson, M. C. & Sheard, G. J. 2012*b* Optimal transient disturbances behind a circular cylinder in a quasi-two-dimensional magnetohydrodynamic duct flow. *Phys. Fluids* **24** (2), 024105.

Jordi, B. E., Cotter, C. J. & Sherwin, S. J. 2015 An adaptive selective frequency damping method. *Phys. Fluids* **27** (9), 094104.

Kaiktsis, L., Karniadakis, G. Em. & Orszag, S. A. 1996 Unsteadiness and convective instabilities in two-dimensional flow over a backward-facing step. *J. Fluid Mech.* **321**, 157–187.

Kamali, R. & Binesh, A. R. 2008 The importance of rib shape effects on the local heat transfer and flow friction characteristics of square ducts with ribbed internal surfaces. *Int. Commun. Heat Mass Transf.* **35** (8), 1032–1040.

Kanaris, N., Albets, X., Grigoriadis, D. & Kassinos, S. 2013 Three-dimensional numerical simulations of magnetohydrodynamic flow around a confined circular cylinder under low, moderate, and strong magnetic fields. *Phys. Fluids* **25** (7), 074102.

Karniadakis, G. Em., Israeli, M. & Orszag, S. A. 1991 High-order splitting methods for the incompressible Navier–Stokes equations. *J. Comput. Phys.* **97** (2), 414–443.

Karniadakis, G. Em. & Sherwin, S. 2013 *Spectral/hp Element Methods for Computational Fluid Dynamics*. Britain: Oxford University Press.

Karniadakis, G. Em. & Triantafyllou, G. S. 1992 Three-dimensional dynamics and transition to turbulence in the wake of bluff objects. *J. Fluid Mech.* **238**, 1–30.

Karwa, R. 2003 Experimental studies of augmented heat transfer and friction in asymmetrically heated rectangular ducts with ribs on the heated wall in transverse, inclined, V-continuous and V-discrete pattern. *Int. Commun. Heat Mass Transf.* **30** (2), 241–250.

Kirillov, I. R., Reed, C. B., Barleon, L. & Miyazaki, K. 1995 Present understanding of MHD and heat transfer phenomena for liquid metal blankets. *Fusion Eng. Des.* **27**, 553–569.

Klein, R. & Pothérat, A. 2010 Appearance of three dimensionality in wall-bounded MHD flows. *Phys. Rev. Lett.* **104** (3), 034502.

Kolesnikov, Y. B. & Tsinober, A. B. 1972 Two-dimensional turbulent flow behind a circular cylinder .

Krasnov, D., Rossi, M., Zikanov, O. & Boeck, T. 2008 Optimal growth and transition to turbulence in channel flow with spanwise magnetic field. *J. Fluid Mech.* **596**, 73–101.

Krasnov, D., Zikanov, O., Rossi, M. & Boeck, T. 2010 Optimal linear growth in magnetohydrodynamic duct flow. *J. Fluid Mech.* **653**, 273–299.

Krasnov, D. S., Zienicke, E., Zikanov, O., Boeck, T. & Thess, A. 2004 Numerical study of the instability of the Hartmann layer. *J. Fluid Mech.* **504**, 183–211.

Kumar, S. & Saini, R. P. 2009 CFD based performance analysis of a solar air heater duct provided with artificial roughness. *Renew. Energ.* **34** (5), 1285–1291.

Kundu, P. K. & Cohen, I. M. 2002 *Fluid mechanics*. Academic Press.

Landahl, M. T. 1975 Wave breakdown and turbulence. *J. Appl. Math.* **28** (4), 735–756.

Landau, L. D. & Lifshitz, E. M. 1976 *Mechanics*, 3rd edn. Pergamon Press.

Lanzerstorfer, D. & Kuhlmann, H. C. 2012*a* Global stability of the two-dimensional flow over a backward-facing step. *J. Fluid Mech.* **693**, 1–27.

Lanzerstorfer, D. & Kuhlmann, H. C. 2012*b* Three-dimensional instability of the flow over a forward-facing step. *J. Fluid Mech.* **695**, 390–404.

Larson, H. K. 1959 Heat transfer in separated flows. *J. Aero. Sci.* **26** (11), 731–738.

Lehoucq, R. B., Sorensen, D. C. & Yang, C. 1998 *ARPACK users' guide: solution of large-scale eigenvalue problems with implicitly restarted Arnoldi methods*. SIAM.

Lingwood, R. J. & Alboussiere, T. 1999 On the stability of the Hartmann layer. *Phys. Fluids* **11** (8), 2058–2068.

Liou, T. M. & Hwang, J. J. 1993 Effect of ridge shapes on turbulent heat transfer and friction in a rectangular channel. *Int. J. Heat Mass Trans.* **36** (4), 931–940.

Lock, R. C. 1955 The stability of the flow of an electrically conducting fluid between parallel planes under a transverse magnetic field. *Proc. R. Soc. Lond. A Math. Phys. Sci.* **233** (1192), 105–125.

Malang, S., Leroy, P., Casini, G.P., Mattas, R.F. & Strebkov, Y. 1991 Crucial issues on liquid metal blanket design. *Fusion Eng. Des.* **16**, 95–109.

Marino, L. & Luchini, P. 2009 Adjoint analysis of the flow over a forward-facing step. *Theor. Comp. Fluid Dyn.* **23**, 37–54.

Marquet, O. & Lesshafft, L. 2015 Identifying the active flow regions that drive linear and nonlinear instabilities. *arXiv preprint arXiv:1508.07620* .

Marquet, O., Lombardi, M., Chomaz, J. M., Sipp, D. & Jacquin, L. 2009 Direct and adjoint global modes of a recirculation bubble: lift-up and convective non-normalities. *J. Fluid Mech.* **622**, 1–21.

Marquet, O., Sipp, D., Chomaz, J. & Jacquin, L. 2008 Amplifier and resonator dynamics of a low-Reynolds-number recirculation bubble in a global framework. *J. Fluid Mech.* **605**, 429–443.

Mei, R. W. & Plotkin, A. 1986 Navier-Stokes solutions for laminar incompressible flows in forward-facing step geometries. *AIAAJ* **24** (7), 1106–1111.

Moffatt, H. K. 1967 On the suppression of turbulence by a uniform magnetic field. *J. Fluid Mech.* **28** (3), 571–592.

Moresco, P. & Alboussiére, T. 2004 Experimental study of the instability of the Hartmann layer. *J. Fluid Mech.* **504**, 167–181.

Morley, N. B., Smolentsev, S., Barleon, L., Kirillov, I. R. & Takahashi, M. 2000 Liquid magnetohydrodynamics – recent progress and future directions for fusion. *Fusion Eng. Des.* **51–52**, 701–713.

Mück, B., Günther, C., Müller, U. & Bühler, L. 2000 Three-dimensional MHD flows in rectangular ducts with internal obstacles. *J. Fluid Mech.* **418**, 265–295.

Müller, U. & Bühler, L. 2013 *Magnetofluiddynamics in Channels and Containers*. Germany: Springer.

Munson, B. R., Young, D. F., Okiishi, T. H. & Huebsch, W. W. 2009 *Fundamentals of Fluid Mechanics*. USA: John Wiley & Sons.

Ng, Z. Y., Vo, T. & Sheard, G. J. 2018 Stability of the wakes of cylinders with triangular cross-sections. *J. Fluid Mech.* **844**, 721.

Orr, W. M. F. 1907 The stability or instability of the steady motions of a perfect liquid and of a viscous liquid. Part II: A viscous liquid. In *Proceedings of the Royal Irish Academy. Section A: Mathematical and Physical Sciences*, pp. 9–68. JSTOR, Royal Irish Academy.

Paladini, E., Marquet, O., Sipp, D., Robinet, J. C. & Dandois, J. 2019 Various approaches to determine active regions in an unstable global mode: application to transonic buffet. *J. Fluid Mech.* **881**, 617–647.

Pollard, A., Wakarani, N. & Shaw, J. 1996 Genesis and morphology of erosional shapes associated with turbulent flow over a forward-facing step. *Coherent flow structures in open channels* pp. 249–265.

Pothérat, A. 2007 Quasi-two-dimensional perturbations in duct flows under transverse magnetic field. *Phys. Fluids* **19** (7), 074104.

Pothérat, A. 2012 Three-dimensionality in quasi–two-dimensional flows: Recirculations and Barrel effects. *Europhys. Lett.* **98** (6), 64003.

Pothérat, A., Sommeria, J. & Moreau, R. 2000 An effective two-dimensional model for MHD flows with transverse magnetic field. *J. Fluid Mech.* **424**, 75–100.

Provansal, M., Mathis, C. & Boyer, L. 1987 Bénard-von Kármán instability: transient and forced regimes. *J. Fluid Mech.* **182**, 1–22.

Reddy, S. C. & Henningson, D. S. 1993 Energy growth in viscous channel flows. *J. Fluid Mech.* **252**, 209–238.

Reed, C. B. & Picologlou, B. F. 1989 Sidewall flow instabilities in liquid metal MHD flow under blanket relevant conditions. *Fusion Technol.* **15** (2P2A), 705–715.

Sapardi, A. M., Hussam, W. K., Pothérat, A. & Sheard, G. J. 2017 Linear stability of confined flow around a 180-degree sharp bend. *J. Fluid Mech.* **822**, 813–847.

Schmid, P. J. & Henningson, D. S. 2001 *Stability and transition in shear flows*. Springer.

Schulz, B. 1991 Thermophysical properties of the Li (17) Pb (83) alloy. *Fusion Eng. Des.* **14** (3–4), 199–205.

Schumann, U. 1976 Numerical simulation of the transition from three-to two-dimensional turbulence under a uniform magnetic field. *J. Fluid Mech.* **74** (1), 31–58.

Sheard, G. J. 2011 Wake stability features behind a square cylinder: focus on small incidence angles. *J. Fluids Struct.* **27** (5–6), 734–742.

Sheard, G. J., Hussam, W. K. & Tsai, T. 2016 Linear stability and energetics of rotating radial horizontal convection. *J. Fluid Mech.* **795**, 1–35.

Sheard, G. J., Thompson, M. C. & Hourigan, K. 2004*a* Asymmetric structure and non-linear transition behaviour of the wakes of toroidal bodies. *Eur. J. Mech. B/Fluids* **23** (1), 167–179.

Sheard, G. J., Thompson, M. C. & Hourigan, K. 2004*b* From spheres to circular cylinders: non-axisymmetric transitions in the flow past rings. *J. Fluid Mech.* **506**, 45–78.

Shroff, G. M. & Keller, H. B. 1993 Stabilization of unstable procedures: the recursive projection method. *SIAM J. Numer. Anal.* **30** (4), 1099–1120.

Singh, I. & Singh, S. 2018 A review of artificial roughness geometries employed in solar air heaters. *Renew. Sust. Energ. Rev.* **92**, 405–425.

Šlančiauskas, A. 2001 Two friendly rules for the turbulent heat transfer enhancement. *Int. J. Heat Mass Trans.* **44** (11), 2155–2161.

Smith, A. M. O. 1955 On the growth of Taylor–Görtler vortices along highly concave walls. *Q. Appl. Math.* **13** (3), 233–262.

Smolentsev, S., Badia, S., Bhattacharyay, R., Bühler, L., Chen, L., Huang, Q., Jin, H-G., Krasnov, D., Lee, D-W., Valls, E Mas. De Les & others 2015 An approach to verification and validation of MHD codes for fusion applications. *Fusion Eng. Des.* **100**, 65–72.

Smolentsev, S., Moreau, R. & Abdou, M. 2008 Characterization of key magnetohydrodynamic phenomena in PbLi flows for the US DCLL blanket. *Fusion Eng. Des.* **83** (5–6), 771–783.

Smolentsev, S., Moreau, R., Bühler, L. & Mistrangelo, C. 2010*a* MHD thermofluid issues of liquid-metal blankets: phenomena and advances. *Fusion Eng. Des.* **85** (7–9), 1196–1205.

Smolentsev, S., Vetcha, N. & Abdou, M. 2013 Effect of a magnetic field on stability and transitions in liquid breeder flows in a blanket. *Fusion Eng. Des.* **88** (6–8), 607–610.

Smolentsev, S., Wong, C., Malang, S., Dagher, M. & Abdou, M. 2010*b* MHD considerations for the DCLL inboard blanket and access ducts. *Fusion Eng. Des.* **85** (7–9), 1007–1011.

Sommeria, J. 1986 Experimental study of the two-dimensional inverse energy cascade in a square box. *J. Fluid Mech.* **170**, 139–168.

Sommeria, J. 1988 Electrically driven vortices in a strong magnetic field. *J. Fluid Mech.* **189**, 553–569.

Sommeria, J. & Moreau, R. 1982 Why, how, and when, MHD turbulence becomes two-dimensional. *J. Fluid Mech.* **118**, 507–518.

Strykowski, P. J. & Sreenivasan, K. R. 1990 On the formation and suppression of vortex 'shedding' at low Reynolds numbers. *J. Fluid Mech.* **218**, 71–107.

Stüer, H., Gyr, A. & Kinzelbach, W. 1999 Laminar separation on a forward facing step. *Eur. J. Mech. B/Fluids* **18** (4), 675–692.

Sukoriansky, S., Klaiman, D., Branover, H. & Greenspan, E. 1989 MHD enhancement of heat transfer and its relevance to fusion reactor blanket design. *Fusion Eng. Des.* **8**, 277–282.

Takashima, M. 1996 The stability of the modified plane Poiseuille flow in the presence of a transverse magnetic field. *Fluid Dyn. Res.* **17** (6), 293.

Takashima, M. 1998 The stability of the modified plane Couette flow in the presence of a transverse magnetic field. *Fluid Dyn. Res.* **22** (2), 105–121.

Taneda, S. 1979 Visualization of separating stokes flows. *J. Phys. Soc. Jpn.* **46** (6), 1935–1942.

Thompson, M. C., Leweke, T. & Williamson, C. H. K. 2001 The physical mechanism of transition in bluff body wakes. *J. Fluids Struct.* **15** (3-4), 607–616.

Ting, A. L., Walker, J. S., Moon, T. J., Reed, C. B. & Picologlou, B. F. 1991 Linear stability analysis for high-velocity boundary layers in liquid-metal magnetohydrodynamic flows. *Int. J. Eng. Sci.* **29** (8), 939–948.

Trefethen, L. N., Trefethen, A. E., Reddy, S. C. & Driscoll, T. A. 1993 Hydrodynamic stability without eigenvalues. *Science* **261** (5121), 578–584.

Tropea, C. D. & Gackstatter, R. 1985 The flow over two-dimensional surface-mounted obstacles at low Reynolds numbers. *J. Fluids Eng. Trans. ASME* **107** (4), 489–494.

de les Valls, E. Mas, Sedano, L. A., Batet, L., Ricapito, I., Aiello, A., Gastaldi, O. & Gabriel, F. 2008 Lead–lithium eutectic material database for nuclear fusion technology. *J. Nucl. Mater.* **376** (3), 353–357.

Wee, D., Yi, T., Annaswamy, A. & Ghoniem, A. F. 2004 Self-sustained oscillations and vortex shedding in backward-facing step flows: Simulation and linear instability analysis. *Phys. Fluids* **16** (9), 3361–3373.

White, F. M. 2006 *Viscous Fluid Flow*. New York: McGraw-Hill.

Wilhelm, D., Härtel, C. & Kleiser, L. 2003 Computational analysis of the two-dimensional–three-dimensional transition in forward-facing step flow. *J. Fluid Mech.* **489**, 1–27.

Williams, P. T. & Baker, A. J. 1997 Numerical simulations of laminar flow over a 3D backward-facing step. *Int. J. Numer. Meth. Fl.* **24** (11), 1159–1183.

Xie, G., Zheng, S., Zhang, W. & Sundén, B. 2013 A numerical study of flow structure and heat transfer in a square channel with ribs combined downstream half-size or same-size rib. *Appl. Therm. Eng.* **61** (2), 289–300.

Yanase, S., Kawahara, G. & Kiyama, H. 2001 Three-dimensional vortical structures of a backward-facing step flow at moderate Reynolds number. *J. Phys. Soc. Jpn.* **70** (12), 3550–3555.

Zang, T. A. 1991 On the rotation and skew-symmetric forms for incompressible flow simulations. *Appl. Numer. Math.* **7** (1), 27–40.

Zhao, Y. & Zikanov, O. 2012 Instabilities and turbulence in magnetohydrodynamic flow in a toroidal duct prior to transition in Hartmann layers. *J. Fluid Mech.* **692**, 288–316.

Zikanov, O. & Thess, A. 1998 Direct numerical simulation of forced MHD turbulence at low magnetic Reynolds number. *J. Fluid Mech.* **358**, 299–333.